



TECHNISCHE UNIVERSITÄT
ILMENAU

Advanced Modeling in Lorentz Force Eddy Current Testing

Dissertation

zur Erlangung des akademischen Grades

**Doktoringenieur
(Dr.-Ing.)**

vorgelegt der

Fakultät für Elektrotechnik und Informationstechnik der
Technischen Universität Ilmenau

von Herrn

M.Sc. Konstantin Weise

(Porzig)

geboren am 12.12.1986 in Leipzig

Gutachter:

Herr Univ.-Prof. Dr.-Ing. habil. Hannes Töpfer (Betreuer)

Technische Universität Ilmenau

Herr Prof. Dr.-Ing. habil. Stanislaw Gratkowski

Westpommersche Technische Universität Stettin, Republik Polen

Herr Prof. Dr.-Ing. Ivo Dolezel

Westböhmisches Universität Pilsen, Tschechische Republik

Datum der wissenschaftlichen Aussprache: 23.03.2016

*"Indes sie forschten, röntgten, filmten, funkten, entstand von selbst die köstlichste Erfindung:
der Umweg als die kürzeste Verbindung zwischen zwei Punkten."*

— Erich Kästner

ABSTRACT

Nowadays, there is an increasing demand on reliable and efficient methods to evaluate materials and components in a nondestructive way. Particularly in the field of aerospace engineering, the components are subject to fulfill high quality and safety standards, which necessitate methods with a high accuracy, repeatability and inspection speed.

This work deals with the nondestructive testing method Lorentz force eddy current testing. Unlike traditional eddy current methods, the induction process is based on relative motion between a permanent magnet and the object under test. An integral part of this thesis is the development of a new magnet system with improved characteristics. The proposed design is based on the Halbach principle and is made of Neodymium-Iron-Boron alloys. Besides that, it contains a piece made of highly saturating iron-cobalt. In this sense, it was possible to increase and focus the magnetic flux density in the vicinity of the specimen. The development of a decent optimization strategy allows to determine problem specific magnet designs in dependence on the measurement requirements.

In the further course of this thesis, numerical simulations are performed addressing the uncertainty and sensitivity analysis of the system. Therefore, the model parameters are investigated in terms of their statistical properties. The resulting stochastic electromagnetic field problem is solved by means of the generalized polynomial chaos technique in combination with the finite element method. This enabled the identification of most influencing parameters in the system.

In the context of the uncertainty analysis, it is observed that the velocity obeys characteristic oscillations. In order to deepen the understanding of this phenomenon, an analytical approach is presented to evaluate the electromagnetic fields and forces while taking into account the resistive and inductive character of the moving conductor.

Finally, an alternative Lorentz force eddy current testing system is proposed where the object under test is encompassed by a ring magnet. The working principle is exemplified by theoretical considerations.

This work contributes to increase the knowledge and understanding about Lorentz force eddy current testing and intends to advance the current state of the art with new and innovative approaches.

ZUSAMMENFASSUNG

In der heutigen Zeit steigt der Bedarf an effizienten und leistungsfähigen Verfahren zur zerstörungsfreien Prüfung von Werkstoffen und Bauteilen rasant an. Besonders in den Bereichen Luft- und Raumfahrttechnik unterliegen die Bauteile hohen Qualitätsstandards im Sinne der Sicherheit. Dies setzt Verfahren mit hoher Genauigkeit, Wiederholbarkeit und Schnelligkeit voraus. Diese Arbeit befasst sich mit der Methode der Lorentzkraft-Wirbelstromprüfung. Im Gegensatz zu klassischen Induktionsverfahren werden die Wirbelströme aufgrund einer Relativbewegung zwischen einem Permanentmagneten und dem Prüfobjekt hervorgerufen.

Ein zentraler Gegenstand dieser Arbeit stellt die Entwicklung eines neuen Magnetsystems dar. Dieses basiert auf dem Halbach-Prinzip und besteht neben den bekannten Neodym-Eisen-Bor Legierungen aus einer Eisen-Kobalt-Verbindung mit hoher Sättigungsmagnetisierung. In diesem Sinn war es möglich die magnetische Flussdichte in der Nähe des Prüfkörpers zu fokussieren und zu verstärken. Die Entwicklung einer geeigneten Optimierungsroutine erlaubt die flexible Identifikation der Magnetgeometrie in Abhängigkeit der gestellten Anforderungen.

Im weiteren Verlauf wurden numerische Simulationen zur Unsicherheits- und Sensitivitätsanalyse durchgeführt. Im Zuge dessen wurden die Modellparameter hinsichtlich ihrer statistischen Eigenschaften untersucht. Das zugrunde liegende stochastische Feldproblem wurde mit Hilfe der Methode des "Generalized Polynomial Chaos" gelöst. Dies ermöglichte die Identifikation der wichtigsten Einflussgrößen im System.

Im Zusammenhang mit der Unsicherheitsanalyse wurden charakteristische Oszillationen der Relativgeschwindigkeit zwischen Permanentmagnet und Prüfkörper beobachtet. Um diese Phänomene besser verstehen zu können, wurde ein analytischer Zugang entwickelt, der die Bestimmung der elektromagnetischen Felder und Lorentzkräfte ermöglicht.

Zu guter Letzt wird ein alternatives System zur Lorentzkraft-Wirbelstromprüfung vorgestellt, indem der Prüfkörper von einem Ringmagneten umschlossen ist. Die prinzipielle Funktionsweise des neuen Systems wird mit theoretischen Vorbetrachtungen in Form von analytischen Lösungen aufgezeigt.

Die Arbeit vertieft die Kenntnisse über die Lorentzkraft-Wirbelstromprüfung und enthält neue sowie innovative Ansätze, die den Stand der Technik vorantreiben.

ACKNOWLEDGMENTS

At first, I want to express my special gratitude to my wife Johanna for her unlimited support during the period as doctoral candidate. Her efforts in all respects contributed enormously to reach this goal. She lovely took care of our son Noah who is gifted with the ability to switch my thoughts to something completely different within seconds.

I also want to express my warmest thanks to my parents Gabriele and Frank for their support during all my life.

Moreover, I sincerely want to express my thanks to Prof. Hannes Töpfer and Prof. Jens Haueisen for their continuous encouragement and criticism. This greatly helped to continuously learn and improve my way of working. They created a delightful and comfortable working environment which enabled the development of this thesis.

I also want to express my warmest thanks to Dr. Marek Ziolkowski and Dr. Hartmut Brauer for their invaluable support during the last years. In any period, they have taken their time to explain, teach and guide young people like me.

I further want to greatly acknowledge the flawless collaboration with my colleague Matthias Carlstedt. The conversations with him greatly advanced the creative process which was needed to continuously proceed further.

Additionally, I want to thank Reinhard Schmidt and Henning Schwanbeck for their support and back up during the last years.

Finally, I want to express my thanks to my colleagues from the whole research training group "Lorentz Force Velocimetry and Lorentz Force Eddy Current Testing". In hindsight, I am looking back to a great and exciting time during the last years.

NOMENCLATURE

Acronyms

ADRA	Absolute defect response amplitude
AGM	Arithmetic geometric mean
ANOVA	Analysis of variance
cdf	Cumulative distribution function
C	Cylinder
CM	Collocation method
dWRA	Direct weak reaction approach
DoF	Degrees of freedom
eWRA	Extended weak reaction approach
ECT	Eddy current testing
FEM	Finite element method
gPC	Generalized polynomial chaos
GMR	Giant magneto-resistance
HC	Halbach-Cylinder
HCp	Halbach-Cylinder with (passive) ferromagnetic material
LET	Lorentz force eddy current testing
LFV	Lorentz force velocimetry
LHS	Latin hypercube sampling
LoFoS	Lorentz force sigmometry
MAGLEV	Magnetic levitation
MC	Monte Carlo sampling
MDA	Moving defect approach
MECT	Motion induced eddy current testing
MMA	Moving magnet approach
NDT	Nondestructive testing
NRMSD	Normalized root mean square deviation
pdf	Probability density function
PoD	Probability of detection
QMC	Quasi Monte Carlo sampling
QSA	Quasi stationary approach

RD	Relative difference
SDT	Spin-dependent tunneling
SNR	Signal-to-noise ratio
SQP	Sequential quadratic programming
SQUID	Superconducting quantum interference device
VaFc	Volume adaptive force constraint
VcFc	Volume constraint force constraint

Variables	(Greek symbols)
------------------	------------------------

α	First shape parameter of a β -distributed random variable or Step size of optimization solver
β	Second shape parameter of a β -distributed random variable
Γ_a	Air boundary
Γ_c	Conductor boundary
$\Gamma(\cdot)$	Gamma function
$\delta(\cdot)$	Dirac delta distribution
Δ	Laplace operator
ε	Electric permittivity
ε_r	Relative electric permittivity
γ	Multi-index of orthogonal basis functions
λ	Set of multi-indices
μ	Magnetic permeability
μ_m	Expected value of the m -th quantity in gPC
μ_r	Relative magnetic permeability
∇	Nabla operator
ω	Angular frequency
ω_v	Angular frequency of the oscillating velocity
Ω_a	Air domain
Ω_c	Conducting domain
Ω_d	Defect domain
Ω_{Fe}	Ferromagnetic domain
Ω_m	Magnet domain
ϕ	Scalar electric potential
ψ	Magnetic scalar potential
$\psi^{(p)}$	Primary magnetic scalar potential
$\psi(\xi)$	Orthogonal basis function
$\Psi(\xi)$	Joint orthogonal basis function
ρ	Electric volume charge density or mass density
σ	Electrical conductivity

$[\sigma]$	Electrical conductivity tensor of second rank
σ_m^2	Variance of the m -th quantity
Σ	Set of events
Θ	Event space
ξ	Vector of random variables

Variables	(Latin symbols)
a	Lower bound of β -distributed random variable in gPC or Edge length of equivalent defect in optimization or Length of parallelepipedial permanent magnet in analytical modeling
\mathbf{a}_σ	Anisotropy vector of the electrical conductivity
\mathbf{A}	Magnetic vector potential
\mathbf{A}^*	Modified magnetic vector potential
$\tilde{\mathbf{A}}$	Fourier transform of the magnetic vector potential
$[\mathbf{A}_{\text{HCp}}]$	Linear inequality constraint matrix for HCp magnets
b	Upper bound of β -distributed random variable or Width of parallelepipedial permanent magnet in analytical modeling
\mathbf{b}_{HCp}	Linear inequality constraint vector for HCp magnets
\mathbf{B}	Magnetic flux density
$\mathbf{B}^{(d)}$	Distorted magnetic flux density
$\mathbf{B}^{(p)}$	Primary magnetic flux density
$\mathbf{B}^{(s)}$	Secondary magnetic flux density
\mathbf{B}_r	Magnetic remanence
c	Height of parallelepipedial permanent magnet in analytical modeling
c_{nl}	Nonlinear inequality constraint
\mathbf{c}_l	Linear inequality constraints
\tilde{C}	Complex constant in analytical modeling
d	Defect depth
\mathbf{d}_x	Search direction in optimization
\tilde{D}	Complex constant in analytical modeling
\mathbf{D}	Electric displacement field
\mathbf{E}	Electric field
f	Frequency
f_v	Frequency of the oscillating permanent magnet
$\Delta\tilde{F}_x$	Absolute defect response signal amplitude
$\Delta\tilde{F}_x^{(s)}$	Scaled absolute defect response signal amplitude
$\Delta\mathbf{F}$	Absolute defect response signal
$F_x^{(c)}$	Scaled maximum drag-force (constraint)
$F_x^{(\text{max})}$	Unscaled maximum drag-force

F	Lorentz force
F ⁽⁰⁾	Stationary unperturbed Lorentz force
\mathcal{F}	Feasible set of solutions
$\mathcal{F}_x(\cdot)$	Fourier transform with respect to the variable x
\mathcal{G}^{gPC}	Computational grid of the gPC
\mathcal{G}^{MC}	Computational grid of the MC
h	Lift-off distance
h	Nonlinear equality constraints
H	Height of permanent magnet
H	Magnetic field strength
$\mathcal{H}(\cdot)$	Hilbert transform
\tilde{I}	Fourier transformed current distribution
$\tilde{\mathbf{I}}$	Vector of Fourier transformed source current distribution
I_n	n -th order modified Bessel function of the first kind
J_n	n -th order Bessel function of the first kind
J	Current density
J _{e}	External current density
$k_{x y}$	Spatial frequencies in x or y
K	Laboratory frame of reference (source)
K'	Fixed frame of reference (conductor)
K_n	n -th order modified Bessel function of the second kind
L	Characteristic length
[L]	Hessian of Lagrangian
\mathcal{L}	Lagrangian
M	Number of output quantities of a system in gPC
M_m	Mass of the magnet
M	Magnetization
n	Unit normal vector
N	Number of random variables
N_c	Number of gPC coefficients
N_d	Number of deterministic forward simulations
p	Expansion order of the gPC
$p(\xi)$	Probability density function
p	Set of system parameters
P	Function assigning an event to a probability
$\mathcal{P}_{N_c}^p$	Polynomial space of dimension N_c and order p
q	Number of grid points in one dimension in gPC
rect(\cdot)	Rectangular function
R	Radius

R_m	Magnetic Reynolds number
\mathbf{s}	Vector of scaling parameters
S	Scaling parameter
$S_{i,m}^{(\delta)}$	Derivative based sensitivity coefficient
$S_{i,m}^{(n)}$	n -th order Sobol index
Δt	Time step
t	Time
\mathbf{T}	Electric current vector potential
\hat{u}	gPC-coefficient
\mathbf{u}	Lagrangian multipliers of equality constraints
U_{sec}	Induced voltage in secondary ECT coil
v_0	Rectilinear part of the velocity
v_1	Oscillation amplitude of the velocity
\mathbf{v}	Velocity or Lagrangian multipliers of inequality constraints
V_d	Volume of defect
V_m	Volume of magnet system
w	Wall-thickness ratio of tubular conductors
\mathcal{W}^{gPC}	Grid of weights used in the Gauss-quadrature of the gPC
Δx	Step size
\mathbf{x}	Design variables
$\tilde{\mathbf{x}}$	Optimal design variables
X_d	x -dimension of the defect
X_s	x -dimension of the specimen
Y_d	y -dimension of the defect
Y_s	y -dimension of the specimen
\mathbf{Y}	Vector of output quantities of a system in gPC
Z_d	z -dimension of the defect
Z_s	z -dimension of the specimen

Constants

ϵ_0	Electrical permittivity of free space ($8.854 \times 10^{-12} \frac{\text{As}}{\text{Vm}}$)
μ_0	Magnetic permeability of free space ($4\pi \times 10^{-7} \frac{\text{Vs}}{\text{Am}}$)
c_0	Velocity of light in vacuum ($2.998 \times 10^8 \frac{\text{m}}{\text{s}}$)
g	Standard gravitational acceleration ($9.807 \frac{\text{m}}{\text{s}^2}$)

TABLE OF CONTENTS

Abstract	iii
Zusammenfassung	v
Acknowledgments	vii
Nomenclature	ix
Table of Contents	xv
List of Tables	xix
List of Figures	xxi
1 Introduction	1
1.1 Motivation	1
1.2 Thesis Aims	2
1.3 Thesis Layout	3
2 State of the Art in Nondestructive Testing	5
2.1 Nondestructive Testing and Evaluation	5
2.2 Eddy Current Testing	7
2.3 Motion-Induced Eddy Current Testing	11
2.4 Lorentz Force Eddy Current Testing	13
2.4.1 General Principle and Preparatory Work	13
2.4.2 Problem Definition and Laboratory Setup	14
2.5 Comparison of ECT and LET	16
3 Theory	19
3.1 Electrodynamics of Moving Media	19
3.2 Numerical Approaches	24
3.2.1 Computational Domains and Potential Functions	25
3.2.2 Time Dependent Approaches	27
3.2.3 Quasi Stationary Approach	29

TABLE OF CONTENTS

3.2.4	Weak Reaction Approaches	31
3.2.5	Summary and Overview	33
3.3	Comparison of Numerical Approaches	33
4	Simulation Studies	43
4.1	Optimal Magnet Design for LET	43
4.1.1	Introduction and Motivation	43
4.1.2	Methods	44
4.1.3	Optimization Results and Discussion	59
4.1.4	Prototypes of Optimized LET Magnet Systems	65
4.1.5	Defect Depth Study	67
4.1.6	Conclusions	69
4.2	Uncertainty Analysis in LET	71
4.2.1	Introduction and Motivation	71
4.2.2	The Generalized Polynomial Chaos Method	73
4.2.3	Problem Definition in LET	80
4.2.4	Uncertainty Quantification of Model Parameters	82
4.2.5	Results and Discussion	85
4.2.6	Conclusions	87
4.3	Lorentz Forces in the Case of Oscillating Velocity Profiles	89
4.3.1	Introduction and Motivation	89
4.3.2	Mathematical Formulation of the Problem	91
4.3.3	Comparison to Numerical Simulations	99
4.3.4	Results and Discussion	103
4.3.5	Conclusions	110
5	Alternative LET System Using a Ring Magnet	111
5.1	Introduction and Motivation	111
5.2	Mathematical Formulation of the Problem	113
5.2.1	Single Wire Model	113
5.2.2	Axially Magnetized Ring Magnets	117
5.2.3	Radially Magnetized Ring Magnets	118
5.2.4	The Creeping Ring Magnet	119
5.2.5	Numerical Model	120
5.3	Results and Discussion	121
5.4	Conclusions	126
5.5	Patented LET System	127
6	Summary and Outlook	129
6.1	Summary	129

6.2 Outlook and Future Work	130
A 2-D Fourier Transform of a Circular Current Loop	133
B Solution of the Magnetic Vector Potential for Ring Magnets	137
B.1 Solid Conductors	137
B.2 Tubular Conductors	137
Bibliography	139

LIST OF TABLES

TABLE	Page
2.1 Overview of ECT studies using different magnetic field sensors	10
2.2 Parameters of the LET setup and characteristic values	14
3.1 Overview of numerical approaches to modeling the field problem in LET	34
3.2 Parameters of the exemplary LET problem	35
4.1 Connection between probability distributions and polynomial basis in gPC	74
4.2 Results of the exemplary problem investigated with the gPC	80
4.3 Limits and shape parameters of fitted probability distributions	85
4.4 Averaged δF between gPC and MC for two characteristic magnet positions	86
4.5 First order Sobol indices of F_x and F_z	87
4.6 Parameters of the exemplary problem used in the analysis of harmonic motion	100
5.1 Parameters of the exemplary problem involving a ring magnet	121

LIST OF FIGURES

FIGURE	Description
2.1	Overview of NDT methods 6
2.2	Expected global sales breakdown by technology of total NDT equipment in 2016 . . 7
2.3	Basic principle of eddy current testing 8
2.4	Two different MECT type methods 11
2.5	General principle and geometrical parameters of the LET system 13
2.6	Schematic eddy current profiles in LET 15
2.7	Laboratory LET setup 16
2.8	X-ray images and FEM model of the ECT probe PKA-48 17
2.9	Normalized defect response signals in case of ECT and LET 17
2.10	Modulated induced voltage in the pick-up coils in case of moving objects under test 18
3.1	The laboratory frame K and the rest frame K' 20
3.2	General principle of the moving defect approach (MDA) 27
3.3	General principle of the moving magnet approach (MMA) 29
3.4	General principle of the quasi-stationary approach (QSA) 30
3.5	General principle of the extended weak reaction approach (eWRA) 32
3.6	General principle of the direct weak reaction approach (dWRA) 33
3.7	Comparison of $\Delta F_{x z}$ between different model approaches for isotropic specimens . . 37
3.8	Comparison of $\Delta F'_{x z}$ between different model approaches for isotropic specimens . . 38
3.9	NRMSD of $\Delta F_{x z}$ for different model approaches 39
3.10	RD of $F_{x z}^{(0)}$ for different model approaches 40
4.1	Geometrical parameters of the LET setup used throughout the optimization 45
4.2	Overview of magnetic materials 46
4.3	Initial magnetization curve of the iron-cobalt-alloy VACOFLUX [®] 50 47
4.4	Optimization procedure of the volume adaptive force constraint (VaFc) approach . . 52
4.5	Procedure to compute the nonlinear objective and constraint function 57
4.6	HCp-magnet system for the system parameters $V_m/V_d = 56$, $d/h = 10$, and $a/h = 5$. 60
4.7	HCp-magnet system for the system parameters $V_m/V_d = 875$, $d/h = 2$, and $a/h = 2$. 62
4.8	Comparison of ADRA between different magnet systems as a function of V_m/V_d . . . 64
4.9	Magnetic flux density and induced current density of optimized magnet systems . . 65

4.10	Relative defect response of segmented HCp-magnet systems	66
4.11	Geometry of the HCp-prototype	66
4.12	Geometry of the experimental setup to detect a deep-lying slits	67
4.13	Measured profiles of the drag- and lift-force in the defect depth study	68
4.14	Overview of methods in uncertainty analysis	72
4.15	2-D example to illustrate the working principle of gPC	79
4.16	Illustration of the computational grids from the gPC and the MC approach	81
4.17	Experimental setup to determine the effective remanence	83
4.18	Determined probability density functions of the model parameters in LET	84
4.19	Numerically and experimentally obtained Lorentz forces in the uncertainty analysis	87
4.20	Permanent magnet moving with a sinusoidal velocity profile	89
4.21	Configuration of current carrying coils moving relative to a conducting slab	91
4.22	Current models used to model permanent magnets	95
4.23	Harmonics of Fourier transformed oscillating magnetic field sources	97
4.24	Comparison of the time-dependent drag- and lift-force density in (N/m)	102
4.25	Induced current density and magnetic flux density in case of oscillating magnets	103
4.26	Stationary drag- and lift-force acting on moving magnets	104
4.27	Time-dependent drag- and lift-force acting on harmonically oscillating magnets	105
4.28	Relative force perturbations as a function of f_v and v_0	107
4.29	Time-dependent drag- and lift-force waveforms for low, moderate and high v_0	108
4.30	Time-dependent drag-force at $v_0^{(\max)} = 29.8$ m/s for different f_v	109
5.1	Moving conductor through a ring magnet	112
5.2	Geometry of the ring magnet problem	113
5.3	Current models of permanent magnet rings	118
5.4	Magnetic flux density of ring magnets computed analytically and by the FEM	122
5.5	Lorentz force as function of $\mu_0\sigma v$ for different wall-thickness ratios w/R_{oc}	123
5.6	Lorentz force as function of $\mu_0\sigma v$ in case of $w/R_{oc} = 1$ for different values of μ_r	123
5.7	Induced eddy current density distribution J_φ for different $\mu_0\sigma v$ products	124
5.8	Time-dependent velocity of ring magnets falling down a solid copper rod	125
5.9	Patented LET system	127
5.10	Lateral forces $F_{x y}$ of a ring magnet system in case of a passing subsurface defect	128

INTRODUCTION

1.1 Motivation

Nondestructive testing (NDT) of materials and products is of great interest in a variety of modern engineering applications. Nowadays, the expectancy in performance of new devices has been increasing. NDT in general enables the initial inspection of test samples to confirm the structural integrity of safety-relevant components without causing damage. In this sense, it provides quality control while being cost effective in the same way. The presence of NDT is hard to perceive in everyday life. However, NDT provides ground to identify and prevent failure of socially relevant parts of our life like airplanes, railroads and power plants. It is therefore essential to maintain a uniform quality level to avoid accidents and save human life. Besides that, it allows in service monitoring of test pieces before assembling. It also plays a major role in the framework of process control to prevent undesirable and dangerous operation of systems. Combining all this, manufacturers and other users are interested to apply methods, which are reliable, accurate and cheap.

The present work focuses on electromagnetic NDT methods and more specifically on the technique Lorentz force eddy current testing (LET). Traditional eddy current testing methods (ECT) make use of time-dependent magnetic fields to induce eddy currents in the object under test. Those are altered in the presence of physical irregularities such as flaws, cracks or inclusions. In ECT, the variations are detected by measuring the magnetic field produced by the eddy currents. In contrast to traditional eddy current methods, LET makes use of relative motion between the object under test and a permanent magnet. The induced eddy currents interact with the applied magnetic field and result in a Lorentz force. Considering Newtons third law, this force acts on both, the specimen and the magnet itself, where it is measured. This quantity is used to evaluate the integrity of the structure under test. In this sense, LET differs

from traditional ECT methods in the way how the eddy currents are induced and how signals are evaluated. The LET method was originally proposed by Brauer and Ziolkowski in 2008 [1]. Decent advantages are lying in the application of stationary magnetic fields, which potentially allows the detection of defects lying deep inside the object under test. The working principle of LET permits the inspection of moving parts as it is frequently found in an industrial setting. The fabrication process of aluminium for example takes place at velocities of up to 20 – 30 m/s. Even higher velocities can be observed in wire drawing processes where speeds in the range of 40 – 60 m/s can be observed. This necessitates an NDT method like LET which is capable to test moving objects.

1.2 Thesis Aims

This thesis aims to enhance and deepen the understanding of the LET method and underlying principles associated with it. The work is primarily focused on the theoretical and numerical analysis of the electromagnetic field problem, which involves moving conductors in the vicinity of stationary magnetic field sources.

One important goal of this thesis is the development of more advanced LET sensor systems in order to increase the feasibility as well as the testing capability of the method. It is intended to propose magnet systems with inherently improved characteristics in form of an increased signal-to-noise ratio. An increase in energy density directly affects the performance of the sensor system. It is intended to determine the optimal volume and mass according to the imposed measuring task, which provides ground for future sensor miniaturization. This way, LET becomes competitive and comparable to other NDT techniques. Another goal is to provide valuable support for an extended experimental validation. Since no laboratory setup can be assumed to be ideal, such an investigation involves a stochastic treatment of the most influencing parameters. It is intended to quantify force intervals by means of numerical simulations in which the measured quantities are expected. This is in accordance to the treatment and analysis of parasitic effects, such as non-constant velocity profiles. When those effects are sufficiently understood, one is able to find a valuable and useful solution to it or even make use thereof.

In order to reach the intended goals, the following objectives are defined:

1. Development of an optimization approach to determine enhanced magnet designs for LET.
2. Sensitivity and uncertainty analysis of the LET system under investigation to identify the most important sources of uncertainty.
3. Analysis of the impact of parasitic effects such as non-constant velocity profiles on the resulting Lorentz force.
4. Verification and validation of the obtained results and expressions by comparing them to other numerical techniques or measurement data.

5. Extension of the fields of application of LET by proposing innovative system designs.

1.3 Thesis Layout

At first, an introduction and overview about NDT is given in Chapter 2, which is primarily focused on eddy current methods including recent developments. The mathematical description and the physical basics of the LET problem is given in Chapter 3. In this regard, the different numerical methods used throughout this thesis are described. Their applicability is studied and a comparison between them is drawn. Chapter 4 contains the main part of this thesis. It is subdivided into three sections, the first of which is concerned with the description of the developed optimization strategy to determine magnet designs with inherently improved characteristics. In the further course of this study, a new type of Halbach-magnet is proposed, designed and manufactured. The second section of this chapter addresses the sensitivity and uncertainty analysis of the present LET setup from the numerical point of view, which is supported by statistical data obtained experimentally. In the last section of this chapter, the impact of time-dependent velocity profiles is investigated. Those were observed during the uncertainty analysis. In Chapter 5, an alternative LET system, consisting of a ring magnet which encompasses the object under test, is presented. Analytical formulas are provided to deepen the understanding of the working principle. The thesis concludes with a summary and suggestions for future work in Chapter 6.

STATE OF THE ART IN NONDESTRUCTIVE TESTING

This chapter is an introduction into the state-of-the-art of nondestructive testing methods with a primary focus on electromagnetic techniques. The basic principle of the traditional eddy current testing method is described, followed by an introduction and overview of motion-induced eddy current testing methods. Finally, the Lorentz force eddy current testing technique is described and a closer look on preparatory work is given. The chapter concludes with a comparison between the classical eddy current testing method and Lorentz force eddy current testing.

2.1 Nondestructive Testing and Evaluation

The first NDT method, which was applied in an industrial setting, was the nowadays well known X-ray technique. It was discovered in 1895 by Wilhelm Conrad Roentgen who explicitly mentioned the possibility of flaw detection [2]. Beside X-ray imaging, numerous NDT methods evolved over time and are commonly used in the field of electrical, mechanical or civil engineering. Nowadays, a variety of methods exist which are developed to solve distinct measurement tasks. An overview of those, depending on the underlying frequencies, is shown in Fig. 2.1. The variety ranges from vibration analysis, acoustic emission up to ultrasonic testing [3]. On the other hand, electromagnetic methods are very popular and find application in form of magnetic particle, eddy current, microwave, thermography, X-ray and gamma-ray inspection [4].

In the general public, one of the most prominent application of NDT is given in the framework of airport security. Every piece of luggage undergoes X-ray inspection prior loading on board. Currently, it can be observed that security screening of passengers based on conventional metal screening devices and palpation is going to be replaced by full body imaging using Terahertz scanners. Those devices provide advanced imaging of non-metallic objects in a shorter

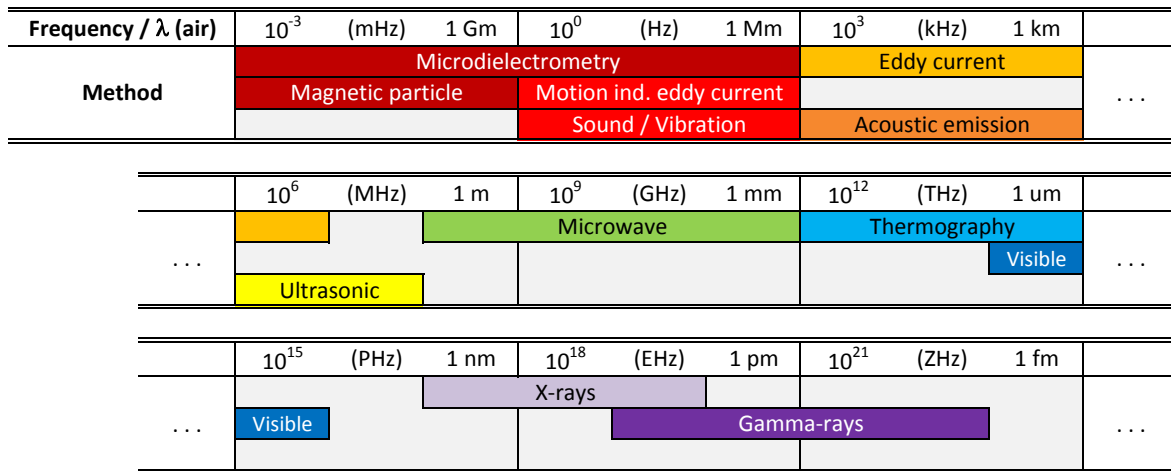


Figure 2.1: Overview of NDT methods.

time. They are already in service in the United States of America since 2010. In Germany, they are still heavily discussed and the passengers have the freedom to decide which security gate to pass.

During the last decades, NDT equipment advanced rapidly. The periphery around the sensor system offers the computational power to adaptively control the NDT equipment or to evaluate a tremendous amount of data in real-time. Considering the sensor technology, regardless of the particular testing method, a trend towards continuous improvement and miniaturization can be observed. The development of more compact, robust and sensitive sensor systems with a high resolution defines the shape of future sensor systems. Besides that, there is a demand of accelerating the testing process. In consequence, the time factor gains in importance expressing the need of faster methods which are capable to fulfill the imposed requirements. Recent developments in ultrasonic testing made use of perfect gas impedance matching to be able to compete with laser profiling technology. By these attempts, it was possible to apply ultrasonic testing in the framework of surface flaw detection in case of moving objects.

In recent decades, a number of companies are founded to access the NDT market. An analysis by Frost & Sullivan [5] points out the expected market share of NDT equipment in 2016. The pie chart in Fig. 2.2 shows that electromagnetic NDT methods are well represented beside ultrasonic, visual, and radiographic testing. The commercialization resulted in a restricted accessibility of knowledge to the scientific community. Much of it is declared as confidential and remains in the companies. This circumstance often hampers the scientific activity.

The present work focuses on the analysis of motion-induced eddy current testing techniques and more specifically, Lorentz force eddy current testing. In motion-induced eddy current testing, a precise classification in terms of frequency, as it is done in Fig. 2.1, is not possible since the incident field is non-harmonic and consists of a plurality of frequencies. However, when the relative velocity between the test object and the stationary magnetic field is in the range of

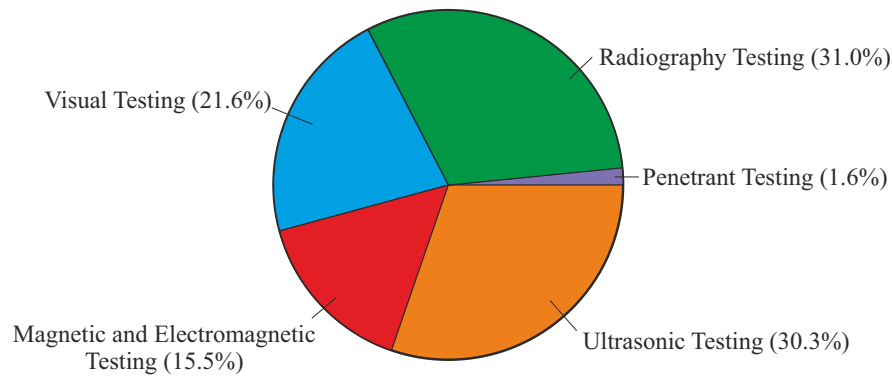


Figure 2.2: Expected global sales breakdown by technology of total NDT equipment in 2016 [5].

a few m/s, the method may be considered as "low-frequency" in the medium Hertz range. In contrast, traditional eddy current methods make use of alternating fields, whose frequency can be adjusted according to the underlying measurement task. In the next section, the state-of-the-art of the traditional ECT method is presented. It is directly followed by an overview of currently available motion-induced eddy current testing methods with a primary focus on LET.

2.2 Eddy Current Testing

Eddy current testing is an extensively used method for the inspection of electrically conducting objects. The method allows the contactless detection of defects in ferromagnetic and non-ferromagnetic materials. The general principle of ECT is shown in Fig. 2.3. It is based on the induction of eddy currents inside the object under test. This is achieved by a coil, driven by an alternating current, which generates a time-dependent primary magnetic field $\mathbf{B}^{(p)}$. Conductivity anomalies are revealed by measuring the variations in the magnetic field resulting from a perturbed eddy current distribution \mathbf{J} . The origin of the method can be traced back to the work done by Dr. Friedrich Foerster in the 1960s. Early work on the analytical analysis of the field problem in ECT is done by Dodd and Deeds in 1968 [6]. They evaluated the impedance variations in secondary pick-up coils as a direct consequence of a perturbed eddy current profile in case of defective conductors.

Typical areas of application include the evaluation of safety-sensitive parts in nuclear power plants, aircraft structures [7, 8] as well as in the petroleum or automotive industry, respectively, or for the inspection of printed circuit boards [9]. Very recently, its application is extended to inspect carbon-fiber-reinforced polymers [10, 11], which shows that the continued development of eddy current techniques is still of great interest. The challenging task in ECT is to detect deep-lying defects. The measurement task lies in the detection of weak changes in the magnetic field in close vicinity of the excitation coil. The induced eddy currents generate a secondary magnetic field $\mathbf{B}^{(s)}$ for itself. This counteracts the exciting primary field $\mathbf{B}^{(p)}$. The total magnetic field $\mathbf{B} = \mathbf{B}^{(p)} + \mathbf{B}^{(s)}$ is expelled out of the conductor with electrical conductivity σ

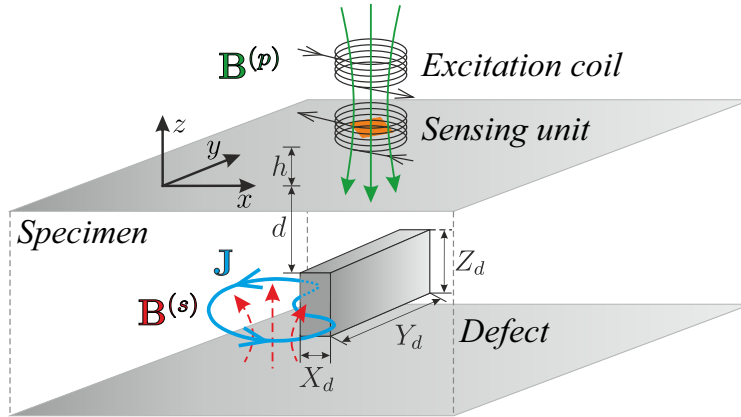


Figure 2.3: Basic principle of eddy current testing. An excitation coil, including a sensing unit, is located at a lift-off distance h above the specimen. A defect of length X_d , width, Y_d , and height Z_d is located at a depth d .

and magnetic permeability μ in case of high frequencies $\omega = 2\pi f$. Thus, the eddy currents are concentrated near the surface of the conductor. This phenomenon is called skin-effect and can be approximated by the skin-depth δ :

$$\delta = \sqrt{\frac{2}{\omega\sigma\mu}}. \quad (2.1)$$

It approximates the depth below the surface of the conductor at which the current density is decreased to $1/e$ of its surface value. This definition is derived from the case of a sinusoidal current in a homogeneous conducting half-space. It represents a physical limit, which cannot be overcome. Therefore, in order to inspect deep-lying defects, the excitation frequency has to be reduced. However, the detection of subsurface defects requires sensors having a high sensitivity and low intrinsic magnetic noise to improve the signal to noise ratio (SNR). At the early stage of ECT, the most common sensors were secondary pick-up coils. In that case, the defect signal consists of the relative change in impedance with respect to the sensor position. When decreasing the frequency, the rate of change of the magnetic flux density perturbation due to impurities is reduced and pick-up coil-type sensors become ineffective. In the following, some alternative magnetic field sensors, applied in the framework of ECT, are presented. It is emphasized that those are not restricted to ECT and are also applied to some extent in the framework of motion-induced eddy current testing.

To overcome the disadvantages of pick-up coils, Hall probes [12] or fluxgate sensors [13] are often used. However, the currently most prevalent magnetic field sensors in ECT are highly sensitive giant-magneto-resistive sensors (GMR) [14]. Some disadvantages are lying in their hysteretic nature and the need to bias them with a distinct external magnetic field in order to reach the linear operating point. A promising alternative to the previously mentioned sensors are spin-dependent tunneling (SDT) devices [15]. This type of sensor makes use of the principle

of the electron spin dependent quantum mechanical tunneling through a thin insulating layer (e.g. 1–2 nm, Al_2O_3) located in between two magnetic layers (e.g. FeCo/CrPtMn and NiFe). This is in contrast to GMR sensors, which make use of a conducting layer. The relative magnetization direction between the two magnetic layers determines the resistance of the device which is in turn proportional to the external magnetic field to be sensed. Their application in the framework of ECT is reported by Wincheski *et al.* in [15]. They showed that the use of SDT sensors allows the detection of defects in close vicinity to ferromagnetic fasteners located in a depth of around 5 mm considering an excitation frequency of 500 Hz.

The application of superconducting quantum interference devices (SQUIDS) seems inherent when it comes to most challenging measuring tasks considering magnetic fields [16]. This technology offers an unrivaled sensitivity which enables the detection of very deep faults. However, these systems are disadvantageous in terms of increased cost and the requirement of cooling. Due to the presence of the cooler, the lift-off distance between the sensor and the specimen is considerable higher compared to room temperature systems. The increased distance between source and sensor influences the effective sensitivity. Typical lift-off values of SQUID ECT systems are in the range of about 7–20 mm [17] compared to 0.5–2 mm of traditional setups. Initial work on this topic can be dated back to the late 1970s [18]. Following this, SQUID based applications in NDT were published in the early 1980s [16]. In general, there are two kinds of systems. These are either shielded systems, which are based on standard SQUIDS or unshielded systems which make use of SQUID gradiometers. One challenge in such systems is the cancellation of the excitation field at the location of the SQUID. This is done either by a double D-shaped excitation coil [19] or by a circular primary coil in combination with a local compensation coil [17]. It is reported, that with the latter it was possible to achieve a considerably better compensation. In 1995 Tavrín *et al.* demonstrated a gradiometric based SQUID ECT system which worked in a magnetically unshielded laboratory environment [20]. This study confirmed that this kind of system could find practical application. The group around Tavrín measured very deep-lying slot like flaws covered by 34.5 mm of aluminium. An overview about potential applications and developed SQUID based ECT systems is given in [21] and [22].

Recently, the ECT method became greatly enhanced in terms of testing time by the development of array based systems. Studies by Mook *et al.* [23], Postolache *et al.* [24] and Jun *et al.* [25] proposed arrays made of secondary coils, GMRs or Hall sensors, respectively. Over the years, a variety of modifications of the ECT method came into existence as for example pulsed eddy current testing [26] or remote field eddy current testing [27]. Further readings about the ECT method, its extensions, and the application of different sensor technologies can be found in [14, 28, 29].

The main disadvantage of ECT is the frequency-dependent field attenuation. In order to provide an overview about the current detection limits in ECT, a summary of selected publications distinguished by the applied sensor technology is given in Table 2.1. It focuses on the detection of subsurface defects located deep inside the specimen. The defect depth d is

Table 2.1: Overview of ECT studies using different magnetic field sensors to detect deep-lying subsurface defects. The geometrical dimensions $[X_d, Y_d, Z_d]$ and d are defined in Fig. 2.3.

Author	Year	Ref.	frequency	X_d in mm	Y_d in mm	Z_d in mm	d in mm
<i>Secondary pick-up coils</i>							
Mook <i>et al.</i>	2006	[30]	350 Hz	3	100	3	8.5
			100 Hz	$< 0.1^c$	$> 100^i$	25	22.5
			50 Hz	$< 0.1^c$	$> 100^i$	25	28.8
Almeida <i>et al.</i>	2013	[31]	100 kHz	$2 - 3^?$	$2 - 3^?$	7	3
Carlstedt <i>et al.</i>	2014	[32]	100 Hz	12	2	2	6
<i>Fluxgate sensors</i>							
Gasparics <i>et al.</i>	1998	[33]	20 kHz	10	$< 0.1^c$	1	4
Kreutzbruck <i>et al.</i>	2000	[13]	180 Hz	$< 0.1^c$	40	0.6	12.4
<i>GMR sensors</i>							
Dogaru <i>et al.</i>	2001	[34]	1.5 kHz	15	0.5	2	1.5
Sikora <i>et al.</i>	2003	[35]	20 – 120 Hz	0.5	$> 50^?$	4	16
Tsukada <i>et al.</i>	2006	[36]	50 Hz	1	25	1	6
Yamada <i>et al.</i>	2008	[37]	50 Hz	1	25	1	8 14*
Wincheski <i>et al.</i>	2010	[8]	185 Hz	0.13	14	1	9
Hamia <i>et al.</i>	2010	[38]	325 Hz	0.5	50	2	8
Cacciola <i>et al.</i>	2010	[39]	60 kHz	2	2	4	4
<i>SQUID sensors</i>							
Tavrin <i>et al.</i>	1996	[20]	10 Hz	$< 0.1^c$	200	1.5	34.5
Krause <i>et al.</i>	2002	[16]	90 Hz	0.15	40	1.2	12.7
Hornig <i>et al.</i>	2002	[40]	400 Hz	1	50	1.5	7.2
Jeng <i>et al.</i>	2002	[41]	2 – 20 kHz	1	50	1.5	7.2
Allweins <i>et al.</i>	2003	[42]	15 Hz	20	$< 0.1^c$	15	31
Fardmanesh <i>et al.</i>	2009	[43]	20 Hz	0.05	$> 100^i$	5	24

? approximated; explicit value not provided

* maximum detectable defect depth for solid and layered specimens respectively

^c the defect was represented by a thin cut whose explicit width is not provided

ⁱ the defect is assumed as infinitely long and extends along the whole specimen; the explicit value is not provided

defined by the distance from the surface of the specimen up to the upper surface of the defect such that it represents the amount of flawless material covering the defect (see Fig. 2.3). The size of the investigated defect $[X_d, Y_d, Z_d]$ plays a major role during the investigations of the detection limit. Most of the studies listed in Table 2.1 do assume slit like cracks such that the length of the defect is much larger than the characteristic diameter of the sensor system itself. This considerably increases the depth limit compared to isolated inclusions of finite size which are surrounded by conductive material. That circumstance has to be considered when comparing

the results of the studies to each other. The advancements of the eddy current technique by applying alternative magnetic field sensors can be clearly seen from Table 2.1. As expected, SQUID sensors outperform all other sensors which operate at room temperature. However, the requirement of cooling and eventually shielding leads to increased maintenance and cost.

In contrast to classical ECT, alternative methods exist which make use of relative motion instead of alternating currents to induce eddy currents in the object under test. These methods are presented in the next section since they obey decent advantageous regarding the penetration of the electromagnetic fields when considering moderate velocities in the range of a few m/s.

2.3 Motion-Induced Eddy Current Testing

The induction of eddy currents in the object under test is not restricted to the use of alternating magnetic field sources. If an electrical conductor and a magnetic field source experience relative movement, eddy currents are induced inside the conductor. Besides in the field of NDT, the calculation of the involved electromagnetic fields and retarding forces is of great general theoretical interest in electromagnetism. Saslow [44] provided a comprehensive review about the theory of motion-induced eddy currents and Maxwell's receding image theory. In the past, this topic was of special practical interest in the framework of magnetic levitation and transportation which was initially proposed in 1912 by Bachelet [45]. However, as late as in the 1970s this topic became popular and Reitz [46, 47], Richards [48], Borcherts and Davis [49–51],

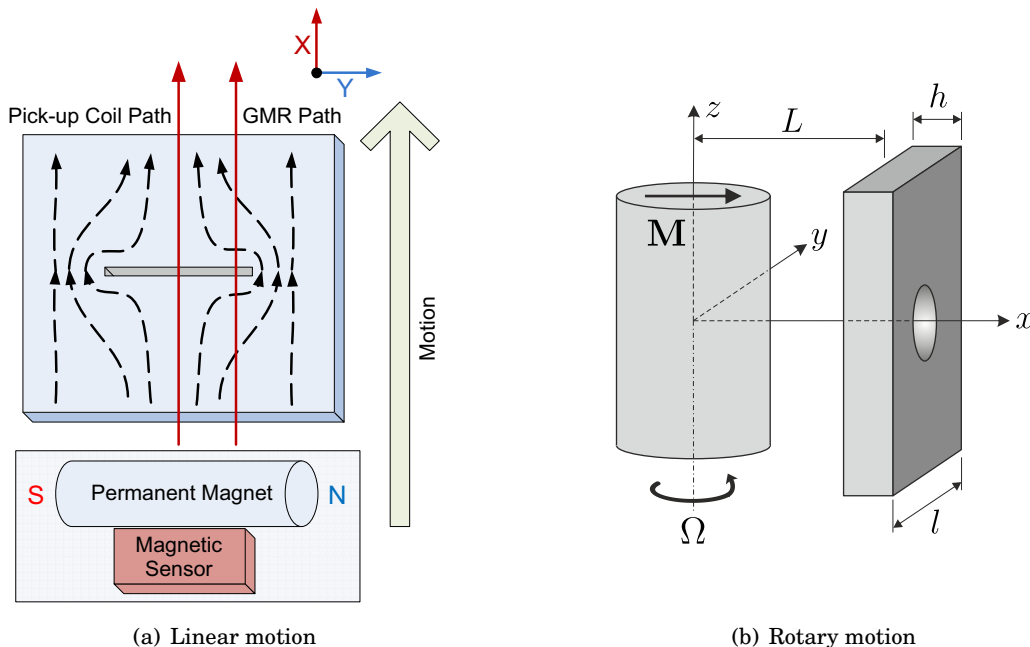


Figure 2.4: Two different MECT methods reported in the literature. (a) Linear motion using a lying axially magnetized permanent magnet [59] and (b) rotary motion of a diametral magnetized permanent magnet in close vicinity of a defective conductor [62].

Lee and Menendez [52] and many others [53–55] studied the behavior of the electromagnetic fields in the vicinity of moving conductors extensively.

In recent years, an increase of a variety of methods can be observed which make use of relative motion between a magnetic field source producing a stationary magnetic field and the object under test. Techniques based on this principle can be classified as motion-induced eddy current testing (MECT) methods. A few examples of MECT type methods which were developed in the recent years are given in the following.

Ramos *et al.* [56, 57] investigated the applicability of moving stationary magnetic field sources using DC coils in the framework of NDT. They measured the disturbances of the magnetic field resulting from a defect directly by means of GMR sensors. Following this approach, these studies are extended in [58] and [59] to the use of single or differential pick-up coils, respectively. Moreover, they also exchanged the magnetic field source with a permanent magnet in order to achieve higher flux densities and an increased induced eddy current density inside the moving specimen. The sensor orientation has to be chosen carefully when using GMR sensors in order to avoid saturation effects. This can be overcome by applying differential coils as magnetic field sensors as it is also done in the framework of ECT. In this way, only the temporal change of the magnetic flux resulting from a passing defect is measured. The general principle of the proposed method is shown in Fig. 2.4(a). Thereupon, Rocha *et al.* extended the analysis to the application of Hall sensors instead of GMRs and pick-up coils in [60]. They also investigated the defect response signals for different permanent magnet configurations and proposed the use of sensor arrays to expedite the assessment of larger areas. In a subsequent study, the application of GMRs, differential coils and Hall sensors is compared in the framework of MECT [61]. As a result, it turned out that GMRs were able to detect defects when crossing the edges of the defect. In contrast, pick-up coils and Hall sensors also provided signals when the probe passed the defect in its centerline (see Fig. 2.4(a)).

In 2015, another MECT technique is proposed by Tan *et al.* [62]. In contrast to previous studies which made use of translational motion, they proposed a system using rotational motion of the magnetic field source to induce eddy currents inside the object under test. The basic principle of the method is shown in Fig. 2.4(b). A diametral magnetized cylindrical permanent magnet rotates in close vicinity of a conductive object and anomalies are analyzed by means of the variations in the electromagnetic torque. The use of rotational motion provides the opportunity to design portable MECT systems according to ECT devices nowadays available.

The presented studies are all limited to the analysis of surface touching defects indicating the early state of MECT systems. However, it is emphasized that MECT is not restricted to detect flaws on the surface which will be shown in the further course of this thesis in the framework of LET.

2.4 Lorentz Force Eddy Current Testing

2.4.1 General Principle and Preparatory Work

LET belongs to the group of MECT type methods. It is a technique for nondestructive and contactless evaluation of electrically conducting specimens. The basic principle, shown in Fig. 2.5, is based on the interaction between a permanent magnet and a moving specimen. As a consequence of their relative motion, eddy currents are induced inside the object under test, which in turn react with the magnetic field, producing a Lorentz force acting on both, the specimen and the permanent magnet itself. The novelty of the method lies in the determination of the measurement signal. In contrast to ECT and other MECT techniques, the force acting on the magnet is measured using force sensors. In the presence of a defect, the eddy current profile and hence, the resulting Lorentz force, are perturbed. The physical principle of LET is in analogy to Lorentz force velocimetry (LFV) [63]. In LFV, the main goal is to determine the flow rate of a conducting liquid by means of the Lorentz force which is proportional to the velocity of the liquid [64].

LET was initially demonstrated as an alternative NDT method by Brauer *et al.* in 2008 [1]. Ziolkowski *et al.* [65] tackled the numerical analysis of the reported experimental setup and proposed techniques to analyze the electromagnetic field problem with increased computational efficiency. The work on LET in an experimental and numerical framework was continued by Uhlig [66] and Zec [67]. A conceptional model of LET is proposed and investigated in [68]. It consists of a modification to the famous creeping magnet experiment [69], where a permanent magnet is slowly falling down a copper pipe. The modification in this study consists of adding defects into the pipe wall such that the eddy current distribution and Lorentz force profile is disturbed. The LET method is extended to the determination of the electrical conductivity of the specimen assuming that the object under test is free of defects [70]. This technique is called

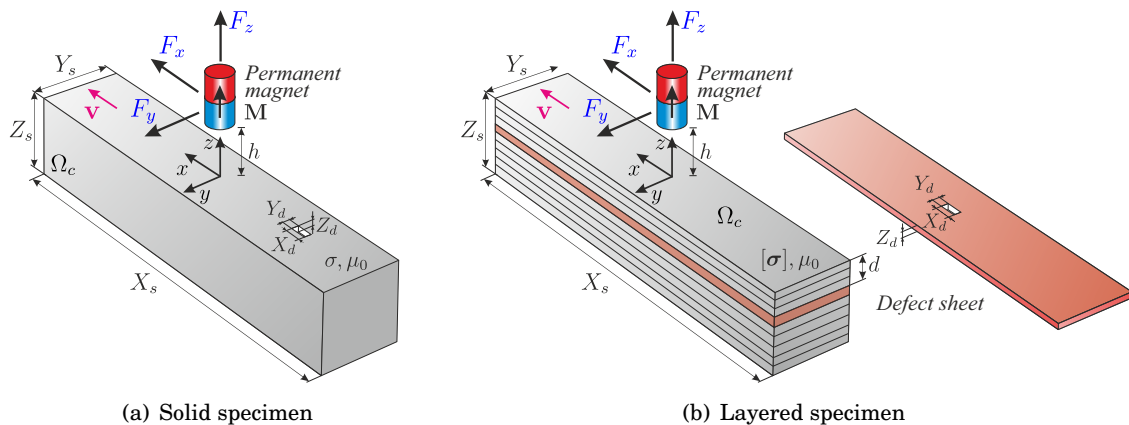


Figure 2.5: General principle of Lorentz force eddy current testing for contactless evaluation of electrically conducting material. The specimens and the geometrical parameters of the LET problem under investigation are shown in (a) for solids and in (b) for layered structures.

Lorentz force sigmometry (LoFoS). It is shown that the lift-to-drag ratio of the Lorentz force components is proportional to the conductivity of the specimen such that $\sigma = \alpha F_z/F_x$ with a calibration factor α which is determined experimentally. Besides the mentioned investigations, fundamental studies exist on the influence of the Lorentz force on geometrical parameters such as the lift-off distance, the size of the magnet as well as the size and depth of the defect [71, 72]. These studies are accomplished with the analysis how the velocity or conductivity affects the resulting Lorentz force profile. The investigations on the forward models are supported by Petković in [73] who addressed the inverse problem. She proposed reconstruction algorithms to determine the shape and the location of the defects solely out of the Lorentz force profiles. In 2014, the state-of-the-art in LET is reported by Brauer *et al.* in [74]. It includes a summary about the experimental setup, the numerical modeling techniques and currently applied defect reconstruction methods.

This thesis aims to continue the work on LET with a primary focus on the optimization of the magnet system, the uncertainty analysis of the LET setup at hand and the development of analytical modeling techniques to analyze time-dependent velocity profiles.

2.4.2 Problem Definition and Laboratory Setup

The LET system investigated numerically is strongly related to the laboratory setup in order to compare the simulation results with experimental data. The problem geometry utilized in the numerical analysis is shown in Fig. 2.5 and an overview of the involved parameters is given in Table 2.2. Throughout this work, two different kinds of specimens are investigated. These are either solid or layered specimen. Both types are shown in Fig. 2.5 together with the

Table 2.2: Parameters of the LET setup and characteristic values.

Parameter	Value	Description
B_r	$\sim 1 \dots 1.4$ T	Remanence of the magnet (NdFeB)
d	$\sim 1 \dots 10$ mm	Depth of the defect
h	1 mm	Lift-off distance
v	$\sim 0.1 \dots 2$ m/s	Velocity of the specimen
X_d	$\sim 1 \dots 10$ mm	Length of the defect
Y_d	$\sim 1 \dots 10$ mm	Width of the defect
Z_d	$\sim 1 \dots 10$ mm	Height of the defect
X_s	250 mm	Length of the specimen
Y_s	50 mm	Width of the specimen
Z_s	50 mm	Height of the specimen
σ_{\square}	(19.88 ± 0.05) MS/m	Electrical conductivity of solid specimen
σ_{\parallel}	(30.61 ± 0.20) MS/m	Electrical conductivity of layered specimen

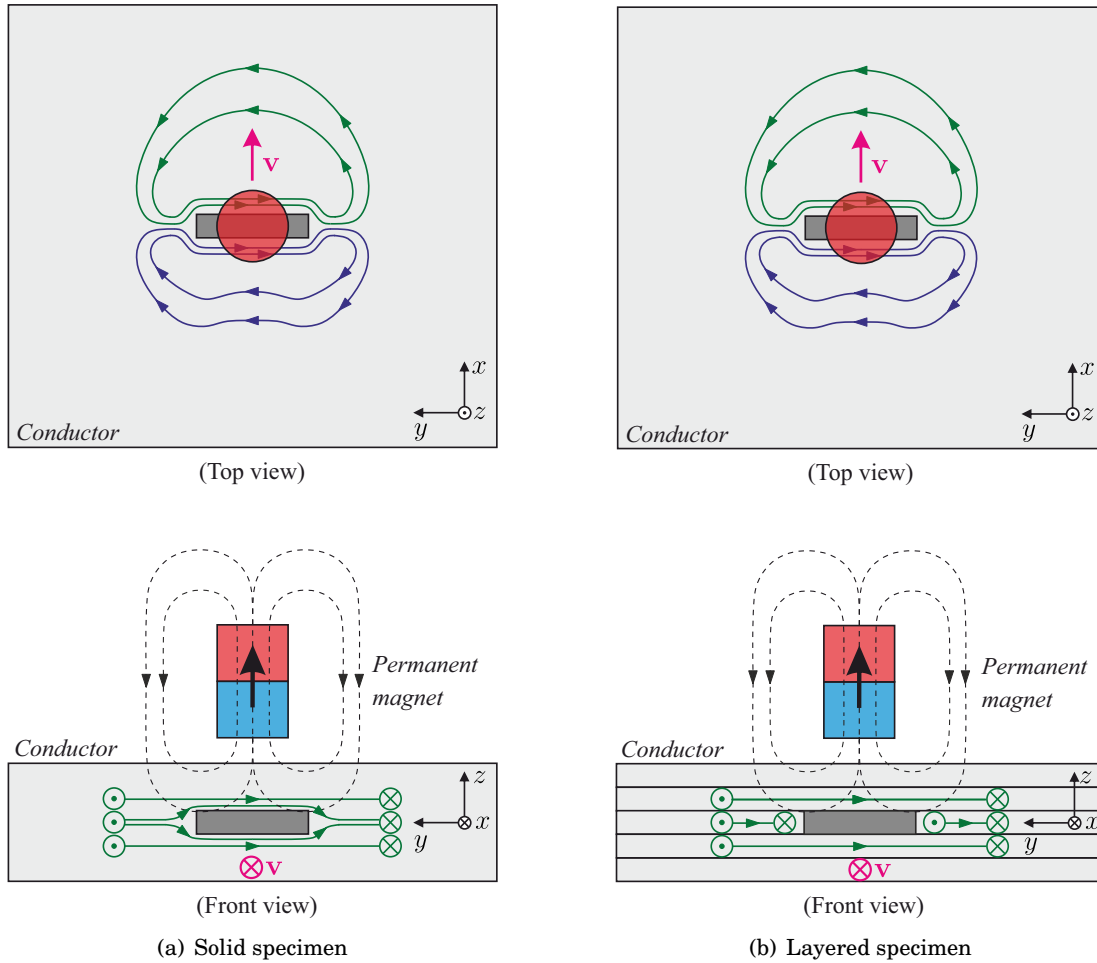


Figure 2.6: Sketch of the perturbed eddy currents induced in a moving plate located below a permanent magnet. Differences between (a) solid and (b) layered specimen. The layered structure restricts the eddy currents to flow in the respective sheet.

corresponding geometrical parameters. The conductivity of solid specimen, shown in Fig. 2.5(a), can be assumed as isotropic. Meanwhile, the layered specimens are advantageous when varying the depth and size of defects which is demanding and expensive in case of solid bars. As a direct consequence, their conductivity profile has to be treated differently compared to solid bodies. As a result of their stratified structure, an oxidation layer on the surface of each conducting sheet is present. This prevents the current to flow from one layer to the next. As an admissible approximation, which was tested experimentally in [74], the anisotropic conductivity profile is homogenized assuming a vanishing vertical conductivity ($\sigma_{zz} = 0$) throughout the whole conductor. The characteristic eddy current profiles are illustrated in Fig. 2.6 for both types of specimen. Throughout this thesis, it is assumed that the defect is non-conductive and non-magnetic. The eddy current profiles would considerably change when one of both assumptions is violated. A permanent magnet, which is magnetized perpendicular to the surface of the

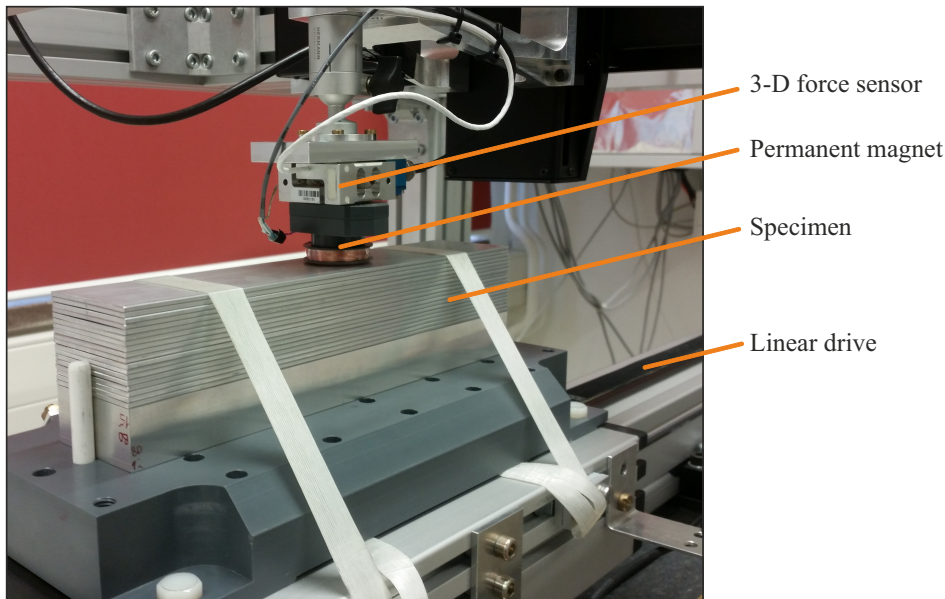


Figure 2.7: Laboratory LET setup developed by R. P. Uhlig [66] and M. Carlstedt [75].

specimen, generates a characteristic eddy current profile in the xy -plane with a shape of an eight. The induced eddy current density is highest right under the permanent magnet. The conductivity anisotropy in the z -direction does not affect this general behavior. In the case of a defect, the induced eddy currents circumvent the defect. The major difference between both conductivity profiles is that in case of anisotropic specimen, the induced eddy currents are restricted to flow in the respective sheet omitting any z -component.

The present laboratory LET setup, shown in Fig. 2.7, is developed by Uhlig [66] and Carlstedt [75]. The 3-D force sensor K3D40 [76] (ME-Messsysteme GmbH, www.me-systeme.de) based on the strain-gauge technology is used to determine the dynamic forces acting on the permanent magnet. The data is acquired using the commercial PXI system NI PXI-1036 (National Instruments Corporation, www.ni.com) together with the signal acquisition module NI PXI-4472. The output voltage of the force sensor amplifier is sampled with a frequency of $f_s = 10$ kHz. The specimen is moved by a customized linear belt-driven drive (Jenaer Antriebstechnik GmbH, www.jat-gmbh.de). The maximum velocity which can be reached is about 2 m/s. More information about the experimental setup can be found in [66] and [75].

2.5 Comparison of ECT and LET

A comparison between the ECT technique and LET is reported by the author and colleagues in [32] and [77]. In the context of this thesis, a brief summary of those studies is given in the following. In order to compare both methods from the numerical point of view, a detailed model of the applied ECT sensor is necessary. For that reason, preliminary work was done by the author in [78]. This study describes the modeling procedure of a commercial ECT probe

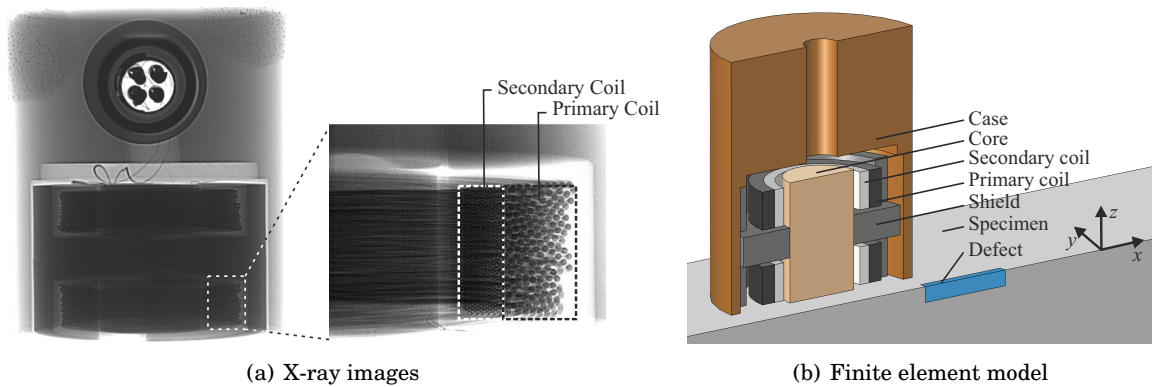


Figure 2.8: X-ray images and model of the ECT probe PKA-48 (Rohmann GmbH) [78].

with unknown internal geometrical and material properties. The probe under investigation (PKA-48, Rohmann GmbH) was of differential type, including secondary pick-up coils. It is used in combination with the ECT device Elotest N300 (Rohmann GmbH). X-ray images were taken in order to get information about the internal structure of the probe. Those are shown together with the constructed finite-element model in Fig. 2.8. This enabled the possibility to compare the defect response signals obtained experimentally with numerical simulations.

The major differences between ECT and LET are given by the shape and the magnitude of the induced eddy current profile as well as by the evaluated signal. In [32], the impedance variations of the imaginary part ΔZ_i and the back induced voltage U_{sec} in the secondary pick-up coil from ECT are compared to the force perturbations in case of LET. An example of the normalized defect response signals from both methods is shown in Fig. 2.9.

Usually, the ECT method is applied in stationary applications. However, when the object

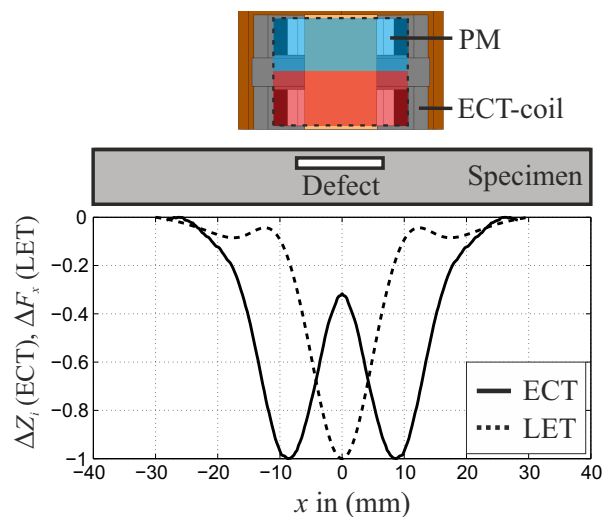


Figure 2.9: Normalized defect response signals in case of ECT and LET assuming equivalent dimensions [77].

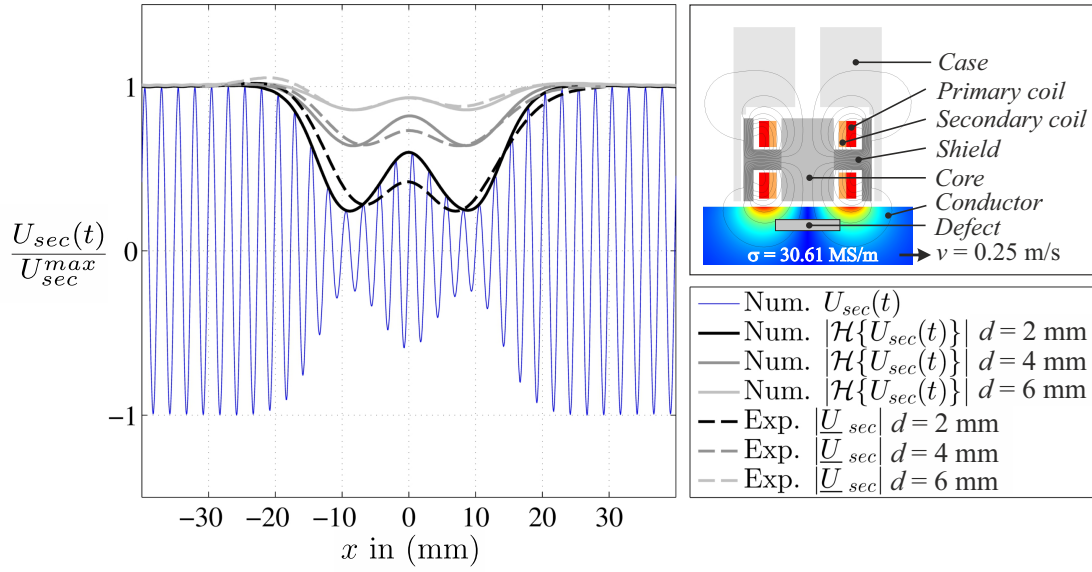


Figure 2.10: Modulated secondary induced voltage in the pick-up coils in case of moving objects under test [32].

under test is moving relative to the ECT probe, the induced voltage in the pick-up coil is modulated in the defect region. This effect is shown in Fig. 2.10. If the velocity-to-frequency ratio v/f increases, the amount of sinusoidal periods in the defect region decreases. It is shown in [32] that the use of the Hilbert transform of the secondary induced voltage $\mathcal{H}\{U_{sec}(t)\}$ is suitable to post-process the modulated defect response signals to determine the envelope of the modulated signal. In practice, this requires additional adjustments of currently available ECT devices. A direct comparison between both methods in terms of defect depth and velocity showed that with ECT it was possible to detect defects of size $[X_d, Y_d, Z_d] = [12, 2, 2]$ mm up to a depth of 6 mm at a velocity of $v = 0.25$ m/s considering a frequency of $f = 100$ Hz. In contrast, the LET method was able to resolve the defect up to a depth of 8 mm at $v = 0.5$ m/s.

It can be concluded that both methods obey individual advantages. The classical ECT method is suitable to inspect stationary objects which is not possible with LET or any other MECT type method. However, if the object is in motion, the use of alternating currents can be omitted. In this way, it is possible to apply permanent magnets which produce considerably higher magnetic flux densities compared to current carrying coils. Comparative studies [32, 77] showed that LET is a promising and competitive alternative to traditional ECT methods considering the contactless evaluation of moving electrical conductors. In the further course of this thesis, a similar defect depth study is conducted as it is presented by Mook *et al.* in Table 2.1. In this way, it is intended to incorporate LET into the current state-of-the-art of electromagnetic NDT methods.

In this chapter, an overview of electrodynamic phenomena in the case of moving media is given. The relations between the electromagnetic fields in two coordinate systems that move with a relative velocity \mathbf{v} with respect to each other are provided. One coordinate system is associated with the magnetic field source and the other is associated with the moving electrical conducting media. In this situation, the Maxwell-Lorentz and the Maxwell-Galilean transformations are studied. The characteristics of motion-induced eddy currents are described. This analysis extends to the formulation of the governing equations of different numerical approaches used throughout this thesis. Several relevant assumptions and simplifications are presented and discussed. Finally, several approaches are compared and their applicability is investigated.

3.1 Electrodynamics of Moving Media

The electrodynamics of moving bodies were a significant challenge to physicists of the nineteenth and twentieth centuries. This chapter provides a brief overview of the underlying physics of electromagnetic fields in the case of relative motion between magnetic field sources and conducting objects. This description is focused on the use of principles to formulate and solve problems in the LET framework.

To describe the effects of relative motion, two frames of reference are defined; both frames are shown in Fig. 3.1. The first frame is associated with the magnetic field source and is called the laboratory frame of reference K . The second frame is fixed with respect to the conductor; it is the rest frame of reference K' . As a consequence of the relativity theorem, time is not absolute between the frames. The famous physicist H. A. Lorentz introduced a local time for the frame K' . To relate both frames to each other, he formulated ad hoc transformation laws for space and

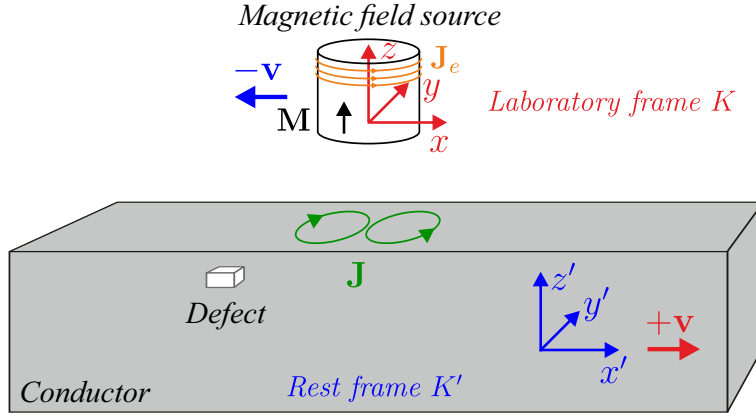


Figure 3.1: Laboratory frame K and rest frame K' . The red and blue colors indicate the frame of reference and the corresponding direction of motion, respectively. Only one velocity vector may be considered, depending on the frame of reference under consideration.

time. For uniform motion in the x direction, these laws are given by:

$$x' = \frac{x - v_x t}{\sqrt{1 - \beta^2}} \quad (3.1a)$$

$$y' = y \quad (3.1b)$$

$$z' = z \quad (3.1c)$$

$$t' = \frac{1}{\sqrt{1 - \beta^2}} \left(t - \beta \frac{x}{c_0} \right) \quad (3.1d)$$

with a velocity ratio $\beta = v_x/c_0$, where c_0 is the speed of light in free space. Using this system, events in K and K' are not simultaneous in time. Moreover, they are contracted in space. Einstein postulated that the laws of electrodynamics are invariant in all frames of reference [79]. This leads to the transformation equations for the fields \mathbf{E} (electric field), \mathbf{D} (electric displacement field), \mathbf{H} (magnetic field), and \mathbf{B} (magnetic flux density):

$$\mathbf{E}' = \mathbf{E}_{\parallel} + \frac{1}{\sqrt{1 - \beta^2}} (\mathbf{E}_{\perp} + \mathbf{v} \times \mathbf{B}) \quad (3.2a)$$

$$\mathbf{D}' = \mathbf{D}_{\parallel} + \frac{1}{\sqrt{1 - \beta^2}} \left(\mathbf{D}_{\perp} + \frac{\mathbf{v} \times \mathbf{H}}{c_0^2} \right) \quad (3.2b)$$

$$\mathbf{H}' = \mathbf{H}_{\parallel} + \frac{1}{\sqrt{1 - \beta^2}} (\mathbf{H}_{\perp} - \mathbf{v} \times \mathbf{D}) \quad (3.2c)$$

$$\mathbf{B}' = \mathbf{B}_{\parallel} + \frac{1}{\sqrt{1 - \beta^2}} \left(\mathbf{B}_{\perp} - \frac{\mathbf{v} \times \mathbf{E}}{c_0^2} \right). \quad (3.2d)$$

Note that the field components parallel " \parallel " and perpendicular " \perp " to the direction of motion must be treated differently in the general case. In the presence of some material, the constitutive

equations in K' are given in the same way as for the stationary case [80]:

$$\mathbf{D}' = \varepsilon \mathbf{E}' \quad (3.3a)$$

$$\mathbf{B}' = \mu \mathbf{H}' \quad (3.3b)$$

$$\mathbf{J}' = \sigma \mathbf{E}', \quad (3.3c)$$

for a permittivity $\varepsilon = \varepsilon_0 \varepsilon_r$ and a permeability $\mu = \mu_0 \mu_r$, which include the permittivity ε_0 and permeability μ_0 of free space. The current density is calculated using the electric field by means of the electrical conductivity σ .

In LET, β is exceedingly small, because $|\mathbf{v}| \ll c_0$. In this case, the Lorentz transformation can be simplified, and the Galilean transformation can be applied. In this case, the absolute time is preserved such that $t = t'$ and (3.2a)-(3.2d) simplify to:

$$\mathbf{E}' = \mathbf{E} + \mathbf{v} \times \mathbf{B} \quad (3.4a)$$

$$\mathbf{D}' = \mathbf{D} \quad (3.4b)$$

$$\mathbf{H}' = \mathbf{H} - \mathbf{v} \times \mathbf{D} \quad (3.4c)$$

$$\mathbf{B}' = \mathbf{B}. \quad (3.4d)$$

Considering Maxwell's equations, which are independent of the frame of reference, the relations between magnetic and electric fields are given by:

$$\nabla \times \mathbf{H} = \mathbf{J} + \frac{\partial \mathbf{D}}{\partial t} \quad (3.5a)$$

$$\nabla \times \mathbf{E} = -\frac{\partial \mathbf{B}}{\partial t} \quad (3.5b)$$

$$\nabla \cdot \mathbf{B} = 0 \quad (3.5c)$$

$$\nabla \cdot \mathbf{D} = \rho. \quad (3.5d)$$

Eq. (3.5d) includes a (possibly present) charge density ρ . By substituting the simplified relations from (3.4a)-(3.4d) into Maxwell's equations (3.5a)-(3.5d) and considering the presence of magnetic field sources, i.e., a permanent magnet with magnetization \mathbf{M} or a DC coil driven by an external current density \mathbf{J}_e , one obtains:

$$\nabla \times \left(\frac{\mathbf{B}'}{\mu_0} - \mathbf{M} \right) = [\sigma](\mathbf{E} + \mathbf{v} \times \mathbf{B}) + \frac{\partial \mathbf{D}}{\partial t} - \nabla \times (\mathbf{v} \times \mathbf{D}) + \rho \mathbf{v} + \mathbf{J}_e \quad (3.6a)$$

$$\nabla \times \mathbf{E}' = -\frac{\partial \mathbf{B}}{\partial t} \quad (3.6b)$$

$$\nabla \cdot \mathbf{B}' = 0 \quad (3.6c)$$

$$\mathbf{E}' = \mathbf{E} + \mathbf{v} \times \mathbf{B} \quad (3.6d)$$

$$\mathbf{J} = \rho \mathbf{v} + [\sigma](\mathbf{E} + \mathbf{v} \times \mathbf{B}) \quad (3.6e)$$

$$\mathbf{B} = \mathbf{B}' = \mu \mathbf{H}', \quad \mathbf{D} = \mathbf{D}' = \varepsilon \mathbf{E}, \quad \rho' = \rho.$$

The conductivity σ is now expressed as a tensor of second rank $[\sigma]$ so as to take the conductivity profile of the conductor into account, which can be either isotropic (in the case of solids) or

anisotropic (in the case of composites, e.g., stacked sheets). Assuming that the material is completely described by the diagonal terms, $[\boldsymbol{\sigma}]$ is given by:

$$[\boldsymbol{\sigma}] = \text{diag}(\boldsymbol{\sigma}) = \begin{bmatrix} \sigma_{xx} & 0 & 0 \\ 0 & \sigma_{yy} & 0 \\ 0 & 0 & \sigma_{zz} \end{bmatrix}. \quad (3.7)$$

The above relations are general and can be applied in the case of finite conductors and in the presence of defects. Introducing the magnetic vector potential \mathbf{A} defined by $\mathbf{B} = \nabla \times \mathbf{A}$ and combining it with the electric scalar potential ϕ , the electric field \mathbf{E} is given by:

$$\mathbf{E} = -\nabla\phi - \frac{\partial\mathbf{A}}{\partial t}. \quad (3.8)$$

The scalar electric potential ϕ inhibits the induced current, causing it to flow through the boundary of the conductor into the air or defect domain.

Laboratory Frame of Reference (Magnetic Field Source): When considering good conductors at non-relativistic speeds, as in the case of LET, the displacement field \mathbf{D} and the displacement current density $\partial\mathbf{D}/\partial t$ can be neglected [81]. In this way, a Coulomb gauge, $\nabla \cdot \mathbf{A} = 0$, applies for the magnetic vector together. Moreover, convection currents, $\rho\mathbf{v}$, do not exist. As a result, (3.6a) and (3.6b) can be further simplified. This simplification yields the governing equations of the electromagnetic fields if the observer is located in the laboratory frame of reference K associated with the magnetic field source (see Fig. 3.1). In this environment, the conductor passes the magnetic field source with a positive velocity $+\mathbf{v}$, and the governing equations are given by:

$$\nabla \times \left(\frac{\mathbf{B}}{\mu_0} - \mathbf{M} \right) = [\boldsymbol{\sigma}](\mathbf{E} + \mathbf{v} \times \mathbf{B}) + \mathbf{J}_e \quad (3.9a)$$

$$\nabla \times \mathbf{E} = -\frac{\partial\mathbf{B}}{\partial t} \quad (3.9b)$$

$$\nabla \cdot \mathbf{B} = 0 \quad (3.9c)$$

$$\mathbf{J} = [\boldsymbol{\sigma}](\mathbf{E} + \mathbf{v} \times \mathbf{B}) \quad (3.9d)$$

$$\nabla \cdot \mathbf{J} = 0. \quad (3.9e)$$

Rewriting (3.9a) and (3.9b) in terms of potentials \mathbf{A} and ϕ yields the transient magnetic diffusion equation in the laboratory frame of reference; combining this equation with the law of current conservation $\nabla \cdot \mathbf{J} = 0$ one obtains:

$$\nabla \times \left(\frac{1}{\mu_0} \nabla \times \mathbf{A} - \mathbf{M} \right) = [\boldsymbol{\sigma}] \left(-\frac{\partial\mathbf{A}}{\partial t} - \nabla\phi + \mathbf{v} \times (\nabla \times \mathbf{A}) \right) + \mathbf{J}_e \quad (3.10a)$$

$$\nabla \cdot \mathbf{J} = 0 \rightarrow \nabla \cdot \left([\boldsymbol{\sigma}] \left(-\nabla\phi + \mathbf{v} \times (\nabla \times \mathbf{A}) \right) \right) = 0. \quad (3.10b)$$

The driving function of the induced eddy currents is given by only the $\mathbf{v} \times (\nabla \times \mathbf{A})$ term if the conductor has an infinite extent and a constant cross section. The observer sees a stationary

magnetic field with $\partial\mathbf{A}/\partial t = \mathbf{0}$. However, if a defect or a boundary passes by or if the body is accelerated such that the velocity is time-dependent, the induced eddy currents change over time, which, in turn, generates a time-dependent magnetic field. As a consequence, $\partial\mathbf{A}/\partial t \neq \mathbf{0}$ and transient induction effects, which are superimposed with the velocity term $\mathbf{v} \times \mathbf{B}$, can be observed. Under certain circumstances, the decoupling between quasi-stationary and time-dependent effects simplifies the analytical calculation of the electromagnetic fields. This fact will be utilized later in this thesis during the analysis of ring magnets in the framework of LET (Chapter 5).

Rest Frame of Reference (Conductor): The field problem can also be solved in the rest frame of reference that is associated with the moving conductor (see Fig. 3.1). In this case, the conductor is stationary and the magnetic field source moves along the conductor with a negative velocity $-\mathbf{v}$. Then, the governing equations are given by:

$$\nabla \times \left(\frac{\mathbf{B}}{\mu_0} - \mathbf{M} \right) = [\sigma]\mathbf{E} + \mathbf{J}_e \quad (3.11a)$$

$$\nabla \times \mathbf{E} = -\frac{\partial \mathbf{B}}{\partial t} \quad (3.11b)$$

$$\nabla \cdot \mathbf{B} = 0 \quad (3.11c)$$

$$\mathbf{J} = [\sigma]\mathbf{E} \quad (3.11d)$$

$$\nabla \cdot \mathbf{J} = 0. \quad (3.11e)$$

Similar to the former case, the transient magnetic diffusion equation can be reformulated by rewriting (3.11a) and (3.11b) in terms of the potentials \mathbf{A} and ϕ :

$$\nabla \times \left(\frac{1}{\mu_0} \nabla \times \mathbf{A} - \mathbf{M} \right) = [\sigma] \left(-\frac{\partial \mathbf{A}}{\partial t} - \nabla \phi \right) + \mathbf{J}_e \quad (3.12a)$$

$$\nabla \cdot \mathbf{J} = 0 \rightarrow \nabla \cdot ([\sigma] \nabla \phi) = 0. \quad (3.12b)$$

In the rest frame K' , the observer is fixed with respect to the conductor and experiences a time-dependent magnetic field when the magnetic field source passes by. Therefore, the driving function of the motion-induced eddy currents is given by only the time-derivative of the magnetic field such that $\partial\mathbf{A}/\partial t \neq \mathbf{0}$ in every case. All time-dependent effects (resulting from, for example, defects or nonuniform motion) are now included in the $\partial\mathbf{A}/\partial t$ term. This characteristic proved to be useful during the analytical treatment of accelerated bodies [82]. Reference to this property will be made at a later time when analytically investigating the effects of oscillatory motion of permanent magnets above a conducting slab (section 4.3).

Magnetic Reynolds Number: The magnitude of the induced eddy currents and their spatial distribution depend on several parameters such as the conductivity σ , the velocity $|\mathbf{v}|$, and the dimensions of the problem. The magnetic Reynolds number R_m can be used to approximate the ratio between the secondary magnetic field $\mathbf{B}^{(s)}$ produced by the induced eddy currents and

the primary magnetic fields $\mathbf{B}^{(p)}$ generated by the magnetic field source ($R_m \sim \mathbf{B}^{(s)}/\mathbf{B}^{(p)}$). The magnetic Reynolds number is a dimensionless quantity that is obtained by normalization of the transient magnetic diffusion equation (3.10a) [83]:

$$R_m = \mu_0 \sigma v L. \quad (3.13)$$

The magnetic Reynolds number is inconclusive, because it includes a characteristic length L that cannot be uniquely defined. The magnetic Reynolds number strongly depends on the problem under investigation. In LET, L is defined by the size of the moving conductor (e.g., $L = Z_s/2$) or, if not applicable, the lift-off distance h of the magnetic field source. Using this convention, one can state that the secondary magnetic fields can be neglected if $R_m \ll 1$. Otherwise, if $R_m \gg 1$, secondary magnetic fields become prevalent and the primary magnetic field is expelled from the conductor. This phenomenon is similar to the well-known skin effect.

Calculation of Forces: The forces acting on the magnetic field source can be calculated using a volume integration of the Lorentz force density over the conducting domain Ω_c , taking into consideration Newton's third law, such that the forces on the magnet and on the conductor are equal but act in opposite directions:

$$\mathbf{F} = - \int_{\Omega_c} \mathbf{J} \times \mathbf{B} \, d\Omega. \quad (3.14)$$

This approach can be applied as long as the conductor is non-ferromagnetic ($\mu_r = 1$); if this is not the case, other methods such as the Maxwell stress tensor method [84], the principle of virtual work [85], or the magnetizing current model [86] must be applied. A comparison of the aforementioned force calculation methods can be found in [86, 87].

3.2 Numerical Approaches

To determine the forces acting on the magnet system in the presence of defects, the finite element method (FEM) is used throughout this thesis [88]. The method is based on the discretization of the computational domain into elementary sub-domains (hereinafter referred to as finite elements). FEM is a suitable method to handle complex geometries with inhomogeneous and anisotropic material properties. The solution inside each element is approximated by low-order polynomials called shape functions. Depending on the unknown quantity, ϕ or \mathbf{A} , scalar shape functions associated with the nodes, or vector shape functions associated with the edges of each finite element, are typically defined. The unknowns are also referred to as degrees of freedom (DoFs). Depending on the differential equation and the technique used to incorporate time-dependent effects in the model, the computational domain, and hence, the number of DoFs, can be reduced. As a consequence, the computational time required to solve the problem is reduced. Further reading regarding FEM can be found in [88–92]. In general, analysis requires accurate and time-efficient numerical approaches to allow either extensive scans of an object under test

or parametric studies. The software package Comsol Multiphysics v4.4 [93] (COMSOL, Inc., Burlington, MA, USA, www.comsol.com) is used in this framework.

3.2.1 Computational Domains and Potential Functions

To efficiently determine the solutions for the magnetic and electric fields from (3.10a) and (3.10b), or (3.12a) and (3.12b), different computational domains and potential functions are defined. The entire computational domain Ω is divided into the magnet domain Ω_m , the ferromagnetic domain Ω_{Fe} , and the surrounding air domain Ω_a . All of these domains are assumed to be non-conducting, such that the induced eddy currents are only present inside the conducting domain Ω_c .

Magnet Domain Ω_m : In the magnet domain Ω_m (i.e. the permanent magnet), the magnetic field \mathbf{H} can be described by the magnetic scalar potential ψ such that $\mathbf{H} = -\nabla\psi$. The magnetic field source is defined by the remanence \mathbf{B}_r of the permanent-magnet material. As a reasonable approximation, the relative permeability of the magnetic material is assumed to be equal to that of free space ($\mu_r = 1$). Thus, the magnetization is given by $\mathbf{M} = \mathbf{B}_r/\mu_0$. Then, the governing equation for the magnetic field in Ω_m is given by:

$$\nabla \cdot (-\nabla\psi + \mathbf{M}) = 0 \quad (3.15a)$$

$$\nabla \cdot \mathbf{B} = 0 \quad (3.15b)$$

$$\mathbf{H} = -\nabla\psi \quad (3.15c)$$

$$\mathbf{B} = \mu_0(\mathbf{H} + \mathbf{M}). \quad (3.15d)$$

Nonlinear Ferromagnetic Domain Ω_{Fe} : The magnet system could include a domain Ω_{Fe} , which is made of soft-magnetic material. It is described by the nonlinear constitutive relation $|\mathbf{B}| = f(|\mathbf{H}|)$. In this case, the magnetization of the material depends on the externally applied magnetic field provided by the permanent magnet in Ω_m . The function $f(|\mathbf{H}|)$ depends on the magnetic material; it must be monotonic so as to prevent instable operation of the numerical solvers. Ω_{Fe} is assumed to be fixed with respect to Ω_m ; a combination of both domains is assumed to represent a magnet system. As long as the time-derivative of the secondary magnetic field is small ($\partial\mathbf{B}^{(s)}/\partial t \rightarrow 0$), the induced eddy currents inside Ω_{Fe} can be neglected, which allows the use of a scalar potential formulation similar to that used in previous cases. The nonlinear governing equations are given by (3.15a)-(3.15c), which use the nonlinear constitutive relation $|\mathbf{B}| = f(|\mathbf{H}|)$ instead of (3.15d):

Air Domain Ω_a : In the surrounding air-region Ω_a , no magnetic material is present and (3.15a) can be simplified to:

$$\Delta\psi = 0. \quad (3.16)$$

Conducting Domain Ω_c : The magnetic and electric fields inside the conducting region Ω_c (i.e. the specimen) can be expressed by the magnetic vector potential \mathbf{A} and the electric scalar potential ϕ , as already given in the governing equations (3.10a) and (3.12a). However, in time-dependent approaches, a modified \mathbf{A}^* formulation is used to more effectively solve the given field problem inside the conducting region [94]. In this way, the modified magnetic vector potential \mathbf{A}^* can be defined as:

$$\mathbf{A}^* = \mathbf{A} - \int_0^t \nabla \phi dt \quad (3.17a)$$

$$\frac{\partial \mathbf{A}^*}{\partial t} = \frac{\partial \mathbf{A}}{\partial t} - \nabla \phi. \quad (3.17b)$$

To ensure the uniqueness of \mathbf{A}^* , the gauge $\nabla \cdot ([\sigma]\mathbf{A}^*) = 0$ must be imposed [94]. Using the modified vector potential formulation, the electric scalar potential ϕ is excluded from the governing equations and the number of DoFs is reduced from 4 to 3 inside the conductor.

Boundary Conditions and Domain Coupling: Across all interfaces, the normal component of the magnetic flux density \mathbf{B} and the tangential component of the magnetic field \mathbf{H} must be continuous:

$$(\mathbf{B}_1 - \mathbf{B}_2) \cdot \mathbf{n} = 0 \quad (3.18a)$$

$$(\mathbf{H}_1 - \mathbf{H}_2) \times \mathbf{n} = \mathbf{0}. \quad (3.18b)$$

To provide continuity at the interface Γ_c between non-conducting and conducting regions, the potential functions must be appropriately coupled:

$$\nabla \times \mathbf{A}^* \cdot \mathbf{n} - \mu_0 \nabla \psi \cdot \mathbf{n} = 0 \quad (3.19a)$$

$$\frac{1}{\mu_0} \nabla \times \mathbf{A}^* \times \mathbf{n} - \nabla \psi \times \mathbf{n} = \mathbf{0}. \quad (3.19b)$$

Note that in the case of a conductivity jump inside the conductor, the normal component of \mathbf{A}^* is not continuous across the interface, because $\mathbf{J} = -[\sigma]\partial\mathbf{A}^*/\partial t$ [95]. However, the description of \mathbf{A}^* based on edge elements allows a jump in the normal component and, at the same time, enforces the continuity of the tangential component [96]. On the contrary, when applying an $\mathbf{A}-\phi$ formulation, the magnetic vector potential \mathbf{A} is continuous and the electric scalar potential ϕ restricts the current to the conducting domain.

The boundary conditions for the electric quantities are defined in a similar way to the magnetic quantities. The normal component of the current density and the tangential component of the electric field are continuous across all interfaces:

$$(\mathbf{J}_1 - \mathbf{J}_2) \cdot \mathbf{n} = 0 \quad (3.20)$$

$$(\mathbf{E}_1 - \mathbf{E}_2) \times \mathbf{n} = \mathbf{0}. \quad (3.21)$$

In finite element analysis, the computational domain must be bounded by an outer air domain. On the boundary, the normal component of the magnetic field is set to zero such that

$\mathbf{n} \cdot (\mu_0 \nabla \psi) = 0$. The air domain chosen must be large enough to avoid field distortion effects. Typically, the air domain is approximately 3-5 times larger than the characteristic size of the problem. A comprehensive summary of the use of different potential functions in conducting and non-conducting domains and their coupling can be found in [96, 97].

In the following, different model approaches, including their applicability and limitations, are described.

3.2.2 Time Dependent Approaches

3.2.2.1 Moving Defect Approach

The electromagnetic fields in the moving defect approach (MDA) are calculated in the laboratory frame of reference (see Fig. 3.1). The basic principle and the computational domains involved are shown in Fig. 3.2. In MDA, it is assumed that the conductor moves with a constant rectilinear velocity \mathbf{v} . Inside the conductor, a defect-domain Ω_d is defined. A special feature of the MDA is used in the defect modeling scheme. Defects are defined by time-dependent logical expressions (LEs) in Ω_d , which is discretized by a structured hexahedral grid. In this case, the conductivity distribution is time-dependent; it is described by:

$$[\boldsymbol{\sigma}(\mathbf{r}, t)] = (1 - LE(\mathbf{r}, t))[\boldsymbol{\sigma}_c] + LE(\mathbf{r}, t)[\boldsymbol{\sigma}_d], \quad (3.22)$$

whereas the indices c and d distinguish the conductivity tensors between the conductor and the defect, respectively. The use of logical expressions allows for the definition of multiple defects at the same time. The defect assembly in Ω'_d moves in the direction of motion by redefining the logical expression at every time step. In MDA, the governing equations from (3.10a) and (3.10b)

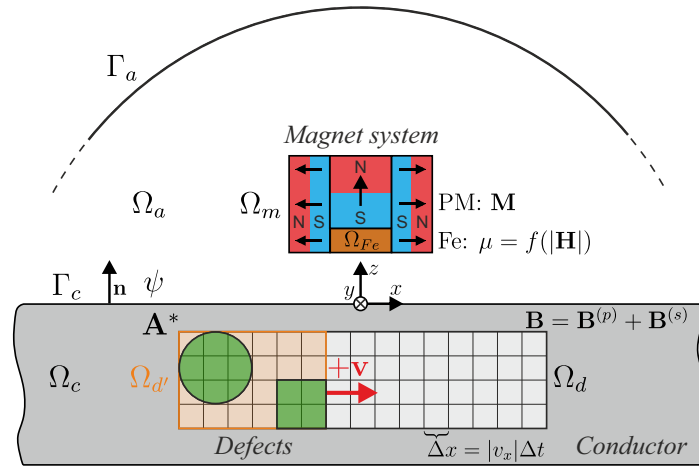


Figure 3.2: General principle of the moving defect approach (MDA).

in terms of the modified magnetic vector potential \mathbf{A}^* are given by:

$$\nabla \times \left(\frac{1}{\mu_0} \nabla \times \mathbf{A}^* - \mathbf{M} \right) = [\boldsymbol{\sigma}] \left(-\frac{\partial \mathbf{A}^*}{\partial t} + \mathbf{v} \times \nabla \times \mathbf{A}^* \right) \quad (3.23a)$$

$$\nabla \cdot \left([\boldsymbol{\sigma}] \left(-\frac{\partial \mathbf{A}^*}{\partial t} + \mathbf{v} \times \nabla \times \mathbf{A}^* \right) \right) = 0. \quad (3.23b)$$

The problem is solved by considering a fixed time step $\nu \Delta t = N \Delta x$ for any positive integer N . Therefore, time consuming re-meshing procedures are avoided. If the time-stepping scheme is not compatible with the structured mesh of the defect domain, numerical oscillations in the Lorentz force due to volume fluctuations may occur [98].

The quasi-stationary part of the induced eddy currents is incorporated in the term $\mathbf{v} \times \nabla \times \mathbf{A}^*$. However, the presence of defects leads to time-dependent magnetic fields, which are represented by the term $\partial \mathbf{A}^* / \partial t$. In this way, the approach includes the reaction of the conductor and the response due to the defect by taking time-dependent secondary magnetic fields $\mathbf{B}^{(s)}$ into account. As a result of the stationarity of Ω_m and Ω_{Fe} with respect to Ω_c , complicated magnet geometries such as Halbach arrays combined with ferromagnetic materials can be considered. However, note that the MDA is applicable as long as the defects are located far from any leading (front) or trailing edge (rear) of the conductor in the direction of motion. Moreover, complex defect shapes require sophisticated definitions in the logical expressions and very fine discretization so as to reduce staircasing effects, which, in turn, directly affects the overall efficiency of the MDA. Further reading regarding this approach can be found in [67] and [98].

3.2.2.2 Moving Magnet Approach

The time-dependent problem can be also solved in the rest frame of reference (see Fig. 3.1) using the moving magnet approach (MMA). The basic principle of MMA is shown in Fig. 3.3. The governing equations in terms of \mathbf{A}^* are given by:

$$\nabla \times \left(\frac{1}{\mu_0} \nabla \times \mathbf{A}^* - \mathbf{M} \right) = -[\boldsymbol{\sigma}] \frac{\partial \mathbf{A}^*}{\partial t} \quad (3.24a)$$

$$\nabla \cdot \left([\boldsymbol{\sigma}] \frac{\partial \mathbf{A}^*}{\partial t} \right) = 0. \quad (3.24b)$$

As mentioned previously, in this formulation, the velocity term is omitted and motion-induced eddy currents are incorporated with the time-derivative of the magnetic vector potential. Both solutions should be equivalent, as shown in section 3.1. In this case, secondary magnetic fields $\mathbf{B}^{(s)}$ and their time-derivatives $\partial \mathbf{B}^{(s)} / \partial t$ are taken into account.

The discretization scheme is similar to the scheme used in MDA, permitting the definition of multiple objects at the same time. However, in the present case, the defects are stationary and the remanence of an assembly of magnets is defined by direction-dependent logical expressions LE_i where $i = \{x, y, z\}$. For the sake of simplicity, the magnet assembly is assumed to be made of the same magnetic material, with a nominal remanence of B_r ; then, its spatial distribution is

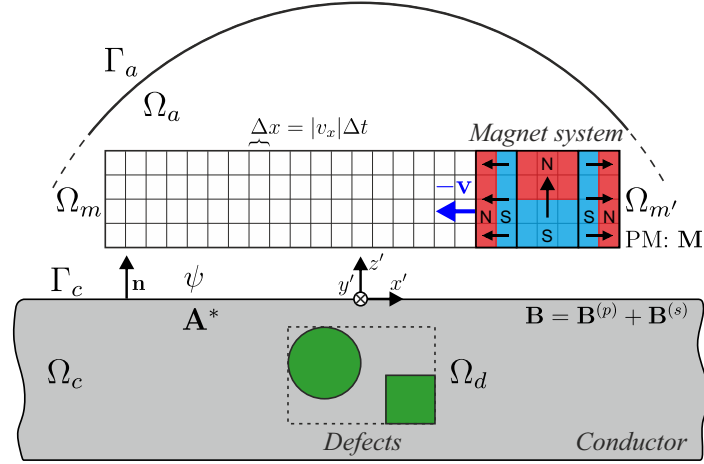


Figure 3.3: General principle of the moving magnet approach (MMA).

given by:

$$\mathbf{B}_r(\mathbf{r}, t) = [LE_x(\mathbf{r}, t), LE_y(\mathbf{r}, t), LE_z(\mathbf{r}, t)]^T B_r. \quad (3.25)$$

The assembly in Ω'_m moves with a constant velocity $-\mathbf{v}$ with respect to the conductor. The magnet domain Ω_m is discretized by an equidistant hexahedral finite element mesh. One advantage of MMA is its ability to model the complete force response signal resulting from specimens of finite size. Transient induction phenomena resulting from leading and trailing edges can be considered in the time-dependent case. Presently, the method is restricted to relatively simple magnet geometries, avoiding the presence of a region of ferromagnetic material Ω_{Fe} .

Both MDA and MMA are applicable in the case of constant velocities, because the time-dependent logical expressions are strongly related to the underlying equidistant finite element mesh. In principle, it is possible to adjust the step size Δx or the time step Δt in the case of time-dependent velocities accordingly. However, this adjustment requires a comprehensive analysis of the stability of the underlying solver (which was not performed in this thesis, but could be part of further investigations). Current implementations of MDA and MMA make use of an initial quasi-stationary solution for the field potentials to achieve fast convergence of physical solutions. An initial magnetic field and eddy current distribution is imported into the time-dependent solver for subsequent transient simulations [99]. Otherwise, the transient simulations must start with a zero initial condition ($\mathbf{A}^*|_{t=0} = 0$, $\psi|_{t=0} = 0$), assuming that no magnetic field penetrates through the conductor in the first time step. This situation would lead to non-physical diffusion effects during analysis. More information regarding MMA can be found in [67] and [98].

3.2.3 Quasi Stationary Approach

The quasi-stationary approach (QSA) is based on the analysis of induction phenomena in the laboratory frame of reference (see Fig. 3.1); its basic principle is shown in Fig. 3.4. In QSA, the

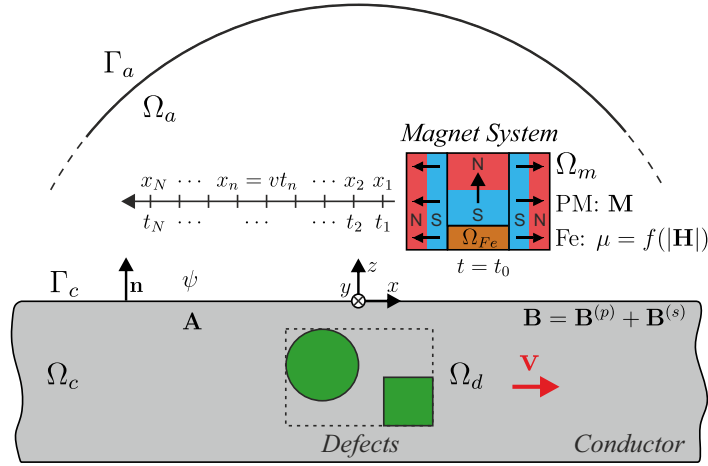


Figure 3.4: General principle of the quasi-stationary approach (QSA).

velocity term is included in the governing equations. Similar to time-dependent approaches, the modified vector potential \mathbf{A}^* from (3.17a) is divided into a magnetic vector potential \mathbf{A} and an electric scalar potential ϕ . The governing equations are simplified into quasi-stationary form, neglecting any time-dependency of the magnetic field, such that $\partial\mathbf{A}/\partial t = 0$ leading to $\partial\mathbf{B}^{(s)}/\partial t = 0$. However, the QSA takes into account the stationary part of $\mathbf{B}^{(s)}$:

$$\nabla \times \left(\frac{1}{\mu_0} \nabla \times \mathbf{A} - \mathbf{M} \right) = [\boldsymbol{\sigma}] (-\nabla\phi + \mathbf{v} \times \nabla \times \mathbf{A}) \quad (3.26a)$$

$$\nabla \cdot ([\boldsymbol{\sigma}] (-\nabla\phi + \mathbf{v} \times \nabla \times \mathbf{A})) = 0. \quad (3.26b)$$

The solution is exact as long as the moving conductor has a constant cross section, which is the case if there are no defects and the leading and trailing edges are far from the magnet system.

One advantage of QSA is that every solution is treated independently, and therefore, the use of logical expressions can be avoided. Thus, no extended structured mesh region is needed in the defect domain or the magnet domain, unlike the cases of MDA and MMA. Thus, the numbers of finite elements and DoFs are reduced. The modeling procedure in the QSA is, therefore, more flexible regarding the positioning of objects. The actual geometry of the objects can be modeled in more detail, especially in the case of shapes with a certain curvature such as spheres, ellipsoids, or cylinders. These advantages are compensated for by the necessity to generate a new finite element mesh when altering the magnet position. Assuming a rectilinear velocity in the x direction, an artificial time scale can be defined such that the position of the magnet system is altered step-wise along the direction of motion to a position $x_n = |v_x|t_n$ (see Fig. 3.4).

Similar to MMA, the force profiles can be determined along the entire specimen, including its edges. However, time-dependent secondary magnetic fields are neglected, which affects the resulting force profile in the case of high magnetic Reynolds numbers $R_m \gg 1$. In general, QSA can be used if defects or other geometrical inhomogeneities are present, as long as the magnetic Reynolds number R_m is moderately large. A more detailed analysis of the applicability of the

quasi-static approximation and the differences in time-dependent solutions will be given in section 3.3.

3.2.4 Weak Reaction Approaches

The induction problem at hand can be further simplified in the case of low magnetic Reynolds numbers ($R_m \ll 1$). In this case, the induced eddy current density is so small that its magnetic field $\mathbf{B}^{(s)}$ is vanishingly small compared to the primary magnetic field $\mathbf{B}^{(p)}$ of the magnet system. By setting $\mathbf{B}^{(s)} = 0$, the magnetic and electric fields are decoupled, and therefore, can be treated independently. Hereinafter, this effect will be referred to as a *weak reaction* by the conductor to the magnetic field. Special attention must be paid to the emerging Lorentz forces when using weak-reaction-based approaches. By neglecting the secondary magnetic field, the spatial symmetry of the electric and magnetic field is enforced. As a consequence, the lift component of the Lorentz force vanishes if the conductor is free of defects and if the magnet is far from any outer edge of the conductor, such that $F_z^{(0)} = 0$. However, in the presence of defects, the symmetry of the fields no longer holds and the defect response signal $\Delta \mathbf{F}$ can be determined. In the following section, two approaches are presented to illustrate the weak reaction principle, because the procedures have major advantages in terms of computational cost.

3.2.4.1 Extended Weak Reaction Approach

The basic principle of the extended weak reaction approach (eWRA) is shown in Fig. 3.5. The electromagnetic fields are determined in the laboratory frame of reference such that the conductor moves with a velocity \mathbf{v} with respect to the magnet system. The eWRA is based on a two-step procedure. In the first step, the primary magnetic field $\mathbf{B}^{(p)}$ is determined using the (primary) scalar magnetic potential $\psi^{(p)}$, including (possibly present) ferromagnetic material and neglecting any conductor in motion:

$$\nabla \cdot \left(-\nabla \psi^{(p)} + \mathbf{M} \right) = 0. \quad (3.27)$$

In the second step, only the moving conductor is considered. The primary magnetic field, $\mathbf{B}^{(p)} = -\mu_0 \nabla \psi^{(p)}$, is imported from the first step and mapped onto the nodes of the finite elements inside the conductor. The induced eddy currents are calculated using the scalar electric potential ϕ . Using Ohm's law for moving conductors, the induced eddy current density is given by:

$$\mathbf{J} = [\sigma] \left[-\nabla \phi - \mu_0 \mathbf{v} \times \left(\nabla \psi^{(p)} \right) \right]. \quad (3.28)$$

Applying the law of current conservation $\nabla \cdot \mathbf{J} = 0$ yields:

$$\nabla \cdot ([\sigma] \nabla \phi) = -\mu_0 \nabla \cdot \left[[\sigma] \mathbf{v} \times \left(\nabla \psi^{(p)} \right) \right]. \quad (3.29)$$

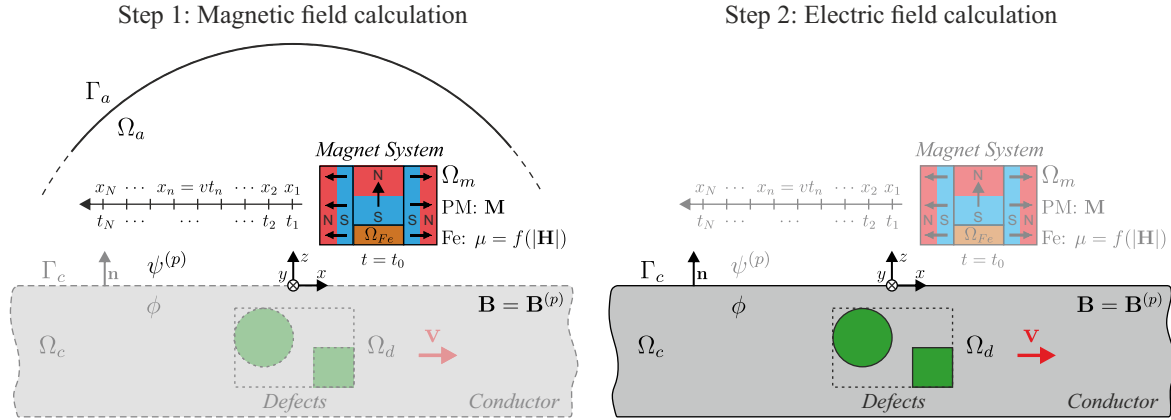


Figure 3.5: General principle of the extended weak reaction approach (eWRA).

The right-hand side of (3.29) can be simplified because the velocity \mathbf{v} and the primary magnetic field $\nabla\psi^{(p)}$ are curl-free inside the conductor, such that:

$$\nabla \cdot \left[\mathbf{v} \times \left(\nabla\psi^{(p)} \right) \right] = -\mathbf{v} \cdot \underbrace{\left[\nabla \times \left(\nabla\psi^{(p)} \right) \right]}_{=0} + \nabla\psi^{(p)} \cdot \underbrace{\left(\nabla \times \mathbf{v} \right)}_{=0} = 0. \quad (3.30)$$

Thus, the governing equation for ϕ is given by the following elliptic differential equation of second order with piecewise homogeneous material properties:

$$\nabla \cdot ([\boldsymbol{\sigma}] \nabla \phi) = 0. \quad (3.31)$$

Defining the boundary conditions $\mathbf{n} \cdot \mathbf{J} = 0$ at the boundaries of the conducting domain allows the computation of ϕ :

$$\nabla \phi \cdot \mathbf{n} = - \left[\mu_0 \mathbf{v} \times \left(\nabla\psi^{(p)} \right) \right] \cdot \mathbf{n}. \quad (3.32)$$

In this way, the current density is forced to flow inside the conducting domain.

Despite using a two-step procedure, eWRA has a higher computational efficiency than QSA, because only scalar potentials are involved, which leads to a decrease in the number of DoFs. The eWRA provides efficient numerical analysis, which is needed, for example, in an optimization framework.

3.2.4.2 Direct Weak Reaction Approach

The direct weak reaction approach (dWRA) is similar to eWRA described in the previous section. However, in dWRA, the primary magnetic field is analytically calculated. Thus, the numerical procedure is reduced to the calculation of the electric scalar potential ϕ . The general principle of the approach is shown in Fig. 3.6. The governing equation and the boundary conditions are given in (3.31) and (3.32), respectively. The dWRA has an even higher computational efficiency than eWRA. However, the analytical treatment of $\mathbf{B}^{(p)}$ permits the analysis of simple magnet geometries and prohibits the presence of ferromagnetic material in Ω_{Fe} .

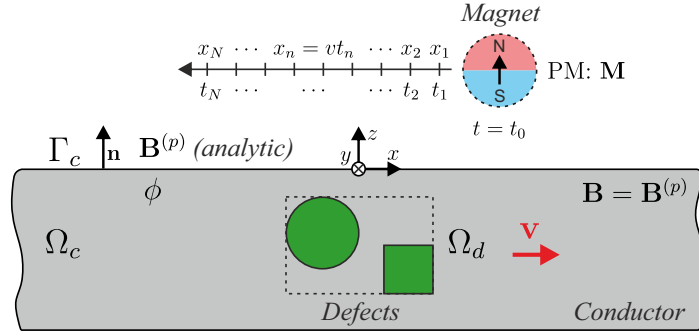


Figure 3.6: General principle of the direct weak reaction approach (dWRA).

Analytical expressions for the magnetic flux density for spherical magnets are obtained by considering a single magnetic dipole with a magnetic moment of $\mathbf{m} = \frac{4}{3}\pi R^3 \mathbf{M}$ [84]. Closed-form analytical expressions for parallelepipedal or cuboidal magnets are given in [100]. However, the magnetic flux density of cylindrical magnets involves elliptic integrals, which cannot be expressed in terms of elementary functions [101]. An implementation in the framework of LET is presented by the author in [102]. The elliptic integrals are approximated using the mid-point rule [103] and the iterative arithmetic geometric mean (AGM) method [104]. AGM proves suitable because it provides fast convergence, which is needed to evaluate the force density in every node within the conductor so as to determine the total force using (3.14).

The magnetic flux density of more complex magnet geometries can be approximated by employing the principle of superposition of the field generated by multiple magnetic dipoles. This modeling approach is addressed by Mengelkamp *et al.* [105] in a framework of Lorentz force evaluation. More information regarding dWRA can be found in [102] and [106].

3.2.5 Summary and Overview

An overview of the presented methods is given in Table 3.1. The methods can be classified as *time-dependent*, *quasi-stationary*, or *weak-reaction* with decreasing computational complexity, as indicated by the governing equations. Additionally, the table provides the unknown quantities (DoFs) to be determined in the respective domains and the driving term of the induced eddy currents (\mathbf{J} -term). The relation between the secondary magnetic field and the range of validity with respect to R_m can be readily identified. In the following section, the methods are compared for a typical LET problem so as to provide more information regarding the actual applicability for different magnetic Reynolds numbers R_m .

3.3 Comparison of Numerical Approaches

The approaches differ in their treatment of the secondary magnetic field $\mathbf{B}^{(s)}$. Hence, it is necessary to investigate their applicability in terms of magnetic Reynolds number R_m . The

Approach	Governing Equation	Eq.	DoFs: Ω_c $\Omega_{a m}$	J-term	$\mathbf{B}^{(s)}$	$\frac{\partial \mathbf{B}^{(s)}}{\partial t}$	R_m	
Time-dependent	MDA	$\nabla \times \left(\frac{1}{\mu_0} \nabla \times \mathbf{A}^* - \mathbf{M} \right) = [\boldsymbol{\sigma}] \left(-\frac{\partial \mathbf{A}^*}{\partial t} + \mathbf{v} \times \nabla \times \mathbf{A}^* \right)$	(3.23a)	\mathbf{A}^* \mathbf{A}^*	$\mathbf{v} \times \nabla \times \mathbf{A}^* - \frac{\partial \mathbf{A}^*}{\partial t}$	yes	yes	high
		$\nabla \cdot \left([\boldsymbol{\sigma}] \left(-\frac{\partial \mathbf{A}^*}{\partial t} + \mathbf{v} \times \nabla \times \mathbf{A}^* \right) \right) = 0$	(3.23b)					
	MMA	$\nabla \times \left(\frac{1}{\mu_0} \nabla \times \mathbf{A}^* - \mathbf{M} \right) = -[\boldsymbol{\sigma}] \frac{\partial \mathbf{A}^*}{\partial t}$	(3.24a)	\mathbf{A}^* \mathbf{A}^*	$-\frac{\partial \mathbf{A}^*}{\partial t}$	yes	yes	high
		$\nabla \cdot \left(-[\boldsymbol{\sigma}] \frac{\partial \mathbf{A}^*}{\partial t} \right) = 0$	(3.24b)					
Quasi-stationary	QSA	$\nabla \times \left(\frac{1}{\mu_0} \nabla \times \mathbf{A} - \mathbf{M} \right) = [\boldsymbol{\sigma}] \left(-\nabla \phi + \mathbf{v} \times \nabla \times \mathbf{A} \right)$	(3.26a)	\mathbf{A}, ϕ ψ	$\mathbf{v} \times \nabla \times \mathbf{A}$	yes	no	med.
		$\nabla \cdot \left([\boldsymbol{\sigma}] \left(-\nabla \phi + \mathbf{v} \times \nabla \times \mathbf{A} \right) \right) = 0$	(3.26b)					
Weak-Reaction	eWRA	$\nabla \cdot \left(-\nabla \psi^{(p)} + \mathbf{M} \right) = 0$	(3.27)	ϕ $\psi^{(p)}$	$-\mu_0 \mathbf{v} \times (\nabla \psi^{(p)})$	no	no	low
		$\nabla \cdot \left([\boldsymbol{\sigma}] \nabla \phi \right) = 0$	(3.31)					
	dWRA	$\mathbf{B}^{(p)}$ (analytic) $\nabla \cdot \left([\boldsymbol{\sigma}] \nabla \phi \right) = 0$	-	ϕ -	$\mathbf{v} \times \mathbf{B}^{(p)}$	no	no	low

Table 3.1: Overview of numerical approaches to modeling the electromagnetic field problem in LFT.

Table 3.2: Parameters of the exemplary LET problem used for comparisons among different model approaches.

Parameter	Value	Description
B_r	1.17 T	Remanence
X_m	10 mm	Length of the magnet
Y_m	10 mm	Width of the magnet
Z_m	10 mm	Height of the magnet
h	1 mm	Lift-off distance
X_d	12 mm	Length of the defect
Y_d	2 mm	Width of the defect
Z_d	2 mm	Height of the defect
d	2 mm	Defect depth
X_s	250 mm	Length of the specimen
Y_s	50 mm	Width of the specimen
Z_s	50 mm	Height of the specimen
σ_{Al}	30.61 MS/m	Electrical conductivity of aluminium
σ_{Cu}	59.8 MS/m	Electrical conductivity of copper

ratio between primary and secondary magnetic fields depends on the underlying geometry of the problem, as indicated by the characteristic length L in R_m in (3.13). To conduct an expressive comparison, an exemplary LET problem that corresponds to the dimensions of the available laboratory setup is defined. In this numerical experiment, a cuboidal permanent magnet, which is magnetized in the z direction, acts as the magnetic field source. Because of the simple geometry of the magnet, dWRA is used in the present analysis. Because eWRA uses the same treatment of secondary magnetic fields, the analysis is limited to dWRA (it will be simply referred to WRA in the following discussion). The direction of motion is defined such that the conductor moves with a positive velocity v_x along the x axis in MDA, QSA, and WRA; in the case of MMA, the magnet moves with a negative velocity $-v_x$ with respect to the conductor. The magnet and the defect are located symmetrically with respect to the specimen at $y = 0$ such that the object is analyzed on its centerline. Therefore, the side component of the Lorentz force F_y vanishes. The geometrical and material parameters of the exemplary problem are summarized in Table 3.2. Because the exemplary problem is strongly related to the experimental setup, all calculations are performed for isotropic specimens where $\sigma_{xx} = \sigma_{yy} = \sigma_{zz}$ (e.g., solids) and anisotropic specimens where $\sigma_{xx} = \sigma_{yy} \neq 0$ and $\sigma_{zz} = 0$ (e.g., composites or stacked sheets).

The absolute defect response signal (ADRS) $\Delta \mathbf{F}$ is defined as the force perturbation resulting from a defect. Because Lorentz forces are also present in the unperturbed case, the ADRS can be mathematically defined by the difference between the perturbed force profile \mathbf{F} and unperturbed

force profile $\mathbf{F}^{(0)}$:

$$\Delta\mathbf{F} = \mathbf{F} - \mathbf{F}^{(0)}. \quad (3.33)$$

The ADRSs are calculated for different magnetic Reynolds numbers R_m by varying the velocity. The force profiles in the case of isotropic and anisotropic specimens are shown in Fig. 3.7 and 3.8, respectively. The ADRS is plotted over the spatial coordinate x . Positive x values are sampled first (in time), based on the direction of motion defined above. Thus, the curves must be read from the right to left when considering the signal over time and not over space.

The first row shows the drag and lift components of the ADRS for low values of R_m . In this case, the secondary magnetic field is considerably smaller than the primary field from the magnet ($\mathbf{B}^{(s)} \ll \mathbf{B}^{(p)}$). The induced eddy current distribution and the total magnetic field are nearly symmetric, which results in a symmetric force profile when the magnet passes the defect. No significant differences can be identified between time-dependent approaches and WRA, which indicates that time-dependent effects are negligible. When increasing R_m , secondary fields and time-dependent effects become prevalent, resulting in non-symmetric field and force profiles. The ADRS obtained using WRA retains its symmetry because the secondary fields are neglected. As a consequence, WRA overestimates the ADRS amplitude by more than 100% compared to time-dependent approaches in the case of high R_m (see Fig. 3.7(e) and (f), and Fig. 3.8(e) and (f)). The ADRS obtained using QSA is closer to ADRS values obtained using MDA and MMA, because it includes the stationary part of the secondary magnetic field ($\mathbf{B}^{(s)} \neq 0$). Specifically, in the case of high R_m , the time-dependent part of the secondary magnetic field $\partial\mathbf{B}^{(s)}/\partial t$ has an increasing influence on the ADRS. By comparing the curve of QSA to those of MDA and MMA in Fig. 3.7(e) and (f), it can be seen that this results in a delayed and damped force response. As expected, the solutions from MMA and MDA are equivalent and yield very similar force profiles, because they only differ in the definition of the frame of reference.

The described effects pertain to both isotropic and anisotropic specimens. However, the ADRS has higher amplitudes in the case of anisotropic specimens than in the case of isotropic specimens. This phenomenon can be explained based on the imposed condition that $J_z = 0$ because $\sigma_{zz} = 0$. As a consequence, the current flows around the defect only in the xy -plane (i.e., not vertically). This phenomenon positively influences the resulting Lorentz force in terms of the ADRS amplitude. The shape of the ADRS is weakly influenced by this condition because in the unperturbed case, the induced eddy currents already flow solely in the xy -plane. However, some differences between the two cases can be identified; their anisotropic profiles show slightly sharper ADRSs, producing higher gradients. We conclude that the present anisotropy condition influences the profile but does not significantly change it, as is, for example, intended in the case of transformer sheets to prevent eddy current losses. This result confirms the applicability of layered specimens for the investigation of deep-lying defects.

To quantify the differences between the individual approaches depending on R_m , the normalized root mean square deviation (NRMSD) is calculated for the solutions obtained using MDA.

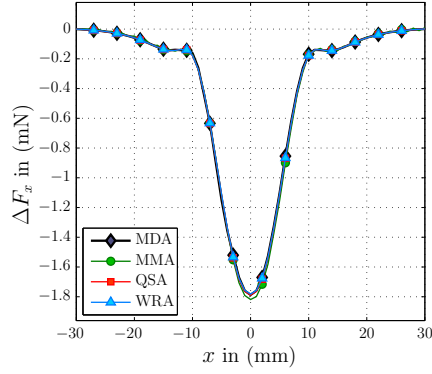
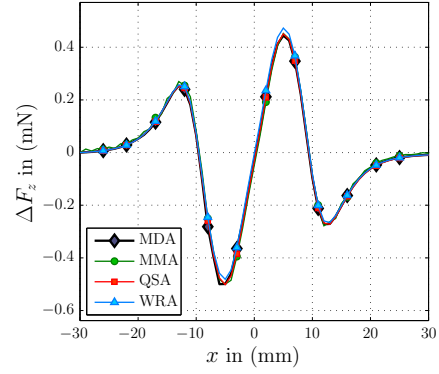
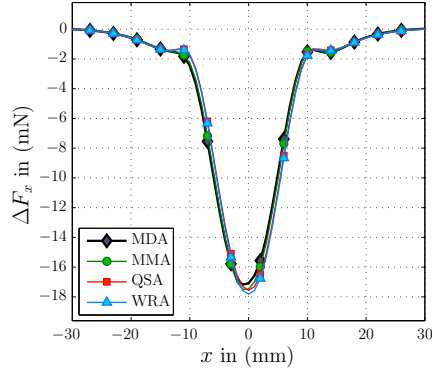
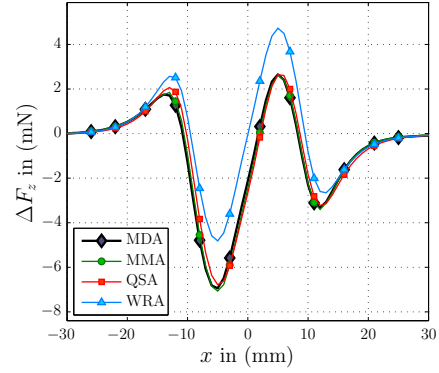
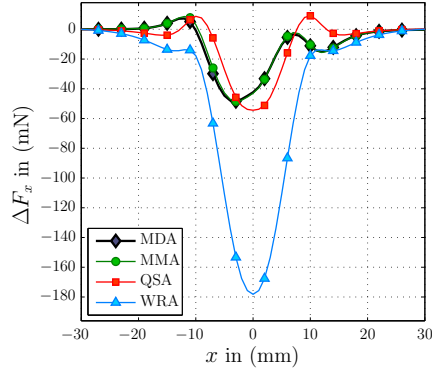
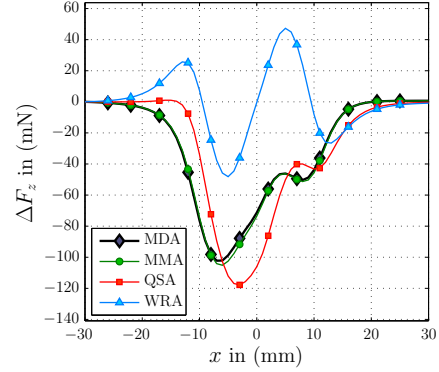

 (a) $R_m = 0.096$, $v_{Al} = 0.1$ m/s, $v_{Cu} = 0.05$ m/s

 (b) $R_m = 0.096$, $v_{Al} = 0.1$ m/s, $v_{Cu} = 0.05$ m/s

 (c) $R_m = 0.961$, $v_{Al} = 1$ m/s, $v_{Cu} = 0.51$ m/s

 (d) $R_m = 0.961$, $v_{Al} = 1$ m/s, $v_{Cu} = 0.51$ m/s

 (e) $R_m = 9.616$, $v_{Al} = 10$ m/s, $v_{Cu} = 5.12$ m/s

 (f) $R_m = 9.616$, $v_{Al} = 10$ m/s, $v_{Cu} = 5.12$ m/s

Figure 3.7: Comparison of the absolute defect response signals of the drag-force ΔF_x (left) and lift-force ΔF_z (right) determined using different model approaches in the case of isotropic specimens. The magnetic Reynolds number R_m and the corresponding velocities in the case of specimens made of aluminium ($\sigma_{Al} = 30.61$ MS/m) or copper ($\sigma_{Cu} = 59.8$ MS/m) are provided. (a) and (b) low R_m , (c) and (d) medium R_m , (e) and (f) high R_m .

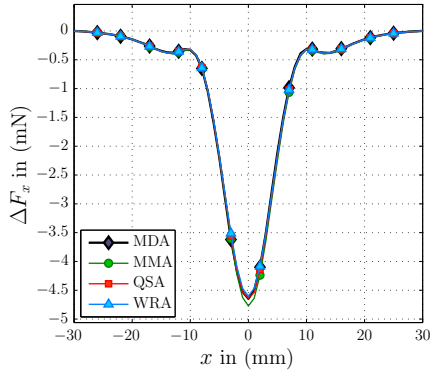
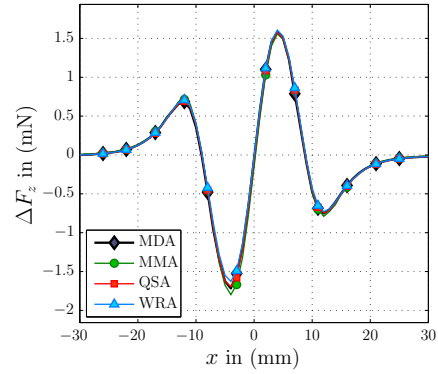
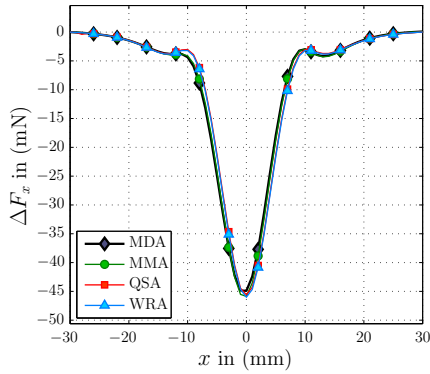
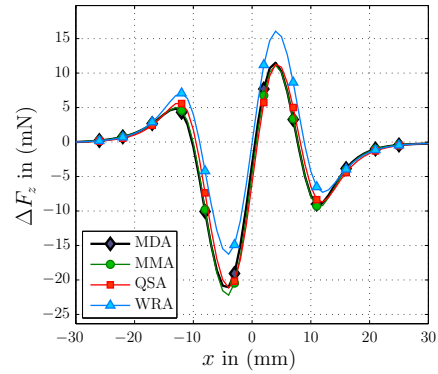
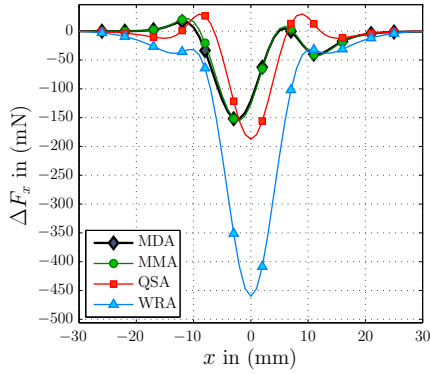
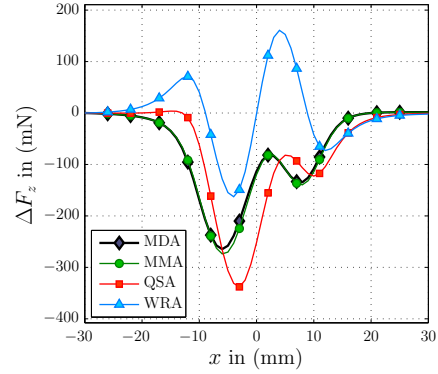

 (a) $R_m = 0.096$, $v_{Al} = 0.1$ m/s, $v_{Cu} = 0.05$ m/s

 (b) $R_m = 0.096$, $v_{Al} = 0.1$ m/s, $v_{Cu} = 0.05$ m/s

 (c) $R_m = 0.961$, $v_{Al} = 1$ m/s, $v_{Cu} = 0.51$ m/s

 (d) $R_m = 0.961$, $v_{Al} = 1$ m/s, $v_{Cu} = 0.51$ m/s

 (e) $R_m = 9.616$, $v_{Al} = 10$ m/s, $v_{Cu} = 5.12$ m/s

 (f) $R_m = 9.616$, $v_{Al} = 10$ m/s, $v_{Cu} = 5.12$ m/s

Figure 3.8: Comparison of the absolute defect response signals of the drag-force ΔF_x (left) and lift-force ΔF_z (right) determined using different model approaches in the case of anisotropic specimens. The magnetic Reynolds number R_m and the corresponding velocities in the case of specimens made of aluminium ($\sigma_{Al} = 30.61$ MS/m) or copper ($\sigma_{Cu} = 59.8$ MS/m) are provided. (a) and (b) low R_m , (c) and (d) medium R_m , (e) and (f) high R_m .

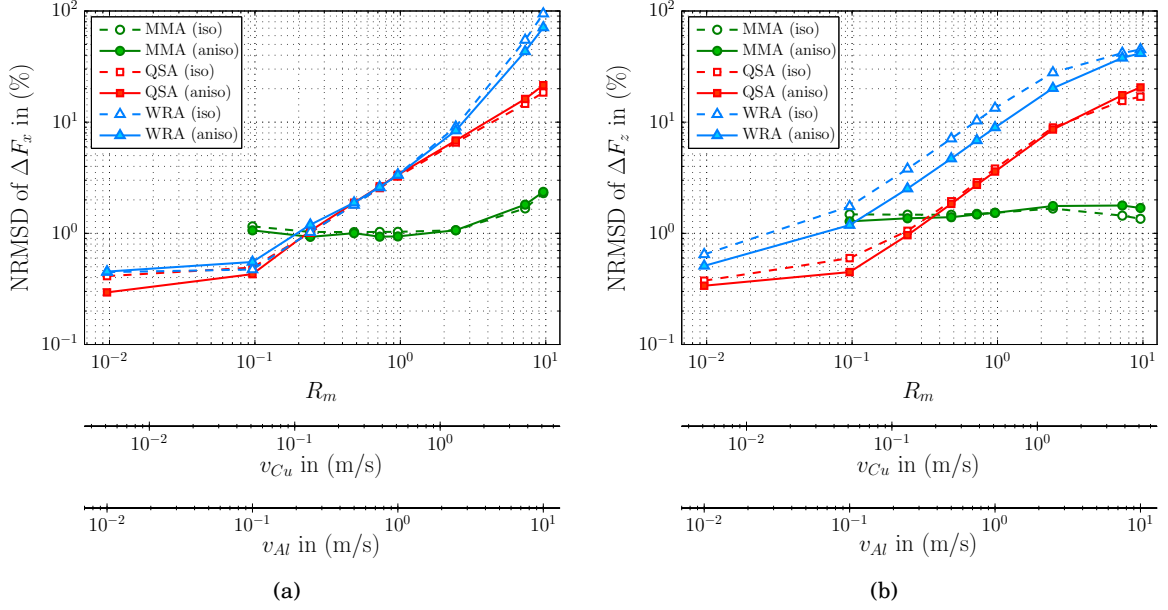


Figure 3.9: Normalized root mean square deviation of the defect response signals of (a) the drag-force ΔF_x and (b) the lift-force ΔF_z for different model approaches in the case of isotropic and anisotropic conductivity profiles. Additional abscissae are provided for velocities of specimens made of copper ($\sigma_{Cu} = 59.8$ MS/m) and aluminium ($\sigma_{Al} = 30.61$ MS/m).

The NRMSD is defined as:

$$\text{NRMSD}_{x|z} = \frac{100\%}{\max(\Delta F_{x|z}^{(\text{MDA})}) - \min(\Delta F_{x|z}^{(\text{MDA})})} \sqrt{\frac{1}{N} \sum_{i=1}^N (\Delta F_{x|z,i} - \Delta F_{x|z,i}^{(\text{MDA})})^2}. \quad (3.34)$$

The force components $\Delta F_{x|z,i}$ are compared at discrete points separated by $\Delta x = 1$ mm indexed by i over the plotted range, as shown in Fig. 3.7 and 3.8. The defined error allows us to quantify the derivation of the shape and the amplitude between the different methods with respect to MDA. The NRMSDs are shown with double logarithmic scale in Fig. 3.9. The abscissa is shown in two different velocity ranges considering specimens made of copper and aluminium to better illustrate the process in terms of potential NDT applications. During the analysis, the applied discretization (a finite element mesh) is defined such that it is as similar as possible among the individual approaches.

The error in the drag-force is shown in Fig. 3.9(a). WRA and QSA are at nearly the same level, up to moderate values of R_m . However, the error in WRA increases to 100% when R_m reaches values of roughly 10, which corresponds to velocities of roughly 6 m/s or 10 m/s for specimens made of copper or aluminium, respectively. The error in the lift-force perturbation is shown in Fig. 3.9(b). The NRMSD is significantly larger in the case of WRA, relative to QSA. This limits the applicability of WRA to the low R_m regime. For both force components, the error in MMA is at a nearly constant level, resulting from numerical inaccuracies. The conductivity anisotropy has a minor effect on the relative error in the case of the drag-force. Slightly larger

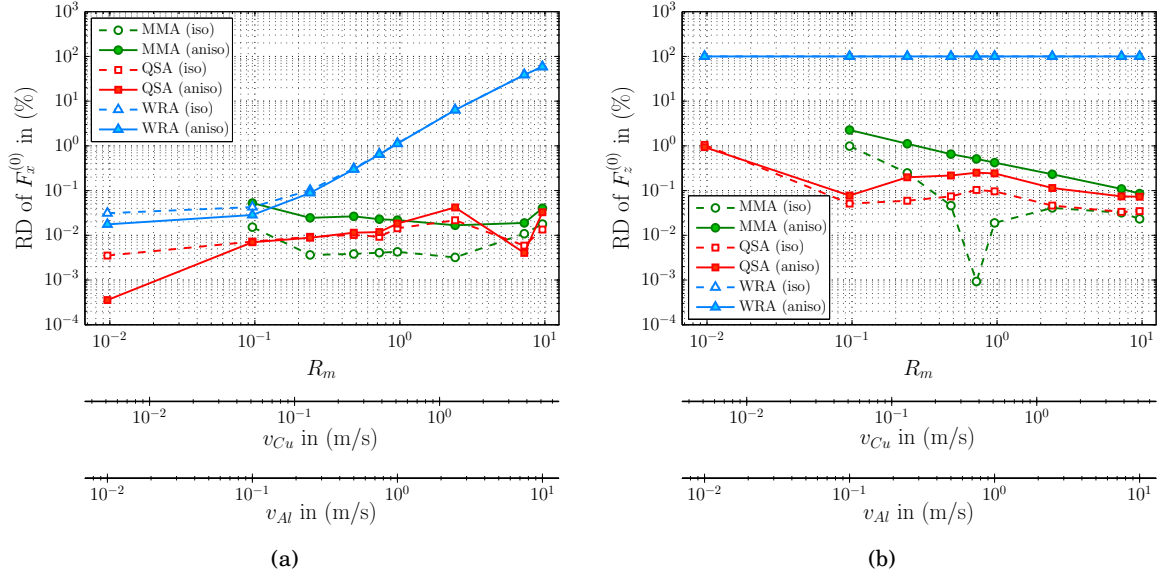


Figure 3.10: Relative difference of (a) the unperturbed drag-force $F_x^{(0)}$ and (b) the unperturbed lift-force $F_z^{(0)}$ for different model approaches in the case of isotropic and anisotropic conductivity profiles. Additional abscissae are provided for velocities of specimens made of copper ($\sigma_{Cu} = 59.8$ MS/m) and aluminium ($\sigma_{Al} = 30.61$ MS/m).

errors can be observed for the lift-force of the isotropic specimen when applying WRA (see the dotted blue line in Fig. 3.9(b)).

In addition to the drag-force perturbation $\Delta \mathbf{F}$, the methods differ in the estimation of the unperturbed drag-force $\mathbf{F}^{(0)}$. Because the Lorentz forces are measured in an absolute sense, a correct estimation of $\mathbf{F}^{(0)}$ is necessary when designing new systems. The absolute value of the relative difference (RD) of the unperturbed drag force is evaluated with respect to the reference solution obtained using MDA. The RD is defined by:

$$\text{RD}_{x|z} = \left| \frac{F_{x|z}^{(0)} - F_{x|z}^{(0,MDA)}}{F_{x|z}^{(0,MDA)}} \right| 100\%. \quad (3.35)$$

Similar to the NRMSD, the individual force components indexed by c are independently compared to each other. The relative errors are shown in Fig. 3.10. Regarding WRA, similar behavior can be observed concerning the drag-force when increasing the magnetic Reynolds number R_m . However, the error in QSA remains at a constant level (as does that of MMA). This result is expected, because QSA yields exact results as long as the stationarity of the process is ensured (which is the case if the material is free of defects).

One major drawback of WRA is the absence of the unperturbed lift force $F_z^{(0)}$, which is an immediate result of the decoupling of electric and magnetic fields. The imposed symmetry in $\mathbf{B}^{(p)}$, and therefore also in \mathbf{J} , eliminates the lift force after the volume integration:

$$F_z^{(0)} = - \int_{\Omega_c} \left(J_x B_y^{(p)} - J_y B_x^{(p)} \right) d\Omega = 0. \quad (3.36)$$

As a consequence, the relative difference of $F_z^{(0)}$ is 100% in Fig. 3.10(b).

The present chapter provides an introduction to the underlying physics of motion-induced eddy currents. The expressions are simplified by analyzing the nondestructive testing problem at hand. Additionally, different numerical approaches are presented and their basic principles are explained. The problem is simplified step-by-step, starting from time-dependent approaches, applying quasi-static approximations, and assuming a weak reaction from the conductor. The applicability of the different approaches is exemplified on a typical (representative) LET problem. The approaches are verified for time-dependent MDA. The derived errors indicate the limits of applicability with respect to the magnetic Reynolds number R_m . The derived errors may slightly change when altering the geometrical parameters of the problem, for example, the size or location of the magnet or the defect. However, the present analysis provides valuable insight regarding how time-dependent effects are projected onto the Lorentz force profile in the case of moving conductors.

SIMULATION STUDIES

This chapter contains the results of different interconnected simulation studies, which are performed to develop and refine the LET method. At first, an optimization strategy to determine improved magnet designs for LET is presented. In this study, optimal magnet designs are proposed and manufactured prototypes for future LET systems are presented. Secondly, an uncertainty analysis of the LET system under investigation is performed. The statistical properties of the dependent parameters are determined experimentally and their influence on the resulting Lorentz force is analyzed by means of numerical simulations. During this analysis, it is observed that the velocity of the specimen varies sinusoidally. A mathematical description of this problem was not yet provided. This phenomenon is addressed in the last section of this chapter, providing an analysis on the influence of time-dependent velocity variations on the Lorentz force.

4.1 Optimal Magnet Design for LET

4.1.1 Introduction and Motivation

Comparative studies between LET and ECT indicated the potential and competitiveness of LET [32, 77]. However, the performance of an LET system can be enhanced further by applying optimization schemes to determine advanced magnet systems with improved characteristics. This involves an appropriate problem definition and associated criteria.

The optimization goal in LET is to maximize the response resulting from an inclusion surrounded by conductive material, thereby increasing the signal-to-noise ratio and, hence, improving the detection rate. However, due to the high variety of NDT problems, it is self-evident that the final details of an optimized setup strongly depend on the detection goal and external testing conditions for the particular application. The proposed methodology is

developed as generally as possible, to describe and address the problem specificity. However, when considering permanent magnet systems, generality is limited by practicability, and so the geometry and associated design variables are chosen such that practical feasibility is assured. The optimization process is performed with nondimensional parameters. This provides the opportunity to determine scale-independent and generalized optimization results while decreasing the number of independent parameters. This approach can then be applied to different applications to determine optimal magnet designs for specific cases.

At first, the required parameters and the optimization problem is described in sections 4.1.2.1 to 4.1.2.4. It is followed by the definition of the objective function and the corresponding constraints in sections 4.1.2.5 and 4.1.2.6, respectively. The developed optimization strategies are presented in section 4.1.2.7 and the applied optimization algorithm, sequential quadratic programming (SQP), is briefly described in section 4.1.2.8. The numerical procedure to evaluate the objective function and the constraints is described in section 4.1.2.9. In section 4.1.3, the numerical optimization results are presented and discussed. The design process of prototypes of optimized magnet designs is described in section 4.1.4. It is followed by a study regarding the current detection limit of deep-lying defects in section 4.1.5. The chapter is summarized and conclusions are drawn in section 4.1.6. The presented optimization approach and the corresponding results are published by the author and can be found in [107].

4.1.2 Methods

4.1.2.1 Problem Definition

The optimal magnet design is focused on non-magnetic, electrically conducting specimens. The optimization is performed under the assumptions of a smooth specimen surface and that the defect is located far from any lateral boundary, to neglect parasitic edge effects. Since the resulting Lorentz force profile depends on the shape and the depth of the inclusion, an equivalent defect of cuboidal shape is defined to represent a general flaw. The assumptions can be modified to any particular case of interest, since this would involve only the geometry of the specimens defined in the forward solution, which are described in one of the following sections. The optimization is performed with respect to the drag-force F_x and the associated absolute defect response amplitude (ADRA) $\Delta\hat{F}_x$, resulting from the difference between the unperturbed drag-force $F_x^{(0)}$ and the perturbed drag-force $F_x^{(d)}$:

$$\Delta\hat{F}_x = \max \left| F_x^{(d)} - F_x^{(0)} \right|. \quad (4.1)$$

As it has been shown in the previous chapter, the force profile is symmetric, if the interaction between the primary magnetic field $\mathbf{B}^{(p)}$, generated by the permanent magnet, and the secondary magnetic field $\mathbf{B}^{(s)}$ from the induced eddy currents, is negligible.

In Fig. 4.1, the geometrical parameters of the problem are shown together with the ADRA. The specimen is modeled as a pseudo-infinite half-space including a defect with edge length a , located at a depth d . The magnet system is located at a lift-off distance h above the specimen.

The optimization scheme presented here covers, but is not limited to, purely isotropic specimens ($\sigma_{xx} = \sigma_{yy} = \sigma_{zz}$) and laminated structures ($\sigma_{xx} = \sigma_{yy} \neq 0, \sigma_{zz} = 0$), as they are shown in Fig. 2.5 on page 13.

4.1.2.2 Magnet System and Design Variables

Three related magnet geometries with increasing manufacturing complexity are investigated, originating from empirical pre-investigations. These are:

- Standard cylindrical permanent magnets (C)
- Cylindrical Halbach-structures (HC)
- Cylindrical Halbach-structures supported by highly saturated soft magnetic material, such as iron-cobalt-alloys (HCp)

In the general case, the nondimensional design variables \mathbf{x} , shown in Fig. 4.1, are defined as:

$$\mathbf{x} = \left[\frac{H_2}{R_2}, \frac{R_1}{R_2}, \frac{H_1}{H_2} \right], \quad (4.2)$$

where H_2 and R_2 are the height and radius of the outer cylinder, respectively; R_1 is the inner radius of the Halbach-structure; and H_1 is the height of the ferromagnetic material. The inner cylinder is axially magnetized, whereas the surrounding cylinder is magnetized in the radial direction.

For C- and HC-systems, particular design variables become constant and the number of free variables is reduced such that for C-systems, $R_1/R_2 = 1$ and $H_1/H_2 = 0$, and for HC-systems

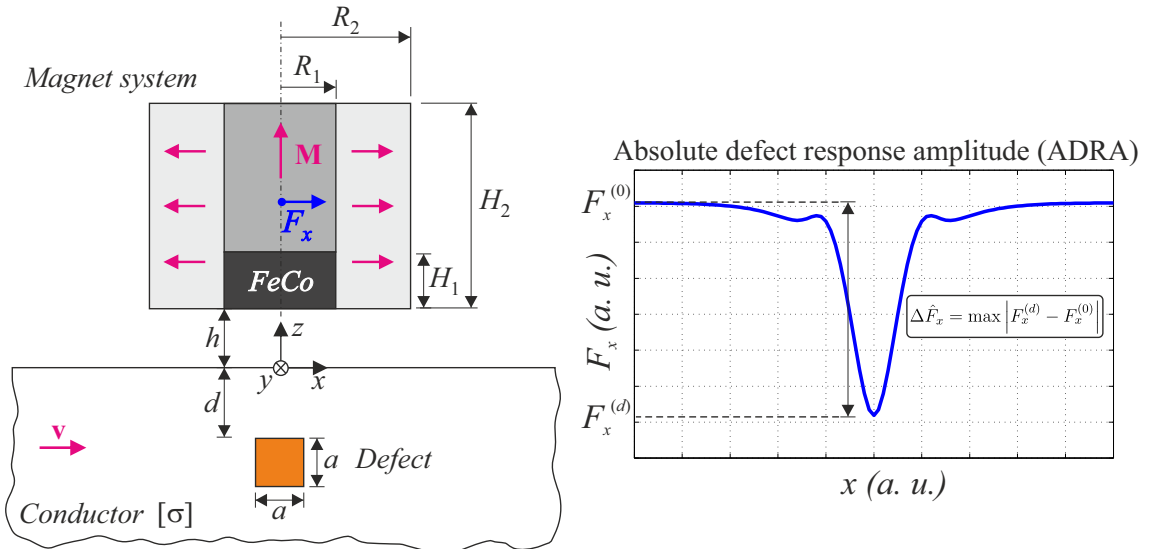


Figure 4.1: Geometrical parameters of the LET setup, design variables of the magnet system and illustration of the absolute defect response amplitude used as objective function [107].

$H_1/H_2 = 0$. Thus, the configurations are subproblems of each other; i.e., C-magnets are included in HC-configurations, which in turn are included in HCp-systems. As a consequence, by applying the presented optimization scheme considering all three design variables as free variables, a wide variety of different designs is included in the optimization. An optimal magnet system can be determined for a standard cylinder or a Halbach-structure with or without ferromagnetic material.

The construction of interchanging magnetization direction corresponds to the concept of Mallinson [110] and Halbach [111]. Changing the magnetization direction of adjacent parts of the magnet forms a semi-open magnetic circuit. Hence, the magnetic flux density is increased on one side of the magnet system and decreased on the opposite side. In the ideal case, it is possible to eliminate the magnetic flux on one side completely by employing dual magnetizations determined by means of the Hilbert transformation [110]. Practical feasibility of this form of magnetization is still a challenge. Nevertheless, geometrical approximations in the form of segments can be employed instead. These structures are typically termed as Halbach-arrays and find application in particle accelerators [111], high-speed motors/generators and servomotors [112], loudspeakers [113], magnetic bearings [114, 115], and nuclear magnetic resonance spectroscopy [116]. In the framework of Lorentz force velocimetry of electrically weak conducting liquids, commonly applied linear Halbach-arrays are already used to increase the

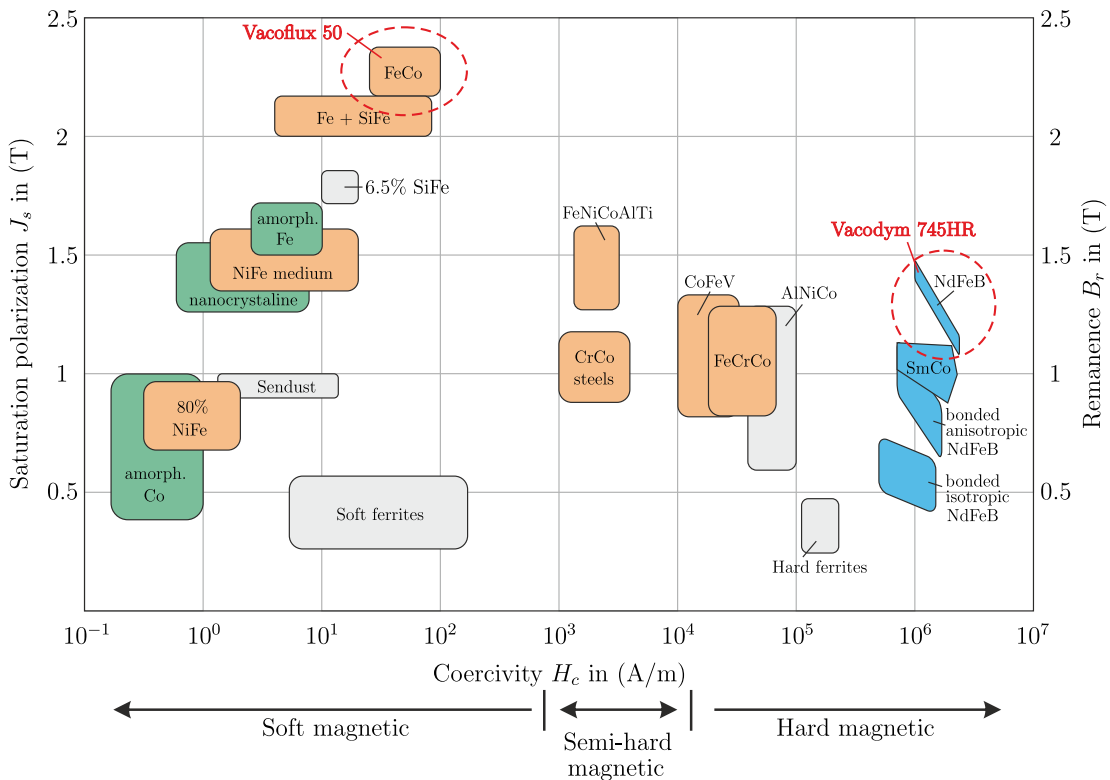


Figure 4.2: Overview of soft and hard magnetic materials. The used materials in the optimization, VACOFLUX[®] 50 [108] and VACODYM[®] 745HR [109], are highlighted.

drag-force signal [117]. These systems are not optimized in terms of the defective specimen, which further motivates to investigate the optimization problem in LET.

A radially magnetized Halbach-cylinder of infinite height produces no magnetic field in the inner or outer air domain surrounding the cylindrical magnet [118]. However, in case of finite heights, this effect vanishes and strong directed fields are present at the terminations. In this work, the concept of Halbach-arrays is extended to a novel rotationally symmetric structure including an axially magnetized cylinder, which is supported by ferromagnetic material to intensify the magnetic flux density close to the object under test.

In this work, a part of the permanent magnet is replaced by ferromagnetic material with high saturation magnetization and hence a stronger residual field [119]. In general, ferromagnetic material can be used to focus and concentrate the flux, known as flux compression. Thus, the magnetic flux density is amplified when the ferromagnetic part is exposed to the external magnetic field of the permanent magnets. Consequently, the resulting Lorentz force is potentially increased. The choice of suitable materials is decisive for a successful optimization. An overview of soft and hard magnetic materials is given in Fig. 4.2. In the present study, the hard magnetic material VACODYM[®] 745HR [109] with a nominal magnetic remanence of $B_r = 1.44$ T is used (VACUUMSCHMELZE GmbH & Co. KG, Hanau, Germany, [120], www.vacuumschmelze.de) together with the soft magnetic iron-cobalt-alloy VACOFLUX[®] 50 [108] with a saturation polarization of 2.3 T. The $B(H)$ curves of both materials are shown in Fig. 4.3, illustrating the principle to increase the magnetic flux density. A similar approach is proposed during the design process of focus lenses for linear collider accelerators [121, 122], as well as for superconducting cyclotron magnets [119]. The chosen materials represent the current state of the art in magnetism and are thus most suitable for an optimal LET sensor.

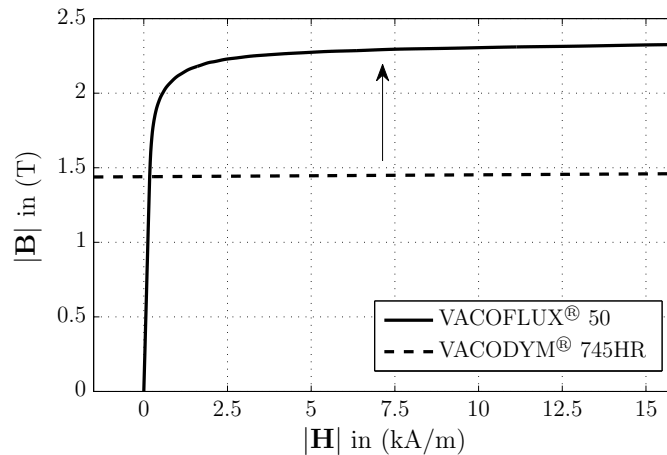


Figure 4.3: $B(H)$ curve of the iron-cobalt-alloy VACOFLUX[®] 50 used as ferromagnetic material in HCp-magnet systems in FEM simulations and a part of the hysteresis of the hard magnetic permanent magnet material NdFeB of type VACODYM[®] 745HR ($B_r = 1.44$ T) at room temperature [107].

4.1.2.3 Scaling Parameters

To reduce the number of parameters, it is advisable to exploit *a priori* known dependencies between certain input parameters and the drag-component of the Lorentz force. A scaling factor S can be defined to scale the forces accordingly. If the ADRA, which will be used later as the objective function, can be simply scaled, the global optimum of the design variables $\tilde{\mathbf{x}}$ is scale invariant with respect to the reduced parameters. This reduces the need to rerun numerically expensive simulations and provides the desired generality. The scaling quantities are summarized in the vector of scaling parameters:

$$\mathbf{s} = [\sigma, v, B_r, h]. \quad (4.3)$$

The scaling properties of individual quantities can be determined considering the following estimate, which is valid provided secondary magnetic fields generated by the induced eddy currents are negligible [63]:

$$F_x \sim \sigma v m^2 h^{-3}, \quad (4.4)$$

where m is the equivalent magnetic dipole moment of the magnet system, which can be expressed in terms of remanence and magnet volume V_m such that $m \sim B_r V_m$. For geometric scaling, it is assumed that the whole geometry of the problem scales with the lift-off distance h so that $V_m \sim h^3$, without loss of generality. Thus, (4.4) can be expressed as:

$$F_x \sim \sigma v B_r^2 h^3. \quad (4.5)$$

Note that the drag-force F_x depends linearly on the velocity v and the electrical conductivity σ . This property can be extended to the case of possibly anisotropic specimens by defining the conductivity tensor $[\boldsymbol{\sigma}]$ from (3.7) in terms of a scalar conductivity σ , which defines the magnitude of the conductivity and the anisotropy vector \mathbf{a}_σ :

$$[\boldsymbol{\sigma}] = \sigma \text{diag}(\mathbf{a}_\sigma^T). \quad (4.6)$$

In the isotropic case, the anisotropy vector is given by $\mathbf{a}_\sigma = [1, 1, 1]^T$. If the specimen is made from metal sheets, as in the case of the laboratory setup (see Fig. 2.7 on page 16), the anisotropy vector is $\mathbf{a}_\sigma = [1, 1, 0]^T$. The prescribed scaling property of the electrical conductivity addresses the scalar conductivity σ , and, thus, holds for both isotropic and anisotropic specimens.

Closer inspection of (4.5) shows that the Lorentz force increases with the square of the remanence B_r . However, this scaling property can be applied if and only if nonlinear ferromagnetic material is omitted or considered as linear in the whole domain. Since the nonlinearity between \mathbf{H} and \mathbf{B} is accounted for, this factor can only be modified for C- and HC-systems, and must be fixed at a predefined remanence in the case of HCp-systems. The magnetic remanence can be used as a scaling factor if the whole magnet system is made from the same magnetic material. If this is not the case, the remanence of each compartment has to be scaled in the same way.

The system parameters, described later in detail, define the geometrical relationships of the problem. However, it is of interest how $F_x^{(0)}$ and $\Delta \hat{F}_x$ scale with respect to the geometrical

size of the problem. Reformulating (4.4) to (4.5) provides the scaling property of the drag-force directly as a cubical relationship with respect to h , serving as the characteristic length and thus defining the geometrical size of the problem. In this sense, h is eliminated from the set of independent parameters and only the geometrical ratios with respect to h define the problem. According to the chosen h , the actual geometry can be stretched or clinched to any scale of interest.

Finally, by combining the individual scaling parameters into one, the scalar scaling factor S contains linear, quadratic, and cubic terms:

$$S = \left(\frac{\sigma v}{\sigma_0 v_0} \right) \left(\frac{B_r}{B_{r0}} \right)^2 \left(\frac{h}{h_0} \right)^3. \quad (4.7)$$

As reference values for the simulations, the velocity is set to $v_0 = 1$ m/s, the conductivity is $\sigma_0 = 1$ MS/m, the magnetic remanence is $B_{r0} = 1$ T, and the lift-off distance is $h_0 = 1$ mm. Consequently, the scaling factor can be used to convert the forces $F_x^{(0,s)} = S F_x^{(0)}$ and $\Delta \hat{F}_x^{(s)} = S \Delta \hat{F}_x$, according to the previously mentioned conditions. Thus, the total number of independent parameters is reduced by the number of scaling parameters.

4.1.2.4 System Parameters

Given the design variables \mathbf{x} of the magnet system and the scaling parameters \mathbf{s} , the LET setup is defined by the set of system parameters:

$$\mathbf{p} = \left\{ \frac{V_m}{V_d}, \frac{d}{h}, \frac{a}{h}, \mathbf{a}_\sigma, B_r, B(H) \right\}, \quad (4.8)$$

where $V_m = \pi R_2^2 H_2$ is the total volume of the magnet system and $V_d = a^3$ is the volume of the equivalent cuboidal defect. The magnet to defect volume ratio V_m/V_d defines the weight of the magnet system at constant defect volumes. The depth-to-lift-off ratio d/h defines the defect depth measured from the surface of the conductor to the upper surface of the defect. The system is geometrically completely described by the third ratio a/h between the edge length of the defect a and the lift-off distance of the magnet h . Since the material anisotropy of the specimen affects the eddy current distribution, the anisotropy vector \mathbf{a}_σ is included in the set of system parameters. The remanence B_r only appears as a system parameter if nonlinear ferromagnetic material is included in the magnet design. Otherwise, B_r is a scaling parameter. Finally, $B(H)$ is the initial magnetization curve of the ferromagnetic material.

4.1.2.5 Objective Function

The optimization goal is to maximize the ADRA $\Delta \hat{F}_x(\mathbf{x}, \mathbf{p})$. The scaling factor S from (4.7) allows generalizing the calculated ADRA independently for conductivity, velocity, and geometric scale (and in the linear case also for magnetic remanence). Given the defined set of system parameters \mathbf{p} , the optimal design variables $\tilde{\mathbf{x}}$ of the magnet system can be determined by applying distinct optimization schemes. Subsequently, the optimal ADRA $\Delta \tilde{F}_x(\tilde{\mathbf{x}}, \mathbf{p})$, together

with its corresponding unperturbed drag-force $\tilde{F}_x^{(0)}(\tilde{\mathbf{x}}, \mathbf{p})$ is provided and the limits of the system are determined. To this end, the objective function $f(\mathbf{x}, \mathbf{p})$ to be minimized is defined by the negative ADRA from (4.1):

$$\min_{\mathbf{x} \in \mathcal{F}} f(\mathbf{x}, \mathbf{p}) = -\Delta \hat{F}_x(\mathbf{x}, \mathbf{p}). \quad (4.9)$$

The objective function is nonlinear and depends on both the design variables and the system parameters. Thus, the optimal solutions $\tilde{\mathbf{x}}(\mathbf{p})$ depend on the predefined system parameters \mathbf{p} , which can be understood as a mathematical description of problem specificity with respect to external conditions. However, the optimal design variables have to be part of the feasible set of solutions \mathcal{F} . The feasibility of a solution is defined by constraints, which are described next.

4.1.2.6 Definition of Constraints

The feasible set of solutions \mathcal{F} is defined by two types of constraints. The first are linear inequality constraints, also known as bound constraints, resulting from the limits of the design variables \mathbf{x} , defined by the geometry of the magnet system. They are covered by the linear inequality constraints \mathbf{c}_1 , which must not be violated:

$$\mathbf{c}_1(\mathbf{x}, \mathbf{p}) \leq \mathbf{0} \quad (4.10)$$

$$\mathbf{c}_1(\mathbf{x}, \mathbf{p}) = [\mathbf{A}_{\text{HCp}}] \mathbf{x}^T - \mathbf{b}_{\text{HCp}}. \quad (4.11)$$

The linear inequality constraint matrix $[\mathbf{A}_{\text{HCp}}]$ and constraint vector \mathbf{b}_{HCp} are determined considering the limits: $H_2/R_2 > 0$, $0 \leq R_1/R_2 \leq 1$, and $0 \leq H_1/H_2 \leq 1$ (see Fig. 4.1):

$$[\mathbf{A}_{\text{HCp}}] = \begin{bmatrix} -1 & 0 & 0 \\ 0 & -1 & 0 \\ 0 & 1 & 0 \\ 0 & 0 & -1 \\ 0 & 0 & 1 \end{bmatrix}, \quad \mathbf{b}_{\text{HCp}} = \begin{bmatrix} \varepsilon \\ 0 \\ 1 \\ 0 \\ 1 \end{bmatrix}, \quad (4.12)$$

with $\varepsilon \rightarrow 0$ to ensure magnet volumes greater than zero ($H_2/R_2 > 0$).

The second type of constraint is a nonlinear inequality c_{nl} . This constraint is defined by the maximum force $F_x^{(\text{max})}$ measurable by the applied force sensor, which corresponds to the maximum drag-force in the unperturbed case $F_x^{(0)}$:

$$c_{\text{nl}}(\mathbf{x}, \mathbf{p}, F_x^{(c)}) \leq 0, \quad (4.13)$$

where

$$c_{\text{nl}}(\mathbf{x}, \mathbf{p}, F_x^{(c)}) = F_x^{(0)}(\mathbf{x}, \mathbf{p}) - F_x^{(c)}, \quad (4.14)$$

with

$$F_x^{(c)} = \frac{F_x^{(\text{max})}}{S} \left(\frac{B_r}{B_{r0}} \right)^2. \quad (4.15)$$

By this definition, optimization is performed in the reference space, such that the forces are determined by the defined reference values v_0 , σ_0 , and h_0 . However, the maximum drag-force $F_x^{(\max)}$ is defined in the unscaled space and has to be scaled accordingly using the scaling factor $S(B_r/B_{r0})^{-2}$. If nonlinear magnetic material is omitted in the magnet design, $F_x^{(c)}$ is simplified and the ratio $(B_r/B_{r0})^{-2}$ may be excluded from (4.15). Depending on external conditions, S can be calculated by (4.7) and acts as a weighting factor in the nonlinear constraint function c_{nl} . The normalized maximum drag-force $F_x^{(c)}$ from (4.15), directly affects the feasible set of solutions and plays a central role in the optimization. By scaling the constraint, it is possible to identify similarities between different LET setups. For example, consider two configurations with the same system parameters \mathbf{p} . The first system which obeys a scaling factor $S_1 = 10$, resulting from a velocity $v_1 = 0.5$ m/s together with a maximum drag-force of $F_x^{(\max)} = 3$ N is equivalent to the second with $S_2 = 20$, $v_2 = 1$ m/s, and $F_x^{(\max)} = 6$ N. In the same way, similarities between the optimal designs can be identified considering the geometric scale of the whole problem defined by h . A more detailed and vivid explanation is given in the results part in section 4.1.3. The nonlinear constraint is optional, since it strongly depends on the system parameters and the force sensor technology employed. As already mentioned, a force sensor based on the strain gauge technology is used in the experimental setup at hand. Linear behavior of this sensor type is guaranteed until a nominal force $F_x^{(\max)}$ is reached. Plastic deformation of the deflection body will occur if the applied force exceeds the safe load, which is approximately in the range of $2F_x^{(\max)}$ [76]. Consequently, an optimized magnet system which operates at the global optimum probably could not be applied and must be replaced by a system which considers the drag-force limit. The constrained optimization problem can now be classified as a parametric multivariate nonlinear optimization problem with linear and nonlinear inequality constraints [123].

4.1.2.7 Optimization Strategies

To address this problem, two different approaches are presented. Depending on the needs and external conditions, one or the other approach can be applied. A combination of both principles is also possible to improve the performance of the magnet system further.

Volume and Force Constraint Optimization: The volume and force constraint optimization approach (VcFc) is based on the definition of a fixed magnet volume as well as a maximum drag-force given by the applied force sensor. Thus, the V_m/V_d ratio is fixed besides all other system parameters, and the constraints are satisfied by adjusting the design variables \mathbf{x} in an optimal way. Depending on previously defined external conditions, it is possible that the nonlinear constraint is active and the constrained solution $\tilde{\mathbf{x}}_c(\mathbf{p})$ is located at the constraint boundary. Consequently, the nonlinear constrained optimum differs from the unconstrained solution ($\tilde{\mathbf{x}}_c(\mathbf{p}) \neq \tilde{\mathbf{x}}(\mathbf{p})$). Thus, the feasible set for the case of a HCp-magnet system is:

$$\mathcal{F} = \left\{ \mathbf{x} \in \mathbb{R}^3 \mid \mathbf{c}_l(\mathbf{x}, \mathbf{p}) \leq \mathbf{0}, c_{\text{nl}}(\mathbf{x}, \mathbf{p}, F_x^{(c)}) \leq 0 \right\}. \quad (4.16)$$

Volume Adaptive Force Constraint Optimization: In general, the system parameters are defined by the given detection goal and the particular application of interest. However, the volume ratio V_m/V_d can be used as a free parameter by the system designer. The volume adaptive force constraint optimization approach (VaFc) is motivated by considerations related to mechanical dynamics. To improve the dynamic range of the sensor system, it is desirable to increase its eigenfrequency. This offers the possibility to perform measurements at higher testing velocities and can be achieved by reducing the mass of the magnet system as much as possible, while retaining the maximum ADRA as the primary optimization goal. The VaFc approach is proposed to determine a magnet system with a V_m/V_d ratio, which operates at the transition before the nonlinear constraint becomes active. The role of the V_m/V_d ratio is changed from fixed to a variable system parameter, while all other system parameters are kept constant. The corresponding optimal solution is then $\tilde{\mathbf{x}}(\mathbf{p}_c)$, and the general procedure is illustrated in Fig. 4.4. The procedure starts by defining the maximum drag-force $F_x^{(\max)}$ and the fixed system parameters d/h , a/h , and \mathbf{a}_σ . The starting point $\mathbf{x}^{(0)}$ and the initial

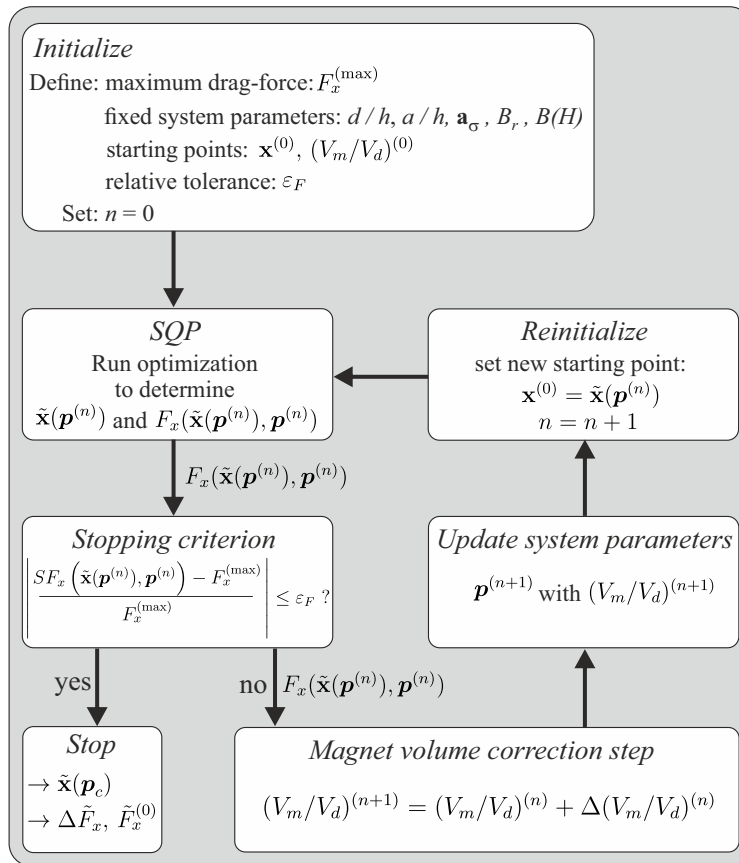


Figure 4.4: Optimization procedure of the volume adaptive force constraint (VaFc) approach to determine the optimal design variables $\tilde{\mathbf{x}}(\mathbf{p}_c)$ of a magnet system operating at the unconstrained global optimum, while retaining the nonlinear constraint given by the limiting drag-force $F_x^{(\max)}$ [107].

volume ratio $(V_m/V_d)^{(0)}$ are defined to initialize the VaFc procedure. The method iterates by determining the unconstrained optimal design $\tilde{\mathbf{x}}(\mathbf{p}^{(n)})$ by a distinct optimization method, where the superscript (n) is an iteration counter. The sequential quadratic programming algorithm is used, as described in the following section. After determining the optimal design by neglecting the nonlinear inequality constraint, the associated drag-force $\tilde{F}_x(\tilde{\mathbf{x}}(\mathbf{p}^{(n)}), \mathbf{p}^{(n)})$ can be calculated. The relative difference to the defined maximal drag-force is evaluated and compared to the predefined relative tolerance ε_F . If the criterion is fulfilled, the algorithm stops and provides the optimal design variables together with the corresponding volume ratio $(V_m/V_d)^{(n)}$. If not, the volume ratio is updated in a correction step. During the first iteration, the next volume is approximated proportional to the force ratio:

$$(V_m/V_d)^{(1)} = \frac{F_x^{(\max)}(V_m/V_d)^{(0)}}{SF_x(\tilde{\mathbf{x}}(\mathbf{p}^{(0)}), \mathbf{p}^{(0)})}. \quad (4.17)$$

For all following iterations $(n > 1)$, a more robust Newton-Raphson step is used, which considers the gradient information of $\tilde{F}_x^{(0)}$ with respect to V_m/V_d :

$$\Delta(V_m/V_d)^{(n)} = -\frac{SF_x(\tilde{\mathbf{x}}(\mathbf{p}^{(n)}), \mathbf{p}^{(n)}) - F_x^{(\max)}}{S \frac{\partial F_x(\tilde{\mathbf{x}}(\mathbf{p}^{(n)}), \mathbf{p}^{(n)})}{\partial (V_m/V_d)}}. \quad (4.18)$$

A backward approximation is applied to determine the partial derivative of the drag-force. After determining $(V_m/V_d)^{(n+1)}$, the system parameters $\mathbf{p}^{(n+1)}$ are updated. Before starting a new iteration, the starting point of the design variables is set to the optimal solution of the previous optimization step $\mathbf{x}^{(0)} = \tilde{\mathbf{x}}(\mathbf{p}^{(n)})$, since the optimal design between two iterations may be assumed to be similar. Thus, the process is accelerated. The proposed approach can be used to determine the critical V_m/V_d ratio when the optimal magnet system still operates at the unconstrained global optimum while still considering the previously defined constraint of maximum drag-force.

4.1.2.8 Sequential Quadratic Programming Algorithm

To solve the optimization problem, the Sequential Quadratic Programming (SQP) algorithm is used. This method is an extension of the Broyden-Fletcher-Goldfarb-Shanno-Quasi-Newton method by introducing Lagrangian multipliers. The first Quasi-Newton based method was introduced by Davidon [124, 125]. The advantage of Newton-type methods is in the use of the gradient and curvature information provided by the Jacobian and Hessian matrix of the objective function. Quasi-Newton methods avoid the computationally intensive evaluation of the Hessian, which is beneficial when comparatively expensive numerical solvers are involved to evaluate the objective function. The Hessian is approximated during the iterative process successively.

Early work on SQP was done by Biggs [126], Han [127], and Powell [128]. However, the method has been continuously improved. The method is also referred to as a quadratic programming based projected Lagrangian method [123]. SQP is one of the most powerful methods in the framework of nonlinear constrained optimization. In the following, the mathematical basics

of the optimization problem and the SQP algorithm are described to provide a general overview about the applied methodology in the present context.

In general, a parametric multivariate nonlinear optimization problem with nonlinear constraints is mathematically described by:

$$\begin{aligned} & \min_{\mathbf{x} \in \mathbb{R}^n} f(\mathbf{x}, \mathbf{p}) \\ & \text{such that } \mathbf{h}(\mathbf{x}, \mathbf{p}) = \mathbf{0} \\ & \mathbf{c}(\mathbf{x}, \mathbf{p}) \leq \mathbf{0}. \end{aligned} \quad (4.19)$$

In the present case, the objective function $f(\mathbf{x}, \mathbf{p})$ is given by (4.9) and the constrained function vector $\mathbf{c}(\mathbf{x}, \mathbf{p})$ of length m contains the inequality constraints $\mathbf{c}_1(\mathbf{x})$ from (4.11) and $c_{nl}(\mathbf{x})$ from (4.14). To provide a general overview about the method, the (possibly nonlinear) equality constraints, concentrated in the vector $\mathbf{h}(\mathbf{x}, \mathbf{p})$ of length w , are included in the description.

In constrained optimization, the Lagrangian \mathcal{L} plays a central role. It combines the objective function with the given constraints by means of Lagrangian multipliers summarized in the vectors \mathbf{u} and \mathbf{v} :

$$\mathcal{L}(\mathbf{x}, \mathbf{p}, \mathbf{u}, \mathbf{v}) = f(\mathbf{x}, \mathbf{p}) + \mathbf{u}^T \mathbf{h}(\mathbf{x}, \mathbf{p}) + \mathbf{v}^T \mathbf{c}(\mathbf{x}, \mathbf{p}). \quad (4.20)$$

For every constraint, there exists one Lagrangian multiplier. It can be proven that the local optimum $\tilde{\mathbf{x}}$ of the objective function with respect to the given constraints is a stationary point of the Lagrangian with the corresponding optimal multipliers $\tilde{\mathbf{u}}$ and $\tilde{\mathbf{v}}$, such that the gradient of the objective function is a linear combination of the gradients of the constraints [123]. The name of the SQP algorithm originates from the approach to solve the nonlinear problem from (4.19). This is done sequentially by approximating the Lagrangian using a quadratic function around the point $\mathbf{x}^{(k)}$, where the superscript (k) is the iteration counter. The constraint functions are linearized so that the quadratic subproblem of (4.19) is given by a Taylor expansion of the Lagrangian from (4.20). The problem is reformulated to determine the optimal search direction $\mathbf{d}^{(k)}$ from the point $\mathbf{x}^{(k)}$, such that the constraints are fulfilled. The vector ∇f is the Jacobian, i.e. the gradient of the objective function with respect to \mathbf{x} . In the SQP algorithm, the quadratic subproblem of (4.20) is solved iteratively. In every iteration, two additional subproblems have to be solved. First, the search direction $\mathbf{d}^{(k)}$ and the Lagrangian multipliers $\mathbf{u}^{(k+1)}$, and $\mathbf{v}^{(k+1)}$ are evaluated. Then the step size α is determined to provide a certain decrease in the objective function while still satisfying the given constraints. The next iteration is performed at the updated point $\mathbf{x}^{(k+1)} = \mathbf{x}^{(k)} + \alpha \mathbf{d}^{(k)}$. In order to determine the first step, the following linear system of equations is solved for $\mathbf{d}^{(k)}$, $\mathbf{u}^{(k+1)}$, and $\mathbf{v}^{(k+1)}$:

$$\begin{bmatrix} [\mathbf{L}^{(k)}] & \nabla \mathbf{h}^{(k)} & \nabla \mathbf{c}^{(k)} \\ \nabla \mathbf{h}^{(k)T} & 0 & 0 \\ \nabla \mathbf{c}^{(k)T} & 0 & 0 \end{bmatrix} \begin{bmatrix} \mathbf{d}^{(k)} \\ \mathbf{u}^{(k+1)} \\ \mathbf{v}^{(k+1)} \end{bmatrix} = \begin{bmatrix} -\nabla f^{(k)} \\ -\mathbf{h}^{(k)} \\ -\mathbf{c}^{(k)} \end{bmatrix}. \quad (4.21)$$

The symmetric matrix $[\mathbf{L}^{(k)}] = \nabla^2 \mathcal{L}$ is an approximation of the second order partial derivatives of the Lagrangian from (4.20), which is also called the Hessian of the Lagrangian. Since the

Hessian is not given analytically, the matrix $[\mathbf{L}^{(k)}]$ is successively approximated rather than explicitly calculated. In the present case, a very robust and efficient approximation, the BFGS-update formula, derived by Broyden [129, 130], Fletcher [131], Goldfarb [132] and Shanno [133] is used. The first row of the system matrix in (4.21) corresponds to the partial derivative of the quadratic approximation of the Lagrangian from (4.20) with respect to $\mathbf{d}^{(k)}$. The remaining rows correspond to the linearly approximated constraint functions.

The step size α is determined by means of a merit function. This function is incorporated into an SQP algorithm for the purpose of robustness. In constrained optimization, a merit function balances the drive to decrease the objective function while satisfying the defined constraints, and measures the progress of convergence towards $\tilde{\mathbf{x}}$ as a function of α . The solution of the quadratic subproblem has a unit step size $\alpha = 1$. If the constraints are not violated, this step size is taken and a new iteration is started. However, if the constraints are violated, the step-length is reduced to the nearest constraint. For the proposed approach, the merit function developed by Han [127] and Powell [128] is employed. The procedure is repeated until the Karush-Kuhn-Tucker conditions [134] are satisfied up to a certain limit of defined tolerances. The SQP converges to a local optimum and returns the corresponding solution. Further literature about nonlinear constrained optimization can be found in, for example, [123, 135] and [136]. SQP theory is covered in detail by Han [127, 137] and Powell [128, 138, 139], to note some of the first but still frequently applied concepts of this method. A more general overview about SQP is given by Boggs and Tolle [140] and by Gill and Wong [141].

The performance of the proposed approach strongly depends on the implementation due to nontrivial technical and algorithmic issues. For that reason, it is highly recommended to use professional and well-tested software. Some of the first successful implementations are reported by Schittkowski [142–144]. These references also cover the proof of convergence of the SQP. More advanced but commercial code is available, for example by the MATLAB[®] function *fmincon* [145] or FORTRAN based routines NPSOL [146] and SNOPT [147, 148] from Gill *et al.*. Partially free software with the restriction to apply the routines in an academic framework is available (NLPQLP) [149]. This implementation is also used in commercial software such as ANSYS[®] [150]. This software has been tested on 306 optimization problems with a reported success rate of better than 90%, which underlines the efforts for implementation of SQP based algorithms [149]. In this work, the MATLAB[®] implementation *fmincon* is used to couple the FEM Solver of COMSOL Multiphysics[®] [93] and the SQP algorithm by means of the MATLAB Livelink[™] [151]. The implementation includes the BFGS-update formula as well as an adaptive step size using the merit function discussed above. In the subsequent sections the methodology to evaluate the objective and nonlinear constraint function with low computational cost is described.

4.1.2.9 Objective and Constraint Function Evaluation

To apply the SQP algorithm, a time-efficient approach is essential to evaluate both the objective function $f(\mathbf{x}, \mathbf{p})$ as well as the nonlinear constraint function $c_{\text{nl}}(\mathbf{x}, \mathbf{p})$. The governing equations are simplified such that secondary magnetic fields are neglected. Hence, it is possible to analyze the problem in the stationary case, which takes into account the symmetry of the field and force profiles. This significantly reduces the computational cost and offers the possibility for efficient numerical analysis. The FEM in combination with eWRA, described in section 3.2.4.1 on page 31, is applied as the numerical method. The nonlinearity of the ferromagnetic material significantly influences the profile and magnitude of the magnetic field. Consequently, the resulting Lorentz force is also affected. This necessitates the use of nonlinear models. Linear models are too inaccurate and falsify the optimization results, especially if the drag-force must not exceed $F_x^{(\text{max})}$. In the case of HCp-magnet systems, the iron-cobalt-alloy VACOFLUX[®] 50, together with the corresponding $B(H)$ curve from Fig. 4.3, is used. To minimize computational cost, the field problem is subdivided into three successive steps, illustrated in Fig. 4.5.

Step 1: Primary Magnetic Flux Density (2-D) In the first step, the primary magnetic flux density $\mathbf{B}^{(p)}$ of the permanent magnet is calculated with a scalar magnetic potential formulation ψ , neglecting any moving conductor. Thus, the primary magnetic field is given by (3.27). Given the axisymmetry of the magnet geometry, the magnetic field is determined in 2-D employing a cylindrical coordinate system, which significantly accelerates the solving process of the nonlinear problem.

Step 2: Induced Eddy Currents in the Conductor Free of Defects (3-D) In the second step, only the conductor in motion is considered. It is modeled as a large cylindrical domain with finite radius $10R_2$ proportional to the outer radius of the magnet system, assuming that the edges are far enough away to prevent any parasitic disturbance of the induced eddy currents. The height H_s of the moving conductor is defined according to the following conditional relation:

$$H_s = \begin{cases} 10R_2, & \text{if } 10R_2 \geq 2d + a \\ 10R_2 + 2d + a, & \text{if } 10R_2 < 2d + a. \end{cases} \quad (4.22)$$

This implies that the size of the conducting domain is adjusted according to the magnet system, while ensuring geometrical models with defects deeper than $10R_2$. Thus, ensuring that the conducting domain is sufficiently large for all sets of \mathbf{p} and \mathbf{x} .

The primary magnetic field $\mathbf{B}^{(p)}$ is imported from the first step and transformed from cylindrical coordinates into the three-dimensional Cartesian coordinate system. The induced eddy currents inside the conductor in motion are calculated by (3.31) and (3.32) using a scalar electric potential formulation ϕ . The 3-D model contains symmetry with respect to the xz - and yz -planes, when secondary magnetic fields are neglected. This reduces the modeled geometry of the specimen to only one quarter. On the xz -plane, the tangential components of the current

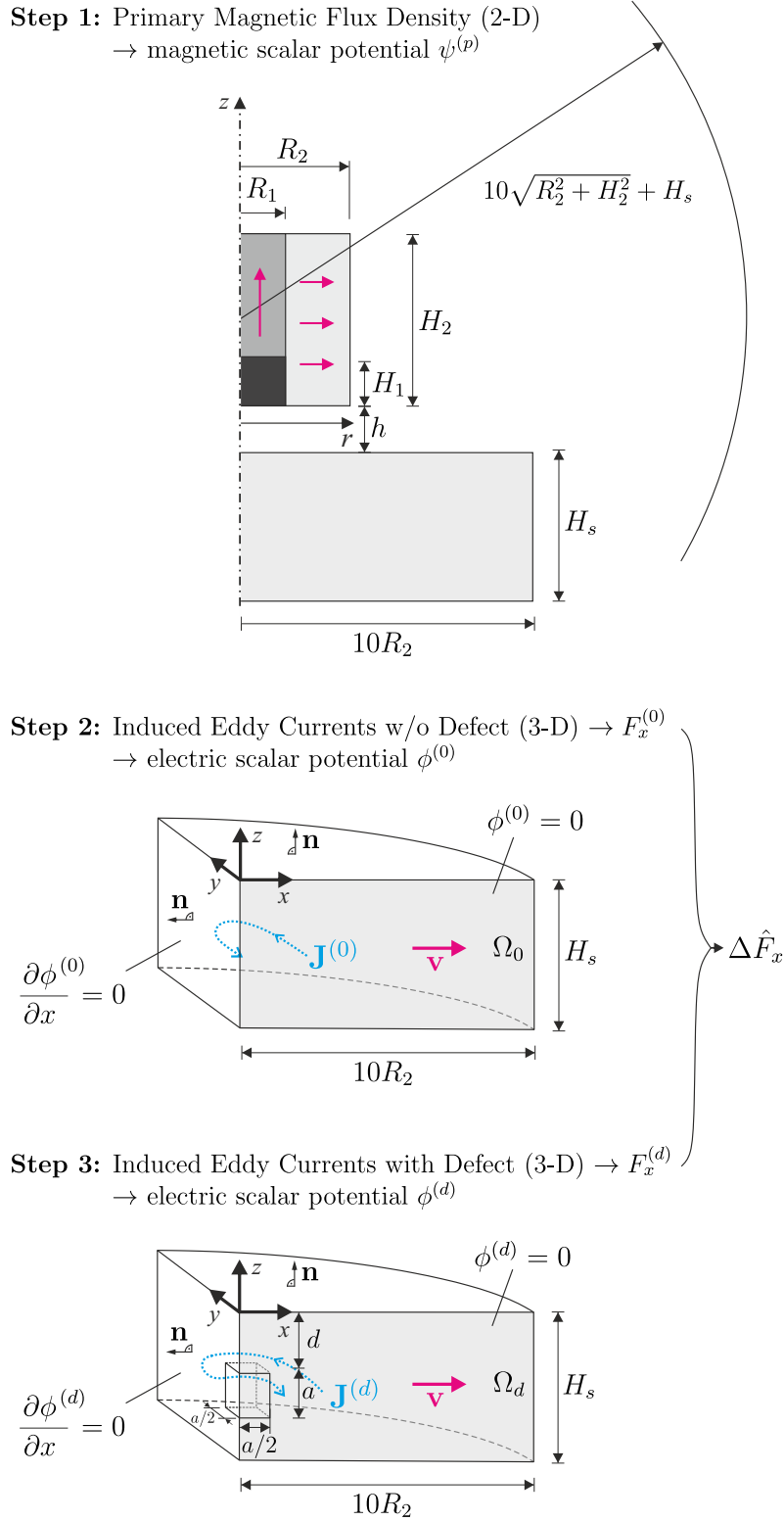


Figure 4.5: Procedure to compute the nonlinear objective and constraint function [107].

density vanish:

$$\mathbf{J}_t = \mathbf{J} \times \mathbf{n} = [\boldsymbol{\sigma}] \left(-\nabla\phi + \mathbf{v} \times \mathbf{B}^{(p)} \right) \times \mathbf{n} = \mathbf{0}. \quad (4.23)$$

As a result of the axisymmetry of the magnet system, the magnetic field is zero in the direction of the boundary normal at this plane ($B_y^{(p)} = 0$). Considering the linear motion of the conductor in the x -direction $\mathbf{v} = [v_x, 0, 0]^T$ leads to $\mathbf{v} \times \mathbf{B}^{(p)} = -v_x B_z^{(p)} \mathbf{e}_y$. Substituting this into (4.23) shows that $\frac{\partial\phi}{\partial x} = 0$ and $\frac{\partial\phi}{\partial z} = 0$, which can be achieved by defining the Dirichlet boundary condition $\phi = \text{const.}$ at the xz -plane.

In contrast, the normal component of the induced current density J_n vanishes at the yz -plane, such that:

$$J_n = \mathbf{J} \cdot \mathbf{n} = [\boldsymbol{\sigma}] \left(-\nabla\phi + \mathbf{v} \times \mathbf{B}^{(p)} \right) \cdot \mathbf{n} = 0. \quad (4.24)$$

On this plane, the magnetic field is zero in the x -direction $B_x^{(p)} = 0$, so:

$$\mathbf{v} \times \mathbf{B}^{(p)} = -v_x B_z^{(p)} \mathbf{e}_y + v_x B_y^{(p)} \mathbf{e}_z. \quad (4.25)$$

Since this expression has no component normal to the boundary, a Neumann boundary condition for the electric scalar potential $\frac{\partial\phi}{\partial x} = 0$ must be defined. All other boundaries of the moving conductor share the boundary condition $\mathbf{J} \cdot \mathbf{n} = 0$ to prevent any current leaving the conducting domain.

Step 3: Induced Eddy Currents in the Conductor With Defect (3-D) To determine the ADRA, a third simulation is performed. The primary magnetic field $\mathbf{B}^{(p)}$ from the first step is incorporated in the same way as in the previous step. However, in this step the conductor contains an equivalent cuboidal defect with volume V_d located at a depth d . The governing equations from the previous step remain valid and in consequence, the boundary condition $\mathbf{J} \cdot \mathbf{n} = 0$ now also applies for the defect boundaries, preventing any current flow into the defect region. To further decrease the computational cost, the same 3-D FEM mesh can be used in step two and three. As a result, the 3-D mesh needs only to be built once and then transferred between steps two and three as necessary. As a positive side effect, using the same mesh decreases numerical noise when computing the ADRA. Finally, the resulting Lorentz force is calculated by spatial integration over the conductor:

$$\begin{aligned} F_x^{(i)} &= -4 \int_{\Omega_i} \mathbf{J}^{(i)} \times \mathbf{B}^{(p)} \, d\Omega \\ &= -4 \int_{\Omega_i} \left([\boldsymbol{\sigma}] \left(-\nabla\phi^{(i)} + \mathbf{v} \times \mathbf{B}^{(p)} \right) \right) \times \mathbf{B}^{(p)} \, d\Omega, \end{aligned} \quad (4.26)$$

where the superscript $i \in \{0, d\}$ indicates the quantities obtained in the defect-free and defective case, respectively.

The computation of one objective function evaluation takes 20–25 s on a common desktop PC (i7-3770, 4 GHz). This includes building the geometry, meshing, assembling the systems of equations, solving, and post-processing of all three steps. The memory consumption is moderate and does not exceed 1 GB since geometrical symmetry is taken into account in all individual steps.

4.1.3 Optimization Results and Discussion

The optimization results of an HCp-system are presented using VACODYM[®] 745HR [109] as permanent magnet material and the iron-cobalt-alloy VACOFLUX[®] 50 [108] as ferromagnetic material. The scaling factor S is chosen such that it corresponds to the currently available laboratory setup. The specimen is constructed from stacked aluminium sheets ($\mathbf{a}_\sigma = [1, 1, 0]^T$) with electrical conductivity $\sigma = 30.66$ MS/m, moving with velocity $v = 0.5$ m/s. The lift-off distance of $h = 1$ mm is assumed, together with a magnetic remanence $B_r = 1.44$ T (VACODYM[®] 745HR). This results in a scaling factor $S^{(\text{lab})} = 31.79$. In the experimental setup, a force sensor based on the strain gauge technology (K3D40, ME-Messsysteme GmbH, Hennigsdorf, Germany, www.me-systeme.de, [76]) is employed. According to the manufacturer, the applied load is limited to $F_x^{(\text{max})} = 3$ N.

Two particular setups of system parameters are investigated. The first represented the case of medium sized defects located deep inside the specimen. The corresponding system parameters are $V_m/V_d = 56$, $d/h = 10$, and $a/h = 5$. The optimization results are shown in Fig. 4.6. The insets in the upper left corner of each figure show cross sections of the optimal magnet systems colored according to Fig. 4.1. The ADRA is shown in Fig. 4.6(a) over the space of design variables $H_2/R_2 = (0 \dots 2.5]$, $R_1/R_2 = (0 \dots 1]$, and $H_1/H_2 = [0 \dots 1]$. The planes intersect in the global unconstrained optimum at $\tilde{\mathbf{x}} = [H_2/R_2, R_1/R_2, H_1/H_2] = [0.5, 0.6, 0]$, with a denormalized ADRA of $\Delta\tilde{F}_x^{(\text{lab})} = 21.9$ mN. The continuous objective function does not contain local optima.

The unperturbed drag-force is shown in Fig. 4.6(b). The ADRA-optimal magnet generates an unperturbed drag-force of $\tilde{F}_x^{(0, \text{lab})} = 5.2$ N, which is too high for the experimental force sensor. To fulfill the constraint, the VcFc approach is applied. To illustrate the impact of nonlinear constraints, Fig. 4.6(c) and (d) show the equi-force surfaces for different values of $F_x^{(\text{max})}$ over the same space of design variables. Figure 4.6(c) shows the surface for $F_x^{(\text{max})} = \tilde{F}_x^{(0, \text{lab})} = 3$ N. This plane is colored according to the value of the objective function (ADRA). The points inside the equi-force surface correspond to solutions which violate the predefined nonlinear constraint ($c_{\text{nl}} > 0$) and hence do not belong to the feasible set of solutions. Since the global optimum is not part of the feasible set, the constrained optimum is located at the constraint boundary. The SQP algorithm converged to the constrained optimal solution, which describes the magnet system as a standard cylinder $\tilde{\mathbf{x}}_c = [1.6, 1, 0]$. The solution is located at the boundary of the design space and the linear inequality constraints (bounds) are active ($H_1/H_2 = 0$). Thus, the number of free design variables is reduced from three to two at the optimal solution. Compared to the unconstrained optimum, the ADRA decreased to $\Delta\tilde{F}_x^{(\text{lab})} = 15.6$ mN. Considering the ADRA projected on the constraint hyperplane, the proposed problem is non-convex. Consequently, if initial values $\mathbf{x}^{(0)}$ are chosen such that $H_2/R_2 < 0.5$ and $R_1/R_2 < 0.4$, the derivative based SQP algorithm converges to a local optimum located in the region of $H_2/R_2 \approx 0.2$ and $R_1/R_2 \approx 0.1$. To avoid local convergence, the use of a multistart approach using three to five different starting points is recommended. In the multistart approach, the first starting point is defined by the user, whereas the following are chosen randomly.

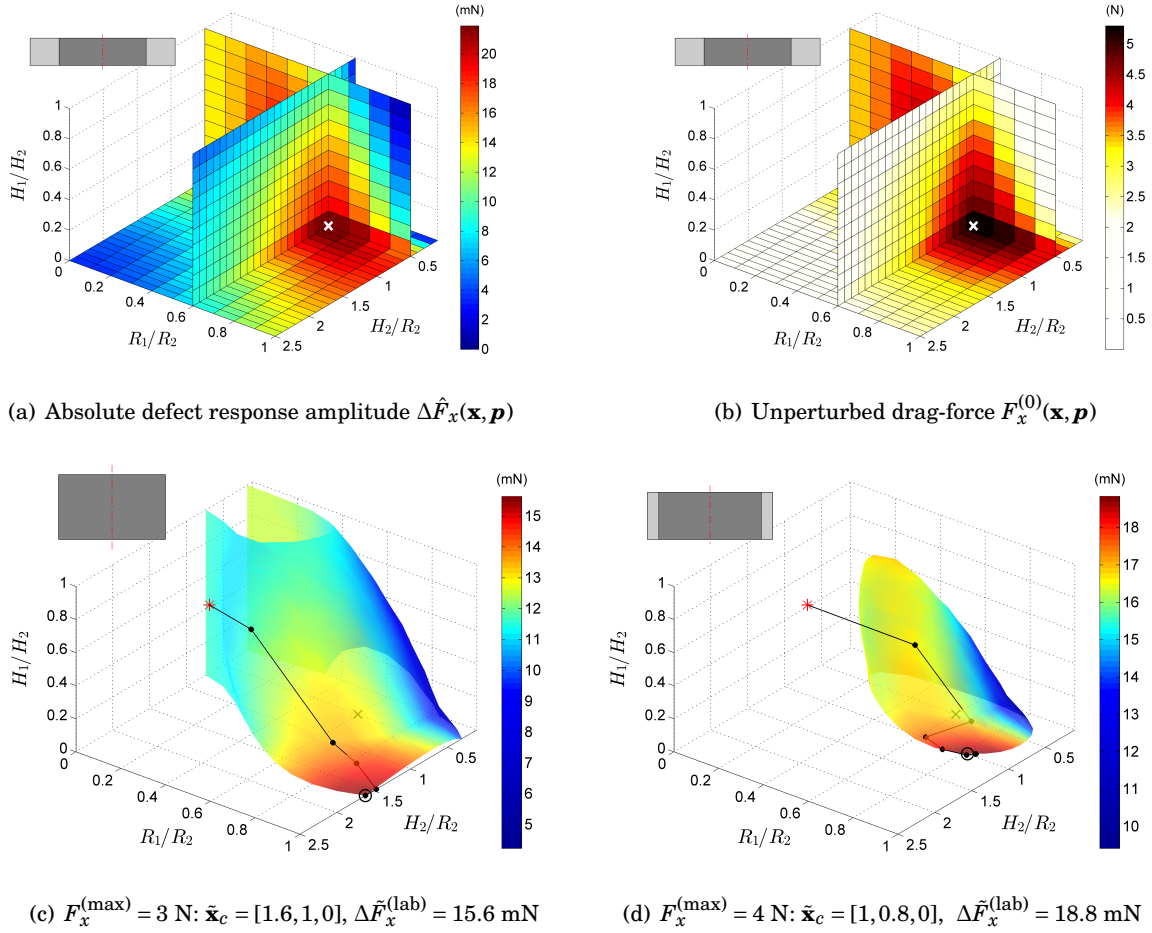


Figure 4.6: Hcp-magnet system made of VACODYM[®] 745HR and VACOFLUX[®] 50 for the case of system parameters $V_m/V_d = 56$, $d/h = 10$, and $a/h = 5$ (anisotropic specimen $\mathbf{a}_\sigma = [1, 1, 0]^T$). The scaling factor of the laboratory setup is $S^{(\text{lab})} = 31.79$. Crosses and circles indicate the unconstrained and constrained optima, $\tilde{\mathbf{x}}$, and $\tilde{\mathbf{x}}_c$, respectively. The insets are sketches of the individual optimized magnet systems. The data are shown as a function of the design variables $\mathbf{x} = [H_2/R_2, R_1/R_2, H_1/H_2]$. (a) Cutplanes of the denormalized ADRA $\Delta F_x(\mathbf{x}, \mathbf{p})$ intersecting at the unconstrained global optimum $\tilde{\mathbf{x}} = [0.5, 0.6, 0]$. (b) Cutplanes of the corresponding denormalized unperturbed drag-force $F_x^{(0)}(\mathbf{x}, \mathbf{p})$. (c) and (d) Semi-transparent isosurfaces of maximum drag-forces $F_x^{(\max)} = \{3, 4\}$ N colored by the according ADRA. The solid lines indicate the optimization paths for the initial starting point, $\mathbf{x}^{(0)} = [1.6, 0.3, 0.8]$ (red star) [107].

The constraint hyperplane for $F_x^{(\max)} = 4 \text{ N}$ is shown in Fig. 4.6(d). As expected, the enclosed domain shrinks and the feasible set increases. The constrained optimal solution changes to $\tilde{\mathbf{x}}_c = [1, 0.8, 0]$ and the ADRA increases to $\Delta\hat{F}_x^{(\text{lab})} = 18.8 \text{ mN}$. The optimization path of the initial starting point is shown in Fig. 4.6(c) and (d) with a solid line. Each dot corresponds to one iteration taken by the SQP algorithm.

In a second example, the system parameters are changed to $V_m/V_d = 875$, $d/h = 2$, and $a/h = 2$, which corresponds to the case of small defects located close to the surface of the

specimen. The associated results are presented in a similar way as in the former case in Fig. 4.7. The unconstrained optimum, shown in Fig. 4.7(a), is relocated compared to the previous case because of the variation in the system parameters. A Halbach-structure emerges, which includes ferromagnetic material ($\tilde{\mathbf{x}} = [0.8, 0.2, 0.5]$). Considering the behavior of the ADRA and the unperturbed drag-force in Fig. 4.7(a) and (b), the maxima do not correlate. Thus, magnet systems which generate high unperturbed drag-forces do not inherently produce high defect responses. This particular magnet system generates an ADRA of $\Delta\tilde{F}_x^{(\text{lab})} = 36$ mN, while generating an unperturbed drag-force of $\tilde{F}_x^{(0,\text{lab})} = 3.6$ N. Since the constraint of maximum drag-force is again not fulfilled, the VcFc approach must be applied. The constraint hyperplane of $F_x^{(\text{max})} = 3$ N is shown in Fig. 4.7(c). The constraint optimum is $\tilde{\mathbf{x}}_c = [1.1, 0.2, 0.6]$ and is located close to the unconstrained solution. The modified magnet has an ADRA of $\Delta\tilde{F}_x^{(\text{lab})} = 34.5$ mN and satisfies the 3 N constraint. Assuming a maximum drag-force $F_x^{(\text{max})} = 4$ N, the unconstrained global optimum is located in the feasible set of solutions. Consequently, the nonlinear constraint is inactive and the SQP algorithm converges to the global optimum as shown in Fig. 4.7(d).

Both examples show that if $F_x^{(c)}$ from (4.15) changes by modifying $F_x^{(\text{max})}$ or the scaling factor S , the constraint hyperplane defined by c_{nl} from (4.16) grows or shrinks accordingly. In a similar sense, the constraint function is influenced by the system parameters \mathbf{p} . As a consequence of scaling, the unconstrained optimization results can be adopted to setups with a different scaling parameter, provided they share the same system parameters. However, the constrained optimization results are generally valid as long as the different setups share the same normalized maximum drag-force from (4.15).

The influence of the V_m/V_d ratio on the ADRA and the optimal magnet design is investigated further. The study is performed assuming the same two sets of system parameters defined previously. To compare the individual magnet systems with each other, the investigation is performed for HCp-, HC-, and C-magnets separately. Since the HCp-configuration covers HC- and C-magnet systems, the corresponding ADRA must be equal or larger than the other cases, which are geometrically restricted beforehand. The optimizations are performed as a function of V_m/V_d in the unconstrained case as well the VaFc and VcFc approaches.

The results for deep defects ($d/h = 10$, $a/h = 5$) are shown in Fig. 4.8(a). Each point on the curves represents an optimal magnet system. The dashed lines indicate the ADRA of the unconstrained optimal solutions (uc). In this parameter range, the ADRA increases almost linearly as a function of the V_m/V_d ratio. The critical V_m/V_d ratios are determined for C-, HC-, and HCp-magnet systems using the VaFc approach, and are shown with a single marker each. The magnet system is defined by the unconstrained global optimum but still satisfies the constraint. The magnet designs which obey these parameters are lying on the constraint hyperplane c_{nl} intersecting with the global optimum $\tilde{\mathbf{x}}$. Hence, the critical V_m/V_d ratio is where the constraint becomes active and the curve of the constrained solution diverges from unconstrained solution. However, magnet systems with higher V_m/V_d ratios have to be restricted by applying the VcFc approach such that all presented configurations indicated with solid lines

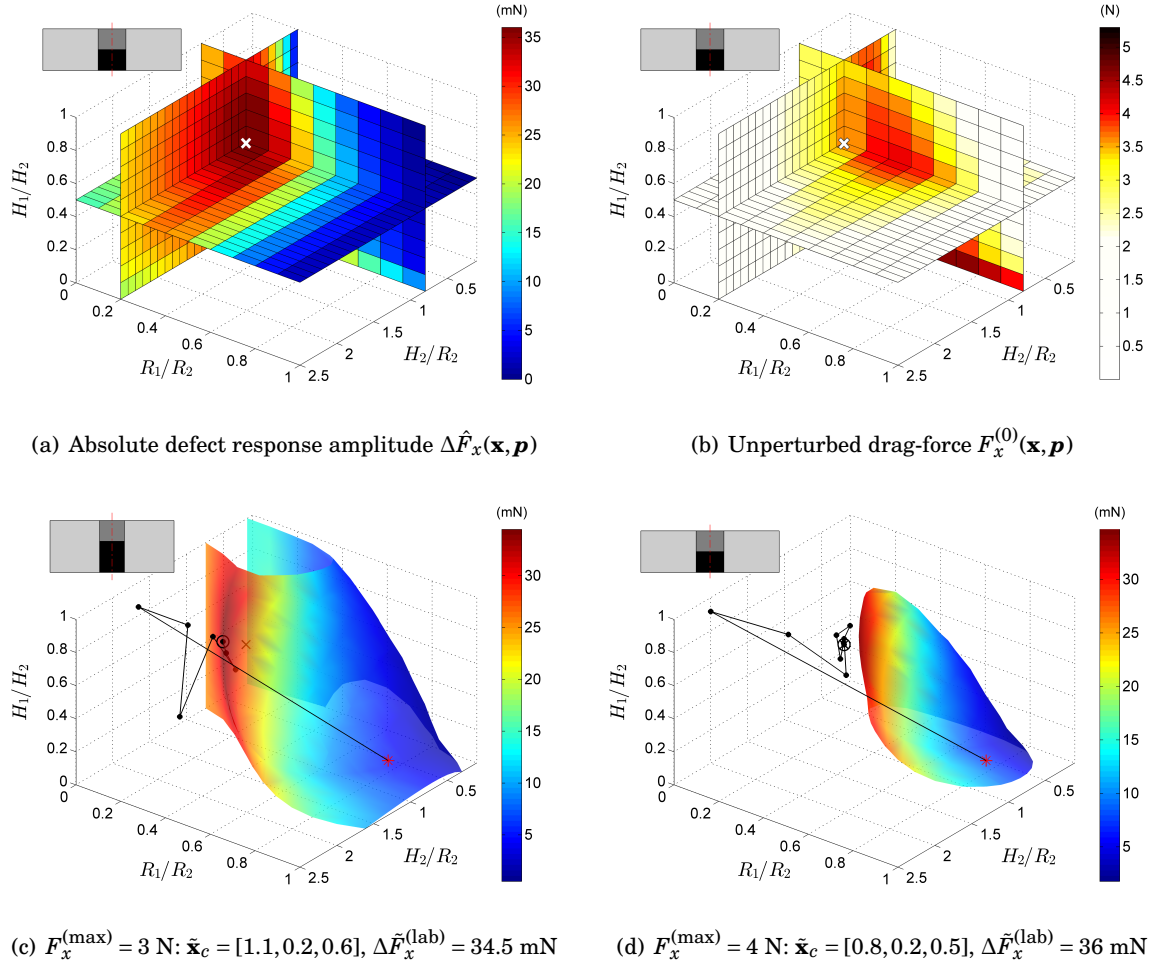


Figure 4.7: HCp-magnet system made of VACODYM[®] 745HR and VACOFLUX[®] 50 for the case of system parameters $V_m/V_d = 875$, $d/h = 2$, and $a/h = 2$ (anisotropic specimen $\mathbf{a}_\sigma = [1, 1, 0]^T$). The scaling factor of the laboratory setup is $S^{(\text{lab})} = 31.79$. Crosses and circles indicate the unconstrained and constrained optima, $\tilde{\mathbf{x}}$, and $\tilde{\mathbf{x}}_c$, respectively. The insets are sketches of the individual optimized magnet systems. The data are shown as a function of the design variables $\mathbf{x} = [H_2/R_2, R_1/R_2, H_1/H_2]$. (a) Cutplanes of the denormalized ADRA $\Delta F_x(\mathbf{x}, \mathbf{p})$ intersecting at the unconstrained global optimum $\tilde{\mathbf{x}} = [0.8, 0.2, 0.5]$. (b) Cutplanes of the corresponding denormalized unperturbed drag-force $F_x^{(0)}(\mathbf{x}, \mathbf{p})$. (c) and (d) Semi-transparent isosurfaces of maximum drag-forces $F_x^{(\max)} = \{3, 4\}$ N colored by the according ADRA; The solid lines indicate the optimization paths for the initial starting point $\mathbf{x}^{(0)} = [0.9, 1, 0.2]$ (red star) [107].

fulfill the defined force constraint $F_x^{(\max)} = 3 \text{ N}$. The insets show cross sections of particular magnet systems together with the corresponding optimal design variables. As expected, optimal magnet systems do not include ferromagnetic material ($H_1/H_2 = 0$) if the defect is located deep within the specimen, which was also shown in Fig. 4.6. Thus, the curves of HCp- and HC-magnet systems are the same. The critical volume ratio obtained by the VaFc approach is 33.7 and 48.5 for HC- and C-magnets, respectively. Hence, VaFc-optimal HC-magnets are smaller but have a

lower ADRA with 11.9 mN compared to 14.8 mN for cylindrical magnets. Increasing the V_m/V_d ratio beyond the critical point and applying the VcFc, saturates the ADRA while keeping the maximum drag-force at the defined limit. The further gain in ADRA results in consequential increased magnet volume and weight. For this set of system parameters, that the optimal design variables of the HC-magnet system converge to a C-magnet, which was observed in context of Fig. 4.6(c). Hence, a further increase in the magnet volume ratio beyond $V_m/V_d > 56$ leads to an overlap of the VcFc-optimal ADRA curves (see solid lines in Fig. 4.8(a)). Meanwhile, the optimal H_2/R_2 ratio increases with V_m/V_d in a specific way such that the magnet gets higher to fulfill the given constraint. Considering the present case for practical reasons, it can be concluded that an increase beyond $V_m/V_d \approx 55...60$ does not lead to further significant gain in ADRA. Regular cylinders are favorable in the case of deep defects if the unperturbed drag-force is limited. However, Halbach-structures generate higher ADRA compared to standard cylinders when comparing both at a given V_m/V_d ratio omitting any constraint (see dashed lines in Fig. 4.8(a)).

Figure 4.8(b) shows the second set of system parameters which covers the case of small defects located close to the surface of the specimen ($d/h = 2$, $a/h = 2$). The optimal magnet designs are presented in a similar way as in the former case. There are distinct performance differences between C-, HC-, and HCp-magnet systems. Cylindrical magnets show a critical volume ratio of 1033 together with an ADRA of 11.5 mN. In contrast, HC- and HCp-configurations are approximately 30% smaller and generate defect responses of 28.1 mN and 32.4 mN which correspond to a gain of approximately 140% and 180%, respectively. Considering the VcFc solutions, the ADRA increases slightly further by increasing the V_m/V_d ratio beyond the critical point. However, this effect is comparatively smaller than in the case of deep defects (see Fig. 4.8(a)). Comparing HC- and HCp-systems, the presence of ferromagnetic material increases the ADRA by about 15%. Regarding the unconstrained solutions, the ADRA is saturating slowly when increasing the V_m/V_d ratio. This has also been observed but not explicitly shown here for high V_m/V_d ratios of the case from Fig. 4.8(a).

In the following, two distinct magnet systems of both scenarios are compared considering the same magnet volume V_m . For medium sized deep defects (green marker in Fig. 4.8(a)), the optimal C-magnet with a volume ratio of $V_m/V_d = 56$ is chosen. The corresponding HCp-magnet system optimized for small subsurface defects (green marker in Fig. 4.8(b)) has a volume ratio $V_m/V_d = 875$. The geometrical parameters are obtained by denormalizing both systems assuming a lift-off distance and hence geometric scale of $h = 1$ mm. The spatial distribution of the magnitude of the magnetic flux density \mathbf{B} and the induced eddy current density \mathbf{J} are shown in Fig. 4.9. The eddy currents for regular C-magnets (Fig. 4.9(a)) are less concentrated compared to HCp-systems (Fig. 4.9(b)). The Halbach-structure leads to a considerably more focused magnetic flux and eddy current distribution under the inner part of the magnet system. The flux density is increased to 1.6 T on the surface of the specimen, which is significant larger compared to standard magnet systems.

All investigations are also performed assuming a specimen with an isotropic conductivity

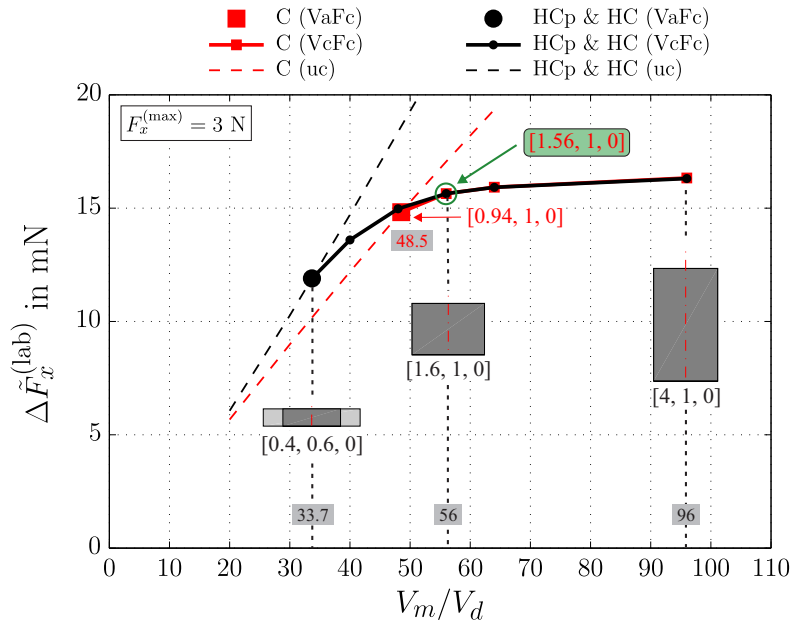
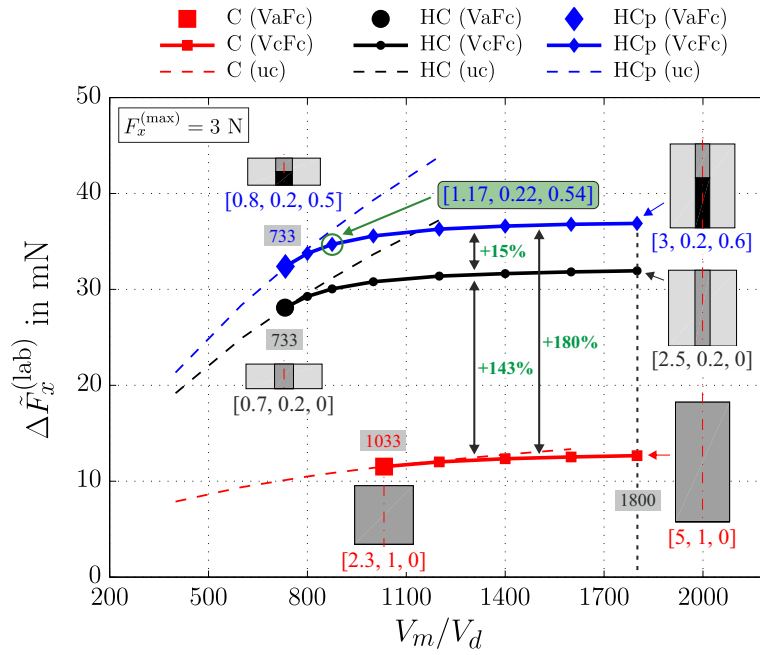

 (a) Medium sized deep defects ($d/h = 10, a/h = 5$)

 (b) Small subsurface defects ($d/h = 2, a/h = 2$)

Figure 4.8: Comparison of the denormalized ADRA between C-, HC- and HCp-magnet systems as a function of the system parameter V_m/V_d in the case of anisotropic specimens, $\mathbf{a}_\sigma = [1, 1, 0]^T$, for two different sets of system parameters. The optimizations are performed in the unconstrained case (dashed lines) as well using the VaFc (single marker) and VcFc (solid lines) approaches. A maximum drag-force of $F_x^{(\text{max})} = 3 \text{ N}$ is considered. The numbers in brackets correspond to the optimal design variables $\tilde{\mathbf{x}}_c = [H_2/R_2, R_1/R_2, H_1/H_2]$ [107].

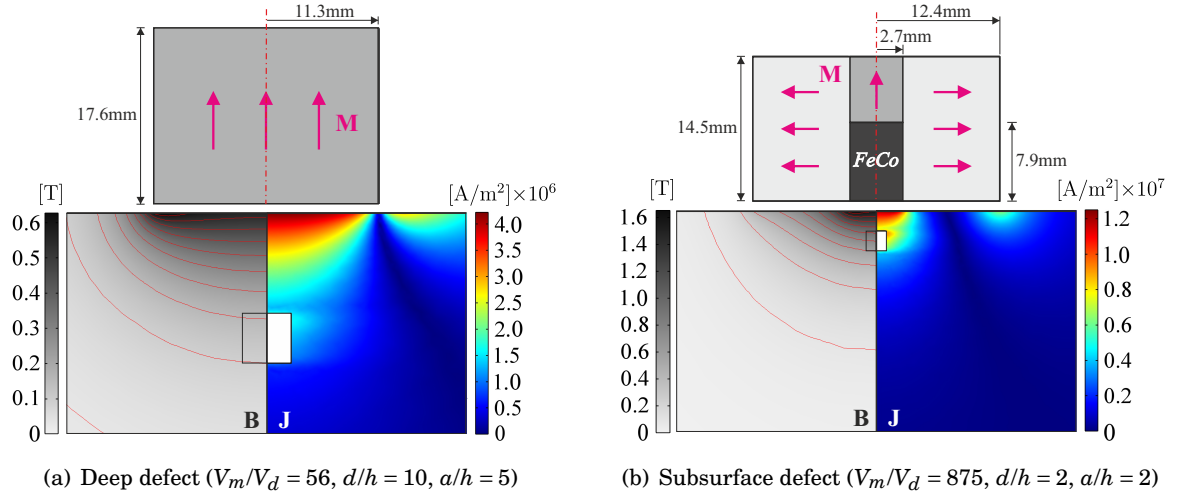


Figure 4.9: Magnitude of the magnetic flux density \mathbf{B} and induced eddy current density \mathbf{J} of VcFc optimized magnet systems for the case of anisotropic specimens, $\mathbf{a}_\sigma = [1, 1, 0]^T$. The magnet systems are denormalized assuming a lift-off distance of $h = 1$ mm. Both generate an unperturbed drag-force of $F_x^{(0, \text{lab})} = 3$ N considering a scaling factor of $S^{(\text{lab})} = 31.79$. Cross section of (a) a cylindrical magnet with $\tilde{\mathbf{x}}_c = [1.56, 1, 0]$ and (b) a Halbach-cylinder with iron-cobalt $\tilde{\mathbf{x}}_c = [1.17, 0.22, 0.54]$ [107].

profile ($\mathbf{a}_\sigma = [1, 1, 1]^T$). In the range of system parameters considered, the optimal design variables differed only by approximately $\pm 5\%$ compared to the anisotropic cases. For deep defects, the ADRA decreased by 23% compared to the anisotropic case. However, for $d/h \leq 2$ the ADRA only decreased by approximately 15%, which can be described by the circumstance that the isotropic profile becomes gradually anisotropic from the top side if the defect gets closer to the surface of the specimen. The nonlinear constraint function is not affected when comparing the two cases of $\mathbf{a}_\sigma = [1, 1, 1]^T$ and $\mathbf{a}_\sigma = [1, 1, 0]^T$. This is due to the unperturbed drag-force $F_x^{(0)}$ being the same for both conductivity profiles, since the unperturbed eddy currents only flow in the xy -plane. Hence, anisotropy in the z -direction does not influence $F_x^{(0)}$, and so the nonlinear constraint function c_{nl} is unaltered.

4.1.4 Prototypes of Optimized LET Magnet Systems

Prototypes of the proposed optimized magnet systems from Fig. 4.9 are designed and manufactured. The optimal C-magnet is a custom design ordered from the company HKCM engineering e.K. (www.hkcm.de). As assumed during the optimization, it is made of NdFeB with a material grade of N52 with a nominal remanence of 1.43 T. The diameter D and height H are $[D, H] = [22.5, 17.6]$ mm.

The realization of the HCP-magnet system is more intricate. The radially magnetized outer part of the magnet system is constructed by diametrically magnetized segments. The influence of the segmented structure on the ADRA, compared to the ideal case with a continuous radial

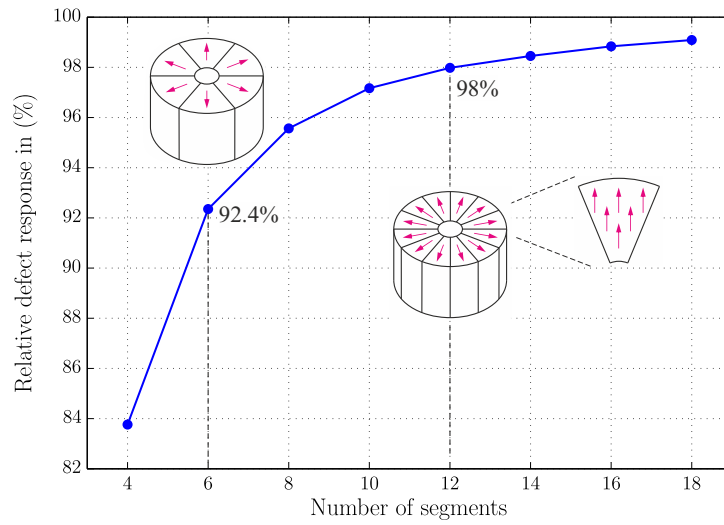


Figure 4.10: Relative defect response of the optimized segmented HCp-magnet. The ADRA is calculated with respect to an ideal HCp-magnet assuming a continuous radial magnetization.

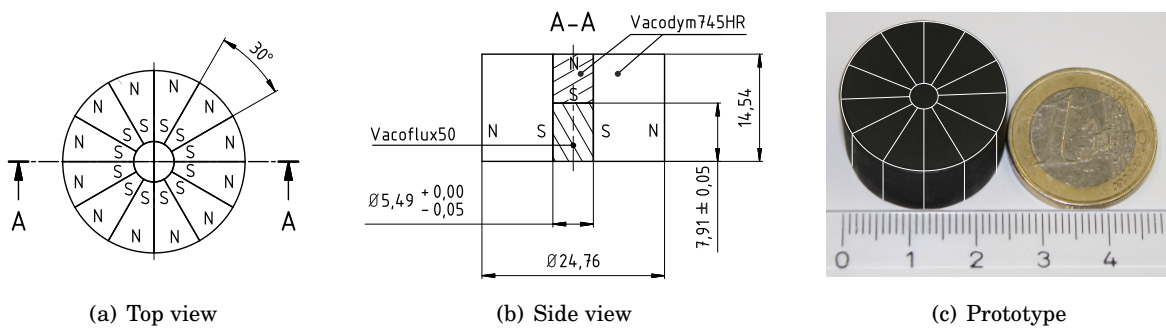


Figure 4.11: Geometry of the HCp-prototype manufactured by the company Vacuumschmelze Hanau GmbH & Co. KG (www.vacuumschmelze.de).

magnetization, is shown in Fig. 4.10. As expected, the ADRA converges with an increasing number of segments. For the prototype of the HCp-magnet system, a structure made of 12 segments is chosen, which results in an ADRA of 98% compared to the ideal case. The final geometry and the manufactured prototype is shown in Fig. 4.11. It is made of the hard magnetic material VACODYM[®] 745HR and the iron-cobalt-alloy VACOFLUX[®] 50 as it is assumed during the optimization. The prototype is manufactured in collaboration with the company Vacuumschmelze Hanau GmbH & Co. KG (www.vacuumschmelze.de). An experimental validation of the proposed magnet systems considering the investigated defect scenarios is presented in [75]. Moreover, both the optimized C- and HCp-magnet are used to detect defects in glass laminate aluminium reinforced epoxy (GLARE) [152]. The presented results demonstrate the expected performance of the proposed designs. In the next section, the depth-optimized C-magnet is used for the detection of deep-lying slits to point out the current state of the art and further perspectives in LET.

4.1.5 Defect Depth Study

Previous ECT studies often assumed quasi-infinite cracks to evaluate the detection limit (see Table 2.1 on page 10). In this case, the defect is a slit obeying a pronounced length compared to the sensor system. In order to provide comparability to the results reported in the literature, the following benchmark problem is defined [153]. The problem geometry is inspired by the study from Mook *et al.* [30] and is shown in Fig. 4.12. The specimen consists of a solid block of size [250, 50, 24] mm made of aluminium, which contains a slit of size $[X_d, Y_d, Z_d] = [75, 1.5, 24]$ mm. The artificial crack is oriented in parallel to the direction of motion. On top of this structure, a variable number of aluminium sheets is situated. Each sheet has a thickness of 2 mm. The defect depth d is varied from 0 to 36 mm using 18 sheets. The sheets which are not on top of the specimen are situated on the bottom in order to ensure a constant height of the total assembly and to not alter the outer dimensions of the problem. By doing so, the magnetic Reynolds number is also kept constant. The overall dimensions of the specimen are then $[X_s, Y_s, Z_s] = [250, 50, 60]$ mm. During the measurements, the magnet is located on the centerline with respect to the y -axis in a height of $h = 1$ mm. All measurements are performed at a velocity of $v = 0.5$ m/s. The picture from Fig 2.7 on page 16 shows the particular laboratory setup with 18 aluminium sheets on top of the slotted bar.

The measurement data is post-processed with a 10-th order Butterworth low-pass filter having a cutoff frequency of 100 Hz. The force profiles are normalized with respect to the stationary values which occur far away from the defect. The results of the normalized drag- and lift-force over the whole specimen are shown in Fig. 4.13(a) and (b), respectively. The area, where the slit is located, is shown on the right hand side in enlarged form. Based on the definition of the velocity of the specimen, the data is recorded over time from the right to left such that positive x -positions are sampled first in time. When the specimen comes close to the magnet, the

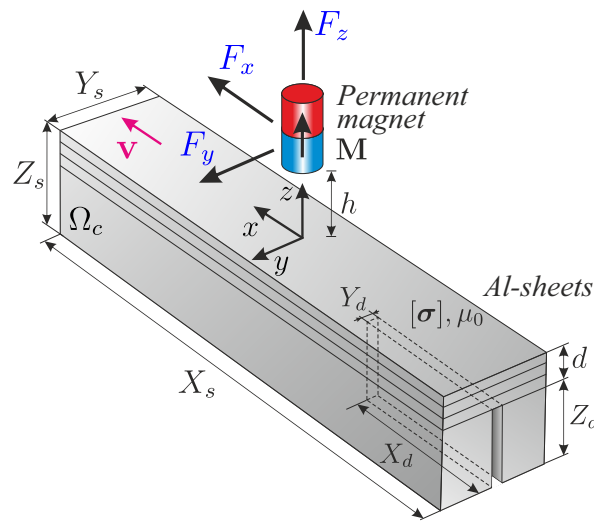


Figure 4.12: Geometry of the experimental setup to detect a deep-lying slit defect.

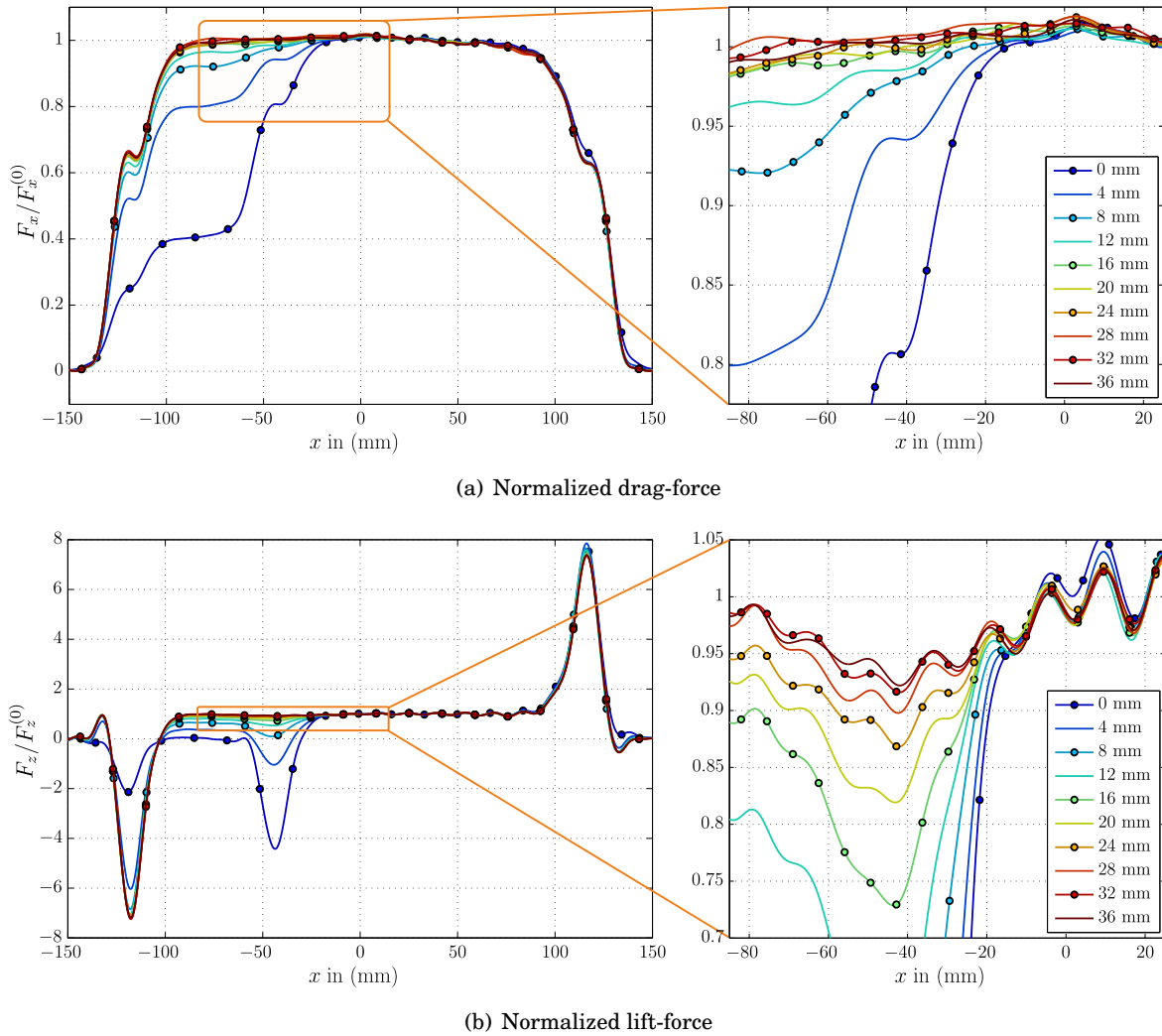


Figure 4.13: Measured profiles of the drag- and lift-force during the investigation on the maximum defect depth. The specimen contains a slit of size $[X_d, Y_d, Z_d] = [75, 1.5, 24]$ mm, which is located at different depths d .

drag-force ramps up and the lift-force shows a characteristic peak before both components reach their steady state ($F_x^{(0)}$ and $F_z^{(0)}$). In the defect region, it can be observed that the perturbations of the Lorentz force can be distinguished up to a depth of $d = 12$ mm for the drag-force. In contrast, when considering the lift-force, the slit can be clearly observed up to a depth of 24 mm.

It can be seen that the lift-component is superimposed by parasitic oscillations. These are systematic in nature and do partially result from the measurement frame of the system, where the magnet and the force sensor are mounted. A more detailed explanation and analysis of this phenomenon can be found in [75]. The presented results chart out the possibility to increase the reported depth limit in the future when the disturbances in both force components can be reduced. An exclusive construction of an optimized magnet system for this particular defect scenario is not necessary since it has less practical relevance.

By means of this analysis, it is possible to classify LET in the framework of electromagnetic eddy current methods in a qualitative sense. Considering the values obtained by Mook *et al.* [30] from Table 2.1 on page 10, it can be stated that the LET method within its present realization is highly comparable in terms of defect depth. It is worth to mention that depth-optimized ECT probes were employed in the comparative study from Mook *et al.* (Leotest MDF 1701 and MDF 3301, Leotest-Medium Center). However, it is emphasized that in LET the object is tested when it is in motion and within fractions of a second while avoiding any contact to its surface, which is the decisive difference to traditional ECT methods.

4.1.6 Conclusions

For the first time, the optimal magnet design in the LET framework is addressed. Parameters were classified as design, system and scaling parameters and the number of free variables was reduced, which simplified the optimization procedure. It was possible to clearly define the optimization problem while preserving universal applicability, motivated by the high specificity of NDT problems. The definition of a scaling factor offers the possibility to identify and convert similarities between different setups. The proposed methodology considers the strong interrelation to the applied force sensor. Therefore, three different optimization approaches were presented, the unconstrained optimization scheme (uc), the volume adaptive force constraint (VaFc), and the volume constraint force constraint (VcFc) approach. The VaFc approach can be employed to determine the critical V_m/V_d ratio. Then the ADRA can be further increased while still satisfying the given force limit by applying the VcFc approach.

Unconstrained optimization schemes are applicable for force sensors with high force limits, e.g. piezoelectric sensors [154]. On the other hand, the VaFc approach in combination with the VcFc approach is especially suited for systems with a limited force range, e.g. strain gauge sensors. The different locations of the unconstrained global optima demonstrate that the detection goal, expressed in form of the system parameters, strongly influences the optimal magnet design. In the case of constrained optimization for subsurface defects, a Halbach-structure in combination with soft magnetic material clearly outperforms cylindrical magnets of the same geometrical dimension. In contrast, for deep defects, the optimal magnet design converged to a regular cylindrical magnet when force constraints have to be considered.

The proposed optimization strategy is highly flexible, i.e., the magnet system can be replaced by a different system in the first evaluation step of the forward solver. Moreover, the model of the specimen and/or the defect in the second and third evaluation step can be adjusted to particular scenarios of interest. The latter has been applied during the optimization of magnet systems, which are used for the inspection of small metal injection molding specimens [155]. In this study, the proposed procedure is extended to cuboidal specimens of finite size and defects of different edge lengths.

When considering high-speed applications, secondary magnetic fields become prevalent and cannot be neglected as it is shown in section 3.3. In this case, the magnetic field formulation

used in the forward solver can be adjusted, e.g. to an $\mathbf{A}, \phi - \psi$ formulation, as it is described in section 3.2, albeit at the expense of computational cost.

In ECT, there exists a trade-off between penetration depth and resolution, which can be controlled by means of the diameter of the exciting coil [30]. This fact can be also observed in LET and is inherently a limiting factor of both methods. Our results (particularly Figs. 4.7 and 4.8(b)) demonstrate the advantage of combining active and passive magnetic materials in form of a Halbach-structure in an LET sensor for selected applications. The results of the unconstrained optimization demonstrate that the use of those structures is counteracting the trade-off between penetration depth and resolution, revealing additional potential of future sensor systems.

In the present case, the optimization procedure is applied considering two different defect scenarios taking into account a force constraint of $F_x^{(0)} = 3$ N. The associated optimal magnet designs are manufactured and made available for experimental studies presented in [75] and [152].

A defect depth study, adopting the concept of a quasi-infinite crack, revealed a current detection limit of 24 mm when considering the lift-component of the Lorentz force.

4.2 Uncertainty Analysis in LET

4.2.1 Introduction and Motivation

Especially in the framework of NDT, the analysis of uncertainties plays an important role during the design process of new systems [156, 157]. Though by means of numerical simulations it is possible to predict the Lorentz force profile but the intrinsic variability of the input parameters were not accounted yet. Hence, one cannot rely on a single deterministic simulation if a comparison to experimental data is intended and a quantification of uncertain model data on the resulting force profiles is essential. As a consequence, it is necessary to identify prior sources of uncertainty in order to improve the experimental setup at hand.

In order to determine the statistical information of the output quantities of a system, such as the mean or the variance, one of the most common methods is Monte Carlo sampling (MC). The MC method is based on repetitive calculations of the forward model, while defining the random inputs according to their probability distributions. This results in an ensemble of solutions from which statistical properties can be derived. However, a large number of simulations is needed due to the slow convergence rate of the MC method. The mean for example converges with $1/\sqrt{N_d}$, where N_d is the number of deterministic forward calculations [158]. This limits the applicability to problems with low computational cost. Nevertheless, different approaches were developed to improve MC type methods in terms of convergence for example Latin Hypercube sampling (LHS) [159] or Quasi Monte Carlo (QMC) [160, 161]. On the other hand, perturbation methods, which are based on Taylor expansions, and operator based methods, based on Neumann expansion, are restricted to small uncertainty intervals in the in- and output variables of around 10% [162] and will not be further discussed here.

The primary focus of this work rests on spectral methods, which are based on the determination of a functional dependence between the probabilistic in- and output of a system by means of a series of suitable selected functionals. The practical realization of spectral methods can be further subdivided into intrusive and non-intrusive approaches. Intrusive approaches are based on Galerkin methods, where the governing equations have to be modified to incorporate the probabilistic character of the model parameters. This includes the determination of the stochastic weak form of the problem according to the given uncertainties [163]. On the contrary, non-intrusive approaches are based on a reduced sampling of the probability space without any modification of the deterministic solvers. Those methods are more flexible and thus more suitable for universal application. Typical applications can be found in the fields of computational fluid dynamics [164–166], heat transfer [167, 168], multibody dynamics [169, 170], robust design optimization [171] or in biomedical engineering [172, 173]. During the last years, spectral approaches are becoming increasingly popular in an engineering framework. However, those are not a reference tool yet and still unknown for many people. For that reason, particular emphasis is placed to describe the method and to further elucidate the principle by means of an example.

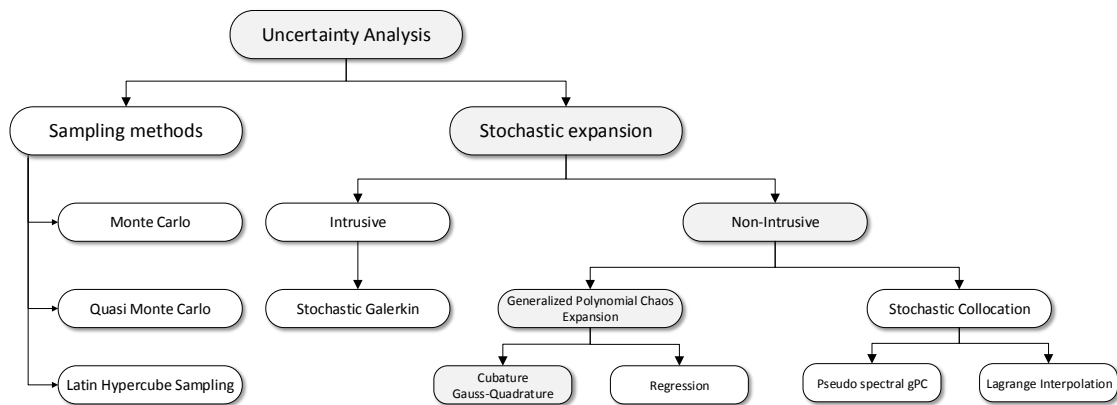


Figure 4.14: Overview of methods in uncertainty analysis. The gray-shaded boxes indicate the approaches used in the following investigations.

In more detail, the focus in this work is on non-intrusive approaches of spectral methods, which can be further subdivided into generalized polynomial chaos expansion (gPC) techniques and collocation methods (CM). The gPC in the framework of the FEM was first introduced by Ghanem in 1991 [174] and is based on the theory of Wiener-Hermite homogeneous chaos [175]. Therein, orthogonal polynomials are used to determine the functional dependence of the problem in the probability space. The CM was first introduced in [176] and later independently in [177]. In contrast to gPC, the CM determines the functional dependence by constructing interpolation functions in the probability space.

From the mathematical point of view, there exists a variety of approaches to determine the gPC-coefficients. On the one hand, it is possible to apply spectral projection techniques, which make use of numerical integration schemes such as the Gauss-quadrature. On the other hand, the regression approach can be applied, which is based on solving a least-square problem. Alternatively, in CM, a pseudo spectral gPC or Lagrange interpolation approach can be applied. An overview about all mentioned approaches is shown in Fig. 4.14. The present work focuses on the gPC expansion using a Gauss-quadrature approach. A comparison between the MC method, the Gauss-quadrature approach, the regression approach and the collocation method in view of an electromagnetic induction problem in a biomedical engineering framework is published by the author in [172] and the results of the present study, which is related to LET, can be found in [178].

At first, the theoretical background of the gPC expansion is described in section 4.2.2. The principle is further illustrated by means of an example. It is followed by the definition of the stochastic problem at hand in section 4.2.3, including a description how the formalism can be applied to an LET scenario. In section 4.2.4, the model parameters are investigated in terms of their variabilities, which is a vital part of every uncertainty analysis. Finally, the results are presented and discussed in section 4.2.5 and conclusions are drawn in section 4.2.6.

4.2.2 The Generalized Polynomial Chaos Method

At first, the theoretical background of the gPC method is explained before it is adopted to the LET problem. The parameters of interest, which are assumed to underlie a distinct level of uncertainty, are denoted as $\xi = (\xi_1, \xi_2, \dots, \xi_N)$. It is assumed that the parameters are statistically mutually independent from each other. In order to perform a gPC expansion, the random variables must have a finite variance, which defines the problem in the L_2 -Hilbert space. The M observables (output quantities), which are going to be analyzed in terms of the input uncertainties, are $\mathbf{Y} = [Y_1, Y_2, \dots, Y_M]$. The input ξ will be modeled as an N -variate random vector in the probability space (Θ, Σ, P) . The event space Θ contains all possible events. Σ is a σ -Algebra over Θ , containing sets of events, and P is a function assigning the probabilities of occurrence to the events.

The probability density function (pdf) $p_n(\xi_n)$, with $n = 1, \dots, N$, has to be defined for each random variable ξ_n . In the present framework, it is advisable to transform the pdf from the original space into the normalized space by shifting and scaling, assuming standardized random variables. For example, uniform or β -distributed random variables are shifted and scaled from a range of (a, b) to $(-1, 1)$, similar to the element basis functions in the FEM. The joint pdf is then given by:

$$p(\xi) = \prod_{n=1}^N p_n(\xi_n). \quad (4.27)$$

In consequence, the probability space in case of uniform or β -distributed random variables is an N -dimensional hypercube of size $(-1, 1)^N$. The idea of the gPC is to find a functional dependence between the random variables ξ and the solutions \mathbf{Y} by means of an orthogonal polynomial basis. Since the random variables are functions, the gPC can be seen as a functional. The set of polynomials for an optimal basis of continuous probability distributions is derived from the Askey scheme [179]. These polynomials $\psi_i(\xi_n)$ are orthogonal with respect to the pdf, e.g. Legendre polynomials are used in the case of uniform distributions or Jacobi polynomials are used for β -distributions.

$$\mathbb{E}[\psi_i \psi_j] = \int_{\Theta} \psi_i(\xi) \psi_j(\xi) p(\xi) d\xi = \delta_{ij} \langle \psi_i^2 \rangle \quad (4.28)$$

Where δ_{ij} is the Kronecker delta function, which equals 1 for $i = j$ and 0 otherwise. The term $\langle \cdot, \cdot \rangle$ denotes the inner product with respect to the pdf and is defined as:

$$\langle x, y \rangle = \int_{\Theta} x(\xi) y(\xi) p(\xi) d\xi. \quad (4.29)$$

Table 4.1 provides examples of the relationship between the families of orthogonal polynomials and different types of pdfs.

The gPC is defined by the following expansion using the joint orthogonal polynomial basis functions $\Psi_k(\xi)$.

$$Y_m(\xi) = \sum_{k=0}^{\infty} \hat{u}_{k,m} \Psi_k(\xi) \approx \sum_{k=0}^{N_c-1} \hat{u}_{k,m} \Psi_k(\xi) \quad (4.30)$$

Table 4.1: Connection between probability distributions and polynomial basis functions [162].

Type	Distribution	Orthogonal polynomials	Range
continuous	uniform	Legendre	(a, b)
continuous	beta	Jacobi	(a, b)
continuous	gaussian	Hermite	$(-\infty, +\infty)$
discrete	poisson	Charlier	$(0, 1, \dots)$

The series is performed for every output quantity separately, indexed by $m = 1, \dots, M$. It is truncated at a certain order p , which results in N_c terms and gPC-coefficients $\hat{u}_{k,m}$. The construction of the multi-variate polynomials $\Psi_k(\xi)$ is described in the following. By introducing a multi-index $\gamma^{(k)} = \{\gamma_1^{(k)}, \dots, \gamma_N^{(k)}\}$, which is an array of integers of size N , a distinct set of multi-indices $\lambda^{(k)}(p)$ can be defined such that its sum is equal to a certain order of expansion p .

$$\lambda^{(k)}(p) = \left\{ \gamma^{(k)} : \sum_{i=1}^N \gamma_i^{(k)} = p \right\} \quad (4.31)$$

The p -th order polynomials are the products over all polynomials associated to the corresponding random variable ξ_n and form the Hilbertian basis.

$$\Psi_k(\xi) = \left\{ \bigcup_{\gamma \in \lambda^{(k)}(p)} \prod_{n=1}^N \psi_{\gamma_n^{(k)}}(\xi_n) \right\} \quad (4.32)$$

It is mentioned, that the number of polynomials increases for higher orders p since the set of multi-indices $\lambda^{(k)}(p)$ grows as a consequence of an increased number of available combinations resulting from (4.31). In a full tensor gPC, the maximum polynomial order of *each* random variable is p . In consequence, the number of coefficients N_c increases exponentially:

$$N_c = (p + 1)^N. \quad (4.33)$$

In practical applications, the more economical maximum order gPC is preferably used. In this case, the *total order* of the polynomial must not exceed p . The number of coefficients, and hence, the dimension of the space spanned by the polynomials, is then given by [180]:

$$N_c = \binom{N+p}{N} = \frac{(N+p)!}{N!p!}. \quad (4.34)$$

In order to elucidate the construction process of the joint basis functions, the following example is considered. Applying a 2nd order approximation ($p = 2$) to a problem with $N = 3$ random variables results in the following $N_c = 10$ polynomials indexed in lexicographic order:

0th order :

$$\Psi_0(\xi) = \prod_{n=1}^3 \psi_{\gamma_n^{(0)}}(\xi_n) = \psi_0(\xi_1) \psi_0(\xi_2) \psi_0(\xi_3) \quad (4.35a)$$

1st order :

$$\Psi_1(\boldsymbol{\xi}) = \prod_{n=1}^3 \psi_{\gamma_n^{(1)}}(\xi_n) = \psi_1(\xi_1)\psi_0(\xi_2)\psi_0(\xi_3) \quad (4.35b)$$

$$\Psi_2(\boldsymbol{\xi}) = \prod_{n=1}^3 \psi_{\gamma_n^{(2)}}(\xi_n) = \psi_0(\xi_1)\psi_1(\xi_2)\psi_0(\xi_3) \quad (4.35c)$$

$$\Psi_3(\boldsymbol{\xi}) = \prod_{n=1}^3 \psi_{\gamma_n^{(3)}}(\xi_n) = \psi_0(\xi_1)\psi_0(\xi_2)\psi_1(\xi_3) \quad (4.35d)$$

2nd order :

$$\Psi_4(\boldsymbol{\xi}) = \prod_{n=1}^3 \psi_{\gamma_n^{(4)}}(\xi_n) = \psi_2(\xi_1)\psi_0(\xi_2)\psi_0(\xi_3) \quad (4.35e)$$

$$\Psi_5(\boldsymbol{\xi}) = \prod_{n=1}^3 \psi_{\gamma_n^{(5)}}(\xi_n) = \psi_1(\xi_1)\psi_1(\xi_2)\psi_0(\xi_3) \quad (4.35f)$$

$$\Psi_6(\boldsymbol{\xi}) = \prod_{n=1}^3 \psi_{\gamma_n^{(6)}}(\xi_n) = \psi_1(\xi_1)\psi_0(\xi_2)\psi_1(\xi_3) \quad (4.35g)$$

$$\Psi_7(\boldsymbol{\xi}) = \prod_{n=1}^3 \psi_{\gamma_n^{(7)}}(\xi_n) = \psi_0(\xi_1)\psi_2(\xi_2)\psi_0(\xi_3) \quad (4.35h)$$

$$\Psi_8(\boldsymbol{\xi}) = \prod_{n=1}^3 \psi_{\gamma_n^{(8)}}(\xi_n) = \psi_0(\xi_1)\psi_1(\xi_2)\psi_1(\xi_3) \quad (4.35i)$$

$$\Psi_9(\boldsymbol{\xi}) = \prod_{n=1}^3 \psi_{\gamma_n^{(9)}}(\xi_n) = \psi_0(\xi_1)\psi_0(\xi_2)\psi_2(\xi_3). \quad (4.35j)$$

After constructing the polynomial basis, the corresponding gPC-coefficients $\hat{u}_{k,m}$ have to be determined. In this regard, the output variable Y_m is projected from the N -dimensional probability space Θ_N into the N_c -dimensional polynomial space $\mathcal{P}_{N_c}^p$ of order p . In this regard, an analytical approximation of the solution Y_m as a function of its random input parameters $\boldsymbol{\xi}$ is derived. This enables computational efficient investigations on its stochastics. Different methods exist to calculate the gPC-coefficients $\hat{u}_{k,m}$, whereas in the following, a cubature approach based on the Gauss-quadrature is described.

Estimation of the gPC Coefficients by Means of the Gauss-Quadrature: Due to the orthogonality of the joint polynomial basis functions $\Psi(\boldsymbol{\xi})$, the gPC-coefficients $\hat{u}_{k,m}$ can be determined by the following expression [163]:

$$\hat{u}_{k,m} = \frac{\langle Y_m(\boldsymbol{\xi}), \Psi_k(\boldsymbol{\xi}) \rangle}{\langle \Psi_k(\boldsymbol{\xi}), \Psi_k(\boldsymbol{\xi}) \rangle}, \quad k = 0, 1, \dots, N_c - 1. \quad (4.36)$$

On the one hand, the denominator in (4.36) acts as a scalar weight for each coefficient. It is given in closed form and can be calculated analytically for each k . For example, in case of $N = 3$ standardized random variables, the denominator would be given by:

$$\langle \Psi_k(\boldsymbol{\xi}), \Psi_k(\boldsymbol{\xi}) \rangle = \int_{-1}^{+1} \int_{-1}^{+1} \int_{-1}^{+1} \Psi_k(\xi_1, \xi_2, \xi_3)^2 \underbrace{p_1(\xi_1)p_2(\xi_2)p_3(\xi_3)}_{p(\boldsymbol{\xi})} d\xi_1 d\xi_2 d\xi_3. \quad (4.37)$$

On the other hand, the integral in the nominator in (4.36) has to be calculated numerically, since the model function $Y_m(\boldsymbol{\xi})$, reflecting the problem under consideration, is not known in closed form. In order to determine the nominator, the problem has to be calculated multiple times on a distinct set of sampling points. For $N = 3$ random variables, the nominator would be given by:

$$\langle Y_m(\boldsymbol{\xi}), \Psi_k(\boldsymbol{\xi}) \rangle = \int_{-1}^{+1} \int_{-1}^{+1} \int_{-1}^{+1} \underbrace{Y_m(\xi_1, \xi_2, \xi_3) \Psi_k(\xi_1, \xi_2, \xi_3)}_{f(\boldsymbol{\xi})} \underbrace{p_1(\xi_1) p_2(\xi_2) p_3(\xi_3)}_{p(\boldsymbol{\xi})} d\xi_1 d\xi_2 d\xi_3. \quad (4.38)$$

In this context, the joint pdf $p(\boldsymbol{\xi})$ can be interpreted as a weighting function. This integral can be solved by means of a distinct type of Gauss-quadrature resulting in the following finite sum over N_g grid points.

$$\int_{-1}^{+1} f(\boldsymbol{\xi}) p(\boldsymbol{\xi}) d\boldsymbol{\xi} \approx \sum_{i=1}^{N_g} f(\boldsymbol{\xi}_i) w_i \quad (4.39)$$

According to the types of the probability distributions, the location of the samples $\boldsymbol{\xi}_i$ and weights w_i are defined. Then, for uniform or β -distributions, a Gauss-Legendre- or a Gauss-Jacobi-quadrature has to be applied. The sampling-points in the i -th dimension $\boldsymbol{x}^{(i)}$ are determined by the roots of the orthogonal polynomial of some order q , which determines the number of grid points. In practice, it is recommended to adapt the grid to the intended expansion order of the gPC, such that $q \geq p$. The grid \mathcal{G}^{gPC} contains all sampling points and is determined by the tensor product of the nodes in each dimension:

$$\mathcal{G}^{\text{gPC}} = \boldsymbol{x}^{(1)} \otimes \dots \otimes \boldsymbol{x}^{(N)}. \quad (4.40)$$

The corresponding weights are calculated by solving the eigenvalue problem considering the recurrence relationship of the orthogonal polynomials [181]. In accordance to the grid coordinates, the set of weights \mathcal{W}^{gPC} is calculated by the tensor product between the weights in each dimension:

$$\mathcal{W}^{\text{gPC}} = \boldsymbol{w}^{(1)} \otimes \dots \otimes \boldsymbol{w}^{(N)}. \quad (4.41)$$

Returning back to (4.38), the cubature formula of the nominator for $N = 3$ random variables would be given by:

$$\langle Y_m(\boldsymbol{\xi}), \Psi_k(\boldsymbol{\xi}) \rangle \approx \sum_{i_1=1}^{m_1} \sum_{i_2=1}^{m_2} \sum_{i_3=1}^{m_3} Y_m(\boldsymbol{\xi}_{i_1, i_2, i_3}) \Psi_k(\boldsymbol{\xi}_{i_1, i_2, i_3}) w_{i_1, i_2, i_3}. \quad (4.42)$$

The parameter m_i denotes the number of sample points in each dimension. In other words, for a given polynomial indexed by k , the integral is approximated by a sum over the determined values $Y_m(\boldsymbol{\xi}_i)$, with $\boldsymbol{i} = (i_1, \dots, i_N)$, calculated at distinct points $\boldsymbol{\xi}_i$, multiplied by the corresponding value of the polynomial $\Psi(\boldsymbol{\xi}_i)$, and weighted by the weights w_i at these points. Finally, the gPC-coefficients $\hat{u}_{k,m}$ can be calculated by (4.36).

Post-processing: After calculating the gPC-coefficients $\hat{u}_{k,m}$, the statistical moments of the output quantity of interest $Y_m(\xi)$ can be calculated. The expectation μ_m and the variance σ_m^2 of the m -th output quantity are then given by:

$$\mu_m = \hat{u}_{0,m} \quad (4.43)$$

$$\sigma_m^2 = \sum_{k=1}^{N_c-1} \hat{u}_{k,m}^2 \langle \Psi_k(\xi), \Psi_k(\xi) \rangle. \quad (4.44)$$

An important part during the investigation of new and partially known systems is an analysis regarding its sensitivity. If it is possible to quantify the sensitivity of a system with respect to its input parameters, it is possible to identify the most important variables which influence the output quantities. This allows the implementation of targeted improvement measures to the setup under investigation. In gPC, the global derivative based sensitivity coefficients $S_{i,m}^{(\partial)}$ with respect to the i -th variable can be approximated by means of the gPC-coefficients and the corresponding partial derivatives of the basis functions. They are given by the following expression [162]:

$$S_{i,m}^{(\partial)} = \mathbb{E} \left[\frac{\partial Y_m}{\partial \xi_i} \right] \approx \sum_{k=0}^{N_c-1} \left(\hat{u}_{k,m} \int_{-1}^{+1} \frac{\partial \Psi_k}{\partial \xi_i} p(\xi) d\xi \right). \quad (4.45)$$

On the other hand, variance-based sensitivity measures indicate the influence of the individual random input variables ξ_i on the total variances σ_m^2 of the output quantities. This concept is also known as analysis of variance (ANOVA). The Sobol indices are determined by a Sobol decomposition [182]. The first order Sobol indices provide an estimate about the influence of the *single* variables ξ_i on the output quantities. In most cases, they are the most significant indices. Introducing subsets \mathcal{K}_i , which contain indices k that target those polynomials Ψ_k that only depend on the i -th random variable, the first order Sobol indices $S_{k,m}^{(1)}$ are given by [183]:

$$S_{i,m}^{(1)} = \frac{1}{\sigma_m^2} \sum_{k \in \mathcal{K}_i} \hat{u}_{k,m}^2 \langle \Psi_k(\xi_i), \Psi_k(\xi_i) \rangle. \quad (4.46)$$

In a similar way, the analysis can be extended up to Sobol indices of the order N , including the influence of *all* random variables at the same time.

The pdf of $Y_m(\xi)$ can be determined by applying sampling strategies such as Monte Carlo, Latin Hypercube or Quasi Monte Carlo sampling with N_{MC} realizations. Since a deterministic functional dependence is calculated by the gPC, a large number of samples such as $N_{MC} \approx 10^5 - 10^6$ can be used with vanishingly small computational effort compared to direct sampling.

Example: The general principle of the gPC is illustrated considering the following two-dimensional model function, which represents the exemplary system to be investigated:

$$Y(\xi_1, \xi_2) = 3(1 - \xi_1)^2 e^{-\xi_1^2 - (\xi_2 + 1)^2} - 10 \left(\frac{\xi_1}{5} - \xi_1^3 - \xi_2^5 \right) e^{-\xi_1^2 - \xi_2^2} - \frac{1}{3} e^{-(\xi_1 + 1)^2 - \xi_2^2}. \quad (4.47)$$

In the present case, there exists only one output quantity such that $M = 1$. The model function is shown in Fig. 4.15(a). The input parameters ξ_1 and ξ_2 are modeled as β -distributed random variables. The probability density function in the range of (a, b) is given by:

$$p(\xi) = \frac{\Gamma(\alpha + \beta)}{\Gamma(\alpha)\Gamma(\beta)(b - a)^{\alpha + \beta - 1}} (\xi - a)^{\alpha - 1} (b - \xi)^{\beta - 1}, \quad (4.48)$$

where $\Gamma(\cdot)$ is the Gamma function [184]. The parameters α and β define the shape of the distribution, whereas the parameters a and b correspond to the outer bounds. It can be noticed that uniform distributions are a subset of (4.48) by choosing $\alpha = \beta = 1$. In the present example, the shape parameters are set to $[\alpha_1, \beta_1] = [5, 10]$ and $[\alpha_2, \beta_2] = [12, 3]$ in the region $[a_1, b_1] = [-1, 1]$ and $[a_2, b_2] = [-1, 0]$ for ξ_1 and ξ_2 , respectively. Both distributions are shown in Fig. 4.15(b). As previously mentioned, the distributions have to be normalized to the range of $(-1, 1)$ in every dimension. Since the random variables are β -distributed, the orthogonal polynomial basis has to be constructed using n -th order Jacobi polynomials $P_n^{\alpha, \beta}(\xi)$ (see Table 4.1 on page 74):

$$P_n^{\alpha, \beta}(\xi) = \frac{\Gamma(\alpha + n + 1)}{n! \Gamma(\alpha + \beta + n + 1)} \sum_{j=0}^n \binom{n}{j} \frac{\Gamma(\alpha + \beta + n + j + 1)}{\Gamma(\alpha + j + 1)} \left(\frac{\xi - 1}{2} \right)^j. \quad (4.49)$$

Those functions are used to construct the polynomial basis according to (4.32). It is noted that the shape parameters α and β significantly influence the shape of the polynomials. If those differ between the random variables, the polynomial basis differs between the dimensions as well. In the next step, the grid of sampling points \mathcal{G}^{gPC} and the corresponding weights \mathcal{W}^{gPC} , needed for the Gauss-quadrature, are constructed. In the present example, a gPC expansion of the order $p = 5$ is performed. According to (4.34), this results in a total number of $N_c = 21$ gPC-coefficients. The number of grid points is defined to be the same in every dimension and is set to $q = 6$. This results in a total number of $N_g = q^N = 36$ grid points. For ξ_1 , the roots $\mathbf{x}^{(1)}$ of the Jacobi polynomials $P_6^{\alpha_1, \beta_1}(\xi_1)$ are determined in addition to their corresponding weights $\mathbf{w}^{(1)}$. The same applies for the second variable ξ_2 . Since the β -distributions differ from each other, the roots and weights are not the same. By applying the tensor products from (4.40) and (4.41), the computational grid \mathcal{G}^{gPC} is determined together with the grid of weights \mathcal{W}^{gPC} . In the next step, the solutions of the model function (4.47) are computed on the grid \mathcal{G}^{gPC} . The gPC-coefficients of the output quantity $Y(\xi_1, \xi_2)$ are then determined by solving (4.36) using the quadrature approach. In this way, a polynomial estimate of the model function is available, which is shown in Fig. 4.15(c) in its denormalized form. The points indicate the location of the grid points and their sizes correspond to their respective weight. It can be observed that the grid obeys an adaptive character such that it is concentrated in the region, where the probability of occurrence of the input variables is high. The accuracy of the approximated model function is evaluated considering the absolute difference to the original function. The results are shown in Fig. 4.15(e). A very good agreement in the region of interest can be observed, whereas the approximation is less accurate at the borders where the probability of occurrence is low. In order to compare the pdf of the output variable, the original and the estimated model

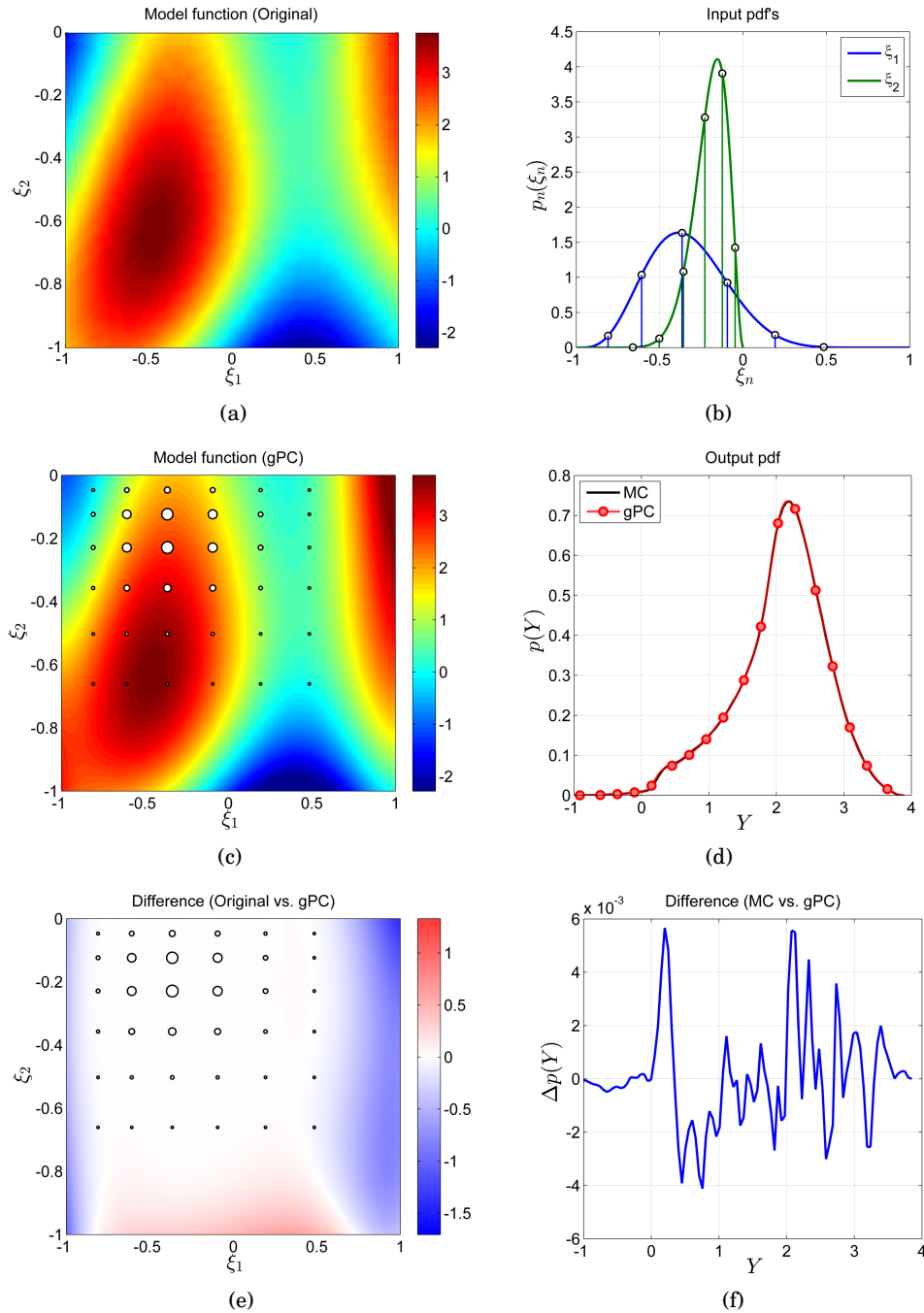


Figure 4.15: Example containing two random variables ξ_1 and ξ_2 to illustrate the working principle of the gPC. The grid \mathcal{G}^{gPC} contains $N_g = 36$ grid points and the gPC is performed with an order $p = 5$ approximation. (a) Original model function $Y(\xi_1, \xi_2)$; (b) pdfs of the β -distributed random input variables; (c) Estimated model function by the gPC; (d) pdf of the output quantity $Y(\xi_1, \xi_2)$; (e) Absolute difference of the model function between the original and the gPC estimate; (f) Absolute difference of the output pdf between MC and gPC; The white points in (b), (c) and (e) indicate the location of the sampling points. Their sizes in (c) and (e) are proportional to the corresponding weight of the Gauss-quadrature integration.

function are both sampled 10^6 times. In the present example, the evaluation of the original model function is computational not demanding. However, in a real scenario, direct sampling of the original model function is often not practical. The resulting output pdfs of both approaches and their absolute difference are shown in Fig. 4.15(d) and (f), respectively. It can be observed that the gPC provides an accurate estimate requiring only $N_g = 36$ evaluations of the original model function compared to traditional MC approaches with 10^6 direct samples. The mean, the standard deviation, and the sensitivity measures of the output quantity are given in Table 4.2. The first order Sobol indices $S_i^{(1)}$ indicate that the first variable ξ_1 contributes to 68.2% of the total variance. The second order Sobol index $S_{12}^{(2)}$ quantifies the impact if both parameters are varied at the same time. As expected, its contribution is substantially lower compared to the linear Sobol indices.

In contrast, the derivative based sensitivity coefficients $S_i^{(\partial)}$ indicate that the model is less sensitive with respect to the first variable ξ_1 . This results from the shape of the model function, which obeys both an increase and a decrease over the investigated range of ξ_1 . In consequence, the gradients do partly compensate over the whole parameter space. However, it can be observed that the model function slowly decreases in the ξ_2 -direction considering the region of interest, which explains the negative derivative based sensitivity coefficient of $S_2^{(\partial)} = -1.835$. The small example demonstrates the working principle of the gPC and the complexity to interpret the results from an uncertainty and sensitivity analysis in a probabilistic context.

In the next section, the gPC is applied to the LET problem, which obeys higher computational cost compared to the previous example.

Table 4.2: Results of the exemplary problem, investigated with the gPC.

Mean μ	Std. σ	Variance based sensitivity			Derivative based sensitivity	
		$S_1^{(1)}$	$S_2^{(1)}$	$S_{12}^{(2)}$	$S_1^{(\partial)}$	$S_2^{(\partial)}$
2.0621	0.6685	68.2%	29.9%	1.9%	0.191	-1.835

4.2.3 Problem Definition in LET

In the present framework of LET, the velocity v , the electrical conductivity σ , the lift-off distance h , and the magnetic remanence B_r are modeled as uniform as well as β -distributed random variables. The corresponding shape parameters $[\alpha, \beta]$ and bounds $[a, b]$ are determined by experiments, which are described in the next section. In this case, the probability space has $N = 4$ dimensions. It is assumed that the specimen is analyzed along its centerline. The quantities of interest are the drag- and lift-component of the Lorentz force $F_{x|z}$. The analysis of the side-force F_y is omitted since it vanishes for symmetry reasons. A non-intrusive gPC is applied considering $M = 11$ characteristic positions of the permanent magnet with respect to the specimen in order to investigate the propagation of uncertainties throughout the LET system.

Therefore, the magnetic convection equation is solved in its quasi-static form using the QSA, described in section 3.2.3, assuming moderate magnetic Reynolds numbers ($R_m = \mu_0 \sigma v Z_s / 2 \leq 1$). In this sense, time-dependent effects resulting from passing defects and the edges of the specimen are neglected.

If $\alpha = \beta = 1$, the Jacobi polynomials of the β -pdfs become Legendre polynomials, which are in turn orthogonal with respect to uniform pdfs. The $N = 4$ random variables are summarized in the vector $\xi = (\xi_1, \dots, \xi_4)$. Similar to the previous example, (4.36) is calculated numerically by means of the Gauss-Jacobi-quadrature scheme using the forces $F_{x|z}$ determined by the FEM at the points in the 4-D grid \mathcal{G}^{gPC} . As in the previous example, the grid points differ between each dimension since they depend on the corresponding input pdfs. On the contrary, the denominator of (4.36) is calculated analytically.

The results of the gPC are verified by evaluating the normalized root mean square deviation of both force components $\delta F_{x|z}$ with respect to MC simulations, which are independently determined in a random grid \mathcal{G}^{MC} containing N_{MC} samples. The general principle is shown in Fig. 4.16. The forces at the grid points in \mathcal{G}^{MC} are approximated by the gPC expansion and termed $\tilde{F}_{x|z}^{\text{gPC}}$. In a consecutive step, the relative difference between the approximated and the exact values is determined by:

$$\delta F_{x|z} = \frac{100\%}{\max(F_{x|z}^{\text{MC}}) - \min(F_{x|z}^{\text{MC}})} \sqrt{\frac{1}{N_{\text{MC}}} \sum_{i=1}^{N_{\text{MC}}} (F_{x|z,i}^{\text{MC}} - \tilde{F}_{x|z,i}^{\text{gPC}})^2} \quad (4.50)$$

$$\delta F = \frac{1}{2} (\delta F_x + \delta F_z), \quad (4.51)$$

where δF denotes the mean error of the Lorentz force. This error definition involves additional computations. However, it is a suitable measure to analyze the convergence properties for different approximation orders p and number of sample points $N_g = q^N$.

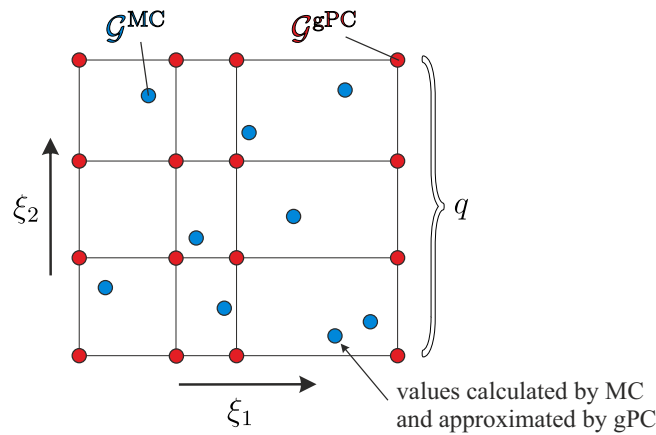


Figure 4.16: Illustration of the computational grids from the gPC and the MC approach. The blue points indicate the locations of the solutions obtained by MC sampling. After the gPC expansion is performed, the approximated solution is computed on \mathcal{G}^{MC} by means of the polynomial expansion and compared to the exact values in a root mean square sense.

4.2.4 Uncertainty Quantification of Model Parameters

In order to perform a gPC expansion, it is necessary to determine the statistical properties of the model parameters. On the one hand, the variations in the lift-off distance are approximated by the accuracy of the 2-D linear stage NLS4 (Newmark Systems Inc., www.newmarksystems.com), as well as by the mounting accuracy and surface roughness of the specimen. On the other hand, the statistical properties of the remaining parameters σ , v , and B_r are determined experimentally.

The conductivity of 60 Al-sheets is measured two times at three different locations, resulting in 360 samples in total. The measurements are performed with the eddy current testing device Elotest N300 (Rohmann GmbH, www.rohmann.de) using the probe KAS 7H190.03.1, operating at a frequency of 60 kHz. The measurement uncertainty is ± 0.06 MS/m considering the standard deviation from the repetitions.

The velocity variations are determined by means of the incremental position encoder TONiC T1000 (Renishaw plc, www.renishaw.com). The position is sampled with a frequency of 10 kHz. After differentiating the position data with respect to the time, the velocity is obtained with a measurement uncertainty of ± 1 mm/s. The total number of samples is approximately 19.000.

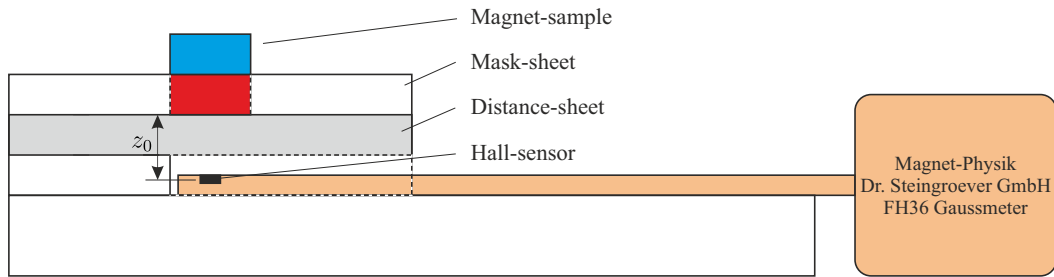
The determination of the stochastic properties of the effective remanence is more difficult. In order to provide comparability to the cylindrical magnet applied in the LET setup, it is ensured that the magnet samples are ordered from the same distributor and are made of the same magnetic material. The statistics are determined by 100 cylindrical magnets of size $[R, H] = [5, 10]$ mm with a material grade of N52 delivered from the company HKCM-engineering (Z10x10Ni-N52, Art.No: 9962-2336, www.hkcm.de). The effective remanence of the magnets is determined by measuring the axial component B_z of the magnetic flux density on the cylinder axis. The experimental setup is shown in Fig. 4.17. The magnetic flux is measured using the Gaussmeter FH36 (Magnet-Physik Dr. Steingroever GmbH, www.magnet-physik.de) in combination with the probe HS-MMT-6J08VH. All measurements are performed at room temperature of about 23° C. The magnets are located at a distance z_0 above the Hall-probe, which is determined during calibration. In order to ensure that all magnets are positioned at almost the same lateral position, a mask-sheet with a hole is used.

The distance z_0 , at which the magnetic flux is measured, has a major influences on the resulting remanence due to the high sensitivity of the magnetic field and its rapid decrease with distance. The calibration of the experimental setup consists of the determination of this distance. It is done using a coil with 5000 turns supplied by a defined current of $I_0 = 3$ mA, which is provided by the high precision current source SMU 2614 (Tektronix GmbH, Keithley Instruments, www.keithley.com). The experimental setup during calibration is shown in Fig. 4.17(b)-(d). The dimensions of the coil are $D_i = 2R_i = 24.5$ mm, $D_o = 2R_o = 30.2$ mm, and $H_c = 5.5$ mm. The winding body has a wall-thickness of 1 mm and the wire has a diameter of only 0.05 mm. Due to the high number of turns, stray fluxes from the coil terminals are reduced. In this way, a well defined magnetic flux distribution is produced, whereas its axial component as a function of the

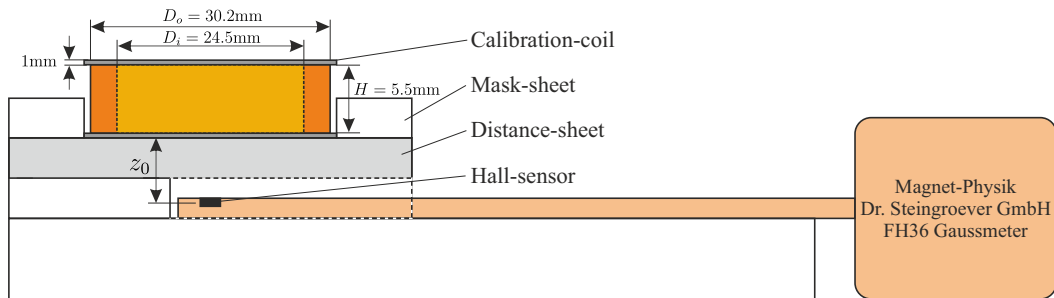
distance is given [185]:

$$B_z(z_0) = \frac{\mu_0}{2} \frac{I_0 N}{H_c(R_o - R_i)} \left[(H_c + z_0) \ln \left(\frac{R_o + \sqrt{(H_c + z_0)^2 + R_o^2}}{R_i + \sqrt{(H_c + z_0)^2 + R_i^2}} \right) - z_0 \ln \left(\frac{R_o + \sqrt{z_0^2 + R_o^2}}{R_i + \sqrt{z_0^2 + R_i^2}} \right) \right]. \quad (4.52)$$

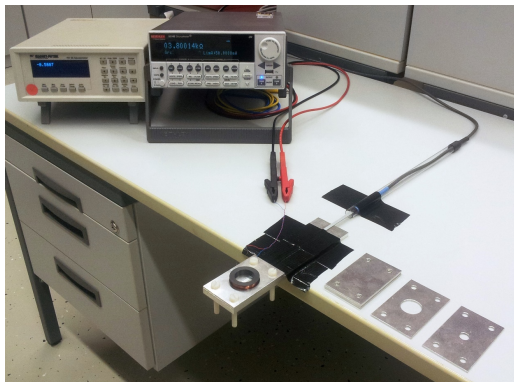
The distance z_0 is found by solving (4.52) iteratively together with the measured values of B_z . In the current setup, it is determined to be $z_0 = 1.155 \pm 0.042$ mm. The measurement uncertainty is determined by 10^4 MC runs of (4.52) considering the tolerances of all geometrical dimensions of ± 0.05 mm resulting from the caliper together with an uncertainty of $\pm 0.25\%$ of the magnetic



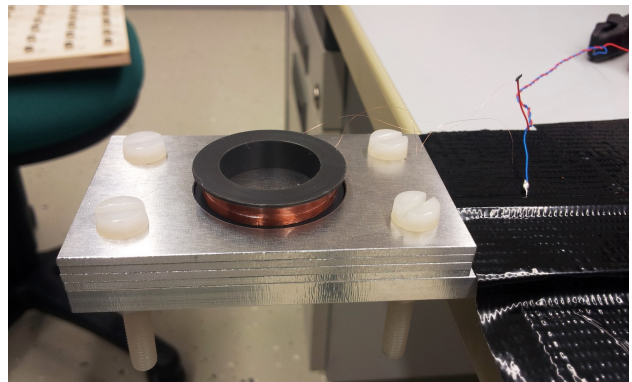
(a) Side view of experimental setup during measurements.



(b) Side view of experimental setup during calibration.



(c) Experimental setup with the Gaussmeter (top left) and high precision current source (to the right)



(d) Detailed view on the calibration coil connected to the high precision current source

Figure 4.17: Experimental setup to determine the effective remanence.

flux measurements. All variables are assumed to be uniform distributed. In a consecutive step, the magnetic flux density from each magnet of the 100 samples is determined. Afterwards, their effective remanences are calculated by:

$$B_r = 2B_z(z_0) \left(\frac{z_0 + H}{\sqrt{(z_0 + H)^2 + R^2}} - \frac{z_0}{\sqrt{z_0^2 + R^2}} \right)^{-1}. \quad (4.53)$$

The measurement uncertainty of the B_r measurements is ± 0.014 T. It is determined by sampling (4.53) while taking into account the variability of the magnetic flux measurements and of all geometrical dimensions including z_0 .

The pdfs of the model parameters are determined by fitting the β -distributions to the obtained data using the software environment "R" together with the package *fitdistrplus* [186]. The limits (a, b) are defined considering a 20% tolerance interval with respect to the extrema of the empirical data. A maximum likelihood estimation is applied to determine the individual shape parameters α and β . The upper and lower bounds of the equivalent uniform distributions are determined numerically in a consecutive step by means of the inverse cumulative distribution function (cdf), assuming that the uniform distributions cover 99% of the fitted β -cdfs. The fitted pdfs are shown in Fig. 4.18 together with their modes \hat{v} , $\hat{\sigma}$, and \hat{B}_r , which are the points of maximum probability density. The corresponding parameters are summarized in Table 4.3. The pdfs of the velocity and the conductivity are in the expected range and are fairly symmetric with respect to the modes. On the contrary, the values of the effective remanence are considerably lower compared to the nominal values provided by the manufacturer. The maximum probability of the fitted distribution is located at $\hat{B}_r = 1.32$ T, which is 7.7% lower compared to $B_r = 1.43$ T as specified by the manufacturer. Moreover, it

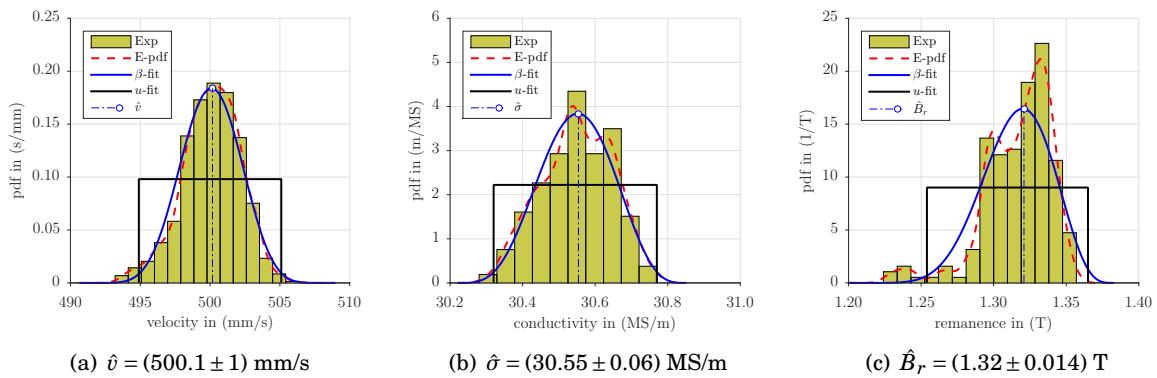


Figure 4.18: Statistical properties and modes of the input parameters: (a) velocity, (b) conductivity and (c) effective remanence. The graphs show the histograms obtained by experiments (Exp), the associated empirical pdfs (E-pdf) and the fitted distributions used in the numerical simulations. The E-pdfs are obtained numerically using a Gaussian kernel smoother together with a bandwidth, which equals 50% of the bin width in the respective histogram. The labels u-fit and β -fit correspond to the fits to the uniform- and β -distribution, respectively [178].

Table 4.3: Limits and shape parameters of the fitted probability distributions of the different model parameters [178].

pdf	parameter	v	σ	B_r	h
uniform	a	0.4949	30.32	1.254	0.9
	b	0.5051	30.77	1.365	1.1
beta	a	0.4906	30.22	1.201	0.86
	b	0.5090	30.85	1.383	1.14
	α	9.4273	5.0283	8.336	5
	β	8.9109	4.6166	4.910	5

can be observed that the distribution is not symmetric, which motivates the choice to model the probability density functions by means of β -distributions. In regard of the experimentally determined intervals from Fig. 4.18, it can be observed that the measurement uncertainty is considerably lower compared to the degree of variation. Hence, it was possible to provide information about the actual variability of the model parameters.

Experimental LET setup: In the setup under investigation, the optimized cylindrical permanent magnet of size $[D, H] = [22.5, 17.6]$ mm is used (see section 4.1). The layered specimen, which is made of stacked aluminium sheets, is used throughout the analysis (see Fig. 2.5(b) on page 13). One sheet contains a defect of size $[X_d, Y_d, Z_d] = [12, 2, 2]$ mm and is located in a depth of $d = 2$ mm. The velocity and the lift-off distance are set to 0.5 m/s and 1 mm, respectively.

4.2.5 Results and Discussion

The gPC is evaluated for different grids \mathcal{G}^{gPC} and approximation orders p , considering $M = 11$ different positions of the magnet. The gPC is expanded as long as the number of coefficients is smaller or equal to the number of sampling points ($N_c \leq N_d$). The mean error (4.51) is computed using $N_{MC} = 10^4$ direct samples. The errors are calculated for two characteristic magnet positions $P_1(x = 0)$, when the magnet is located right over the defect (highly perturbed eddy current profile) and $P_2(x = 65.5 \text{ mm})$, when the magnet is located between the defect and the outer edge of the specimen (unperturbed eddy current profile). The estimated errors are summarized in Table 4.4.

Differences below 0.3% can be observed even in case of coarse grids, i.e., $q = 2$ ($N_g = 16$). The error is converging fast to the accuracy limit of the FEM indicated by the slightly higher errors if the magnet is located in P_1 . The study indicates that a grid with $q = 3$ points in each dimension in combination with an approximation order of $p = 3$ is sufficient in this case to determine the uncertainties of both force components with an error of $< 0.18\%$.

Table 4.4: Averaged δF between gPC and MC for two characteristic magnet positions P_1 and P_2 in case of β -distributions (p expansion order, N_c number of coefficients, q number of grid points in one dimension, N_g total number of grid points) [178].

p	N_c	pos.	q / N_g			
			2 / 16	3 / 81	4 / 256	5 / 625
1	5	P_1	0.3613	0.3366	0.3326	0.3311
		P_2	0.2912	0.2911	0.2907	0.2908
2	15	P_1	0.2851	0.1705	0.1614	0.1583
		P_2	0.1877	0.0178	0.0162	0.0149
3	35	P_1	-	0.1705	0.1615	0.1599
		P_2	-	0.0172	0.0163	0.0136
4	70	P_1	-	0.2403	0.1615	0.1614
		P_2	-	0.1647	0.0164	0.0140
5	126	P_1	-	-	0.1615	0.1620
		P_2	-	-	0.0172	0.0141
6	210	P_1	-	-	0.2034	0.1638
		P_2	-	-	0.1263	0.0139
7	330	P_1	-	-	-	0.1655
		P_2	-	-	-	0.0140
8	495	P_1	-	-	-	0.2014
		P_2	-	-	-	0.1680

The estimated force profiles are depicted in Fig. 4.19 together with the experimental data. The graphs show the uncertainty intervals $\mu_{x|z} \pm 2\sigma_{x|z}$ for the forces $F_{x|z}$ obtained by the gPC in case of β -distributed random variables. The intervals are shown at the $M = 11$ selected points of interest. The dashed line shows one single deterministic simulation considering the modes of the input parameters. The measurements are in the numerically predicted range when uncertainties are taken into account. The relative standard deviation with respect to the mean value of both force components is nearly independent of the observation point and amounts 3.8% and 5.2% in case of β - and uniform distributed random variables, respectively. Moreover, the pdfs of the forces are evaluated by sampling the gPC expansion 10^6 times. They are shown in the lower part of Fig. 4.19 in the event that the magnet is located right over the defect at the point P_1 . The pdfs are compared to those obtained by the MC method using $N_{MC} = 10^4$ direct samples. As expected from the estimated errors, a very good agreement between both approaches can be observed.

The first order Sobol indices of F_x and F_z are determined at each of the $M = 11$ points and showed only minor variations with respect to the magnet position. They are averaged over all M positions and listed in Table 4.5. The first order Sobol indices are most significant and

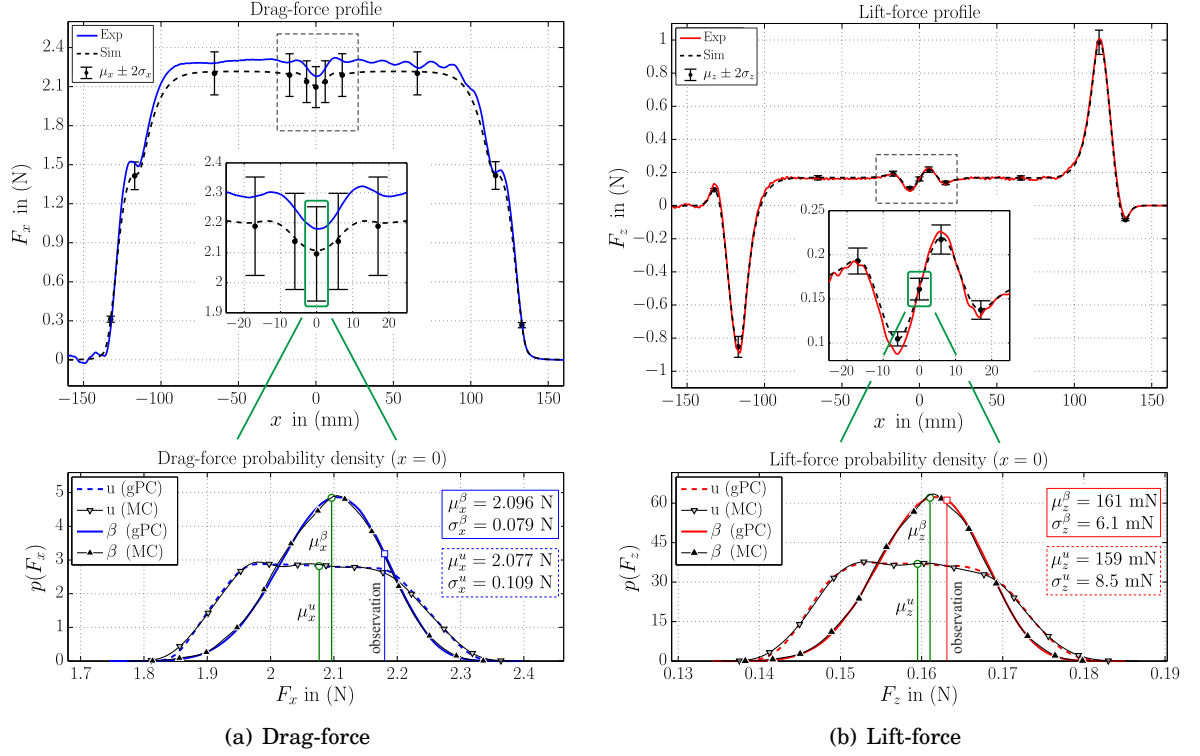


Figure 4.19: Numerical and experimental results of the Lorentz forces profiles. The uncertainty intervals are shown in case of β -distributed random variables for $\mu_{x|z} \pm 2\sigma_{x|z}$ using a grid with $q = 3$ points in each direction and an expansion order of $p = 3$. The figures at the bottom show the estimated pdfs in the point P_1 when the magnet is located over the defect at $x = 0$ for uniform distributions (u) and β -distributions (β) [178].

Table 4.5: First order Sobol indices of F_x and F_z averaged over $M = 11$ magnet positions calculated with a grid of $q = 3$ points in each direction and an expansion order of $p = 3$ [178].

pdf	$S_{x,B}^{(1)}$	$S_{z,B}^{(1)}$	$S_{x,h}^{(1)}$	$S_{z,h}^{(1)}$	$S_{x,v}^{(1)}$	$S_{z,v}^{(1)}$	$S_{x,\sigma}^{(1)}$	$S_{z,\sigma}^{(1)}$
uni	88.4	84.2	9.6	10.2	1.3	3.7	0.7	1.9
beta	87.9	83.7	10.2	10.7	1.2	3.6	0.7	2.0

almost cover the total variance. Keeping in mind that the whole system is treated as a black box, assuming that the experimentalist has no detailed knowledge about the applied magnet, it is observed that the uncertainty in the magnetic remanence has with $\sim 85\%$ the greatest influence on the total variance of the resulting forces. In addition, the lift-off distance contributed to approximately $\sim 10\%$, whereas the velocity and the conductivity showed only minor impact.

4.2.6 Conclusions

The present study shows that the analysis of uncertainties by means of gPC based methods can be readily used for extended experimental validation in the framework of LET. The

applied methodology is very efficient in terms of computation time compared to traditional MC approaches. The gPC already converged after $N_g = 81$ simulations using an order $p = 3$ approximation. The statistical properties of the velocity, the conductivity, and the magnetic remanence were determined experimentally. The use of β -distributions allowed to model each variable individually and in a more realistic sense compared to uniform distributions. The analysis provides the possibility to identify most influencing parameters in order to improve the measurement accuracy of the experimental setup. This serves as a starting point to reduce the variance of the resulting Lorentz forces and to increase the SNR, which directly enhances the reproducibility and the defect detection capabilities of the LET method.

The study shows that the magnetic remanence is the most influencing factor when considering the absolute value of the Lorentz force. If possible, it should be determined in advance using the proposed experimental setup. It could be observed that the effective remanence is generally lower compared to the values specified by the manufacturer. This should be taken into account during the optimization of magnet systems in the future. However, the use of the dimensionless scaling factor from (4.7) allows to correct the remanence variations retrospectively by increasing the velocity accordingly, while ensuring that the system does not violate the constraints and remains to operate in the linear R_m regime. Nevertheless, its value does not change over time and is thus not contributing to the noise level considering the SNR. The quantities, which may change over time, are the lift-off distance and the velocity. Since the eddy current density is highest at the surface of the specimen, the lift-off distance should be kept at a constant level in order to decrease the disturbances resulting from lift-off variations.

Despite of that, the velocity variations have an apparently small share of about 1 – 4% to the total variance, their time-dependent nature blurs the defect signal and reduces the SNR. Comparing the relative contribution to the experimental data of the defect depth study in section 4.1.5, it seems inherent that the velocity variations and vibrations should be reduced as much as possible in order to keep the Lorentz force at a constant level. This would enable the identification of weakest force perturbations resulting from small or deep lying defects.

It is emphasized that the current study is valid for the proposed working point of the system. It is assumed that the system operates in the linear regime of low to moderate R_m , where the back-reaction of the induced eddy currents is moderate (QSA). If the working point considerably changes, the study has to be repeated together with an estimation of the involved uncertainties. In the same way, alternative numerical approaches have to be considered, as for example MDA or MMA described in section 3.2.

During the present analysis, it is observed that the velocity profile obeys characteristic oscillations, which superimpose the rectilinear part of the motion. So far, the influence of sinusoidal velocity profiles on the Lorentz force has not been investigated in detail. In the next section, this effect is studied further and a full 3-D analytical approach is presented to solve this kind of electromagnetic field problem.

4.3 Lorentz Forces in the Case of Oscillating Velocity Profiles

4.3.1 Introduction and Motivation

The present study addresses the analysis of motion-induced eddy currents in the case of harmonic motion of current carrying coils or permanent magnets in the vicinity of electrical conductors. The study is motivated by the observation of velocity oscillations of the specimen, resulting for example from the control circuit of the linear drive. Three normalized velocity profiles, which are obtained during operation, are shown in Fig. 4.20. The velocities are determined using the incremental position encoder TONiC T1000 (Renishaw plc, www.renishaw.com). It has been observed that the relative oscillation amplitudes reach up to 3% in the present case. The time-dependent velocity influences the induced eddy current density together with the total magnetic field. In consequence, the Lorentz force is influenced as well. The goal of the present study is to determine this electromagnetic force $\mathbf{F}^{(EM)}$ resulting from the observed oscillations. This quantity serves as an input of the force sensing unit. An ideal sensor would convert this force into another physical quantity, which is proportional to the measured force without any alteration such that $\mathbf{F}^{(EM)} = \mathbf{F}^{(MEAS)}$. However, in reality, every sensor obeys a distinct characteristic, which can be described by its transfer function. As a result, the output of the sensor differs with respect to its input. Despite of the academic nature of this problem, analogies can be found in many modern engineering problems where oscillations occur and motion-induced eddy currents, together with the associated forces, are utilized. A typical example are eddy current brakes. Strong magnetic fields are used to generate drag-forces, which act on moving actuators [187, 188]. In the contrary, in magnetic levitation (MAGLEV), one is interested to maximize the lift-to-drag ratio for increased efficiency. This kind of transportation systems avoid ground friction and are able to provide high speed transportation [189]. First reports on this topic can be dated back to Bachelet [45] in 1912. Several analytical approaches considering constant motion, especially in case of high speeds, can be found in the literature [44, 46, 47, 52, 54, 55, 190–192].

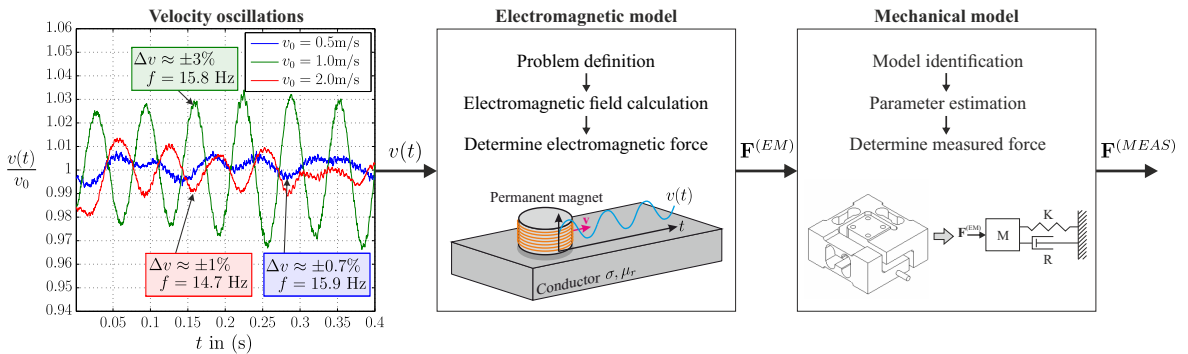


Figure 4.20: Problem under investigation. A permanent magnet moves with a sinusoidal velocity profile relative to a conductive slab. (left) Observed velocity oscillations in the experimental LET setup; (middle) Electromagnetic model including time-dependent velocities; (right) Mechanical model of the force sensor unit altering the electromagnetic input force.

Another area of application is given in the framework of electromagnetic damping [193–195] and electromagnetic coupling [196]. Modern skyscrapers for example include passive structural dampers in the basement to reduce vibrations [197]. Velocity induced eddy currents and Lorentz forces are also used in electromagnetic vibration isolation systems such as gravity compensation devices or suspension systems [198, 199]. Very recent activities can be also found in the framework of energy harvesting, where electromagnetic transducers are used to convert the energy from mechanical vibrations to electric energy [200]. Large scale vibrations occur as a consequence of wind-induced oscillations of civil structures [201]. Linear electromagnetic transducers are either analyzed with simplified analytical approximations neglecting the reactance of the conductor [202] or by means of time-consuming numerical simulations [203]. Together with LET, all these applications have in common that they involve mechanical systems which obey eigenfrequencies and the tendency to oscillate, either intended or parasitic, in form of undesired vibrations of laboratory setups. A typical example of the latter was also observed by Ramos *et al.* [59] in the framework of NDT.

The time-dependent velocity accounts for a more intricate eddy current profile inside the conductor. As a consequence, the problem cannot be treated as stationary or quasi-static anymore. The resistive and inductive nature of the conductor implies a complex interaction between the primary magnetic field generated by the magnetic field source, which oscillates at a given frequency, and the temporally as well as spatially pulsating secondary magnetic field generated by the induced eddy currents. During analytical analysis of oscillating systems, the back reaction of the conductor was merely taken into account [204]. Admittedly, Amati *et al.* [205] addressed the question of sinusoidal speed variations in torsional eddy current dampers but neglected the inductive character of the conductor supported by the assumption of small amplitude oscillations. Considerable studies from Ooi *et al.* [206–210] tackled the analysis of several transient problems using the concept of dynamic circuit theory. The method is based on the evaluation of lumped parameter matrices which are determined by the stored magnetic energy. Besides the good agreement to experimental results, the modeling of source- and induced eddy currents as pure surface currents can be disadvantageous. Recently, Weidemann *et al.* [211] addressed the problem of time-dependent velocities and the associated Lorentz forces in the framework of LFV in 2014. However, they assumed a homogeneous external magnetic field and simplified the problem to the 1-D case. Besides the intelligible and descriptive nature of this study, it is far from a realistic scenario. Its actuality indicates a lack of knowledge in this field and confirms the need for more advanced solutions. In the following, an analytical approach is presented to model this kind of electromagnetic field problems bypassing the mentioned simplifications. The present study is published by the author of this thesis and can be found in [82].

At first, the problem is formulated and the solution of the governing equations is presented in section 4.3.2. The obtained analytical expressions are verified by comparing them to FEM simulations in section 4.3.3. Subsequently, the influence of oscillatory motion on the resulting

Lorentz force is investigated in section 4.3.4. The chapter closes by drawing the conclusions in section 4.3.5.

4.3.2 Mathematical Formulation of the Problem

4.3.2.1 Solution of the Governing Equation

In this section, the solution of the governing equations is presented. A sketch of the investigated problem is given in Fig. 4.21. The computational domain is divided into four sub-domains. Domain I, II and IV are air domains and domain III represents the conductor. The origin of the Cartesian coordinate system is defined at the surface of the conductor. The conducting slab is infinitely extended in the xy -plane but has a finite thickness d . The magnetic field source is modeled by an arrangement of current carrying wires located at a height z' . It moves along the x -axis with a time-dependent velocity $v(t) = v_0 + v_1 \cos(\omega_v t)$. The problem is addressed in rest frame of reference K' , considering that the magnetic field source moves and the conductor is at rest. Hence, motion-induced eddy currents are induced in consequence of a time-dependent magnetic field $\mathbf{B}(t)$. Displacement currents are neglected under the assumption that the velocity is much smaller than the speed of light and that the oscillation frequency is moderate such that $\omega\varepsilon/\sigma \ll 1$. If bodies are accelerated, stresses can arise which could alter the material properties. However, the present analysis is based on the hypothesis that the electrical properties in the instantaneous rest frame K' are unaffected by the acceleration [81]. The negligence of acceleration effects can be motivated by an electron-theoretical viewpoint considering an example of rotary motion. This particular effect was studied by Shiozawa in [212]. It is stated that acceleration effects can be neglected if the angular frequency of the solid body ω_v is much smaller than the angular frequency of the mass m_e and the electron-nucleus spring

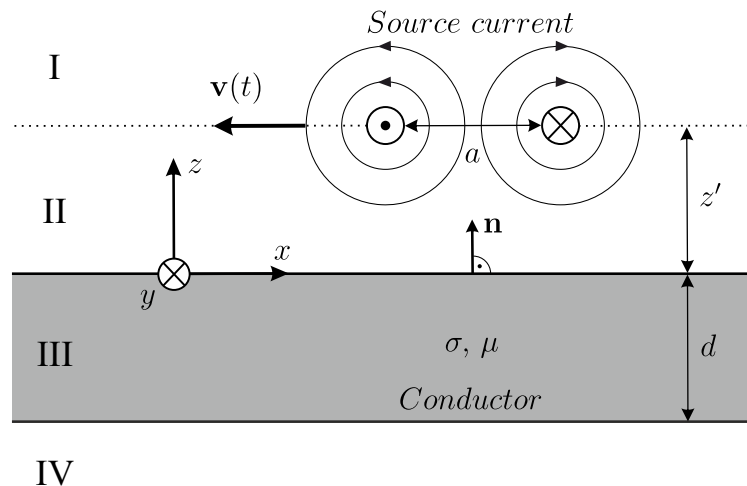


Figure 4.21: Cross section of the problem under investigation. A configuration of current carrying coils is moving over a conducting slab, infinitely extended in the xy -plane but of finite thickness d [82].

ω_0 , which lies in the range of infrared and ultraviolet light. Because moderate velocities are assumed in the present analysis, it is possible to continue with the phenomenological viewpoint, where electromagnetic effects of matter are solely described by the material properties σ , μ , and ε , without taking into account its internal structure. In this sense, the constitutive equations derived in section 3.1 are still valid and hold [213, 214].

In short, the governing equations are derived from Maxwell's equations in the rest frame K' , omitting primed quantities to simplify matters:

$$\nabla \times \mathbf{H} = \mathbf{J} \quad (4.54a)$$

$$\nabla \times \mathbf{E} = -\frac{\partial \mathbf{B}}{\partial t}. \quad (4.54b)$$

The magnetic flux density $\mathbf{B} = \mu \mathbf{H}$ is expressed by the magnetic vector potential \mathbf{A} ($\mathbf{B} = \nabla \times \mathbf{A}$, $\nabla \cdot \mathbf{A} = 0$) under the assumption that the magnetic material is linear and obeys a constant relative permeability μ_r . In the present case, the induced eddy currents are given by $\mathbf{J} = -\sigma(\nabla \phi + \partial \mathbf{A}/\partial t)$. Because the source currents are assumed to flow solely in the xy -plane, the scalar electric potential ϕ is constant and can be omitted in further calculations. Additionally, $A_z = 0$ and the calculations are simplified to the components A_x and A_y . As a result, (4.54a) and (4.54b) can be written as:

$$\frac{\partial^2 A_{x|y}}{\partial x^2} + \frac{\partial^2 A_{x|y}}{\partial y^2} + \frac{\partial^2 A_{x|y}}{\partial z^2} = \mu\sigma \frac{\partial A_{x|y}}{\partial t} \quad (4.55)$$

The variable separation method is applied by taking the Fourier transform of \mathbf{A} with respect to the spatial coordinates x and y as well as with respect to the time t such that $\tilde{\mathbf{A}} = \mathcal{F}_x \mathcal{F}_y \mathcal{F}_t \{\mathbf{A}\}$. In consequence, the problem is described in the aforementioned dimensions by the spatial angular frequencies k_x and k_y and the temporal angular frequency ω . In the following, the x - and y -component of the magnetic vector potential are termed as $\tilde{A}_{x|y}$.

The governing equations in the respective domains are then given by:

$$\frac{\partial^2 \tilde{A}_{x|y}^{\text{I,II,IV}}}{\partial z^2} = k^2 \tilde{A}_{x|y}^{\text{I,II,IV}} \quad (4.56a)$$

$$\frac{\partial^2 \tilde{A}_{x|y}^{\text{III}}}{\partial z^2} = \gamma^2 \tilde{A}_{x|y}^{\text{III}}, \quad (4.56b)$$

with

$$k = \sqrt{k_x^2 + k_y^2} \quad (4.57a)$$

$$\gamma = \sqrt{k_x^2 + k_y^2 + j\omega\mu\sigma}. \quad (4.57b)$$

The corresponding solutions of (4.56a) and (4.56b) are:

$$\tilde{A}_{x|y}^{\text{I,II,IV}} = \tilde{C}_{x|y}^{\text{I,II,IV}} e^{kz} + \tilde{D}_{x|y}^{\text{I,II,IV}} e^{-kz} \quad (4.58a)$$

$$\tilde{A}_{x|y}^{\text{III}} = \tilde{C}_{x|y}^{\text{III}} e^{\gamma z} + \tilde{D}_{x|y}^{\text{III}} e^{-\gamma z}. \quad (4.58b)$$

This results in a total number of 16 constants $\tilde{C}_{x|y}^{I-IV}$ and $\tilde{D}_{x|y}^{I-IV}$, which are determined by means of the underlying boundary conditions.

The magnetic vector potential vanishes at infinity, such that:

$$\tilde{A}_{x|y}^I = 0 \Big|_{z \rightarrow \infty} \quad (4.59a)$$

$$\tilde{A}_{x|y}^{IV} = 0 \Big|_{z \rightarrow -\infty} \quad (4.59b)$$

Hence, $\tilde{C}_{x|y}^I = 0$ and $\tilde{D}_{x|y}^{IV} = 0$.

The normal component of the magnetic flux density $\tilde{\mathbf{B}}$ is continuous across the interfaces such that $\tilde{B}_z^i = \tilde{B}_z^{i+1}$, where $i = \{I, II, III\}$. This condition is fulfilled by ensuring the continuity of $\tilde{A}_{x|y}$ across the interfaces:

$$\tilde{A}_{x|y}^I = \tilde{A}_{x|y}^{II} \Big|_{z=z'} \quad (4.60a)$$

$$\tilde{A}_{x|y}^{II} = \tilde{A}_{x|y}^{III} \Big|_{z=0} \quad (4.60b)$$

$$\tilde{A}_{x|y}^{III} = \tilde{A}_{x|y}^{IV} \Big|_{z=-d} \quad (4.60c)$$

The remaining constants are determined by ensuring the continuity of the tangential component of the magnetic field $\tilde{\mathbf{H}}$ across the interfaces, such that $\tilde{H}_{x|y}^i = \tilde{H}_{x|y}^{i+1}$:

$$\frac{\partial \tilde{A}_{x|y}^{II}}{\partial z} - \frac{\partial \tilde{A}_{x|y}^I}{\partial z} = \mu_0 \tilde{I}_{x|y} \Big|_{z=z'} \quad (4.61a)$$

$$\frac{\partial \tilde{A}_{x|y}^{II}}{\partial z} - \frac{1}{\mu_r} \frac{\partial \tilde{A}_{x|y}^{III}}{\partial z} = 0 \Big|_{z=0} \quad (4.61b)$$

$$\frac{\partial \tilde{A}_{x|y}^{IV}}{\partial z} - \frac{1}{\mu_r} \frac{\partial \tilde{A}_{x|y}^{III}}{\partial z} = 0 \Big|_{z=-d} \quad (4.61c)$$

The function $\tilde{I}_{x|y} = \mathcal{F}_x \mathcal{F}_y \mathcal{F}_t \{I_{x|y}\}$ in (4.61a) is the Fourier transform of the x - and y -component of the oscillating source current above the conductor.

Using the boundary conditions together with the ansatz from (4.58a) and (4.58b), a system of equations (4.62) can be derived to determine the unknown constants. The solutions are given in (4.63a)-(4.63f). The expressions for \tilde{A}_x and \tilde{A}_y are similar, with the only difference regarding the source current \tilde{I}_x and \tilde{I}_y .

$$\begin{bmatrix} e^{-kz'} & -e^{kz'} & -e^{-kz'} & 0 & 0 & 0 \\ e^{-kz'} & e^{kz'} & -e^{-kz'} & 0 & 0 & 0 \\ 0 & 1 & 1 & -1 & -1 & 0 \\ 0 & k & -k & -\gamma\mu_r^{-1} & \gamma\mu_r^{-1} & 0 \\ 0 & 0 & 0 & e^{-\gamma d} & e^{\gamma d} & -e^{-\gamma d} \\ 0 & 0 & 0 & \gamma\mu_r^{-1}e^{-\gamma d} & -\gamma\mu_r^{-1}e^{\gamma d} & -ke^{-kd} \end{bmatrix} \begin{bmatrix} \tilde{D}_{x|y}^I \\ \tilde{C}_{x|y}^{II} \\ \tilde{D}_{x|y}^{II} \\ \tilde{C}_{x|y}^{III} \\ \tilde{D}_{x|y}^{III} \\ \tilde{C}_{x|y}^{IV} \end{bmatrix} = \begin{bmatrix} 0 \\ k^{-1}\mu_0\tilde{I}_{x|y} \\ 0 \\ 0 \\ 0 \\ 0 \end{bmatrix} \quad (4.62)$$

$$\tilde{D}_{x|y}^I = \mu_0 \tilde{I}_{x|y} \frac{\frac{\gamma}{k} \sinh(kz') [k\mu_r + \gamma \tanh(\gamma d)] + \mu_r \cosh(kz') [\gamma + k\mu_r \tanh(\gamma d)]}{(\gamma^2 + k^2 \mu_r^2) \tanh(\gamma d) + 2k\gamma\mu_r} \quad (4.63a)$$

$$\tilde{C}_{x|y}^{II} = \mu_0 \tilde{I}_{x|y} \frac{e^{-kz'}}{2k} \quad (4.63b)$$

$$\tilde{D}_{x|y}^{II} = \mu_0 \tilde{I}_{x|y} \frac{k^2 \mu_r^2 - \gamma^2}{(\gamma^2 + k^2 \mu_r^2) + 2k\gamma\mu_r \tanh^{-1}(\gamma d)} \frac{e^{-kz'}}{2k} \quad (4.63c)$$

$$\tilde{C}_{x|y}^{III} = \mu_0 \tilde{I}_{x|y} \frac{\mu_r(\gamma + k\mu_r)}{(\gamma + k\mu_r)^2 - (\gamma - k\mu_r)^2 e^{-2d\gamma}} e^{-kz'} \quad (4.63d)$$

$$\tilde{D}_{x|y}^{III} = \mu_0 \tilde{I}_{x|y} \frac{\mu_r(\gamma - k\mu_r)}{(\gamma + k\mu_r)^2 e^{2d\gamma} - (\gamma - k\mu_r)^2} e^{-kz'} \quad (4.63e)$$

$$\tilde{C}_{x|y}^{IV} = \mu_0 \tilde{I}_{x|y} \frac{\gamma\mu_r e^{(d-z')k}}{2k\gamma\mu_r \cosh(\gamma d) + (\gamma^2 + k^2 \mu_r^2) \sinh(\gamma d)} \quad (4.63f)$$

4.3.2.2 Fourier Transform of the Source Current

The Fourier transformation with respect to the spatial coordinates x and y as well as the time t of the x - and y -component of the source current is required in order to evaluate the magnetic vector potential. It is assumed that the magnetic field source moves along the negative x -direction with a periodically changing velocity $\mathbf{v} = -v(t)\mathbf{e}_x$. The velocity oscillates with a frequency of $\omega_v = 2\pi f_v$ around a nominal value of v_0 with an amplitude of v_1 :

$$v(t) = v_0 + v_1 \cos(\omega_v t). \quad (4.64)$$

Hence, the time-dependent position of the magnetic field source is given by:

$$\xi(t) = v_0 t + \frac{v_1}{\omega_v} \sin(\omega_v t). \quad (4.65)$$

The ratio v_1/ω_v can be interpreted as a displacement amplitude of the magnetic field source.

In the present context, rectangular and circular coil shapes are considered. In the further course of this work, the planar cases are extended to stacked configurations as they are shown in Fig. 4.22. This is equivalent to the current model of permanent magnets [100]. Hence, cuboidal and cylindrical permanent magnets are included in the present analysis.

Rectangular Current Sources: The x - and y -component of the source current of a rectangular coil in the spatial domain are given by:

$$I_x^{(\text{rect})} = I_s \left[\text{rect}\left(\frac{x - \xi(t)}{a}\right) \delta\left(y + \frac{b}{2}\right) - \text{rect}\left(\frac{x - \xi(t)}{a}\right) \delta\left(y - \frac{b}{2}\right) \right] \quad (4.66a)$$

$$I_y^{(\text{rect})} = I_s \left[\text{rect}\left(\frac{y}{b}\right) \delta\left(x - \frac{a}{2} - \xi(t)\right) - \text{rect}\left(\frac{y}{b}\right) \delta\left(x + \frac{a}{2} - \xi(t)\right) \right], \quad (4.66b)$$

where $\text{rect}(\cdot)$ is the rectangular function, $\delta(\cdot)$ is the Dirac delta distribution, and I_s is the current strength. In the case of permanent magnets, I_s is the outer surface current density in A/m

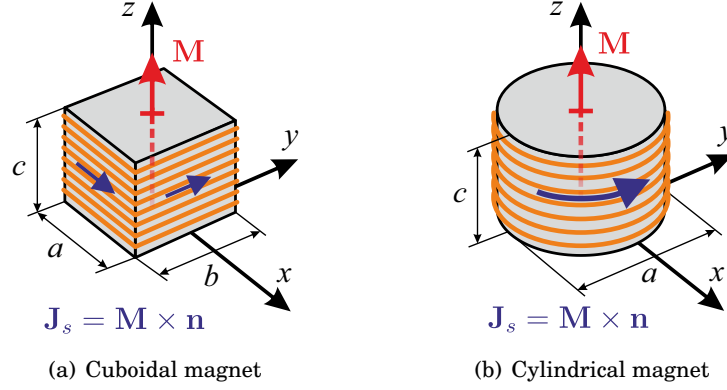


Figure 4.22: Current models used to model permanent magnets [82].

determined by $\mathbf{J}_s = I_s \mathbf{t} = \mathbf{M} \times \mathbf{n}$, where \mathbf{M} is the magnetization, and \mathbf{n} and \mathbf{t} are the unit normal and tangential vectors of the outer surface of the magnet, respectively. Their spatial Fourier transforms with respect to the coordinates x and y are:

$$\mathcal{F}_x \mathcal{F}_y \{I_x^{(\text{rect})}\} = I_s \underbrace{\frac{4j}{k_x} \sin\left(k_x \frac{a}{2}\right) \sin\left(k_y \frac{b}{2}\right)}_{\hat{I}_x^{(\text{rect})}} \bar{f}(t) \quad (4.67a)$$

$$\mathcal{F}_x \mathcal{F}_y \{I_y^{(\text{rect})}\} = -I_s \underbrace{\frac{4j}{k_y} \sin\left(k_x \frac{a}{2}\right) \sin\left(k_y \frac{b}{2}\right)}_{\hat{I}_y^{(\text{rect})}} \bar{f}(t). \quad (4.67b)$$

The terms which solely depend on the spatial frequencies k_x and k_y are indicated by $\hat{I}_{x|y}$ in further calculations. The complex function $\bar{f}(t)$ includes the time-dependency of the vibrating source current. Since the magnetic field source moves as a whole, it does not depend on the explicit geometry of the current carrying wire and can be treated independently. The calculation of the Fourier transform will be treated separately in the further course.

Circular Current Sources: In case of circular coils, the x - and y -component of the source current can be described by:

$$I_x^{(\text{circ})} = -2I_s \frac{y}{a} \delta\left(\sqrt{(x - \xi(t))^2 + y^2} - \frac{a}{2}\right) \quad (4.68a)$$

$$I_y^{(\text{circ})} = 2I_s \frac{x}{a} \delta\left(\sqrt{(x - \xi(t))^2 + y^2} - \frac{a}{2}\right). \quad (4.68b)$$

Their Fourier transforms with respect to x and y are:

$$\mathcal{F}_x \mathcal{F}_y \{I_x^{(\text{circ})}\} = ja\pi I_s \underbrace{\frac{k_y}{k} J_1\left(k \frac{a}{2}\right)}_{\hat{I}_x^{(\text{circ})}} \bar{f}(t) \quad (4.69a)$$

$$\mathcal{F}_x \mathcal{F}_y \{I_y^{(\text{circ})}\} = -j\alpha\pi I_s \underbrace{\frac{k_x}{k} J_1\left(k \frac{a}{2}\right)}_{\tilde{f}_y^{(\text{circ})}} \tilde{f}(t), \quad (4.69b)$$

where $J_1(\cdot)$ is the first order Bessel function of the first kind. The calculation of the Fourier transform is explained in more detail in Appendix A.

Mathematical Modeling of Oscillating Current Sources: The expressions in (4.67a) and (4.67b) as well as in (4.69a) and (4.69b) have to be additionally transformed with respect to the time t . The complex function $\tilde{f}(t)$ results from applying the law of displacement to the $x - \xi(t)$ terms in (4.66a), (4.66b) and (4.68a), (4.68b), and is given by:

$$\tilde{f}(t) = \exp \left[-jk_x \left(v_0 t + \frac{v_1}{\omega_v} \sin(\omega_v t) \right) \right]. \quad (4.70)$$

It is noted, that it contains a harmonic function in the exponent due to the periodically changing velocity. This function bears analogies to phase modulated signals, which are well known in communication engineering [215]. Its Fourier transform is obtained by applying the Jacobi-Anger expansion [184] of the nested harmonics using the following identities:

$$\cos(\alpha \sin(\beta)) = J_0(\alpha) + 2 \sum_{n=1}^{\infty} J_{2n}(\alpha) \cos(2n\beta) \quad (4.71a)$$

$$\sin(\alpha \sin(\beta)) = 2 \sum_{n=1}^{\infty} J_{2n-1}(\alpha) \sin((2n-1)\beta), \quad (4.71b)$$

where $J_n(\cdot)$ are the n -th order Bessel functions. In this sense, $\tilde{f}(t)$ is decomposed to an infinite sum of harmonics:

$$\begin{aligned} \tilde{f}(t) = & \left[\cos(k_x v_0 t) - j \sin(k_x v_0 t) \right] \times \quad (4.72) \\ & \times \left[J_0\left(k_x \frac{v_1}{\omega_v}\right) + 2 \sum_{n=1}^{\infty} J_{2n}\left(k_x \frac{v_1}{\omega_v}\right) \cos(2n\omega_v t) - j J_{2n-1}\left(k_x \frac{v_1}{\omega_v}\right) \sin((2n-1)\omega_v t) \right]. \end{aligned}$$

In consequence, its Fourier transform can be represented by a sum of Dirac delta distributions:

$$\begin{aligned} \mathcal{F}_t \{\tilde{f}(t)\} = & J_0\left(k_x \frac{v_1}{\omega_v}\right) \delta(\omega + k_x v_0) + \quad (4.73) \\ & + \sum_{n=1}^{\infty} (-1)^n J_n\left(k_x \frac{v_1}{\omega_v}\right) \left[\delta(\omega - n\omega_v + k_x v_0) + (-1)^n \delta(\omega + n\omega_v + k_x v_0) \right]. \end{aligned}$$

A graphical representation of the signal in the frequency domain is shown in Fig. 4.23. The main component of the spectrum is determined by the nominal velocity v_0 . However, the oscillatory motion introduces additional side components, displaced by multiples of the oscillation frequency ω_v . Their magnitudes are determined by the corresponding n -th order Bessel functions of the first kind $J_n(\cdot)$. The higher order harmonics vanish if the magnetic field source moves at a constant velocity v_0 with $v_1 = 0$ since $J_n(0) = 0$ for $n > 0$ and $J_0(0) = 1$.

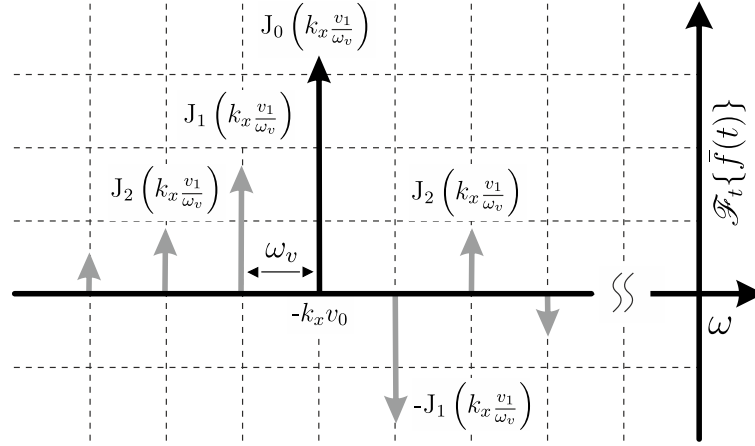


Figure 4.23: Harmonics of Fourier transformed oscillating magnetic field sources [82].

4.3.2.3 Force Calculation

As a result of the harmonic oscillation, the forces which act on the current carrying wires are time-dependent. They can be determined directly in the Fourier domain by applying the theorem of Parseval [216]:

$$\mathbf{F}(t) = \frac{1}{8\pi^3} \int_{-\infty}^{\infty} \int_{-\infty}^{\infty} \int_{-\infty}^{\infty} \tilde{\mathbf{I}}^* \times \tilde{\mathbf{B}}^{I(d)} e^{j\omega t} d\omega dk_x dk_y, \quad (4.74)$$

where $\tilde{\mathbf{I}}$ is the Fourier transformed source current vector and the superscript * indicates complex conjugation. The distorted magnetic flux $\tilde{\mathbf{B}}^{I(d)}$ can be interpreted as the part of the total magnetic field, $\tilde{\mathbf{B}}^I$, in the air domain I, which is affected by the magnetic flux of the induced eddy currents and the magnetic properties of the conductor. The drag-force F_x and the lift-force F_z are then:

$$F_x(t) = \frac{1}{8\pi^3} \int_{-\infty}^{\infty} \int_{-\infty}^{\infty} \int_{-\infty}^{\infty} \tilde{I}_y^* \tilde{B}_z^{I(d)} e^{j\omega t} d\omega dk_x dk_y \quad (4.75a)$$

$$F_z(t) = \frac{1}{8\pi^3} \int_{-\infty}^{\infty} \int_{-\infty}^{\infty} \int_{-\infty}^{\infty} \left(\tilde{I}_x^* \tilde{B}_y^{I(d)} - \tilde{I}_y^* \tilde{B}_x^{I(d)} \right) e^{j\omega t} d\omega dk_x dk_y. \quad (4.75b)$$

The components of $\tilde{\mathbf{B}}^{I(d)}$ can be determined by subtracting the primary field $\tilde{\mathbf{B}}^{I(p)}$, generated by the magnetic field source, from the total field:

$$\tilde{\mathbf{B}}^{I(d)} = \tilde{\mathbf{B}}^I - \tilde{\mathbf{B}}^{I(p)} = \nabla \times \left(\tilde{\mathbf{A}}^I \Big|_{\sigma}^{\mu_r} - \tilde{\mathbf{A}}^I \Big|_{\sigma=0}^{\mu_r=1} \right). \quad (4.76)$$

For $\tilde{B}_x^{I(d)}$, one gets:

$$\tilde{B}_x^{I(d)} = \left(\tilde{D}_y^I - \mu_0 \tilde{I}_y \frac{e^{kz'}}{2k} \right) k e^{-kz}. \quad (4.77)$$

Since the constant \tilde{D}_y^I contains \tilde{I}_y , the following expressions can be simplified by using the identity $\tilde{D}_y^I = \tilde{I}_y \hat{D}^I$:

$$\tilde{B}_x^{I(d)} = k \tilde{I}_y \underbrace{\left(\hat{D}^I - \mu_0 \frac{e^{kz'}}{2k} \right)}_{G(\omega, \mathbf{k}) e^{-kz'}}, \quad (4.78)$$

with $\mathbf{k} = [k_x, k_y]$. The remaining components of the distorted magnetic field can be determined in a similar way:

$$\tilde{B}_x^{I(d)} = k \tilde{I}_y G(\omega, \mathbf{k}) e^{-k(z+z')} \quad (4.79a)$$

$$\tilde{B}_y^{I(d)} = -k \tilde{I}_x G(\omega, \mathbf{k}) e^{-k(z+z')} \quad (4.79b)$$

$$\tilde{B}_z^{I(d)} = j \left(k_y \tilde{I}_x - k_x \tilde{I}_y \right) G(\omega, \mathbf{k}) e^{-k(z+z')}. \quad (4.79c)$$

The function $G(\omega, \mathbf{k})$ contains properties of the conductor such as its thickness, conductivity and relative permeability:

$$G(\omega, \mathbf{k}) = \frac{\mu_0 (e^{2d\gamma} - 1) (k^2 \mu_r^2 - \gamma^2)}{2k [(\gamma + k \mu_r)^2 e^{2d\gamma} - (\gamma - k \mu_r)^2]}. \quad (4.80)$$

The final expression for the drag- and lift-force in case of a single winding can be determined by combining the following expressions in (4.75a) and (4.75b):

- The Fourier transformed source currents, i.e., the functions describing the spatial transformation from (4.67a) and (4.67b) or (4.69a) and (4.69b)
- The transformed time-dependent part of the source currents from (4.73)
- The distorted magnetic field from (4.79a)-(4.79c) at the location $z = z'$ of the current

Additionally, an inverse Fourier transform from frequency to time domain is applied in order to evaluate the waveforms of both force components. As a consequence of the symmetry in the spatial Fourier domain, the integration limits can be changed to 0 and ∞ . Finally, $F_{x|z}(t)$ is then given by:

$$F_{x|z}(t) = \frac{1}{\pi^2} \int_0^\infty \int_0^\infty \mathcal{F}_{x|z}(\mathbf{k}) \mathcal{G}(t, \mathbf{k}) \mathcal{S}_{\omega|m}(\mathbf{k}) \bar{f}(t)^{-1} dk_x dk_y, \quad (4.81)$$

with the auxiliary functions:

$$\mathcal{F}_x(\mathbf{k}) = -j \hat{I}_y^* (k_y \hat{I}_x - k_x \hat{I}_y) \quad (4.82a)$$

$$\mathcal{F}_z(\mathbf{k}) = -k \left(\hat{I}_x^* \hat{I}_x + \hat{I}_y^* \hat{I}_y \right), \quad (4.82b)$$

$$\mathcal{G}(t, \mathbf{k}) = \mathbf{J}_0 \left(k_x \frac{v_1}{\omega_v} \right) \mathbf{G}(-k_x v_0, \mathbf{k}) e^{-j k_x v_0 t} + \sum_{n=1}^N (-1)^n \mathbf{J}_n \left(k_x \frac{v_1}{\omega_v} \right) \times \\ \times \left[\mathbf{G}(-k_x v_0 + n \omega_v, \mathbf{k}) e^{-j(v_0 k_x - n \omega_v) t} + (-1)^n \mathbf{G}(-k_x v_0 - n \omega_v, \mathbf{k}) e^{-j(v_0 k_x + n \omega_v) t} \right], \quad (4.83)$$

$$\mathcal{S}_w(\mathbf{k}) = e^{-2kz'}. \quad (4.84)$$

The functions $\mathcal{S}_x(\mathbf{k})$ and $\mathcal{S}_z(\mathbf{k})$ include information about the shape of the source current in the xy -plane and have to be used depending on the force component to be calculated. They can be determined using (4.67a) and (4.67b) for rectangular current sources or (4.69a) and (4.69b) for circular current sources, respectively. The function $\mathcal{G}(t, \mathbf{k})$ includes the time-dependence of the magnetic field, originating from the oscillating current source. The infinite bandwidth of the function leads to a sum of harmonics with their amplitudes determined by the velocity oscillation amplitude v_1 and the frequencies ω_v and k_x . In numerical calculations, the sum in (4.83) is truncated after N terms. Finally, the function $\mathcal{S}_{w,m}(\mathbf{k})$ includes the height information of the magnetic field source. The index w and m distinguishes between the single wire with $c = 0$ or a magnet of height $c > 0$, respectively.

The solution of a single wire can be extended to permanent magnets by means of the surface current model shown in Fig. 4.22. It is assumed that the permanent magnets have a height of c and their lower surface is located at a lift-off distance h above the plate. The total force is determined by integrating the force on each wire over the z -coordinate, resulting from the superposition of the total distorted magnetic flux density generated from all wires. Hence, (4.81) becomes:

$$F_{x|z}(t) = \frac{1}{\pi^2} \int_{-\infty}^{\infty} \int_{-\infty}^{\infty} \mathcal{S}_{x|z} \mathcal{G}(t, \mathbf{k}) f(t)^{-1} \underbrace{\int_h^{h+c} \int_h^{h+c} e^{-k(z+z')} dz dz'}_{\mathcal{S}_m(\mathbf{k})} dk_x dk_y. \quad (4.85)$$

Carrying out the integration over z and z' yields the expression of the function $\mathcal{S}_m(\mathbf{k})$ valid as long as $c > 0$:

$$\mathcal{S}_m(\mathbf{k}) = \frac{1}{k^2} \left(e^{-kh} - e^{-k(h+c)} \right)^2. \quad (4.86)$$

By inserting (4.86) in (4.81), one gets the final expression for the drag- and lift-force for permanent magnets. In order to evaluate (4.81) at a certain point in time, an adaptive two dimensional numerical integration technique based on a weighted quadrature approach is applied [217, 218].

4.3.3 Comparison to Numerical Simulations

The analytical solution is compared to numerical simulations obtained using the FEM. The numerical simulation of the complete time-dependent 3-D problem is not trivial. Difficulties are

arising in the case of high velocities, when the skin-effect becomes dominant. Hence, the element size has to be reduced, which results in large system matrices. Moreover, the time-step has to be chosen appropriately, depending on the oscillation frequency ω_v , and the conducting slab has to be truncated at a sufficient distance to avoid edge effects. In view of those circumstances, the decision was taken to perform the verification in a simplified 2-D model, which can be solved numerically with a high accuracy and within reasonable time. At first, the numerical model is described, which is followed by the derivation of the analytical solution in 2-D. It is noted that the basic concept of the analytical approach is unaltered by the dimensional reduction and that the solutions of the 2-D and 3-D case are similar.

4.3.3.1 The 2-D Numerical Model

The FEM model is set up using the software environment Comsol Multiphysics [93]. The problem is defined in the same way as in the 3-D case from Fig. 4.21, on the assumption that the setup has an infinite extend along the y -axis. The geometrical parameters of the model are given in Table 4.6. The problem can be completely described by the y -component of the magnetic vector potential A_y . Efficient numerical modeling is realized by changing the frame of reference from the conductor to the magnet. In this way, the time-dependent velocity is modeled by the $\mathbf{v} \times \mathbf{B}$ term rather than the $\partial \mathbf{B} / \partial t$ term used in the analytical approach. In this way, it is possible to use a stationary mesh, avoiding the time consuming re-meshing procedure after every time-step. The governing equation for A_y in the whole computational domain, including the conductor, the magnet, and the surrounding air region, is given by:

$$\sigma \left(\frac{\partial A_y}{\partial t} + v_x \frac{\partial A_y}{\partial x} \right) + \frac{\partial}{\partial x} \left(\frac{1}{\mu} \frac{\partial A_y}{\partial x} \right) + \frac{\partial}{\partial z} \left(\frac{1}{\mu} \frac{\partial A_y}{\partial z} \right) = 0. \quad (4.87)$$

Equation (4.87) is solved by the FEM in the time-domain using a fifth order backward differentiation formula. The time-step is chosen such that every oscillation period contains 100 steps $\Delta t = 1/(100f_v)$.

Table 4.6: Parameters of the exemplary problem used in the analysis of harmonic motion [82].

Parameter	Value	Description
a	15 mm	Length of the magnet
b	15 mm	Width of the magnet
c	25 mm	Height of the magnet
d	50 mm	Thickness of the plate
h	1 mm	Lift-off distance
B_r	1.17 T	Remanence of the magnet (NdFeB-N35)
σ_{Al}	30.66 MSm^{-1}	Electrical conductivity of aluminium
μ_r	1	Relative permeability

4.3.3.2 The 2-D Analytical Model

The evaluation of the 2-D analytical solution follows the same procedure as in the former case. The geometry of the problem is unaltered and already given in Fig. 4.21. The governing equation (4.55) is simplified to determine A_y since $A_x = 0$. As a consequence of the infinite extend in the y -direction, the spatial frequency k_y vanishes, which simplifies the expressions for k and γ from (4.57a) and (4.57b), respectively. Applying the boundary conditions (4.59a)-(4.61c) results in the same coefficients $\tilde{C}^{\text{I-IV}}$ and $\tilde{D}^{\text{I-IV}}$ from (4.63a)-(4.63f) as in the 3-D case.

The major difference between the 2-D and 3-D solution arises considering the source current above the conducting slab, which is now described by:

$$I_y^{(2D)} = I_s \left[\delta \left(x + \frac{a}{2} - \xi(t) \right) - \delta \left(x - \frac{a}{2} - \xi(t) \right) \right]. \quad (4.88)$$

Its Fourier transform with respect to x is:

$$\mathcal{F}_x\{I_y^{(2D)}\} = \underbrace{2jI_s \sin\left(k_x \frac{a}{2}\right)}_{\hat{I}_y^{(2D)}} \bar{f}(t). \quad (4.89)$$

The expressions for the magnetic field can be readily derived from the 3-D case considering $\tilde{I}_x = 0$ and $k_y = 0$ in (4.79a)-(4.79c). The forces are calculated by integrating (4.81), but now only with respect to the spatial frequency k_x . It is noted that the pre-factor of $1/\pi^2$ becomes $1/\pi$ by omitting the integration with respect to k_y . This confirms the analogy between the 2-D and 3-D solution necessary to perform a meaningful verification.

4.3.3.3 Comparison of Analytical and Numerical Results

The verification problem is defined using the parameters from Table 4.6. The rectilinear part of the velocity is $v_0^{(\text{max})} = 14.5$ m/s. The velocity is chosen such that the system operates at the point of maximal drag-force, i.e., in the nonlinear regime. This characteristic velocity will be addressed and explained in more detail in section 4.3.4.1 for the 3-D case. The velocity oscillates at a frequency of $f_v = 100$ Hz considering a rather high oscillation amplitude of $v_1 = 0.5v_0$. The direction of motion is chosen such that the drag-force is positive (see Fig. 4.21). The parameters of the verification are defined to correspond to a numerically challenging benchmark problem. The relative difference between analytical (ANA) and numerical (FEM) results are quantified using the NRMSD over one oscillation period T :

$$\text{NRMSD}_{x|z} = \frac{100\%}{\max\left(F_{x|z}^{\text{FEM}}(t)\right) - \min\left(F_{x|z}^{\text{FEM}}(t)\right)} \sqrt{\frac{1}{T} \int_0^T \left(F_{x|z}^{\text{FEM}}(t) - F_{x|z}^{\text{ANA}}(t)\right)^2 dt}. \quad (4.90)$$

The results obtained by both approaches are shown in Fig. 4.24. They show an almost perfect agreement with an NRMSD of only 0.051% and 0.049% for the drag-force F_x and lift-force F_z , respectively. It can be clearly seen that both force components are delayed and do not follow

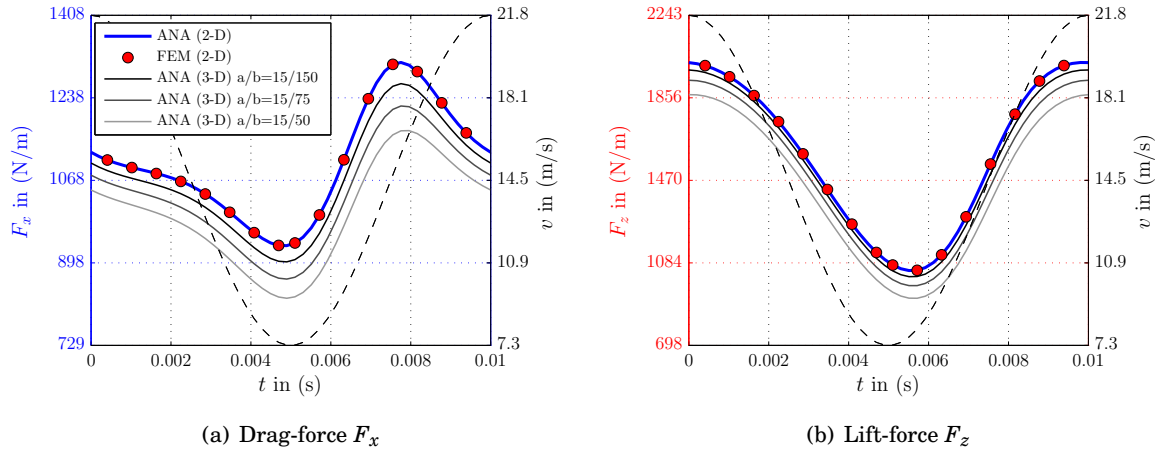


Figure 4.24: Comparison of the time-dependent drag- and lift-force density in (N/m) acting on a moving rectangular magnet evaluated by the analytical and numerical approaches. The dashed line indicates the underlying velocity profile considering a rectilinear velocity, superimposed by an oscillation with a frequency of $f_v = 100$ Hz, and an amplitude of $v_1 = 0.5v_0$. The different 3-D analytical solutions are normalized with respect to the individual y -extensions of the magnet b [82].

the underlying velocity profile. Especially the drag-force is heavily distorted, illustrating the presence of higher order harmonics. A more comprehensive analysis on the amplitude and phase-shift of the Lorentz force will be given in section 4.3.4 for the 3-D case.

If the y -extension of the magnet is sufficiently large compared to the other dimensions, the 3-D problem can be approximated by the 2-D model. Hence, in order to compare the results of the 3-D analytical solution, the force profiles are evaluated for different y -extensions b of the magnet. By normalizing the forces with respect to the individual b values, it is possible to determine the equivalent force densities. The expected convergence towards the 2-D case can be clearly seen in Fig. 4.24, which proves the validity of the 3-D solution.

In order to illustrate the impact of skin-effect and the influence of time-dependent velocity profiles, the induced eddy current density is shown in Fig. 4.25 together with the streamlines of the magnetic flux density. The first illustration in Fig. 4.25(a) exemplifies the situation when the velocity reaches its minimum value of $v(t) = 7.5$ m/s at $t = 5$ ms (see Fig. 4.24). At this stage, field suppression can be already observed. With progression in time, the velocity is rising and the induced eddy current density increases. As a consequence, the secondary magnetic field increases and further expels the primary field out of the conductor. This procedure is harmonically repeating. The time-dependent current density fluctuations generate an also time-dependent magnetic flux density. This in turn leads to the induction of (secondary) induced eddy currents, which counteract the periodic oscillation. This particular effect explains the inductive character of the conductor and the observed phase-shift between the force and the velocity oscillation.

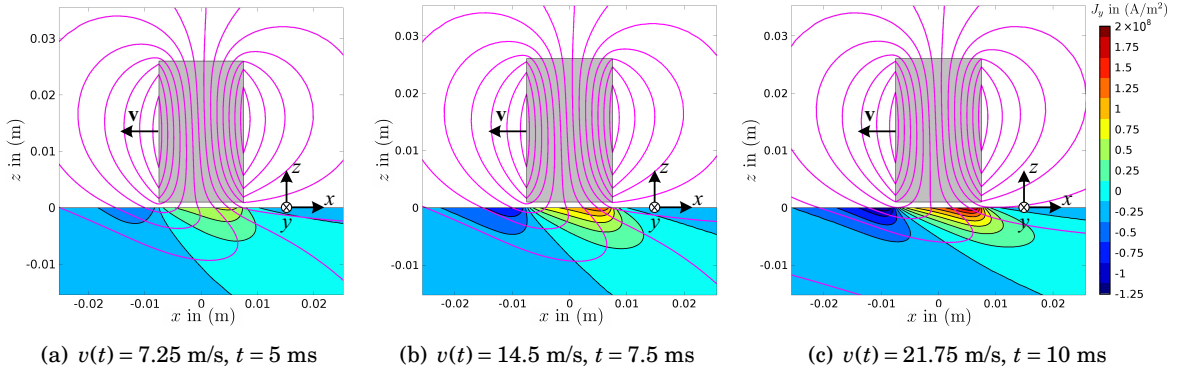


Figure 4.25: Induced eddy current density J_y and streamlines of the total magnetic flux density \mathbf{B} for three different instances, namely at (a) the minimal velocity, (b) the mean velocity, and (c) the maximal velocity [82].

4.3.4 Results and Discussion

As mentioned previously, the parameters influencing the time-dependent force profiles are v_0 , v_1 , and f_v . In this section, the underlying effects are described, differentiating between three different kinds of motion: (i) Constant rectilinear motion without oscillation ($v_0 \neq 0$, $v_1 = 0$) similar to those already reported in the literature [47, 52], (ii) pure harmonic motion ($v_0 = 0$, $v_1 \neq 0$) such that the magnet is vibrating over the conductive slab and (iii), the most complicated case, a mixture of both ($v_0 \neq 0$, $v_1 \neq 0$).

4.3.4.1 Constant Rectilinear Motion

At first, the case of constant rectilinear motion is considered, such that the oscillation amplitude of the velocity is zero ($v_1 = 0$). This case is in analogy to electromagnetic damping or magnetic levitation where the speed is assumed to be constant or slowly varying. The results are obtained considering an axially magnetized cylindrical permanent magnet with a diameter of 15 mm and a height of 25 mm and a cuboidal permanent magnet of size $[a, b, c] = [15, 15, 25]$ mm. The remaining parameters of the magnet and the conducting slab are the same used during the verification and are given in Table 4.6.

The drag- and lift-force as a function of the nominal velocity v_0 is shown in Fig. 4.26. As expected from Lenz's law, the drag-component acts against the direction of motion and the lift-component intends to push the magnet away from the conductor. It can be observed that the cuboidal magnet generates higher Lorentz forces than the cylindrical one. On the one hand, this originates from the difference in magnet volume. On the other hand, it results from the difference in area of the magnet surface close to the specimen. Both are higher in case of the cuboidal magnet. In general, three characteristic velocity regions indicated by ① - ③ can be identified.

Region ① corresponds to the low velocity regime which extends in this particular example

up to 5 m/s. In this regime, diffusion effects dominate over advection phenomena and the resistive nature of the conductor is prevalent. The secondary magnetic field from the induced eddy currents is much weaker than the primary magnetic field from the source ($B^{(s)} \ll B^{(p)}$). Numerical methods dealing with computational expensive problems benefit from this circumstance by simplifying the numerical model (see the e/dWRA in section 3.2). Typical examples can be found in magneto-hydro dynamics [64]. As already observed by Reitz [46] and others, the drag- and lift-force show a linear and quadratic proportionality with respect to the σv product. It can be stated that the reaction from the conductor is low compared to the primary field of the magnetic field source.

In region ②, advection phenomena become more important and inductive effects can be observed. For example, the drag-force generated by the cylindrical permanent magnet reaches its maximum at a velocity of $v_0^{(\max)} = 29.8$ m/s, which is higher compared to the 2-D case, where the maximum was already reached at 14.5 m/s (see section 4.3.3.3). This can be explained by emerging edge effects originating from the finite y -extension of the magnet. In contrast to the drag-force, the lift-force behaves different and starts to saturate.

Finally, regime ③ is characterized by the precedence of advection phenomena. The secondary magnetic field, generated by the induced eddy currents, is as strong as the primary field inside the conductor. Hence, the effect of field suppression is distinctive and cannot be neglected. As a consequence, Joule losses, which are directly proportional to the drag-force, decrease while the lift-force continues to saturate.

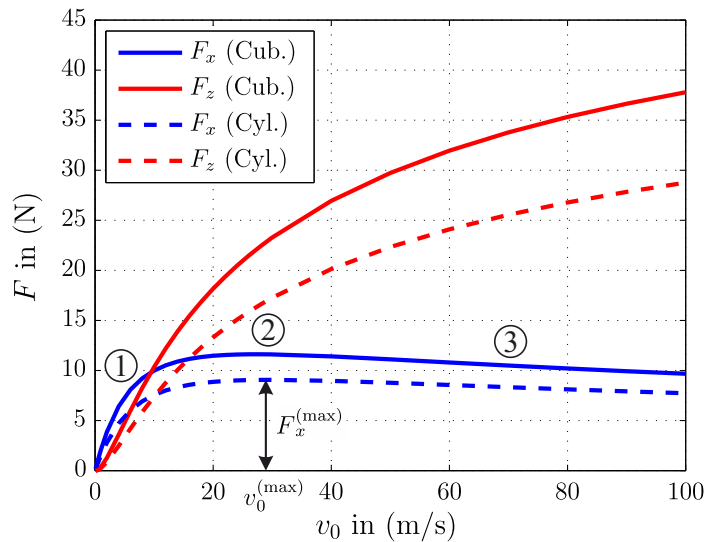


Figure 4.26: Stationary drag- (F_x) and lift-force (F_z) acting on a moving cuboidal or cylindrical permanent magnet as a function of constant velocity v_0 for three characteristic regions without oscillations ($v_1 = 0$) [82].

4.3.4.2 Harmonic Motion

In the following, the force on a periodically oscillating cylindrical permanent magnet is investigated. This case corresponds to the damping mode in electromagnetic damping. The same geometrical parameters as in the previous section are used for the calculations. It is assumed that the magnet moves with a nominal velocity of $v_0 = 0$ but oscillates with a frequency of $f_v = 100$ Hz. The oscillation amplitude is varied between $v_1 = 0.1 \dots 0.5$ m/s, which is typical for a shock absorber [201].

The drag- and lift-force over one period are shown in Fig. 4.27(a) and (b), respectively. The dashed line indicates the normalized velocity profile for the purpose of illustration. As expected, it can be observed that the drag-force changes the direction with respect to the underlying velocity. In contrast, the lift-force stays positive over the whole period, resulting in a doubled frequency. When the oscillation amplitude v_1 increases, the lift-force does not become zero at the reversal point. However, if only the maxima are considered, the linear and quadratic behavior of both components can still be observed in this velocity regime. A clear phase shift between the velocity profile and the forces is visible, resulting from the inductive nature of the conductor, which nicely illustrates Lenz's law of induction. It is observed that the lift-force is influenced slightly more by this effect than the drag-force.

4.3.4.3 Constant Rectilinear Motion Superimposed by Harmonic Oscillations

The present study is extended to the case of mixed motion. In analogy to electromagnetic damping, this corresponds to the coupler operation. In this sense, the cylindrical permanent magnet moves rectilinear with a constant velocity v_0 superimposed by an oscillation of $v_1 \cos(\omega_v t)$. The forces are calculated as a function of the oscillation frequency f_v and the nominal velocity v_0 .

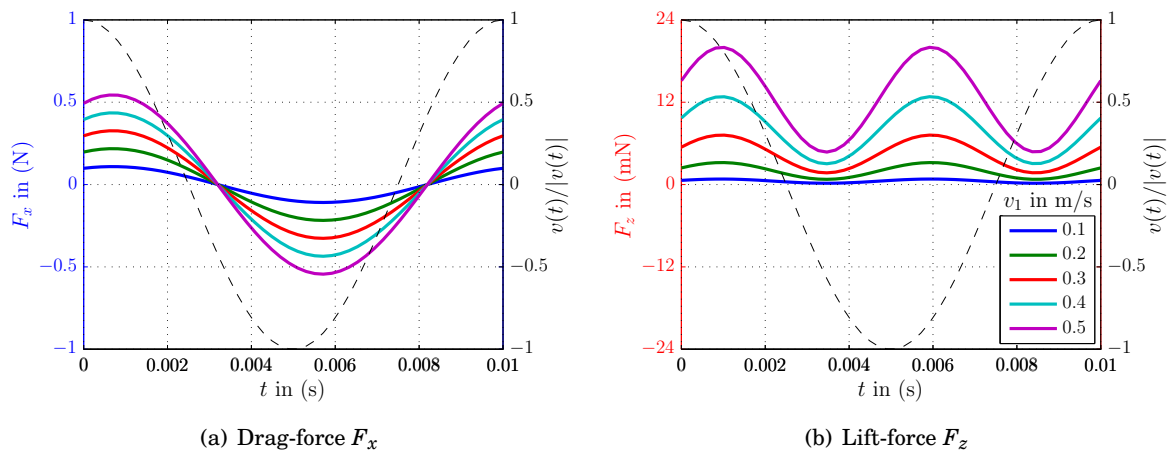


Figure 4.27: Time-dependent drag- and lift-force acting on a cylindrical permanent magnet purely harmonically oscillating ($v_0 = 0$) with a frequency of $f_v = 100$ Hz for different oscillation amplitudes v_1 . The dashed line indicates the normalized velocity profile [82].

The oscillation amplitude v_1 is chosen to be 3% of v_0 such that $v_1/v_0 = 0.03$. In this regard, it corresponds to the observations from the laboratory LET setup shown in Fig. 4.20 on page 89.

At very low frequencies, i.e. $f_v < 10$ Hz, it is observed that a high approximation order of around $N = 200$ in (4.83) is needed in order to evaluate a converged solution of (4.81). Lower approximation orders lead to noisy signals in the frequency domain which complicated the numerical integration. In order to provide compact information about the magnitude of the time-dependent forces, the relative oscillation amplitude $\Delta F_{x|z}^{(\text{rel})}$ with respect to the stationary force $F_{x|z}^{(0)}$, without any oscillation ($v_1 = 0$), is calculated as:

$$\Delta F_{x|z}^{(\text{rel})} = \frac{\max(F_{x|z}(t)) - \min(F_{x|z}(t))}{F_{x|z}^{(0)}} 100\%. \quad (4.91)$$

It provides a relative measure of the force perturbation at a given working point. The corresponding results for the cylindrical permanent magnet, analyzed in the previous section, are shown in Fig. 4.28(a) and (b) for the drag- and lift-component of the Lorentz force, respectively. It can be observed that both components show diverse characteristics. The highest relative oscillation amplitude of the drag-force can be observed at low frequencies and when the system operates at low velocities, i.e., in the linear regime (see ① in Fig. 4.28(a)). As expected from the linear relationship between the velocity and the drag-force, slow velocity oscillations are directly projected onto the drag-force, i.e., oscillations of about $v_1/v_0 = 0.03$ result in relative force perturbations of $\Delta F_x^{(\text{rel})} \approx 6\%$. The force oscillations are damped by the secondary magnetic field of the induced eddy currents when the frequency of the velocity oscillation increases. In this sense, the conductor acts like a nonlinear inductance and similarities to a low pass filter can be observed. In consequence, high-frequency oscillations are weakly projected onto the Lorentz force. On the other hand, the relative oscillation amplitudes of both forces also decrease, when increasing the nominal velocity v_0 . A local minimum can be observed in region ② in Fig. 4.28(a), where the drag-force reaches its maximum at $v_0^{(\text{max})} = 29.8$ m/s (see ② in Fig. 4.28(a)). Reason for this effect is the small gradient of the drag-force with respect to the velocity in this region. However, with increasing frequency, the oscillation amplitude increases before high-frequency damping effects become inherent. This can be explained by the time-dependent secondary induced eddy currents, emerging from the oscillating velocity.

The relative oscillation amplitude of the lift-force is shown in Fig. 4.28(b). Compared to the drag-force, similar characteristics regarding the oscillation frequency f_v can be observed. However, its quadratic behavior at low velocities leads to relative force oscillation amplitudes of $\Delta F_z^{(\text{rel})} > 11\%$. In contrast to the drag-force, no local minimum can be observed at $v_0^{(\text{max})} = 29.8$ m/s, resulting from its overall monotonic increasing nature.

The above observations are further illustrated by showing the waveforms of the forces for distinct parameter combinations, which are marked by crosses in Fig. 4.28. The chosen nominal velocities are $v_0 = \{0.5, 29.8, 100\}$ m/s, which correspond to the three velocity regions ① - ③ described previously. The results are presented considering velocity oscillation frequencies of $f_v = \{10, 100\}$ Hz. The forces are calculated over one period, and are shown in Fig. 4.29.

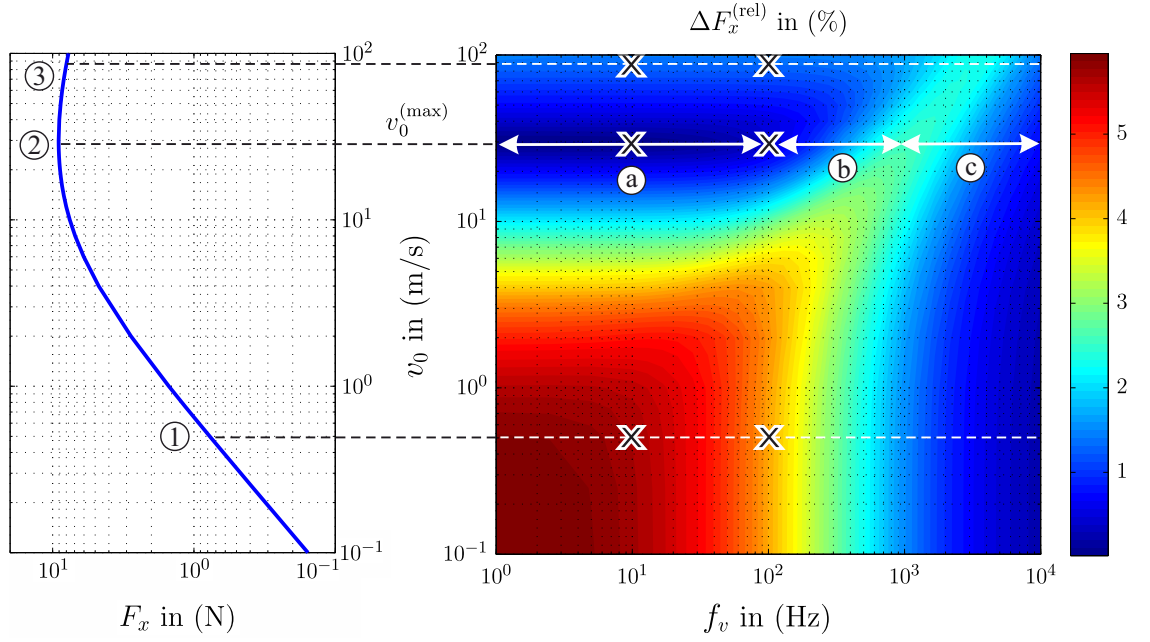
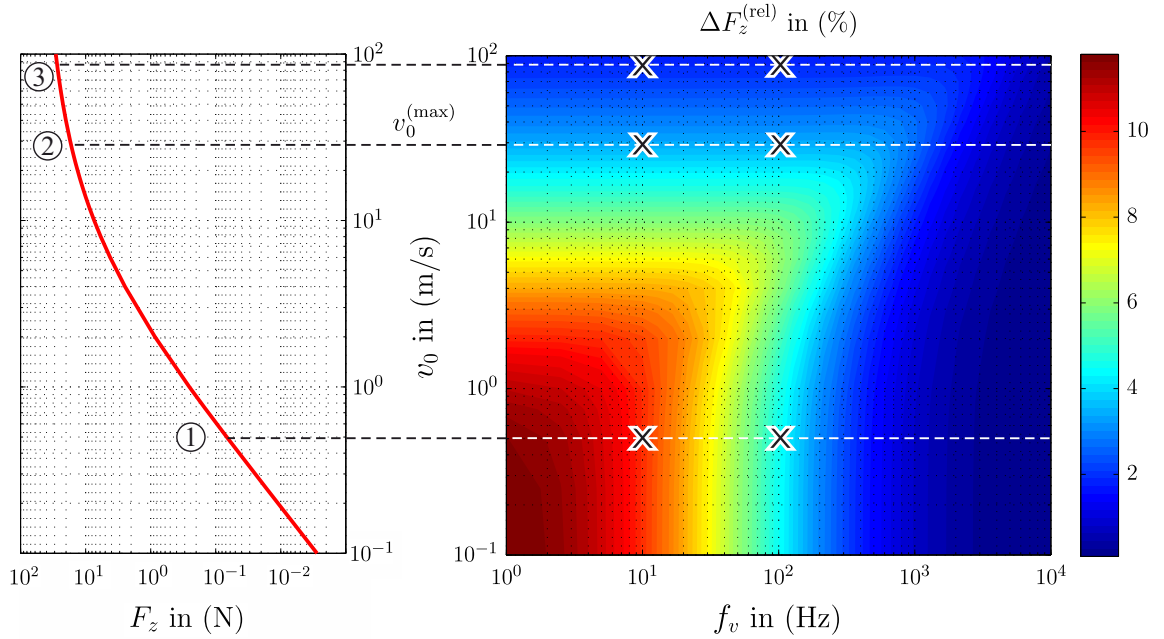

 (a) Relative force perturbation of the drag-force $\Delta F_x^{(\text{rel})}$.

 (b) Relative force perturbation of the lift-force $\Delta F_z^{(\text{rel})}$.

Figure 4.28: Relative force perturbations defined by (4.91) as a function of the oscillation frequency f_v and the nominal velocity v_0 . The plots on the left correspond to the forces for constant rectilinear motion in logarithmic scale (see Fig. 4.26). All calculations are performed with a cylindrical magnet considering a velocity oscillation amplitude of $v_1/v_0 = 0.03$. The markers indicate the parameters used in the calculations shown in Fig. 4.29 [82].

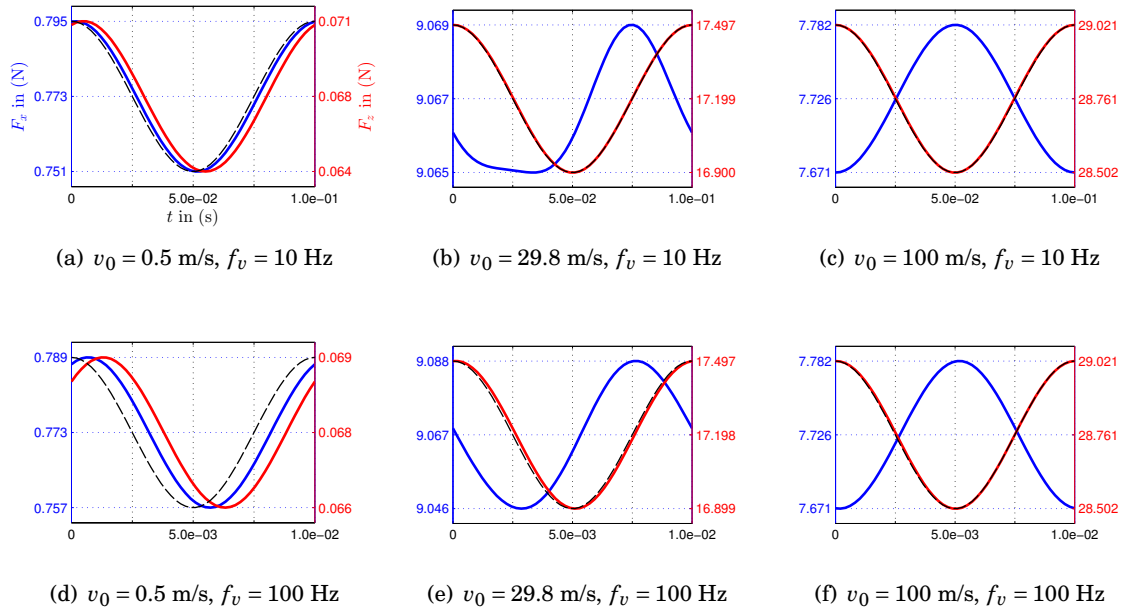


Figure 4.29: Time-dependent drag- and lift-force waveforms in case of (a) and (d) low velocities ($v_0 = 0.5$ m/s), (b) and (e) moderate velocities ($v_0 = 29.8$ m/s) and (c) and (f) high velocities ($v_0 = 100$ m/s), considering a relative velocity oscillation amplitude of $v_1/v_0 = 0.03$. The top row corresponds to an oscillation frequency of $f_v = 10$ Hz and the bottom row to $f_v = 100$ Hz. The results correspond to the working points marked with crosses in Fig. 4.28. The blue and red lines correspond to the drag- and lift-force, respectively. The dotted line indicates the principal velocity profile of the permanent magnet for visual orientation [82].

The force profiles of $v_0 = 0.5$ m/s and $f_v = 10$ Hz are shown in Fig. 4.29(a). Both force components are oscillating almost in phase with respect to the velocity. Due to the low oscillation amplitude of $v_1/v_0 = 0.03$, the quadratic behavior of the stationary lift-force in this regime is weakly projected to the oscillating case. In Fig. 4.29(b), the velocity is increased up to the turning point of the drag-force ($v_0^{(\max)} = 29.8$ m/s). The perturbed waveform indicates the superposition of multiple harmonics. As shown before, the oscillation amplitude of the drag-force is very small in this region. Finally, the case of $v_0 = 100$ m/s is shown in Fig. 4.29(c). It can be observed that the waveform of the drag-force is inverted with respect to the velocity as a result of its degressive proportionality and the regressive characteristic in this regime (see ③ in Fig. 4.28(a)).

The bottom row of Fig. 4.29 shows both forces considering a velocity frequency of $f_v = 100$ Hz. At higher frequencies, inductive effects become prevalent and the phase shift between the forces and the velocity increases. Concomitant with the observations from Fig. 4.27, it can be seen that the drag- and lift-forces do not obey the same delay. The effect of magnetic inertia is well exemplified by comparing the drag-forces between Fig. 4.29(b) and (e). In a figurative sense, the drag-force is not able to follow the nonlinear profile anymore. Hence, higher order harmonics are damped and the number of effective harmonics is reduced. Formally, this can be explained by the fact that ω_v is in the denominator of the argument of the higher order Bessel functions

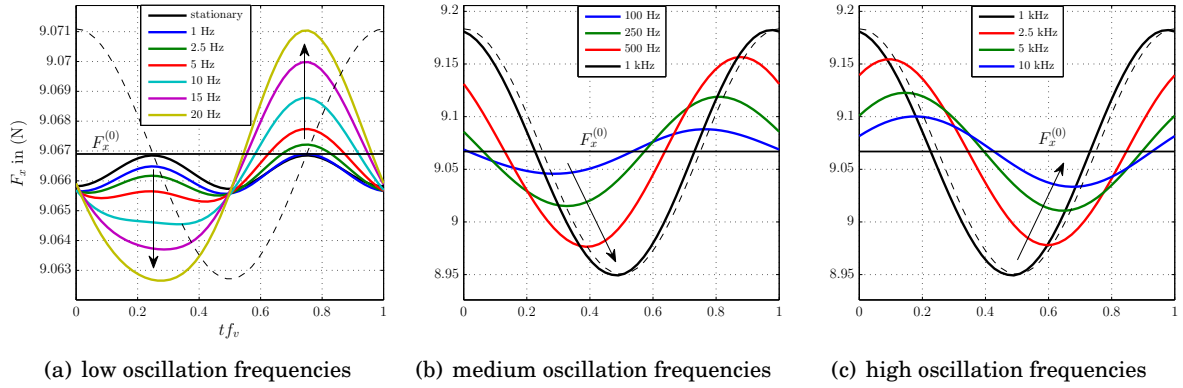


Figure 4.30: Time-dependent drag-force at the nominal velocity of $v_0^{(\max)} = 29.8$ m/s for different velocity oscillation frequencies f_v , considering an oscillation amplitude of $v_1/v_0 = 0.03$. The dashed line indicates the underlying velocity profile of the cylindrical permanent magnet; (a)-(c) correspond to the highlighted regions in Fig. 4.28 [82].

in (4.83). As a consequence, the nonlinearities are linearized and (4.83) can be truncated after a few terms, e.g. $N = 10$. Considering the lift-force at $f_v = 100$ Hz for different values of v_0 , it can be seen that the phase delay decreases when the nominal velocity v_0 increases.

The behavior of the time-dependent drag-force in the nonlinear region ② around the point of maximal drag-force is further illustrated in Fig. 4.30. The results correspond to the highlighted intervals in Fig. 4.28(a). The abscissae in Fig. 4.30 are normalized with respect to f_v to compare the different waveforms to each other. It can be seen that the explicit waveform strongly depends on the velocity oscillation frequency f_v . Fig. 4.30(a) illustrates the non-harmonic character of the drag-force in the low frequency regime. The time-dependent results are compared to the stationary case obtained by sampling the force-velocity-curve from Fig. 4.26 according to the harmonic oscillation. The stationary maximum $F_x^{(0)}$ is indicated by the horizontal solid line. It can be observed that the amplitude of the drag-force increases with increasing frequency and even exceeds the maximum from the stationary study in the second half of the period.

Fig. 4.30(b) shows the drag-force for frequencies up to 1 kHz. It can be seen, that the force perturbation amplitude continuously increases together with the phase-shift. At $f_v = 1$ kHz, the time-dependent drag-force has its maximum and exceeds $F_x^{(0)}$ by up to 1.3%. The waveforms for frequencies up to 10 kHz are shown in Fig. 4.30(c). It can be observed that the low-pass character of the conductor becomes predominant and the amplitudes decrease, while the phase-shift still increases. The present study demonstrates the complexity of the problem and underlines the necessity to consider the reactance of the conductor in the case of time-dependent velocity profiles.

4.3.5 Conclusions

Vibrations play a major role in laboratory setups or electromagnetic dampers. The present study shows that the force profiles strongly depend on the operating point of the system under investigation, which is determined by the level of constant motion together with the oscillation amplitude and frequency. The complex interaction between induced eddy currents, resulting from the constant part and the time-dependent part of the velocity is exemplified. The back reaction of the conductor and its reactance cause phase shifts and lower damping forces. This should be taken into account when evaluating the dynamic characteristics of oscillating systems in the future. Due to the nonlinear characteristic of the drag-force as a function of velocity v_0 , higher order harmonics are emerging in the oscillatory case.

In contrast, the gradual nature of the lift-force mitigates this effect. It seems inherent that these effects should be considered in future developments of new systems involving time-dependent motion in order to provide more accurate predictions. Current research for example is devoted to apply ball screw mechanisms to energy harvesters which can significantly magnify the vibrational motion [198] and in turn increase the performance of such devices.

The analytical integral expressions can be easily modified according to different coil geometries by replacing the corresponding Fourier transforms of the source current in (4.82a) and (4.82b), respectively. The presented approach to model the time-dependent velocity term by means of the Jacobi-Anger expansion could be adopted to other application scenarios as for example to analyze the dynamics of linear or rotating eddy current couplers [219] or MAGLEV systems. Moreover, the presented approach can be used as a reference during the development of more advanced numerical models.

The phase and amplitude of the drag- and lift-force provide information about the material properties of the conductor. Oscillating magnet systems could be applied in the future within the context of NDT as an alternative to systems which are based on constant rectilinear motion. By this analysis, it is possible to provide the required electromagnetic force $\mathbf{F}^{(EM)}$, acting on a mechanical system to determine the measured force $\mathbf{F}^{(MEAS)}$ (see Fig. 4.20 on page 89). Future investigations could proceed further to construct a mechanical model of the force sensor and to couple into the electromagnetic force, provided in the present study.

ALTERNATIVE LET SYSTEM USING A RING MAGNET

In this chapter, a new type of LET system is presented. It consists of a ring magnet which encompasses the object under test. The boundary value problem is solved using the variable separation method and the Fourier transformation while considering the interaction between the magnetic field of the ring magnet and the induced eddy currents. The Lorentz force and the induced eddy current density is evaluated in integral form including modified Bessel functions of the first and second kind. The famous creeping magnet problem, where a magnet travels inside a conducting pipe, is extended to ring magnets. Finally, the ring magnet is combined with the proposed HCp-magnet system, which forms the basis for a novel generation of LET systems.

5.1 Introduction and Motivation

The previously investigated LET systems made use of sensor systems, which locally induced a distinct eddy current profile. Thus, an exhaustive test of the whole object requires sophisticated scanning procedures. This considerably increases the inspection time and could be disadvantageous during production processes. One possible solution is the application of a magnet system, which encompasses the whole object under test as it is shown in Fig. 5.1. In this way, a homogeneous eddy current distribution is induced, which spins around the circumference of the conductor. Such a system could be applied to monitor the material characteristics of pre-products in rolling mills or during casting processes. Other fields of application include the contactless inspection of wires, pipes, tube welding lines or valve springs, which must obey high standards. All these examples entail moving objects, which predestines the application of MECT techniques such as LET. This kind of ring magnet can be also applied in the framework of Lorentz force velocimetry (LFV) [64, 220] to determine the flow rate of moving media. Similar

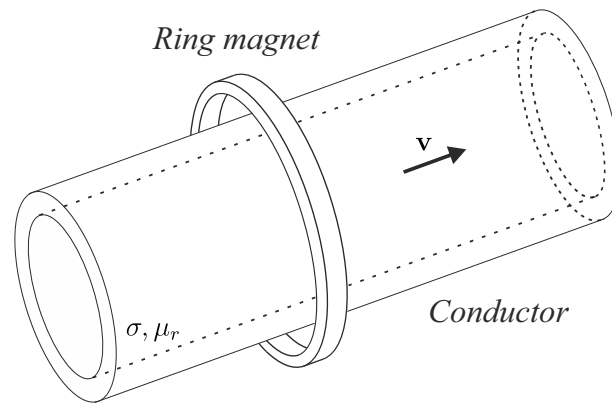


Figure 5.1: A ferromagnetic electrical conductor is moving with a constant rectilinear velocity through a ring magnet [236].

configurations are reported in the framework of time-of-flight LFV [221] and electromagnetic LFV [222], where the problem of a cylindrical conductor surrounded by a single wire is addressed under the assumption of low magnetic Reynolds numbers. A very similar problem is addressed in [223] considering solid rods, taking into account secondary magnetic fields.

In this chapter, the electromagnetic field problem of motion-induced eddy currents is further studied and extended to the case of permanent magnets with different magnetization directions moving along solid rods and pipes. A mathematical model is described to determine the unperturbed stationary forces. In this context, the famous creeping magnet experiment, where a permanent magnet is slowly falling down a conducting pipe, is extended to ring magnets. Because of its ease and inexpensive realization, it is a great illustration of Faraday's law for undergraduate students. Previous studies only treated falling magnets inside the pipe. They either neglected self inductance effects of the conductor [68, 69, 224–229] or included the back reaction resulting from the induced eddy currents [101, 230, 231]. Besides the impressing presentation of Faraday's law, the disadvantage of the original experiment is that the magnet is hidden inside the conducting pipe.

The calculation of the magnetic field of an axial or radial magnetized ring includes non-trivial analysis including elliptical integrals [114, 232–235]. In this thesis, the boundary value problem is solved for non-relativistic speeds such that the velocity is much smaller than the speed of light ($|\mathbf{v}| \ll c$). The Lorentz force acting on the ring magnet is determined for both magnetization directions of the magnet. The results are compared to numerical simulations using the FEM. Self-inductance effects are taken into account such that the magnetic field of the induced eddy currents interacts with the primary magnetic field of the ring magnet. The effect of field suppression at high velocities is illustrated by calculations of the induced eddy current density inside a conducting pipe of finite thickness at both low and high velocities.

At first, the mathematical formulation of the problem is given in section 5.2. It includes the solution of the boundary value problem of a single current carrying wire. The solution

is extended to axially and radially magnetized ring magnets. Moreover, the creeping magnet problem and the finite element model are described. The results part in section 5.3 contains studies on the electromagnetic fields as well as on the Lorentz forces in case of different velocities, permeabilities, and wall thicknesses of the conducting pipe. The conclusions of this study are given in section 5.4. The obtained results are published by the author and can be found in [236]. At the end of this chapter, in section 5.5, the patented concept of an alternative LET system is presented. It summarizes the gained knowledge from the individual simulation studies presented in this thesis into one system and is a key result of this work.

5.2 Mathematical Formulation of the Problem

5.2.1 Single Wire Model

In order to determine general expressions for the magnetic field, the problem of a single wire wound around a tubular conductor is considered first. The underlying geometry of the problem is shown in Fig. 5.2. The symmetry allows to describe the problem using cylindrical coordinates. In contrast to the study of harmonic oscillations from section 4.3, the present problem is addressed in the laboratory frame of reference K , which is associated to the magnetic field source (see section 3.1). Assuming non-relativistic velocities such that $|\mathbf{v}| \ll c$, the governing equations are given in (3.9a)-(3.9e) on page 22. As long as the velocity and the cross section of the conductor do not change over time, the problem can be treated as quasi-stationary such that $\partial \mathbf{B} / \partial t = \mathbf{0}$. As in the previous analysis, the calculations can be simplified by expressing the magnetic flux density \mathbf{B} in terms of the magnetic vector potential \mathbf{A} . In the present analysis, only linear ferromagnetic

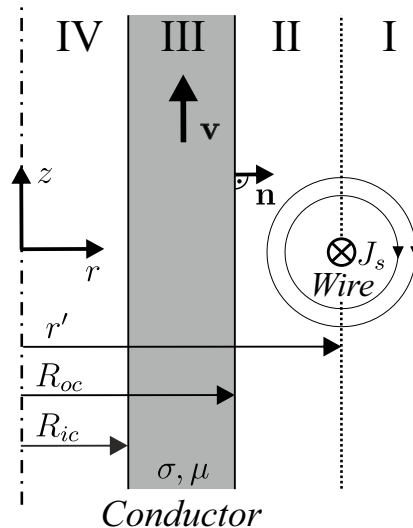


Figure 5.2: Symmetry-plane of the problem under investigation divided into four computational domains [236].

materials are considered such that $\mu = \mu_0 \mu_r$. The governing equation is then given by:

$$\nabla \times \left(\frac{1}{\mu} \nabla \times \mathbf{A} \right) = \sigma (-\nabla \phi + \mathbf{v} \times \nabla \times \mathbf{A}) + \mathbf{J}_e. \quad (5.1)$$

In the present case, the external source current density \mathbf{J}_e , i.e. the wire in Fig. 5.2, can be described by:

$$\mathbf{J}_e = \mathbf{J}_s \delta(r - r') = J_s(z) \delta(r - r') \mathbf{e}_\varphi, \quad (5.2)$$

where \mathbf{J}_s is the source surface current density and $\delta(\cdot)$ is the Dirac delta function (see Fig. 5.2). Because the source current flows only on the boundary, it can directly be incorporated in the boundary conditions between domain I and II, and omitted in the field equations in a similar way as it has been done in the previous analysis. Since the source current flows only in the azimuthal direction, the magnetic vector potential \mathbf{A} has only an azimuthal component A_φ and (5.1) can be written as:

$$\nabla \times \left(\frac{1}{\mu} \nabla \times \mathbf{A} \right) - \sigma \left(-\nabla \phi - \begin{bmatrix} 0 \\ v_z \frac{\partial A_\varphi}{\partial z} \\ 0 \end{bmatrix} \right) = \mathbf{0}. \quad (5.3)$$

As a result of the cylindrical symmetry of the problem, the scalar electric potential ϕ is constant and its gradient can be omitted in further calculations. Finally, by expressing the double curl operator from (5.3) in the cylindrical coordinate system, one gets:

$$\frac{\partial^2 A_\varphi}{\partial r^2} + \frac{1}{r} \frac{\partial A_\varphi}{\partial r} - \frac{A_\varphi}{r^2} + \frac{\partial^2 A_\varphi}{\partial z^2} - \mu \sigma v_z \frac{\partial A_\varphi}{\partial z} = 0. \quad (5.4)$$

By applying the Fourier transform to the magnetic vector potential in the axial direction:

$$\mathcal{F}_z\{A_\varphi\} = \tilde{A}_\varphi = \int_{-\infty}^{\infty} A_\varphi e^{-jkz} dz, \quad (5.5)$$

the governing equation (5.4) can be written as:

$$\frac{\partial^2 \tilde{A}_\varphi}{\partial r^2} + \frac{1}{r} \frac{\partial \tilde{A}_\varphi}{\partial r} - \frac{\tilde{A}_\varphi}{r^2} - k^2 \tilde{A}_\varphi - jk \mu \sigma v_z \tilde{A}_\varphi = 0. \quad (5.6)$$

In order to determine \tilde{A}_φ , the computational domain is divided into four sub-domains, as shown in Fig. 5.2. The inner and outer radius of the conductor are denoted as R_{ic} and R_{oc} , respectively. The current carrying wire is located at the radius r' . Domains I, II and IV are air domains, whereas domain III includes the moving ferromagnetic conductor. Hence, the following modified Bessel equations describe the magnetic vector potential in the specific domains:

$$\frac{d^2 \tilde{A}_\varphi^{I,II,IV}}{dr^2} + \frac{1}{r} \frac{d \tilde{A}_\varphi^{I,II,IV}}{dr} - \left(k^2 + \frac{1}{r^2} \right) \tilde{A}_\varphi^{I,II,IV} = 0 \quad (5.7a)$$

$$\frac{d^2 \tilde{A}_\varphi^{III}}{dr^2} + \frac{1}{r} \frac{d \tilde{A}_\varphi^{III}}{dr} - \left(k^2 + j \mu \sigma v_z k + \frac{1}{r^2} \right) \tilde{A}_\varphi^{III} = 0. \quad (5.7b)$$

The corresponding solutions are given by first order modified Bessel functions of the first and second kinds $I_1(kr)$ and $K_1(kr)$, respectively [237]:

$$\tilde{A}_\varphi^{I,II,IV}(r,k) = \tilde{C}^{I,II,IV} I_1(kr) + \tilde{D}^{I,II,IV} K_1(kr) \quad (5.8a)$$

$$\tilde{A}_\varphi^{III}(r,k) = \tilde{C}^{III} I_1(k'r) + \tilde{D}^{III} K_1(k'r), \quad (5.8b)$$

with $k' = \sqrt{k^2 + j\lambda k}$ and $\lambda = \mu_0 \mu_r \sigma v_z$. The complex constants \tilde{C}^I to \tilde{C}^{IV} and \tilde{D}^I to \tilde{D}^{IV} can be determined from the imposed boundary conditions:

$$\tilde{A}_\varphi^I = 0 \Big|_{r \rightarrow \infty} \quad (5.9a)$$

$$\tilde{A}_\varphi^{IV} = 0 \Big|_{r=0} \quad (5.9b)$$

$$\tilde{A}_\varphi^I = \tilde{A}_\varphi^{II} \Big|_{r=r'} \quad (5.9c)$$

$$\tilde{A}_\varphi^{II} = \tilde{A}_\varphi^{III} \Big|_{r=R_{oc}} \quad (5.9d)$$

$$\tilde{A}_\varphi^{III} = \tilde{A}_\varphi^{IV} \Big|_{r=R_{ic}} \quad (5.9e)$$

$$\frac{1}{\mu_r} \frac{\partial}{\partial r} (r \tilde{A}_\varphi^{III}) = \frac{\partial}{\partial r} (r \tilde{A}_\varphi^{II}) \Big|_{r=R_{oc}} \quad (5.9f)$$

$$\frac{1}{\mu_r} \frac{\partial}{\partial r} (r \tilde{A}_\varphi^{III}) = \frac{\partial}{\partial r} (r \tilde{A}_\varphi^{IV}) \Big|_{r=R_{ic}} \quad (5.9g)$$

$$\frac{1}{r} \frac{\partial}{\partial r} (r \tilde{A}_\varphi^{II} - r \tilde{A}_\varphi^I) = \mu_0 \tilde{J}_s(k) \Big|_{r=r'}. \quad (5.9h)$$

The boundary conditions (5.9a) and (5.9b) imply that the radial component of the magnetic field vanishes at the cylinder axis and at infinity. As a consequence of the asymptotic behavior of the modified Bessel functions, such that K_1 is singular at $r = 0$ and I_1 diverges exponentially as $r \rightarrow \infty$, the constants $\tilde{C}^I = \tilde{D}^{IV} = 0$ can be readily determined. Equations (5.9c)-(5.9e) ensure the continuity of the normal component of the magnetic flux density at the domain interfaces. Moreover, (5.9f)-(5.9h) result from the continuity of the tangential component of the magnetic field, where \tilde{J}_s denotes the Fourier transform of the source current density at the interface between domain I and II. The source current is now designated with the letter J to avoid confusion with the modified Bessel function of the first kind I_1 .

Substituting (5.8a) and (5.8b) into the boundary conditions results into the following linear system of equations for the unknown constants:

$$\begin{bmatrix} K_1(kr') & -I_1(kr') & -K_1(kr') & 0 & 0 & 0 \\ K_0(kr') & I_0(kr') & -K_0(kr') & 0 & 0 & 0 \\ 0 & I_1(kR_{oc}) & K_1(kR_{oc}) & -I_1(k'R_{oc}) & -K_1(k'R_{oc}) & 0 \\ 0 & kI_0(kR_{oc}) & -kK_0(kR_{oc}) & -k'\mu_r^{-1}I_0(k'R_{oc}) & k'\mu_r^{-1}K_0(k'R_{oc}) & 0 \\ 0 & 0 & 0 & I_1(k'R_{ic}) & K_1(k'R_{ic}) & -I_1(kR_{ic}) \\ 0 & 0 & 0 & k'\mu_r^{-1}I_0(k'R_{ic}) & -k'\mu_r^{-1}K_0(k'R_{ic}) & -kI_0(kR_{ic}) \end{bmatrix} \begin{bmatrix} \tilde{D}^I \\ \tilde{C}^{II} \\ \tilde{D}^{II} \\ \tilde{C}^{III} \\ \tilde{D}^{III} \\ \tilde{C}^{IV} \end{bmatrix} = \begin{bmatrix} 0 \\ k^{-1}\mu_0 \tilde{J}_s \\ 0 \\ 0 \\ 0 \\ 0 \end{bmatrix} \quad (5.10)$$

The differentiation of the modified Bessel functions is carried out considering the following identities [184]:

$$\frac{\partial}{\partial r} \left(r I_1(kr) \right) = kr I_0(kr) \quad (5.11a)$$

$$\frac{\partial}{\partial r} \left(r K_1(kr) \right) = -kr K_0(kr). \quad (5.11b)$$

The solutions of (5.10) are lengthy expressions of modified Bessel functions and are given in Appendix B. It is noted, that the same principle can also be applied for a solid cylindrical conductor. In this case, the air domain inside the conductor has to be omitted and the problem simplifies to only four unknown constants. As a result, the magnetic field is completely described by the obtained analytical expressions.

In order to determine the force on the current carrying wire, the theorem of Parseval is employed¹ [216]. As in the previous analysis of harmonic motion, the force is calculated in the frequency domain by integrating the cross product $\tilde{\mathbf{J}}_s^* \times \tilde{\mathbf{B}}^{I(d)}$ between the distorted part of the magnetic flux density $\tilde{\mathbf{B}}^{I(d)}$ and the complex conjugate of the source surface current density $\tilde{\mathbf{J}}_s^*$ in domain I. Additional integrations have to be performed with respect to the azimuthal coordinate φ and the position of the current carrying coils located at r' representing the ring magnet. The model of the ring magnet for axial and radial magnetizations is described in more detail in the next section. Due to the fact that the radial component of the primary magnetic field $\tilde{\mathbf{B}}^{I(p)}$ vanishes at the position of the wire, the total magnetic flux $\tilde{\mathbf{B}}^I$ can be used instead of $\tilde{\mathbf{B}}^{I(d)}$. Finally, the force acting on the ring magnet is given by:

$$\mathbf{F} = \Re \left\{ \frac{1}{2\pi} \int_{-\infty}^{\infty} \int_{R_{im}}^{R_{om}} \int_0^{2\pi} \tilde{\mathbf{J}}_s^* \times \tilde{\mathbf{B}}^I r' d\varphi dr' dk \right\}. \quad (5.12)$$

Due to the symmetry of the problem, the radial component of the Lorentz force F_r vanishes and the analysis is limited to the axial component F_z .

The radial and axial component of $\tilde{\mathbf{B}}^I$ are determined by differentiation of the magnetic vector potential $\tilde{\mathbf{A}}^I$ such that:

$$\tilde{B}_r^I = -jk \tilde{A}_\varphi^I \quad (5.13a)$$

$$\tilde{B}_z^I = \frac{1}{r} \frac{\partial}{\partial r} \left(r \tilde{A}_\varphi^I \right) = \frac{1}{r} \tilde{A}_\varphi^I + \frac{\partial \tilde{A}_\varphi^I}{\partial r}. \quad (5.13b)$$

The axial component of the Lorentz force F_z is calculated by inserting (5.13a) and (5.13b) in (5.12) and by integrating over the azimuthal angle φ . Finally, considering that the Lorentz force is a symmetric function in the frequency domain, F_z is given by:

$$F_z = 2 \Re \left\{ \int_0^{\infty} \int_{R_{im}}^{R_{om}} jkr' \tilde{J}_s^* \tilde{A}_\varphi^I dr' dk \right\}. \quad (5.14)$$

¹Alternatively, the axisymmetry of the problem makes the Poynting vector an elegant tool to calculate the drag-force out of the resulting power loss as it is used by Ciric in [223].

The induced eddy current density in the frequency domain inside the conductor can be calculated by $\tilde{\mathbf{J}} = \sigma \mathbf{v} \times (\nabla \times \tilde{\mathbf{A}}^{\text{III}})$, using the magnetic vector potential $\tilde{\mathbf{A}}^{\text{III}}$ given in (5.8b):

$$\tilde{J}_\varphi = \sigma v_z \tilde{B}_r^{\text{III}} = -j\sigma v_z k \tilde{A}_\varphi^{\text{III}}. \quad (5.15)$$

This expression has to be transformed from the frequency domain back into the spatial domain by an inverse Fourier transformation:

$$J_\varphi = -\frac{\sigma v_z}{\pi} \Re \left\{ \int_0^\infty jk \tilde{A}_\varphi^{\text{III}} e^{jkz} dk \right\}. \quad (5.16)$$

In the following, the above considerations are used to determine J_φ and F_z for axially and radially magnetized ring magnets by means of the surface current model of permanent magnets [100].

5.2.2 Axially Magnetized Ring Magnets

In order to model axially magnetized ring magnets, an azimuthal source surface current density J_s is considered on the inner and outer face of the magnet as shown in Fig. 5.3(a). The inner and outer radius of the ring magnet is given by R_{im} and R_{om} , respectively. The magnitude and the direction of the source surface current density is determined by $\mathbf{J}_s = J_s \mathbf{e}_\varphi = \mathbf{M} \times \mathbf{n}$, where $\mathbf{M} = \mathbf{B}_r / \mu_0$. The vector \mathbf{n} denotes the unit normal vector of the corresponding face. In this way, the source current in the spatial domain is given by:

$$J_s = J_{si} + J_{so} = J_{s0} \text{rect} \left(\frac{z}{H_m} \right) \left[\delta(r - R_{om}) - \delta(r - R_{im}) \right],$$

where $J_{s0} = B_r / \mu_0$ is the magnitude of the source surface current density and $\text{rect}(\cdot)$ is the rectangular function. The quantities J_{si} and J_{so} are the source surface currents on the inner and outer face, respectively. The Fourier transform of the source surface current density $\tilde{J}_s = \mathcal{F}_z\{J_s\}$ with respect to z is given by:

$$\tilde{J}_s = \tilde{J}_{si} + \tilde{J}_{so} = J_{s0} H_m \text{sinc} \left(k \frac{H_m}{2} \right) \left[\delta(r - R_{om}) - \delta(r - R_{im}) \right]. \quad (5.17)$$

As a consequence of the Dirac delta function in the radial direction, the Lorentz force can be calculated by the superposition of the force acting on the inner and outer equivalent coil. Substituting (5.17) in (5.12) yields:

$$F_z = 2 \Re \left\{ \int_0^\infty \left[R_{im} \tilde{J}_{si}^* \tilde{B}_r(R_{im}) + R_{om} \tilde{J}_{so}^* \tilde{B}_r(R_{om}) \right] dk \right\}. \quad (5.18)$$

The Fourier transformed source surface currents on the inside and outside face are equivalent but flow in opposite direction such that $\tilde{J}_{si} = -\tilde{J}_{so}$. The radial component of the magnetic flux density $\tilde{B}_r^{\text{I}}(r)$ in the air domain can be calculated by (5.13a), while considering the superposition of terms from both source surface currents:

$$\tilde{B}_r^{\text{I}}(r) = jk \left(\tilde{D}^{\text{I}}|_{r'=R_{im}} + \tilde{D}^{\text{I}}|_{r'=R_{om}} \right) \text{K}_1(kr). \quad (5.19)$$

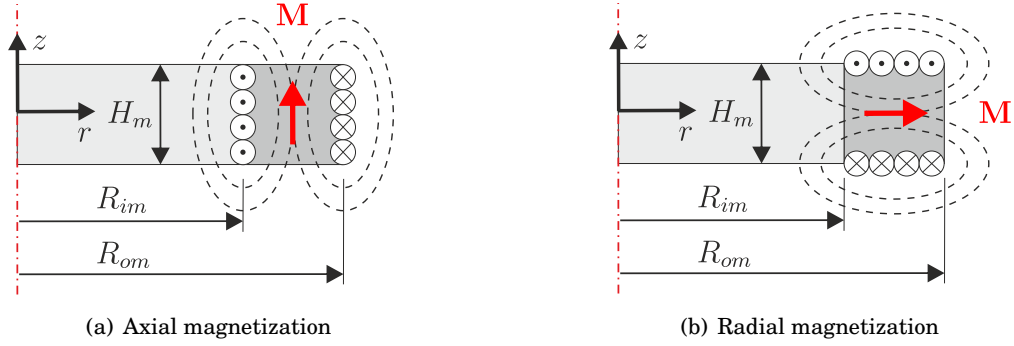


Figure 5.3: Current models of permanent magnet rings [236].

The constant \tilde{D}^I is given by solving (5.10) and is provided in Appendix B. Substituting (5.17) and (5.19) in (5.18) and using the identity $\tilde{D}^I = \tilde{J}_s \hat{D}^I$ yields the integral expression for F_z :

$$F_z = 2J_{s0}^2 H_m^2 \mathfrak{Re} \left\{ \int_0^\infty jk \operatorname{sinc}^2 \left(k \frac{H_m}{2} \right) \left[\hat{D}^I|_{r'=R_{im}} - \hat{D}^I|_{r'=R_{om}} \right] \times \right. \quad (5.20)$$

$$\left. \times \left[R_{im} K_1(kR_{im}) - R_{om} K_1(kR_{om}) \right] dk \right\}.$$

Similarly, the induced eddy current density can be calculated by means of (5.8b), (5.16) and (5.17) using the identities $\tilde{D}^{III} = \tilde{J}_s \hat{D}^{III}$ and $\tilde{C}^{III} = \tilde{J}_s \hat{C}^{III}$. The final expression for $J_\varphi(r, z)$ is then given by:

$$J_\varphi(r, z) = -\frac{J_{s0} H_m \sigma v_z}{\pi} \mathfrak{Re} \left\{ \int_0^\infty jk \operatorname{sinc} \left(k \frac{H_m}{2} \right) \left(I_1(k'r) \left[\hat{C}^{III}|_{r'=R_{om}} - \hat{C}^{III}|_{r'=R_{im}} \right] \right. \quad (5.21)$$

$$\left. + K_1(k'r) \left[\hat{D}^{III}|_{r'=R_{om}} - \hat{D}^{III}|_{r'=R_{im}} \right] \right) e^{jkz} dk \right\}.$$

5.2.3 Radially Magnetized Ring Magnets

Radially magnetized ring magnets can be modelled by defining the source surface current density on the upper and lower surface of the magnet as it is shown in Fig. 5.3(b). Hence, in the spatial domain, J_s is given by:

$$J_s = J_{s0} \operatorname{rect} \left(\frac{r}{R_{om} - R_{im}} \right) \left[\delta \left(z + \frac{H_m}{2} \right) - \delta \left(z - \frac{H_m}{2} \right) \right]. \quad (5.22)$$

Its Fourier transform with respect to z can be determined by applying the displacement law of the Dirac delta function:

$$\tilde{J}_s = 2jJ_{s0} \text{rect}\left(\frac{r}{R_{om} - R_{im}}\right) \sin\left(k \frac{H_m}{2}\right). \quad (5.23)$$

The Lorentz force and the induced eddy current density can be calculated in the similar way as for axially magnetized ring magnets. However, this case involves additional integrations with respect to the radial coordinate, resulting from the superposition of the magnetic field from and between each source current element. The expression for F_z is then given by:

$$F_z = 2\Re\left\{ \int_0^{\infty} \int_{R_{im}}^{R_{om}} \tilde{J}_s^* \tilde{B}_r^I(r') r' dr' dk \right\}. \quad (5.24)$$

The radial component of the magnetic flux density $\tilde{B}_r^I(r)$ can be determined by (5.13a) considering the superposition of each current element:

$$\tilde{B}_r^I(r) = jkK_1(kr) \int_{R_{im}}^{R_{om}} \hat{D}^I|_{r'=r''} dr''. \quad (5.25)$$

Substituting (5.23) and (5.25) in (5.12) yields the final expression for F_z :

$$F_z = 8J_{s0}^2 \Re\left\{ \int_0^{\infty} \int_{R_{im}}^{R_{om}} \int_{R_{im}}^{R_{om}} jkr' \sin^2\left(k \frac{H_m}{2}\right) K_1(kr') \hat{D}^I|_{r'=r''} dr'' dr' dk \right\}. \quad (5.26)$$

The expression for the eddy current density is determined by substituting (5.8b) and (5.17) in (5.16). The final expression for $J_\varphi(r, z)$ is then given by:

$$J_\varphi(r, z) = \frac{2J_{s0}\sigma v_z}{\pi} \Re\left\{ \int_0^{\infty} \int_{R_{im}}^{R_{om}} k \sin\left(k \frac{H_m}{2}\right) \left[I_1(k'r) \hat{C}^{III}|_{r'} + K_1(k'r) \hat{D}^{III}|_{r'} \right] e^{jkz} dr' dk \right\}. \quad (5.27)$$

5.2.4 The Creeping Ring Magnet

In the following, a ring magnet, which is falling along the axis of the conductor starting with an initial velocity of $v = 0$, is considered. After an acceleration phase, the gravitational force $M_m g$ is in equilibrium with the Lorentz force $F_z(v)$, and the magnet reaches the terminal velocity v_t . The velocity as a function of time is calculated considering the differential equation of motion:

$$M_m \frac{\partial v}{\partial t} = M_m g - F_z(v), \quad (5.28)$$

where $M_m = \rho V_m$ denotes the mass of the magnet, ρ its mass density and V_m its volume. Equation (5.28) is a nonlinear differential equation of first order, which can be solved numerically. The damping term $F_z(v)$ is calculated by (5.20) or (5.26) depending on the magnetization direction. It is mentioned that the derived expressions for $F_z(v)$ are determined under the assumption of a constant velocity. Hence, the solution can only be approximated by the analytical method since the velocity is time-dependent. On the contrary, the terminal velocity v_t can be directly calculated by setting the left hand side of (5.28) to zero. Thereat, an iterative scheme can be applied in order to determine the roots of the right-hand side.

5.2.5 Numerical Model

In order to check the rather intricate expressions for F_z and J_φ for correctness, the analytical results are compared to numerical simulations obtained by means of the FEM. Maxwell's equations are solved in the laboratory frame of reference K neglecting the presence of displacement currents (see section 3.1). A magnetic vector potential formulation is used while taking the axisymmetry of the problem into account. The governing equation solved by the FEM is given by:

$$\nabla \times \left(\frac{1}{\mu} \nabla \times \mathbf{A} - \mathbf{M} \right) - \sigma \mathbf{v} \times (\nabla \times \mathbf{A}) + \sigma \frac{\partial \mathbf{A}}{\partial t} = \mathbf{0}. \quad (5.29)$$

By expressing (5.29) in cylindrical coordinates, it is possible to identify the equivalence to the governing equation of the analytical approach (5.4) in the spatial domain:

$$\frac{\partial^2 A_\varphi}{\partial r^2} + \frac{1}{r} \frac{\partial A_\varphi}{\partial r} - \frac{A_\varphi}{r^2} + \frac{\partial^2 A_\varphi}{\partial z^2} + \sigma \frac{\partial A_\varphi}{\partial t} + \mu \underbrace{\left(\frac{\partial M_z}{\partial r} - \frac{\partial M_r}{\partial z} - \sigma v_z \frac{\partial A_\varphi}{\partial z} \right)}_{J_s} = 0. \quad (5.30)$$

Assuming homogeneous permanent magnets, the spatial derivatives of the magnetizations $\partial M_z / \partial r$ and $\partial M_r / \partial z$ are non-zero at the respective boundaries. Hence, the sources are incorporated in the same way as in the analytical approach (see Fig. 5.3). In the FEM, (5.30) is solved considering a discretized geometry by finite elements using second-order shape functions. In case of constant velocities ($\partial A_\varphi / \partial t = 0$), both approaches are equivalent and should yield the same results under the assumption that numerical errors are negligible. However, for time-dependent velocities, as in the case of the creeping ring magnet, the magnetic field is non-stationary ($\partial A_\varphi / \partial t \neq 0$) during the acceleration phase. As it could be shown during the analysis of time-dependent velocities in section 4.3, this accounts for a modified eddy current density inside the conductor which affects the force as well as the resulting velocity profile.

For non-magnetic conductors, the Lorentz force exerted on the magnet is calculated by integrating the force density over the volume of the moving conductor Ω_c :

$$F_z = - \int_{\Omega_c} J_\varphi B_r \, d\Omega. \quad (5.31)$$

However, for $\mu_r > 1$, the force is calculated by means of the Maxwell stress tensor on the surface of the conductor Γ_c , which has proved to be the more accurate approach in this particular

problem:

$$F_z = -\frac{2\pi}{\mu_0} \int_{\Gamma_c} r B_r B_z dS. \quad (5.32)$$

During the numerical analysis, it is ensured that the conductor sufficiently extends towards the axial direction to avoid edge effects.

5.3 Results and Discussion

Magnetic Flux Density: The obtained analytical expressions for the magnetic vector potential, and hence, the magnetic flux density, are compared to numerical results obtained by the FEM for both magnetization directions. The calculations are performed considering the parameters given in Table 5.1. The integrals are determined numerically using a Gauss-Legendre quadrature [238] for axially magnetizations and a global adaptive Simpson quadrature [239] for radial magnetizations.

The difference between analytical and FEM solutions is quantified by means of the normalized root mean square deviation (NRMSD) over N equidistantly spaced data points:

$$\delta F_z = \frac{100\%}{\max(F_z^{(\text{ANA})}) - \min(F_z^{(\text{ANA})})} \sqrt{\frac{1}{N} \sum_{i=1}^N (F_{z,i}^{(\text{ANA})} - F_{z,i}^{(\text{FEM})})^2}. \quad (5.33)$$

As an exemplary configuration, a tubular conductor with a wall-thickness ratio of $w/R_{oc} = (R_{oc} - R_{ic})/R_{oc} = 0.2$, and a relative permeability of $\mu_r = 10$ is considered. The conductivity and the velocity of the conductor are chosen such that $\mu_0 \sigma v = 10 \text{ m}^{-1}$. The remaining parameters are given in Table 5.1. Both components of the magnetic flux density are evaluated along a radial line crossing all computational domains, located at a height of $z = H_m$. The corresponding results are shown in Fig. 5.4. It should be noted that the evaluation of the magnetic flux density

Table 5.1: Parameters of the exemplary problem involving a ring magnet [236].

Parameter	Value	Description
R_{ic}	0...24.5 mm	Inner radius of the conductor
R_{oc}	25 mm	Outer radius of the conductor
R_{im}	30 mm	Inner radius of the ring magnet
R_{om}	40 mm	Outer radius of the ring magnet
H_m	10 mm	Height of the ring magnet
B_r	1 T	Remanence of the ring magnet
$\mu_0 \sigma v$	0...7800 m^{-1}	Diffusion coefficient
μ_r	1...100	Relative permeability
ρ	7500 kg/m^3	Mass density of NdFeB
σ_{Cu}	58.1 MS/m	Electrical conductivity of copper

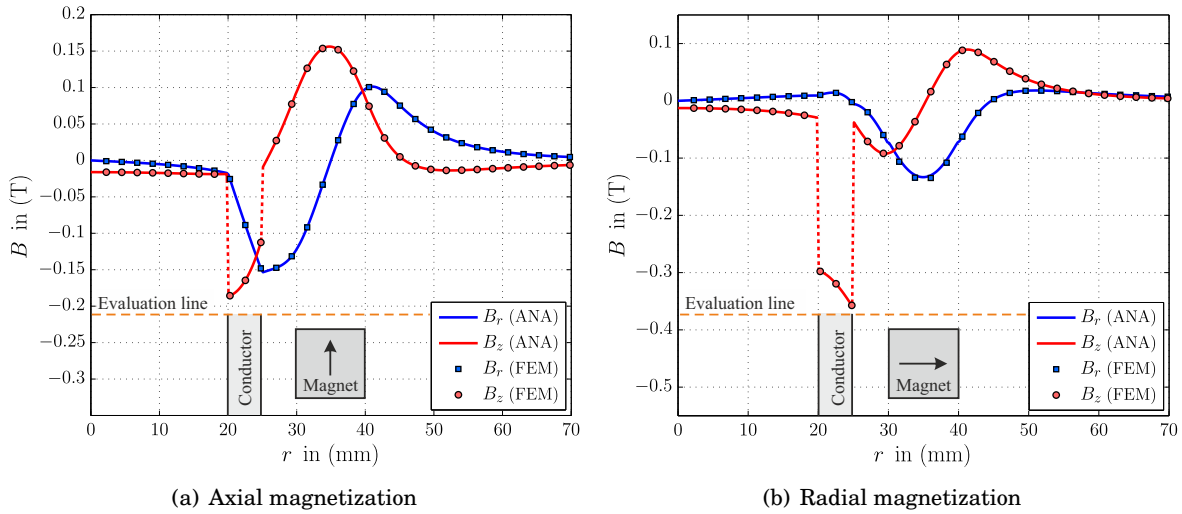


Figure 5.4: Components of the magnetic flux density computed analytically and by means of the FEM along the radial axis at $z = H_m$ for $\mu_0\sigma v = 10 \text{ m}^{-1}$, $\mu_r = 10$, and a wall-thickness ratio of $w/R_{oc} = 0.2$. The insets indicate the location where the magnetic flux is evaluated [236].

in between the magnet region, where $R_{im} < r < R_{om}$, merits special attention. The integration has to be divided into two parts, one contributing from domain I and the second from domain II, considering the corresponding limits. A very good agreement between analytical and numerical results is observed for both magnetization directions. The NRMSD over $N = 300$ data points did not exceed 0.3% and 1%, respectively. The reason for the slightly increased error in case of the magnet with radial magnetization results from the numerical integration accuracy in the region $R_{im} < r < R_{om}$. The relative permeability of the conductor leads to discontinuities of B_z . However, B_r is continuous across the interfaces and therewith fulfills the imposed boundary condition.

Lorentz Force: The Lorentz force is calculated as a function of the diffusion coefficient $\mu_0\sigma v$ for both magnetization directions. In this way, it is assumed that the magnet is fixed and the conductor travels through it with a given velocity. Moreover, the wall-thickness ratio w/R_{oc} of the pipe is varied according to the values from Table 5.1.

At first, non-magnetic conductors are considered assuming a relative permeability of $\mu_r = 1$. The corresponding results are shown in Fig. 5.5(a) and (b) for axially and radially magnetized ring magnets, respectively. As expected, a very good agreement between analytical and numerical results can be observed in case of constant velocities. For every w/R_{oc} ratio, the NRMSD over $N = 100$ data points is smaller than 0.03%. It can be seen that the Lorentz force is about 25% higher in case of radially magnetized magnets compared to axially magnetized ones. As expected, for low $\mu_0\sigma v$ values, a linear dependency of the Lorentz force can be observed. In this regime, the magnetic field generated by the induced eddy currents is negligible. However, if the conductor moves faster (or has a higher conductivity), the electromagnetic field gets suppressed

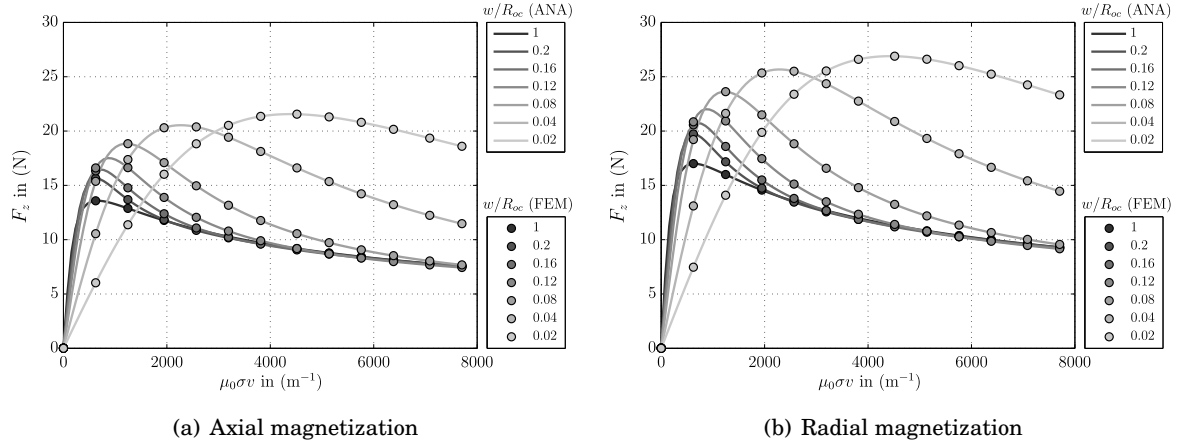


Figure 5.5: Lorentz force as function of the parameter $\mu_0\sigma v$ for different wall-thickness ratios w/R_{oc} [236].

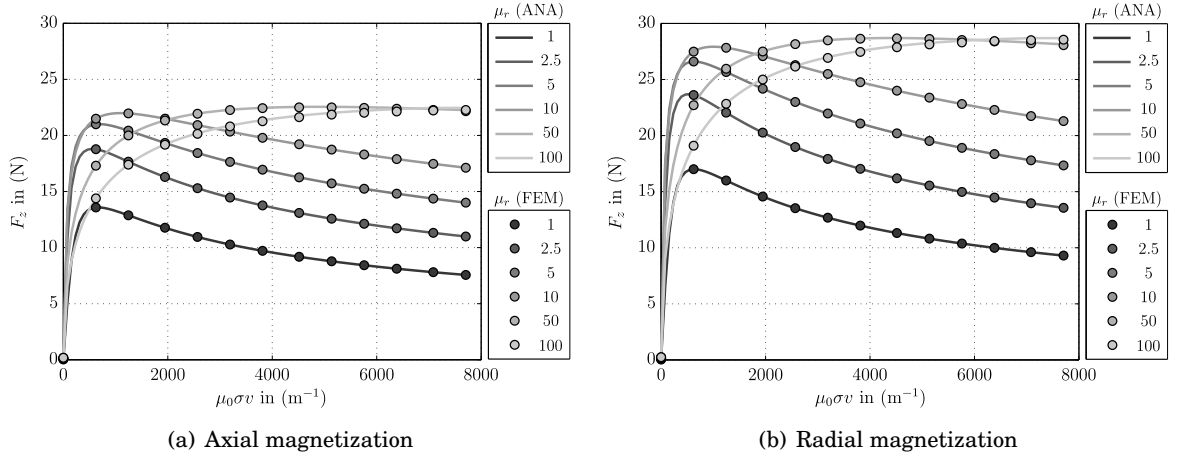


Figure 5.6: Lorentz force as function of $\mu_0\sigma v$ in case of $w/R_{oc} = 1$ for different values of μ_r [236].

out of the conductor and the resulting Lorentz force decreases. It can be observed, that the wall-thickness ratio w/R_{oc} of the conductor greatly affects the resulting Lorentz force profile due to the complex interaction between the primary and secondary magnetic fields. For thin walls, the linear regime lasts longer and the maximum Lorentz force increases. This effect can be explained by a decrease of the total conductance. As a consequence, the amount of Joule heat and power loss increases, which is directly proportional to the evaluated Lorentz force.

The study is extended to the case of ferromagnetic conductors with $\mu_r > 1$. In Fig. 5.6, the Lorentz force profiles are shown for different values of μ_r , now only considering a solid cylinder ($w/R_{oc} = 1$). Again, the analytical and the numerical results show a very good agreement with an NRMSD not exceeding 0.1%. As expected, the linear regime shifts to lower $\mu_0\sigma v$ values compared to non-magnetic conductors since μ_r is included in λ . Besides that, ferromagnetic conductors affect the magnetic field even without any motion-induced eddy currents. It can

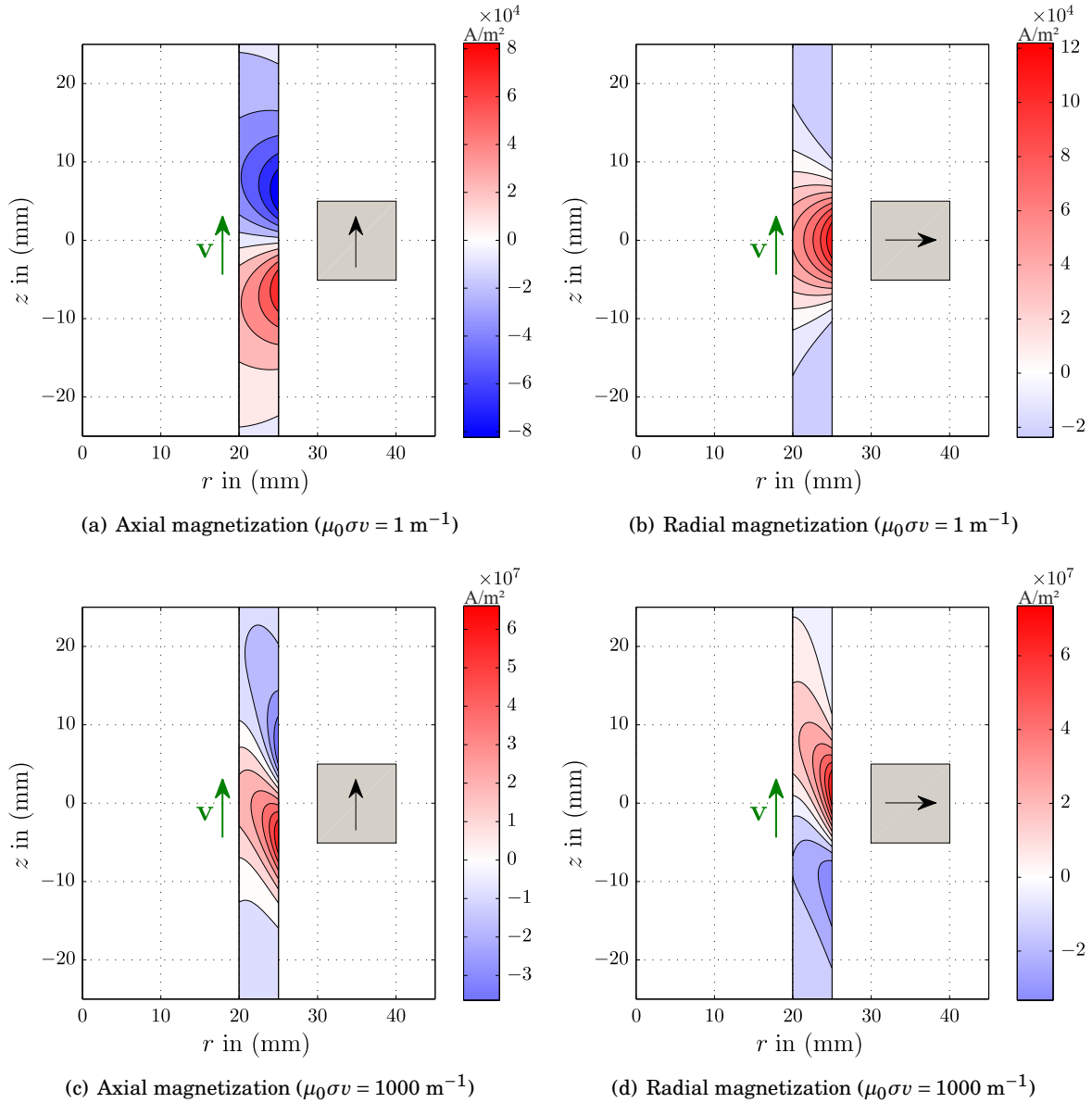


Figure 5.7: Induced eddy current density distribution J_φ for different $\mu_0\sigma v$ products considering non-ferromagnetic conductors ($\mu_r = 1$) and a wall-thickness ratio of $w/R_{oc} = 0.2$ [236].

be seen that an increase in μ_r leads to higher Lorentz forces. However, for $\mu_r > 10$, the force profile changes considerably and the Lorentz force is saturating instead of decreasing for high $\mu_0\sigma v$ values. Similar to the former case, the analytical and numerical results show a very good agreement. It is mentioned that such a scenario is difficult to handle from the experimental point of view since stable operation is hard to maintain. However, it is of expressive nature from the numerical point of view to proof the validity of the analytical expressions.

Induced Eddy Current Density: In order to illustrate the effect of field suppression, the induced eddy current density is exemplarily calculated for a wall-thickness ratio of $w/R_{oc} = 0.2$. Fig 5.7(a) and (c) show the field distributions for axially magnetized ring magnets in case of $\mu_0\sigma v = 1 \text{ m}^{-1}$ and $\mu_0\sigma v = 1000 \text{ m}^{-1}$, respectively. The field profile is symmetric at low velocities and conductivities and has similarities to an odd function with respect to the z -axis. In the upper part, the induced eddy currents flow clockwise, whereas in the lower part, the eddy currents flow in the opposite direction. However, for higher velocities, self inductance effects dominate over self resistance effects and the field is distorted in the direction of motion. The induced eddy current density generated by radially magnetized ring magnets is shown in Fig. 5.7(b) and (d). It can be seen that the distribution of the induced eddy currents for $\mu_0\sigma v = 1 \text{ m}^{-1}$ is more concentrated close to the magnet and similarities to an even function with respect to the z -axis can be observed. Together with the strong magnetic field in this region, this accounts for an increased Lorentz force observed previously. For $\mu_0\sigma v = 1000 \text{ m}^{-1}$, the field is distorted into the direction of motion in a similar sense compared to the axial case.

Creeping Ring Magnet: Next, the velocity profile of the ring magnet falling down a solid copper rod ($w/R_{oc} = 1$) with an electrical conductivity of $\sigma_{Cu} = 58.1 \text{ MS/m}$ is studied. The remaining dimensions of the investigated problem are listed in Table 5.1. The differential equation of motion from (5.28) is solved by calculating the damping term of the Lorentz force with the analytical and the numerical approaches. In the case of the analytic calculations, the time-dependent velocity profile is determined using the explicit Runge-Kutta-based Dormand-Prince method [240]. In the case of the FEM, the generalized- α method is used [241]. The solutions are shown in Fig. 5.8. Both magnets reach the steady state after approximately 0.15 s.

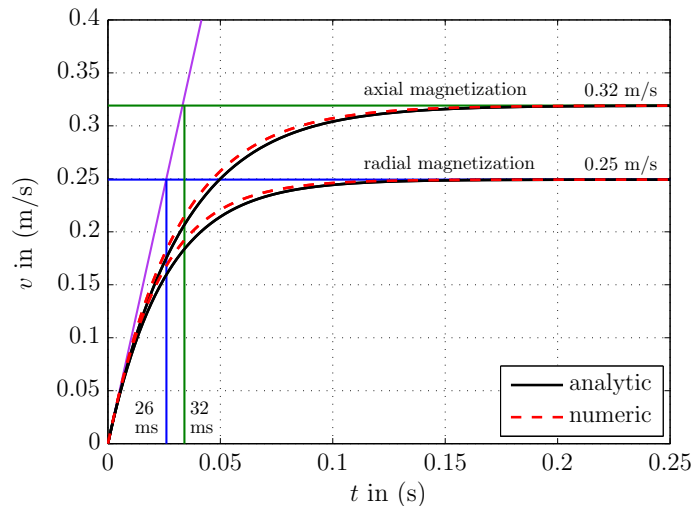


Figure 5.8: Time-dependent velocity of axially and radially magnetized ring magnets falling down a solid copper rod ($w/R_{oc} = 1$, $\mu_r = 1$) [236].

The time constants for the radially and the axially magnetized ring magnet are approximated to 26 ms and 32 ms, respectively. The terminal velocity of the axially magnetized magnet is $v_t = 0.32$ m/s and thus 28% higher compared to its radial counterpart with $v_t = 0.25$ m/s. This observation is in accordance to the previous results, where radially magnetized magnets generated higher Lorentz forces compared to axial ones (see Figs. 5.5 and 5.6).

In general, a good agreement between the velocity profiles obtained by the analytical and the numerical method can be observed. However, small differences arise during the acceleration phase, which can be explained by the time-dependent character of the velocity. By calculating the magnetic diffusion time $\tau = \mu\sigma L^2$, it is possible to approximate the influence of magnetic advection. The characteristic length of the problem L is chosen as $L = R_{oc}$. This results in a diffusion time of $\tau = 45.6$ ms, which is in the range of the observed time constants, providing ground to consider time-dependent effects.

An explanation regarding the mutual influence of electric and magnetic fields during the acceleration phase is given in the following. At the beginning, the velocity increases and the (primary) induced eddy currents increase as well due to the relative motion. These in turn generate a time-dependent secondary magnetic field, which in turn induces (secondary) eddy currents. They are directed in such a way to oppose the change which produces them. As a consequence, the total induced eddy current density decreases together with the damping term in the differential equation of motion. This leads to higher accelerations and slightly increased velocities compared to the analytical method, which neglects the presence of the secondary induced eddy currents.

5.4 Conclusions

The presented study provides analytic expressions for the magnetic vector potential generated by a ring-shaped permanent magnet falling down a possibly ferromagnetic electrical conducting pipe. Moreover, integral expressions are provided for the Lorentz force and the induced eddy current density. The magnetic field can be readily determined by means of the magnetic vector potential. The obtained expressions are applicable as long as the velocity is much lower than the speed of light ($|\mathbf{v}| \ll c$). The interaction between the magnetic field of the ring magnet and the induced eddy currents is considered, and the effect of flux expulsion is demonstrated for axially and radially magnetized ring magnets. The terminal velocity of one exemplary setup is calculated by solving the underlying differential equation of motion. Such a design could be used as a laboratory project at an intermediate or advanced undergraduate level.

Besides the application in LET, the obtained expressions could be adopted and applied in the framework of eddy current damping [195] or energy harvesting [202], where ring magnets are used in electromagnetic transducers to generate braking forces or electric energy. In this sense, the analytical expressions provide valuable support for time efficient analysis as it is required for example in optimization studies.

5.5 Patented LET System

In this thesis, an alternative LET system is proposed, which is a pending patent at the German Patent and Trade Mark Office [242]. An overview of the system is shown in Fig. 5.9. It consists of a magnet system, which encompasses the moving object under test. It is supported by additional magnet systems located further downstream together with a marker device. In the presence of a defect, the symmetry of the structure is disturbed. This leads to perturbations of the lateral forces in the xy -plane. The waveforms of the perturbations depend on the angular position of the defect φ_{def} . The resulting perturbations are exemplarily shown in Fig. 5.10, considering four different defect positions. Hence, it is possible to determine the angular position of the defect in real-time by evaluating the obtained force profiles of the ring magnet. This information is used for positioning of the downstream magnet systems. Depending on the defined detection goal, these systems are optimized for a variety of defect classes and could consist of different C-, HC- or HCp-systems as it is proposed in section 4.1. Finally, a marker device indicates the position of the suspected defect. The proposed system is capable to detect and localize subsurface defects in conducting objects during production processes, while considering the thermal constraints of permanent magnets in hot environments, which could require additional equipment for cooling.

The application of encompassing magnet systems, such as ring magnets, shares similarities to the principle of tomography. It enables the targeted search for defects with highly specialized magnet systems and avoids time-consuming scanning procedures.

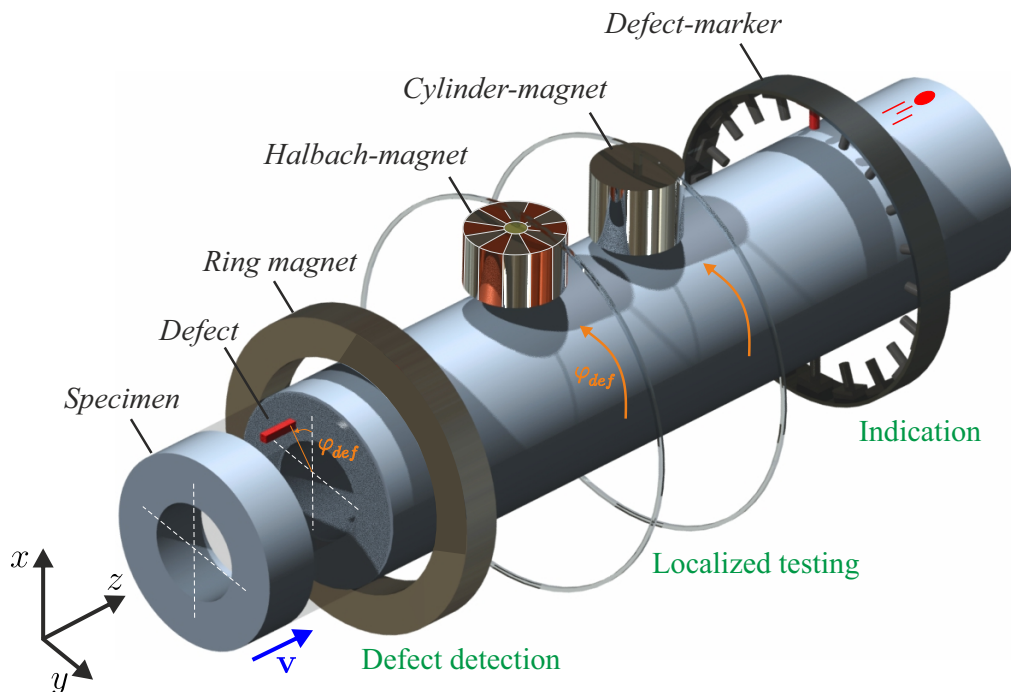


Figure 5.9: Patented LET system consisting of a ring magnet and different optimized positionable magnet systems for the local evaluation of material anomalies [242].

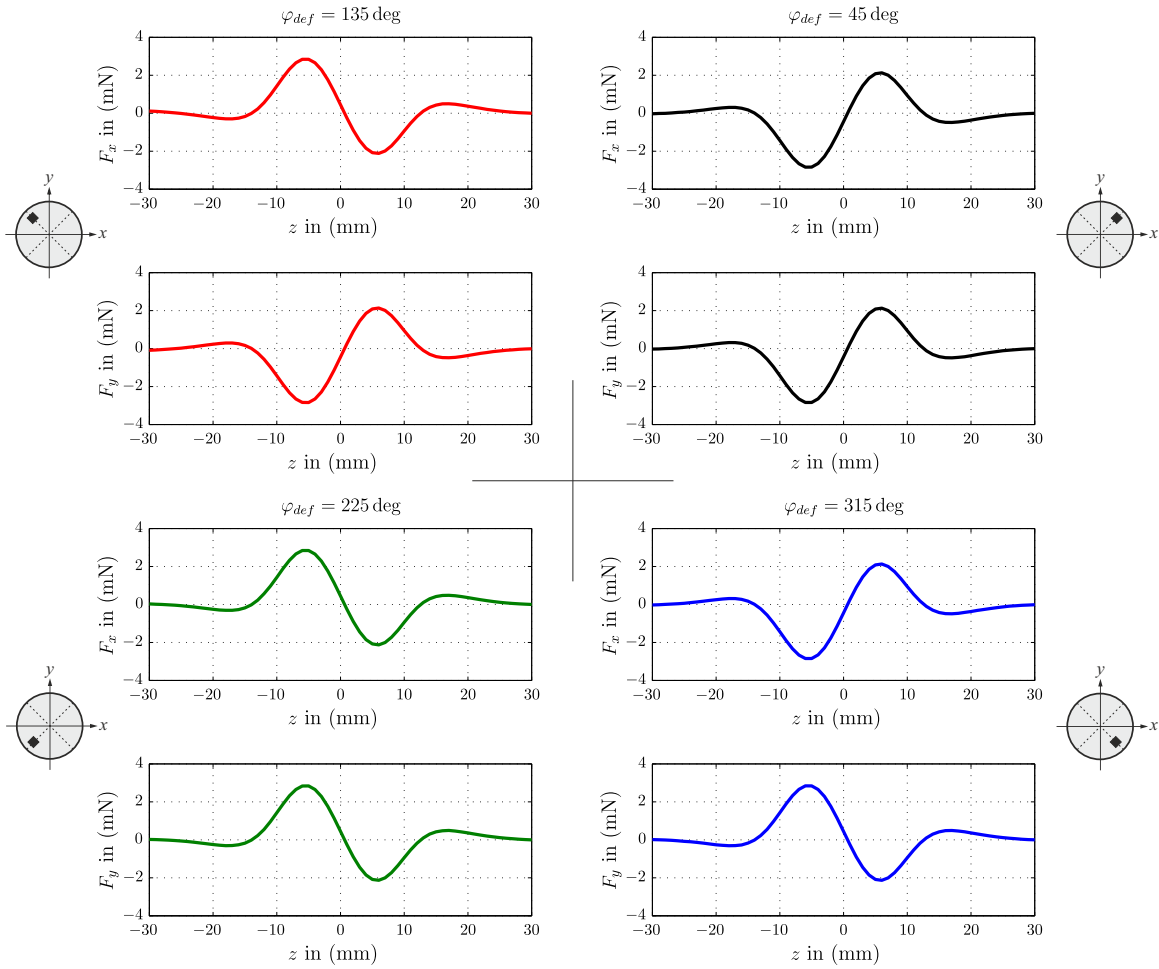


Figure 5.10: Lateral forces F_x and F_y of a ring magnet system in case of a passing subsurface defect, located at different angular positions φ_{def} . The results are obtained from a 3-D FEM model using the QSA ($R_{im} = 30$ mm, $R_{om} = 40$ mm, $H_m = 10$ mm, $B_r = 1.17$ T (radially magnetized), $R_{ic} = 0$ mm (solid cylinder), $R_{oc} = 25$ mm, $\sigma = 30.66$ MS/m, $v = 0.5$ m/s, $\mu_r = 1$, $[X_d, Y_d, Z_d] = [2, 2, 12]$ mm (parallelepiped), $d = 2$ mm (defect depth)).

SUMMARY AND OUTLOOK

6.1 Summary

In this work, the nondestructive testing technique Lorentz force eddy current testing (LET) was successfully developed further and it is believed that the obtained results will stand the test of time. The undertaken investigations elucidated and deepened the understanding of underlying mechanism related to motion-induced eddy currents and the detection of defects in conductive specimens by means of LET.

A procedure to determine optimal magnet systems in the framework of LET is proposed. The underlying optimization problem is clearly defined considering the problem specificity of nondestructive testing scenarios. The proposed optimization procedure is highly adaptive and provides a high level of generality. It is thus suitable for future developments. The optimization studies demonstrate that the limiting factor in LET, which is given by the confined value of the magnetic remanence, can be counteracted by the proposed Halbach-magnet system. This design shows inherently improved characteristics in terms of weight and performance. The impressed magnetic flux density into the specimen is focused and increased compared to standard geometries. As a consequence, it was possible to further increase the defect response signal. The combination of both soft and hard magnetic materials using highly saturating iron-cobalt-alloys leads to a new generation of LET sensors. The proposed concepts are made available for experimental studies by the design of prototypes. Moreover, a defect depth study considering the concept of a quasi-infinite crack, exemplified the potential of the LET method and revealed a maximum defect depth of 24 mm in aluminium when considering the lift-force.

The LET setup is further investigated in terms of the underlying uncertainties. A non-intrusive generalized polynomial chaos expansion is used in order to quantify the impact and interaction of multiple unknown input parameters. In this context, the stochastic properties

of the velocity and the conductivity of the specimen as well as the magnetic remanence of the permanent magnet are determined experimentally. The quantities under investigation are modeled as β - and uniform distributed random variables. The results are compared to Monte Carlo simulations and showed errors $< 0.2\%$. Furthermore, the experimentally obtained force profiles are compared to the numerical predictions and do lie in the prognosticated range. The sensitivity analysis considerably contributed to extend the knowledge about the most influencing parameters. A Sobol decomposition revealed that the magnetic remanence and the lift-off distance contribute to more than 90% to the total variance of the resulting Lorentz force profile and should be considered first to improve reproducibility. It turned out that the numerical treatment of this kind of problem in a probabilistic framework is an essential part during the experimental validation.

The electromagnetic fields and forces are calculated, which emerge when a coil or a permanent magnet moves with a sinusoidal velocity profile relative to a conducting slab of finite thickness. The 3-D time-dependent analytical solution of this problem is presented. Besides of the application in LET, the results can be readily used in application scenarios related to electromagnetic damping, eddy current braking or energy harvesting in order to analyze diffusion and advection processes in case of harmonic motion efficiently. The study is performed for rectangular and circular coils as well as for cuboidal and cylindrical permanent magnets. The back reaction of the conductor and therewith associated inductive effects are considered. The solutions of the governing equations and the integral expressions for the time-dependent drag- and lift-force are provided. The analytical results are verified by a comparison to numerical simulations obtained by the FEM. The relative difference between the analytically and numerically evaluated force profiles was $< 0.1\%$. Exemplary calculations showed that the waveforms of both force components strongly depend on the level of constant nominal velocity v_0 , the magnitude of the velocity oscillation amplitude v_1 , and the underlying oscillation frequency f_v .

The proposed ring magnet design enables new fields of application. Analytical solutions of the electromagnetic fields and Lorentz forces, generated by axially or radially magnetized ring magnets due to passing conductors, are provided. The results are verified by numerical simulations. In this regard, the analytical solutions are an important basis when assessing new numerical techniques and can be referred to for comparison. It has been shown numerically that such a system has the potential for advanced defect detection and localization.

6.2 Outlook and Future Work

The present work provides valuable theoretical support of the LET method. On this basis, suggestions for future investigations are provided in the following:

- Besides of the applied magnetic vector potential formulation described in section 3.2, the use of alternative magnetic field formulations could be subject of numerical studies in the future. In this regard, the electric current vector potential \mathbf{T} in combination with

the magnetic scalar potential ψ could be applied. This formulation is often referred to as the $\mathbf{T} - \Omega$ formulation. It is noted that special attention has to be paid in the presence of a defect. In this case, the air region is not simply connected. However, multivalued scalar potentials can be avoided by defining very low conductivities inside the defect region. The $\mathbf{T} - \Omega$ formulation is advantageous for the modeling of thin flaws, where the normal component of the induced current density can be set to zero by enforcing that the tangential component of \mathbf{T} vanishes over the defect surface [96].

- The application of highly saturating iron-cobalt-alloys in LET sensors to focus and magnify the impressed magnetic flux density could play a central role in future sensor designs. The ADRA generated by more advanced magnet geometries could be investigated to further increase the signal to noise ratio of LET sensors. In this context, the application of anisotropic topology optimization schemes has the potential to identify the optimal magnetization directions inside the permanent magnet system. However, care must be taken to ensure practical feasibility.
- During the development of new magnet systems, the effective remanence instead of its nominal value, provided by the manufacturer, should be considered. As a direct consequence of the quadratic dependency with respect to the Lorentz force, this significantly influences the obtained critical volume ratios obtained by the volume adaptive force constraint approach (VaFc) during the optimization.
- Current research is devoted to investigate the influence of the demagnetizing field on the effective remanence, theoretically and experimentally. The knowledge gained from this study should be considered when performing numerical simulations in the future.
- The parasitic oscillations in the Lorentz force, which were observed in the experimental data, should be reduced as much as possible. This would increase the signal-to-distortion ratio and could enable the detection of smaller and deeper lying defects.
- The ring magnet system provides certain advantages in combination with local LET sensors. However, an experimental validation of the proposed system is not yet provided. The design of such a system is challenging and requires decent expertise in mechanical engineering and force measurement systems.
- An important step towards the application of the LET method in an industrial setting is to provide reliable statements about the probability of detection (PoD) [243]. This is usually done by determining the probability of detected flaws as a function of its size [244]. As a result, the so called PoD-curve can be provided together with a certain confidence interval. Those studies are done experimentally and do require a large number of specimens. Besides of the usual question of "What is the smallest flaw that can be found?", one has to reformulate this question in the framework of NDT to "What is the largest flaw that could be missed?" [244].



2-D FOURIER TRANSFORM OF A CIRCULAR CURRENT LOOP

In the following, the Fourier transform of a circular current loop is derived. The time dependency of its position is omitted in the first place, without loss of generality. The current loop in the spatial domain, considering a Cartesian coordinate system, is described by:

$$I_x^{(\text{circ})} = -2I_s \frac{y}{a} \delta\left(\sqrt{x^2 + y^2} - \frac{a}{2}\right) \quad (\text{A.1a})$$

$$I_y^{(\text{circ})} = 2I_s \frac{x}{a} \delta\left(\sqrt{x^2 + y^2} - \frac{a}{2}\right). \quad (\text{A.1b})$$

The parameter a denotes the diameter of the current loop. In analogy, the expressions can be described in the cylindrical coordinate system:

$$I_x^{(\text{circ})} = -I_s \sin(\varphi) \delta\left(r - \frac{a}{2}\right) \quad (\text{A.2a})$$

$$I_y^{(\text{circ})} = I_s \cos(\varphi) \delta\left(r - \frac{a}{2}\right). \quad (\text{A.2b})$$

The Fourier transform of a two dimensional function $f(x, y)$ is given by:

$$\mathcal{F}_x \mathcal{F}_y \{f(x, y)\} = \int_{-\infty}^{\infty} \int_{-\infty}^{\infty} f(x, y) e^{-j(xk_x + yk_y)} dx dy, \quad (\text{A.3})$$

with the spatial frequencies k_x and k_y . This expression can be transformed into the cylindrical coordinate system by considering the following identities:

$$k e^{j\beta} = k_x + jk_y \quad \rightarrow \quad \sin(\beta) = \frac{k_y}{k}, \quad \cos(\beta) = \frac{k_x}{k}, \quad k = \sqrt{k_x^2 + k_y^2} \quad (\text{A.4})$$

$$r e^{j\varphi} = x + jy \quad \rightarrow \quad \sin(\varphi) = \frac{y}{r}, \quad \cos(\varphi) = \frac{x}{r}, \quad r = \sqrt{x^2 + y^2} \quad (\text{A.5})$$

$$xk_x = kr \cos(\beta) \cos(\varphi) \quad (\text{A.6})$$

$$yk_y = kr \sin(\beta) \sin(\varphi) \quad (\text{A.7})$$

$$xk_x + yk_y = kr(\cos(\beta)\cos(\varphi) + \sin(\beta)\sin(\varphi)) \quad (\text{A.8})$$

$$= kr\cos(\varphi - \beta). \quad (\text{A.9})$$

Substituting (A.9) in (A.3) and performing the integration with respect to the radial coordinate, r , and the azimuthal angle, φ , yields:

$$\int_{-\infty}^{\infty} \int_{-\infty}^{\infty} f(x, y) e^{-j(xk_x + yk_y)} dx dy = \int_0^{\infty} \int_0^{2\pi} f(r, \varphi) e^{-jkr\cos(\varphi - \beta)} r dr d\varphi. \quad (\text{A.10})$$

By substituting $\theta = \varphi - \beta$ one gets:

$$\int_0^{\infty} \int_{-\beta}^{2\pi - \beta} f(r, \theta + \beta) e^{-jkr\cos(\theta)} r dr d\theta. \quad (\text{A.11})$$

Substituting the expressions of the current loop (A.2a) and (A.2b) in (A.11) for the function $f(r, \theta + \beta)$ leads to:

$$I_s \int_0^{\infty} \int_{-\beta}^{2\pi - \beta} \begin{bmatrix} -\sin(\theta + \beta) \\ \cos(\theta + \beta) \end{bmatrix} \delta\left(r - \frac{a}{2}\right) e^{-jkr\cos(\theta)} r dr d\theta \quad (\text{A.12})$$

The integral over the radial coordinate can be solved by using the sifting property of the Dirac delta function at $r = \frac{a}{2}$.

$$I_s \frac{a}{2} \int_{-\beta}^{2\pi - \beta} \begin{bmatrix} -\sin(\theta + \beta) \\ \cos(\theta + \beta) \end{bmatrix} e^{-jk\frac{a}{2}\cos(\theta)} d\theta \quad (\text{A.13})$$

By reformulating the expressions in brackets by means of the following trigonometric identities:

$$\sin(\theta + \beta) = \sin(\theta)\cos(\beta) + \cos(\theta)\sin(\beta) = \frac{1}{k}(k_x \sin(\theta) + k_y \cos(\theta)) \quad (\text{A.14})$$

$$\cos(\theta + \beta) = \cos(\theta)\cos(\beta) - \sin(\theta)\sin(\beta) = \frac{1}{k}(k_x \cos(\theta) - k_y \sin(\theta)), \quad (\text{A.15})$$

eq. (A.13) can be written as:

$$I_s \frac{a}{2k} \int_{-\beta}^{2\pi - \beta} \begin{bmatrix} -k_x \sin(\theta) - k_y \cos(\theta) \\ -k_y \sin(\theta) + k_x \cos(\theta) \end{bmatrix} e^{-jk\frac{a}{2}\cos(\theta)} d\theta. \quad (\text{A.16})$$

In the following, only the first component is considered since the considerations do also apply for the second one.

Splitting up the integral involving the sine and the cosine term, one can identify the following relationship using Eulers identity:

$$\int_{-\beta}^{2\pi - \beta} \sin(\theta) e^{-jk\frac{a}{2}\cos(\theta)} d\theta = \int_{-\beta}^{2\pi - \beta} \sin(\theta) \cos\left(k\frac{a}{2}\cos(\theta)\right) d\theta - j \int_{-\beta}^{2\pi - \beta} \sin(\theta) \sin\left(k\frac{a}{2}\cos(\theta)\right) d\theta \quad (\text{A.17})$$

$$= - \underbrace{\left[\frac{\sin\left(k\frac{a}{2}\cos(\theta)\right)}{k\frac{a}{2}} \right]_{-\beta}^{2\pi - \beta}}_{=0} - j \underbrace{\left[\frac{\cos\left(k\frac{a}{2}\cos(\theta)\right)}{k\frac{a}{2}} \right]_{-\beta}^{2\pi - \beta}}_{=0} = 0. \quad (\text{A.18})$$

As a consequence, the integrals involving the sine terms vanish. Next, the cosine terms are considered, taking into account the following identities of the Bessel functions of the first kind [184]:

$$\mathbf{J}_n(z) = \frac{i^{-n}}{\pi} \int_0^\pi \cos(n\theta) e^{jz \cos(\theta)} \quad (\text{A.19})$$

$$\mathbf{J}_n(ze^{jm\pi}) = e^{jm\pi n} \mathbf{J}_n(z) \xrightarrow{m=n=1} \mathbf{J}_1(-z) = -\mathbf{J}_1(z). \quad (\text{A.20})$$

Substituting $z = -k \frac{a}{2}$ and considering the symmetry of the function, one gets:

$$-2\pi j \mathbf{J}_1\left(k \frac{a}{2}\right) = \int_0^{2\pi} \cos(\theta) e^{-jk \frac{a}{2} \cos(\theta)}. \quad (\text{A.21})$$

Finally, by using this analogy in (A.16), the two dimensional Fourier transforms of both current components are given by:

$$\mathcal{F}_x \mathcal{F}_y \{I_x^{(\text{circ})}\} = ja\pi I_s \frac{k_y}{k} \mathbf{J}_1\left(k \frac{a}{2}\right) \quad (\text{A.22a})$$

$$\mathcal{F}_x \mathcal{F}_y \{I_y^{(\text{circ})}\} = -ja\pi I_s \frac{k_x}{k} \mathbf{J}_1\left(k \frac{a}{2}\right). \quad (\text{A.22b})$$

SOLUTION OF THE MAGNETIC VECTOR POTENTIAL FOR RING MAGNETS

B.1 Solid Conductors

In case of cylindrical conductors, domain IV from Fig. 5.2 on page 113 vanishes. The remaining constants \tilde{C}^{II} , \tilde{C}^{III} , \tilde{D}^{I} , and \tilde{D}^{II} are determined by solving the system of equations resulting from the corresponding boundary conditions. The argument r' denotes the radial position of the source current. The corresponding constants are given in (B.1a)-(B.1d). The functions $I_n(\cdot)$ and $K_n(\cdot)$ are the n -th order modified Bessel functions of the first and second kind respectively [184].

$$\tilde{D}^{\text{I}} = \frac{\mu_0 \tilde{J}_s r'}{Q_0} \left\{ k I_1(\beta_o) \left[I_1(\gamma) K_0(\alpha_o) + I_0(\alpha_o) K_1(\gamma) \right] + \frac{k'}{\mu_r} I_0(\beta_o) \left[I_1(\gamma) K_1(\alpha_o) - I_1(\alpha_o) K_1(\gamma) \right] \right\} \quad (\text{B.1a})$$

$$\tilde{C}^{\text{II}} = \mu_0 \tilde{J}_s r' K_1(\gamma) \quad (\text{B.1b})$$

$$\tilde{D}^{\text{II}} = \frac{\mu_0 \tilde{J}_s r'}{Q_0} K_1(\gamma) \left[k I_1(\beta_o) I_0(\alpha_o) - \frac{k'}{\mu_r} I_1(\alpha_o) I_0(\beta_o) \right] \quad (\text{B.1c})$$

$$\tilde{C}^{\text{III}} = \frac{\mu_0 \tilde{J}_s r' K_1(\gamma)}{Q_0 R_{oc}} \quad (\text{B.1d})$$

B.2 Tubular Conductors

Tubular conductors, such as pipes, contain an air domain inside. The constants \tilde{C}^{II} to \tilde{C}^{IV} and \tilde{D}^{I} to \tilde{D}^{III} are determined by solving the system of equations in (5.10). The corresponding solutions are given in (B.2a)-(B.2f). Auxiliary functions, which are included in the expressions,

are provided in (B.3a)-(B.3f).

$$\tilde{D}^I = \frac{\mu_0 \tilde{J}_s r'}{\mathcal{Q}_1} \left\{ \mathbf{I}_1(\gamma) \left[\mathbf{K}_1(\alpha_0) \mathbf{Q}_2 + \mathbf{K}_0(\alpha_0) \mathbf{Q}_3 \right] - \mathbf{K}_1(\gamma) \left[\mathbf{I}_1(\alpha_0) \mathbf{Q}_2 - \mathbf{I}_0(\alpha_0) \mathbf{Q}_3 \right] \right\} \quad (\text{B.2a})$$

$$\tilde{C}^{\text{II}} = \mu_0 \tilde{J}_s r' \mathbf{K}_1(\gamma) \quad (\text{B.2b})$$

$$\tilde{D}^{\text{II}} = \frac{\mu_0 \tilde{J}_s r'}{\mathcal{Q}_1} \mathbf{K}_1(\gamma) \left[\frac{k'}{\mu_r} \mathbf{I}_1(\alpha_i) \mathbf{Q}_4 + k \mathbf{I}_0(\alpha_i) \mathbf{Q}_5 \right] \quad (\text{B.2c})$$

$$\tilde{C}^{\text{III}} = \frac{\mu_0 \tilde{J}_s r'}{R_{oc} \mathcal{Q}_1} \mathbf{K}_1(\gamma) \left[\frac{k'}{\mu_r} \mathbf{I}_1(\alpha_i) \mathbf{K}_0(\beta_i) + k \mathbf{K}_1(\beta_i) \mathbf{I}_0(\alpha_i) \right] \quad (\text{B.2d})$$

$$\tilde{D}^{\text{III}} = \frac{\mu_0 \tilde{J}_s r'}{R_{oc} \mathcal{Q}_1} \mathbf{K}_1(\gamma) \left[\frac{k'}{\mu_r} \mathbf{I}_1(\alpha_i) \mathbf{I}_0(\beta_i) - k \mathbf{I}_1(\beta_i) \mathbf{I}_0(\alpha_i) \right] \quad (\text{B.2e})$$

$$\tilde{C}^{\text{IV}} = \frac{\mu_0 \tilde{J}_s r'}{\mu_r R_{ic} R_{oc} \mathcal{Q}_1} \mathbf{K}_1(\gamma) \quad (\text{B.2f})$$

Auxiliary functions:

$$\mathbf{Q}_0 = k \mathbf{I}_1(\beta_o) \mathbf{K}_0(\alpha_o) + \frac{k'}{\mu_r} \mathbf{I}_0(\beta_o) \mathbf{K}_1(\alpha_o) \quad (\text{B.3a})$$

$$\begin{aligned} \mathbf{Q}_1 = & \frac{k'^2}{\mu_r^2} \mathbf{I}_1(\alpha_i) \mathbf{K}_1(\alpha_o) \left[\mathbf{I}_0(\beta_o) \mathbf{K}_0(\beta_i) - \mathbf{I}_0(\beta_i) \mathbf{K}_0(\beta_o) \right] + \\ & + k^2 \mathbf{I}_0(\alpha_i) \mathbf{K}_0(\alpha_o) \left[\mathbf{I}_1(\beta_o) \mathbf{K}_1(\beta_i) - \mathbf{I}_1(\beta_i) \mathbf{K}_1(\beta_o) \right] + \\ & + k \frac{k'}{\mu_r} \left\{ \mathbf{I}_0(\alpha_i) \mathbf{K}_1(\alpha_o) \left[\mathbf{I}_0(\beta_o) \mathbf{K}_1(\beta_i) + \mathbf{I}_1(\beta_i) \mathbf{K}_0(\beta_o) \right] + \right. \\ & \left. + \mathbf{I}_1(\alpha_i) \mathbf{K}_0(\alpha_o) \left[\mathbf{I}_1(\beta_o) \mathbf{K}_0(\beta_i) + \mathbf{I}_0(\beta_i) \mathbf{K}_1(\beta_o) \right] \right\} \end{aligned} \quad (\text{B.3b})$$

$$\mathbf{Q}_2 = \frac{k'^2}{\mu_r^2} \mathbf{I}_1(\alpha_i) \left[\mathbf{I}_0(\beta_o) \mathbf{K}_0(\beta_i) - \mathbf{I}_0(\beta_i) \mathbf{K}_0(\beta_o) \right] + k \frac{k'}{\mu_r} \mathbf{I}_0(\alpha_i) \left[\mathbf{I}_0(\beta_o) \mathbf{K}_1(\beta_i) + \mathbf{I}_1(\beta_i) \mathbf{K}_0(\beta_o) \right] \quad (\text{B.3c})$$

$$\mathbf{Q}_3 = k^2 \mathbf{I}_0(\alpha_i) \left[\mathbf{I}_1(\beta_o) \mathbf{K}_1(\beta_i) - \mathbf{I}_1(\beta_i) \mathbf{K}_1(\beta_o) \right] + k \frac{k'}{\mu_r} \mathbf{I}_1(\alpha_i) \left[\mathbf{I}_1(\beta_o) \mathbf{K}_0(\beta_i) + \mathbf{I}_0(\beta_i) \mathbf{K}_1(\beta_o) \right] \quad (\text{B.3d})$$

$$\mathbf{Q}_4 = \frac{k'}{\mu_r} \mathbf{I}_1(\alpha_o) \left[\mathbf{I}_0(\beta_i) \mathbf{K}_0(\beta_o) - \mathbf{I}_0(\beta_o) \mathbf{K}_0(\beta_i) \right] + k \mathbf{I}_0(\alpha_o) \left[\mathbf{I}_1(\beta_o) \mathbf{K}_0(\beta_i) + \mathbf{I}_0(\beta_i) \mathbf{K}_1(\beta_o) \right] \quad (\text{B.3e})$$

$$\mathbf{Q}_5 = -\frac{k'}{\mu_r} \mathbf{I}_1(\alpha_o) \left[\mathbf{I}_0(\beta_o) \mathbf{K}_1(\beta_i) + \mathbf{I}_1(\beta_i) \mathbf{K}_0(\beta_o) \right] + k \mathbf{I}_0(\alpha_o) \left[\mathbf{I}_1(\beta_o) \mathbf{K}_1(\beta_i) - \mathbf{I}_1(\beta_i) \mathbf{K}_1(\beta_o) \right] \quad (\text{B.3f})$$

$$k' = \sqrt{k^2 + j\lambda k}, \quad \lambda = \mu_0 \mu_r \sigma v_z, \quad \alpha_o = k R_{oc}, \quad \beta_o = k' R_{oc}, \quad \alpha_i = k R_{ic}, \quad \beta_i = k' R_{ic}, \quad \gamma = k r'$$

BIBLIOGRAPHY

- [1] H. Brauer and M. Ziolkowski, "Eddy Current Testing of Metallic Sheets with Defects Using Force Measurements," *Serbian Journal of Electrical Engineering*, vol. 5, no. 1, pp. 11–20, 2008.
(pages 2, 13).
- [2] W. C. Roentgen, "Ueber eine neue Art von Strahlen: (Vorläufige Mittheilung)," *Sonderabdruck aus den Sitzungsberichten der Wuerzburger Physik.-medic. Gesellschaft*, pp. 1–19, 1895.
(page 5).
- [3] P. E. Mix, *Introduction to nondestructive testing: A training guide*, 2nd ed. Hoboken, N.J.: Wiley, 2005.
(page 5).
- [4] C. Hellier, *Handbook of nondestructive evaluation*. New York: McGraw-Hill, 2003.
(page 5).
- [5] N. Jain. Analysis of the Global Nondestructive Test Equipment Market: Understanding Industry Dynamics Key to Growth. [Online]. Available: <http://www.frost.com/c/10057/sublib/display-report.do?id=NAEE-01-00-00-00> [Accessed: 09.09.2015]
(pages 6, 7).
- [6] C. V. Dodd and W. E. Deeds, "Analytical Solutions to Eddy-Current Probe-Coil Problems," *Journal of Applied Physics*, vol. 39, no. 6, pp. 2829–2838, 1968.
(page 7).
- [7] N. V. Nair, V. R. Melapudi, H. R. Jimenez, X. Liu, Y. Deng, Z. Zeng, L. Udpa, T. J. Moran, and S. S. Udpa, "A GMR-Based Eddy Current System for NDE of Aircraft Structures," *IEEE Transactions on Magnetics*, vol. 42, no. 10, pp. 3312–3314, 2006.
(page 7).
- [8] B. Wincheski, "Deep flaw detection with giant magnetoresistive (GMR) based self-nulling probe," *26th Annual review of progress in quantitative nondestructive evaluation*, pp. 465–472, 2010.
(pages 7, 10).
- [9] K. Chomsuwan, S. Yamada, M. Iwahara, H. Wakiwaka, and S. Shoji, "Application of Eddy-Current Testing Technique for High-Density Double-Layer Printed Circuit Board Inspection," *IEEE Transactions on Magnetics*, vol. 41, no. 10, pp. 3619–3621, 2005.
(page 7).
- [10] J. Cheng, H. Ji, J. Qiu, T. Takagi, T. Uchimoto, and N. Hu, "Role of interlaminar interface on bulk conductivity and electrical anisotropy of CFRP laminates measured by eddy current method," *NDT & E International*, vol. 68, no. 1, pp. 1–12, 2014.
(page 7).
- [11] K. Mizukami, Y. Mizutani, A. Todoroki, and Y. Suzuki, "Detection of delamination in thermoplastic CFRP welded zones using induction heating assisted eddy current testing," *NDT & E International*, vol. 74, no. 1, pp. 106–111, 2015.
(page 7).

BIBLIOGRAPHY

- [12] J. Garcia-Martin and J. Gomez-Gil, "Comparative evaluation of coil and hall probes in hole detection and thickness measurement on aluminum plates using eddy current testing," *Russian Journal of Nondestructive Testing*, vol. 49, no. 8, pp. 482–491, 2013.
(page 8).
- [13] M. v. Kreutzbruck, K. Allweins, and C. Heiden, "Fluxgate-magnetometer for the detection of deep lying defects," *Proceedings of the 15th World Conference on Non-Destructive Testing*, pp. 1–5, 2000.
(pages 8, 10).
- [14] H. G. Ramos and A. L. Ribeiro, "Present and Future Impact of Magnetic Sensors in NDE," *Procedia Engineering*, vol. 86, no. 1, pp. 406–419, 2014.
(pages 8, 9).
- [15] B. Wincheski, F. Yu, J. Simpon, P. Williams, and K. Rackow, "Development of SDT sensor based eddy current probe for detection of deep fatigue cracks in multi-layer structure," *NDT & E International*, vol. 43, no. 8, pp. 718–725, 2010.
(pages 8, 9).
- [16] H. J. Krause and M. von Kreutzbruck, "Recent developments in SQUID NDE," *Physica C: Superconductivity*, vol. 368, no. 1-4, pp. 70–79, 2002.
(pages 9, 9, 10).
- [17] M. Mueck, M. von Kreutzbruck, U. Baby, J. Troell, and C. Heiden, "Eddy Current Nondestructive Material Evaluation based on HTS SQUIDS," *Physica C: Superconductivity*, vol. 282, no. 1, pp. 407–410, 1997.
(page 9, 9).
- [18] H. Weinstock, "A Review of SQUID Magnetometry Applied to Nondestructive Evaluation," *IEEE Transactions on Magnetics*, vol. 27, no. 2, pp. 3231–3236, 1991.
(page 9).
- [19] J. A. Lobera-Serrano, J. R. Claycomb, J. H. Miller, and K. Salama, "Hybrid Double-D Sheet-Inducer for SQUID-Based NDT," *IEEE Transactions on Applied Superconductivity*, vol. 11, no. 1, pp. 1283–1286, 2001.
(page 9).
- [20] Y. Tavrín, H. J. Krause, W. Wolf, V. Glyantsev, J. Schubert, W. Zander, and H. Bousack, "Eddy current technique with high temperature SQUID for non-destructive evaluation of non-magnetic metallic structures," *Cryogenics*, vol. 36, no. 2, pp. 83–86, 1996.
(pages 9, 10).
- [21] W. G. Jenks, Sadeghi, S S H, and J. P. Wikswo, "SQUIDS for nondestructive evaluation," *Journal of Physics D: Applied Physics*, vol. 30, no. 3, pp. 293–323, 1997.
(page 9).
- [22] A. Braginski and H.-J. Krause, "Nondestructive evaluation using high-temperature SQUIDS," *Physica C: Superconductivity*, vol. 335, no. 1-4, pp. 179–183, 2000.
(page 9).
- [23] G. Mook, F. Michel, and J. Simonin, "Electromagnetic Imaging Using Probe Arrays," *SV-JME (Strojniški vestnik - Journal of Mechanical Engineering)*, vol. 57, no. 3, pp. 227–236, 2011.
(page 9).
- [24] O. Postolache, A. L. Ribeiro, and H. G. Ramos, "GMR array uniform eddy current probe for defect detection in conductive specimens," *Measurement*, vol. 46, no. 10, pp. 4369–4378, 2013.
(page 9).

- [25] J. Jun, J. Hwang, and J. Lee, "Quantitative Nondestructive Evaluation of the Crack on the Austenite Stainless Steel Using the Induced Eddy Current and the Hall Sensor Array," *Proceedings of the IEEE Instrumentation & Measurement Technology Conference IMTC*, pp. 1–6, 2007.
(page 9).
- [26] Y. He, M. Pan, F. Luo, and G. Tian, "Pulsed eddy current imaging and frequency spectrum analysis for hidden defect nondestructive testing and evaluation," *NDT & E International*, vol. 44, no. 4, pp. 344–352, 2011.
(page 9).
- [27] D. L. Atherton, "Remote field eddy current inspection," *IEEE Transactions on Magnetics*, vol. 31, no. 6, pp. 4142–4147, 1995.
(page 9).
- [28] B. A. Auld and J. C. Moulder, "Review of advances in quantitative eddy current nondestructive evaluation," *Journal of Nondestructive Evaluation*, vol. 18, no. 1, pp. 3–36, 1999.
(page 9).
- [29] J. García-Martín, J. Gómez-Gil, and E. Vázquez-Sánchez, "Non-Destructive Techniques Based on Eddy Current Testing," *Sensors*, vol. 11, no. 3, pp. 2525–2565, 2011.
(page 9).
- [30] G. Mook, O. Hesse, and V. Uchanin, "Deep Penetrating Eddy Currents and Probes," *Proceeding of the ECNDT*, pp. Tu.3.6.2(1–14), 2006.
(pages 10, 67, 69, 70).
- [31] G. Almeida, J. Gonzalez, L. Rosado, P. Vilaça, and T. G. Santos, "Advances in NDT and Materials Characterization by Eddy Currents," *Procedia CIRP*, vol. 7, no. 1, pp. 359–364, 2013.
(page 10).
- [32] M. Carlstedt, K. Porzig, R. P. Uhlig, M. Zec, M. Ziolkowski, and H. Brauer, "Application of Lorentz force eddy current testing and eddy current testing on moving nonmagnetic conductors," *International Journal of Applied Electromagnetics and Mechanics*, vol. 45, no. 1, pp. 519–526, 2014.
(pages 10, 16, 17, 18, 18, 18, 43).
- [33] A. Gasparics, C. S. Daroczi, G. Vertesy, and J. Pavo, "Improvement of ECT Probes Based on Fluxset Type Magnetic Field Sensor," *Studies in Applied Electromagnetics and Mechanics, Electromagnetic Non-Destructive Evaluation (II)*, vol. 14, no. 1, pp. 146–151, 1998.
(page 10).
- [34] T. Dogaru and S. T. Smith, "Giant Magnetoresistance-Based Eddy-Current Sensor," *IEEE Transactions on Magnetics*, vol. 37, no. 5, pp. 3831–3838, 2001.
(page 10).
- [35] R. Sikora, T. Chady, S. Gratkowski, M. Komorowski, and K. Stawicki, "Eddy Current Testing of Thick Aluminum Plates with Hidden Cracks," *Review of Quantitative Nondestructive Evaluation*, vol. 22, no. 1, pp. 427–434, 2003.
(page 10).
- [36] K. Tsukada, T. Kiwa, T. Kawata, and Y. Ishihara, "Low-Frequency Eddy Current Imaging Using MR Sensor Detecting Tangential Magnetic Field Components for Nondestructive Evaluation," *IEEE Transactions on Magnetics*, vol. 42, no. 10, pp. 3315–3317, 2006.
(page 10).
- [37] H. Yamada, T. Hasegawa, Y. Ishihara, T. Kiwa, and K. Tsukada, "Difference in the detection limits of flaws in the depths of multi-layered and continuous aluminum plates using low-frequency eddy current testing," *NDT & E International*, vol. 41, no. 2, pp. 108–111, 2008.
(page 10).

BIBLIOGRAPHY

- [38] R. Hamia, C. Cordier, S. Saez, and C. Dolabdjian, "Eddy-Current Nondestructive Testing Using an Improved GMR Magnetometer and a Single Wire as Inducer: A FEM Performance Analysis," *IEEE Transactions on Magnetism*, vol. 46, no. 10, pp. 3731–3737, 2010.
(page 10).
- [39] M. Cacciola, G. Megali, D. Pellicano, S. Calcagno, M. Versaci, and F. C. Morabito, "Modelling and Validating Ferrite-core Probes for GMR-eddy Current Testing in Metallic Plates," *PIERS Online*, vol. 6, no. 3, pp. 237–241, 2010.
(page 10).
- [40] H. Horng, J. Jeng, H. Yang, and J. Chen, "Evaluation of the flaw depth using high-Tc SQUID," *Physica C: Superconductivity*, vol. 367, no. 1-4, pp. 303–307, 2002.
(page 10).
- [41] J.-T. Jeng, H.-E. Horng, and H.-C. Yang, "Crack detection for the graphite slab using the high-Tc SQUID in unshielded environment," *Physica C: Superconductivity*, vol. 372-376, no. 1, pp. 174–177, 2002.
(page 10).
- [42] K. Allweins, G. Gierelt, H.-J. Krause, and M. v. Kreutzbruck, "Defect Detection in Thick Aircraft Samples Based on HTS SQUID-Magnetometry and Pattern Recognition," *IEEE Transactions on Applied Superconductivity*, vol. 13, no. 2, pp. 250–253, 2003.
(page 10).
- [43] M. Fardmanesh, F. Sarreshtedari, A. Pourhashemi, E. Ansari, M. A. Vesaghi, J. Schubert, M. Banzet, and H.-J. Krause, "Optimization of NDE Characterization Parameters for a RF-SQUID Based System Using FEM Analysis," *IEEE Transactions on Applied Superconductivity*, vol. 19, no. 3, pp. 791–795, 2009.
(page 10).
- [44] W. M. Saslow, "Maxwell's theory of eddy currents in thin conducting sheets, and applications to electromagnetic shielding and MAGLEV," *American Journal of Physics*, vol. 60, no. 8, pp. 693–711, 1992.
(pages 11, 89).
- [45] E. Bachelet, "Foucault and Eddy Currents put to Service," *The Engineer*, vol. 114, pp. 420–421, Oct. 1912.
(pages 11, 89).
- [46] J. R. Reitz, "Forces on Moving Magnets due to Eddy Currents," *Journal of Applied Physics*, vol. 41, no. 5, pp. 2067–2071, 1970.
(pages 11, 89, 104).
- [47] —, "Force on a Rectangular Coil Moving above a Conducting Slab," *Journal of Applied Physics*, vol. 43, no. 4, pp. 1547–1553, 1972.
(pages 11, 89, 103).
- [48] P. L. Richards, "Magnetic Suspension and Propulsion Systems for High-Speed Transportation," *Journal of Applied Physics*, vol. 43, no. 6, pp. 2680–2691, 1972.
(page 11).
- [49] R. H. Borcherts, "Force on a Coil Moving over a Conducting Surface Including Edge and Channel Effects," *Journal of Applied Physics*, vol. 43, no. 5, pp. 2418–2427, 1972.
(page 11).
- [50] R. H. Borcherts, L. C. Davis, J. R. Reitz, and D. F. Wilkie, "Baseline specifications for a magnetically suspended high-speed vehicle," *Proceedings of the IEEE*, vol. 61, no. 5, pp. 569–578, 1973.
(page 11).
- [51] L. C. Davis, "Drag force on a magnet moving near a thin conductor," *Journal of Applied Physics*, vol. 43, no. 10, pp. 4256–4257, 1972.
(page 11).

- [52] S.-W. Lee and R. C. Menendez, "Force on current coils moving over a conducting sheet with application to magnetic levitation," *Proceedings of the IEEE*, vol. 62, no. 5, pp. 567–577, 1974.
(pages 12, 89, 103).
- [53] J. van Bladel and D. de Zutter, "Magnetic Levitation: The Track Currents," *Applied Physics B: Lasers and Optics*, vol. 34, no. 4, pp. 193–201, 1984.
(page 12).
- [54] D. de Zutter, "Levitation force acting on a three-dimensional static current source moving over a stratified medium," *Journal of Applied Physics*, vol. 58, no. 7, pp. 2751–2758, 1985.
(pages 12, 89).
- [55] S. Panas and E. E. Kriezis, "Eddy current distribution due to a rectangular current frame moving above a conducting slab," *Archiv für Elektrotechnik*, vol. 69, no. 3, pp. 185–191, 1986.
(pages 12, 89).
- [56] H. M. G. Ramos, T. Rocha, D. Pasadas, and A. Ribeiro, "Velocity induced eddy currents technique to inspect cracks in moving conducting media," *Proceedings of the International Instrumentation and Measurement Technology Conference (I2MTC)*, pp. 931–934, 2013.
(page 12).
- [57] H. G. Ramos, T. Rocha, D. Pasadas, and A. L. Ribeiro, "Faraday induction effect applied to the detection of defects in a moving plate," *Review of Progress in Quantitative Nondestructive Evaluation*, vol. 32, no. 1, pp. 1490–1497, 2013.
(page 12).
- [58] T. Rocha, H. Ramos, A. L. Ribeiro, and D. Pasadas, "Sub-Surface Defect Detection with Motion Induced Eddy Currents in Aluminium," *Proceedings of the International Instrumentation and Measurement Technology Conference (I2MTC)*, pp. 930–934, 2015.
(page 12).
- [59] H. G. Ramos, T. Rocha, A. L. Ribeiro, and D. Pasadas, "GMR versus differential coils in velocity induced eddy current testing," *Proceedings of the International Instrumentation and Measurement Technology Conference (I2MTC)*, pp. 915–918, 2014.
(pages 11, 12, 90).
- [60] T. J. Rocha, H. G. Ramos, A. Lopes Ribeiro, D. J. Pasadas, and C. S. Angani, "Studies to optimize the probe response for velocity induced eddy current testing in aluminium," *Measurement*, vol. 67, no. 1, pp. 108–115, 2015.
(page 12).
- [61] T. J. Rocha, H. G. Ramos, A. Lopes Ribeiro, and D. J. Pasadas, "Magnetic sensors assessment in velocity induced eddy current testing," *Sensors and Actuators A: Physical*, vol. 228, no. 1, pp. 55–61, 2015.
(page 12).
- [62] Y. Tan, X. Wang, and R. Moreau, "An innovative contactless method for detecting defects in electrical conductors by measuring a change in electromagnetic torque," *Measurement Science and Technology*, vol. 26, no. 3, pp. 035 602(1–0 356 028), 2015.
(pages 11, 12).
- [63] A. Thess, E. Votyakov, and Y. Kolesnikov, "Lorentz Force Velocimetry," *Physical Review Letters*, vol. 96, no. 16, pp. 164 501(1–1 645 014), 2006.
(pages 13, 48).
- [64] A. Thess, E. Votyakov, B. Knaepen, and O. Zikanov, "Theory of the Lorentz force flowmeter," *New Journal of Physics*, vol. 9, no. 8, pp. 299(1–2927), 2007.
(pages 13, 104, 111).

BIBLIOGRAPHY

- [65] M. Ziolkowski and H. Brauer, "Fast Computation Technique of Forces Acting on Moving Permanent Magnet," *IEEE Transactions on Magnetics*, vol. 46, no. 8, pp. 2927–2930, 2010.
(page 13).
- [66] R. P. Uhlig, "Identification of Material Defects in Metallic Materials Using Lorentz Force Eddy Current Testing," Ph.D. dissertation, Technische Universität Ilmenau, Ilmenau, Germany, 2013.
(pages 13, 16, 16, 16).
- [67] M. Zec, "Theory and Numerical Modelling of Lorentz Force Eddy Current Testing," Ph.D. dissertation, Technische Universität Ilmenau, Ilmenau, Germany, 2013.
(pages 13, 28, 29).
- [68] R. P. Uhlig, M. Zec, H. Brauer, and A. Thess, "Lorentz Force Eddy Current Testing: a Prototype Model," *Journal of Nondestructive Evaluation*, vol. 31, no. 4, pp. 357–372, 2012.
(pages 13, 112).
- [69] G. Donoso, C. L. Ladera, and P. Martín, "Damped fall of magnets inside a conducting pipe," *American Journal of Physics*, vol. 79, no. 2, pp. 193–200, 2011.
(pages 13, 112).
- [70] R. P. Uhlig, M. Zec, M. Ziolkowski, H. Brauer, and A. Thess, "Lorentz force sigmometry: A contactless method for electrical conductivity measurements," *Journal of Applied Physics*, vol. 111, no. 9, pp. 094914(1–0949147), 2012.
(page 13).
- [71] R. P. Uhlig, M. Zec, M. Ziolkowski, and H. Brauer, "Lorentz Force Eddy Current Testing: Validation of Numerical Results," *Proceedings of the Electrotechnical Institute*, no. 251, pp. 135–145, 2011.
(page 14).
- [72] M. Zec, R. P. Uhlig, M. Ziolkowski, and H. Brauer, "Three-dimensional Numerical Investigations of Lorentz Force Eddy Current Testing," *Studies in Applied Electromagnetics and Mechanics, Electromagnetic Nondestructive Evaluation XVI*, vol. 38, no. 1, pp. 83–93, 2014.
(page 14).
- [73] B. Petković, "Assessment of Linear Inverse Problems in Magnetocardiography and Lorentz Force Eddy Current Testing," Ph.D. dissertation, Technische Universität Ilmenau, Ilmenau, Germany, 2013.
(page 14).
- [74] H. Brauer, K. Porzig, J. Mengelkamp, M. Carlstedt, M. Ziolkowski, and H. Toepfer, "Lorentz force eddy current testing: a novel NDE-technique," *COMPEL*, vol. 33, no. 6, pp. 1965–1977, 2014.
(pages 14, 15).
- [75] M. Carlstedt, "A Contribution to the Experimental Validation in Lorentz Force Eddy Current Testing," Ph.D. dissertation, Technische Universität Ilmenau, Ilmenau, Germany, 2016.
(pages 16, 16, 16, 66, 68, 70).
- [76] ME-Meßsysteme GmbH, "Datenblatt: Mehrachsen-Kraftsensor K3D40," 2014.
(pages 16, 51, 59).
- [77] M. Carlstedt, K. Porzig, M. Ziolkowski, R. P. Uhlig, H. Brauer, and H. Toepfer, "Comparison of Lorentz Force Eddy Current Testing and Common Eddy Current Testing - Measurements and Simulations," *Studies in Applied Electromagnetics and Mechanics*, vol. 39, no. 1, pp. 218–225, 2013.
(pages 16, 17, 18, 43).
- [78] K. Porzig, M. Carlstedt, M. Ziolkowski, H. Brauer, and H. Toepfer, "Reverse engineering of ECT probes for nondestructive evaluation of moving conductors," *AIP Conference Proceedings*, vol. 1581, no. 1, pp. 1519–1525, 2014.
(pages 16, 17).

- [79] A. Einstein, “Zur Elektrodynamik bewegter Körper,” *Annalen der Physik*, vol. 17, no. 1, pp. 891–921, 1905. (page 20).
- [80] H. Minkowski, “Die Grundgleichungen fuer die elektromagnetischen Vorgaenge in bewegten Koerpern,” *Mathematische Annalen*, vol. 68, no. 4, pp. 472–525, 1910. (page 21).
- [81] J. van Bladel, *Electromagnetic fields*, 2nd ed. Piscataway: Wiley-IEEE Press, 2007. (pages 22, 91).
- [82] K. Weise, M. Ziolkowski, M. Carlstedt, H. Brauer, and H. Toepfer, “Oscillatory Motion of Permanent Magnets Above a Conducting Slab,” *IEEE Transactions on Magnetics*, vol. 51, no. 10, pp. 7 209 113(1–72 091 113), 2015. (pages 23, 90, 91, 95, 97, 100, 102, 103, 104, 105, 107, 108, 109).
- [83] P. A. Davidson, *An introduction to magnetohydrodynamics*, ser. Cambridge texts in applied mathematics. Cambridge and New York: Cambridge University Press, 2001. (page 24).
- [84] J. D. Jackson, *Classical electrodynamics*, 3rd ed. New York: Wiley, 1999. (pages 24, 33).
- [85] C. Lanczos, *The variational principles of mechanics*, 4th ed., ser. Dover books on physics and chemistry. New York: Dover Publications, 1970. (page 24).
- [86] Z. Ren, “Comparison of Different Force Calculation Methods in 3D Finite Element Modelling,” *IEEE Transactions on Magnetics*, vol. 30, no. 5, pp. 3471–3474, 1994. (page 24, 24).
- [87] M. Ito, F. Tajima, and H. Kanazawa, “Evaluation of Force Calculating Methods,” *IEEE Transactions on Magnetics*, vol. 26, no. 2, pp. 1035–1038, 1990. (page 24).
- [88] O. C. Zienkiewicz, R. L. Taylor, and J. Z. Zhu, *The Finite Element Method: Its Basis and Fundamentals*, 6th ed. Amsterdam: Elsevier Butterworth-Heinemann, 2005. (page 24, 24).
- [89] J. P. Bastos and N. Sadowski, *Electromagnetic Modeling by Finite Element Methods*, ser. Electrical and computer engineering. New York: Marcel Dekker, Inc., 2003, vol. 117. (page 24).
- [90] S. Humphries, *Field Solutions on Computers*. Boca Raton: CRC Press, 1998. (page 24).
- [91] M. N. O. Sadiku, *Numerical Techniques in Electromagnetics*, 2nd ed. Boca Raton: CRC Press, 2000. (page 24).
- [92] W. B. J. Zimmerman, *Process Modelling and Simulation with Finite Element Methods*, ser. Series on stability, vibration, and control of systems. Series A. Singapore and Hackensack, NJ: World Scientific, 2004, vol. 15. (page 24).
- [93] “COMSOL Multiphysics,” 2014. Version 4.4. COMSOL, Inc., Burlington, MA, USA. (pages 25, 55, 100).
- [94] C. Emson and J. Simkin, “An Optimal Method for 3-D Eddy Currents,” *IEEE Transactions on Magnetics*, vol. 19, no. 6, pp. 2450–2452, 1983. (page 26, 26).

BIBLIOGRAPHY

- [95] P. J. Leonard and D. Rodger, "Comparison of Methods for Modelling Jumps in Conductivity using Magnetic Vector Potential based Formulations," *IEEE Transactions on Magnetism*, vol. 33, no. 2, pp. 1295–1298, 1997.
(page 26).
- [96] O. Biro, "Edge element formulations of eddy current problems," *Computer Methods in Applied Mechanics and Engineering*, vol. 169, no. 3-4, pp. 391–405, 1999.
(pages 26, 27, 131).
- [97] O. Biro and K. Preis, "On the Use of the Magnetic Vector Potential in the Finite Element Analysis of Three-Dimensional Eddy Currents," *IEEE Transactions on Magnetism*, vol. 25, no. 4, pp. 3145–3159, 1989.
(page 27).
- [98] M. Zec, R. P. Uhlig, M. Ziolkowski, and H. Brauer, "Finite Element Analysis of Nondestructive Testing Eddy Current Problems With Moving Parts," *IEEE Transactions on Magnetism*, vol. 49, no. 8, pp. 4785–4794, 2013.
(pages 28, 28, 29).
- [99] —, "Lorentz Force Eddy Current Testing: Two-Dimensional Numerical Study," *Proceedings of the Electrotechnical Institute*, vol. 252, pp. 55–66, 2011.
(page 29).
- [100] E. P. Furlani, *Permanent magnet and electromechanical devices: Materials, analysis, and applications*. San Diego and London: Academic Press, 2001.
(pages 33, 94, 117).
- [101] N. Derby and S. Olbert, "Cylindrical magnets and ideal solenoids," *American Journal of Physics*, vol. 78, no. 3, pp. 229–235, 2010.
(pages 33, 112).
- [102] R. Jankoski, K. Porzig, and H. Brauer, "Extended Version of the Weak Reaction Approach in Lorentz Force Eddy Current Testing," *Proceedings of the 9th International Workshop of Electromagnetic Compatibility (CEM)*, pp. 1–4, 2014.
(page 33, 33).
- [103] P. J. Davis and P. Rabinowitz, *Methods of numerical integration*, 2nd ed. Mineola: Dover Publications, 2007.
(page 33).
- [104] J. M. Borwein and P. B. Borwein, *Pi and the AGM: A study in analytic number theory and computational complexity*. New York: Wiley, 1987.
(page 33).
- [105] J. Mengelkamp, M. Ziolkowski, K. Weise, M. Carlstedt, H. Brauer, and J. Haueisen, "Permanent Magnet Modeling for Lorentz Force Evaluation," *IEEE Transactions on Magnetism*, vol. 51, no. 7, pp. 6201211(1–6201211), 2015.
(page 33).
- [106] M. Zec, R. P. Uhlig, M. Ziolkowski, and H. Brauer, "Fast Technique for Lorentz Force Calculations in Nondestructive Testing Applications," *IEEE Transactions on Magnetism*, vol. 50, no. 2, pp. 7003104(1–7003104), 2014.
(page 33).
- [107] K. Weise, R. Schmidt, M. Carlstedt, M. Ziolkowski, H. Brauer, and H. Toepfer, "Optimal Magnet Design for Lorentz Force Eddy Current Testing," *IEEE Transactions on Magnetism*, vol. 51, no. 9, pp. 6201415(1–6201415), 2015.
(pages 44, 45, 47, 52, 57, 60, 62, 64, 65).

- [108] VACUUMSCHMELZE GmbH & Co. KG, Hanau, "Weichmagnetische Kobalt-Eisen-Legierungen: Vacoflux 48, Vacoflux 50 Vacodur 49, Vacodur 50, Vacodur S Plus, Vacoflux 17, Vacoflux 18 HR, Vacoflux 9 CR," Hanau, 2001.
(pages 46, 47, 59).
- [109] VACUUMSCHMELZE GmbH & Co. KG, Hanau. Selten-Erd-Dauermagnete: Vacodym, Vacomax. Hanau. [Online]. Available: http://www.vacuumschmelze.de/fileadmin/Medienbibliothek_2010/Downloads/DM/Vdym_Vmax_de.pdf [Accessed: 07.10.2014]
(pages 46, 47, 59).
- [110] J. C. Mallinson, "One-sided fluxes – A magnetic curiosity?" *IEEE Transactions on Magnetics*, vol. 9, no. 4, pp. 678–682, 1973.
(page 46, 46).
- [111] K. Halbach, "Design of Permanent Multipole Magnets with Oriented Rare-Earth Cobalt Material," *Nuclear Instrumentation & Methods*, vol. 169, no. 1, pp. 1–10, 1980.
(page 46, 46).
- [112] Z. Q. Zhu and D. Howe, "Halbach permanent magnet machines and applications: a review," *IEE Proceedings - Electric Power Applications*, vol. 148, no. 4, pp. 299–308, 2001.
(page 46).
- [113] G. Lemarquand, "Ironless Loudspeakers," *IEEE Transactions on Magnetics*, vol. 43, no. 8, pp. 3371–3374, 2007.
(page 46).
- [114] R. Ravaut, G. Lemarquand, V. Lemarquand, and C. Depollier, "Discussion about the Analytical Calculation of the Magnetic Field Created by Permanent Magnets," *Progress In Electromagnetics Research B*, vol. 11, no. 1, pp. 281–297, 2009.
(pages 46, 112).
- [115] A. N. Vučković, N. B. Raičević, S. S. Ilić, S. R. Aleksić, and M. T. Perić, "Axial Force Calculation of Passive Magnetic Bearing," *Serbian Journal of Electrical Engineering*, vol. 11, no. 4, pp. 649–660, 2014.
(page 46).
- [116] N. Dogan, R. Topkaya, H. Subaşı, Y. Yerli, and B. Rameev, "Development of Halbach magnet for portable NMR device," *Journal of Physics: Conference Series*, vol. 153, pp. 012 047(1–0 120 478), 2009.
(page 46).
- [117] M. Werner and B. Halbedel, "Optimization of NdFeB Magnet Arrays for Improvement of Lorentz Force Velocimetry," *IEEE Transactions on Magnetics*, vol. 48, no. 11, pp. 2925–2928, 2012.
(page 47).
- [118] Quanling Peng, S. M. McMurry, and J. Coey, "Cylindrical Permanent-Magnet Structures Using Images in an Iron Shield," *IEEE Transactions on Magnetics*, vol. 39, no. 4, pp. 1983–1989, 2003.
(page 47).
- [119] M. Kumada, T. Fujisawa, Y. Hirao, M. Endo, M. Aoki, T. Kohda, I. Bolshakova, and R. Holyaka, "Development of 4 Tesla Permanent Magnet," *Proceedings of the Particle Accelerator Conference*, pp. 3221–3223, 2001.
(page 47, 47).
- [120] VACUUMSCHMELZE GmbH & Co. KG, Hanau. Hanau. [Online]. Available: <http://www.vacuumschmelze.de/> [Accessed: 07.10.2014]
(page 47).

BIBLIOGRAPHY

- [121] T. Mihara, Y. Iwashita, M. Kumada, A. Evgeny, and C. M. Spencer, “Super Strong Permanent Magnet Quadrupole for a Linear Collider,” *IEEE Transactions on Applied Superconductivity*, vol. 14, no. 2, pp. 469–472, 2004.
(page 47).
- [122] Y. Iwashita, T. Mihara, E. Antokhin, M. Kumada, and M. Aoki, “Permanent Magnet Quadrupole for Final Focus for Linear Collider,” *Proceedings of the Particle Accelerator Conference*, pp. 2198–2200, 2003.
(page 47).
- [123] P. E. Gill, W. Murray, and M. H. Wright, *Practical Optimization*. London and New York: Academic Press, 1981.
(pages 51, 53, 54, 55).
- [124] W. C. Davidon, *Variable Metric Methods for Minimization*. Lemont: Argonne National Laboratory, 1959.
(page 53).
- [125] —, “Variable Metric Method for Minimization,” *SIAM Journal on Optimization*, vol. 1, no. 1, pp. 1–17, 1991.
(page 53).
- [126] M. C. Biggs, “Constrained Minimization Using Recursive Quadratic Programming,” *Proceedings of a workshop towards global optimisation*, pp. 341–349, 1975.
(page 53).
- [127] S. P. Han, “A Globally Convergent Method for Nonlinear Programming,” *Journal of Optimization Theory and Applications*, vol. 22, no. 3, pp. 297–309, 1977.
(pages 53, 55, 55).
- [128] M. J. D. Powell, “A Fast Algorithm for Nonlinearly Constrained Optimization Calculations,” *Proceedings of the Biennial Conference on numerical analysis*, pp. 144–157, 1978.
(pages 53, 55, 55).
- [129] C. G. Broyden, “The Convergence of a Class of Double-rank Minimization Algorithms 1. General Considerations,” *Journal of the Institute of Mathematics and Its Applications*, vol. 6, no. 3, pp. 76–90, 1970.
(page 55).
- [130] —, “The Convergence of a Class of Double-rank Minimization Algorithms 2. The New Algorithm,” *Journal of the Institute of Mathematics and Its Applications*, vol. 6, no. 3, pp. 222–231, 1970.
(page 55).
- [131] R. Fletcher, “A New Approach to Variable Metric Algorithms,” *Computer Journal*, vol. 13, no. 3, pp. 317–322, 1970.
(page 55).
- [132] D. Goldfarb, “A Family of Variable-Metric Methods Derived by Variational Means,” *Mathematics of Computation*, vol. 24, no. 109, pp. 23–26, 1970.
(page 55).
- [133] D. F. Shanno, “Conditioning of Quasi-Newton Methods for Function Minimization,” *Mathematics of Computation*, vol. 24, no. 111, pp. 647–656, 1970.
(page 55).
- [134] W. Karush, “Minima of Functions of Several Variables with Inequalities as Side Conditions,” Ph.D. dissertation, Department of Mathematics, University of Chicago, Chicago, IL, USA, 1939.
(page 55).
- [135] W. Alt, *Nichtlineare Optimierung: Eine Einfuehrung in Theorie, Verfahren und Anwendungen*, 2nd ed. Wiesbaden: Vieweg und Teubner, 2011.
(page 55).

-
- [136] J. Nocedal and S. J. Wright, *Numerical Optimization*, 2nd ed. New York: Springer, 2006. (page 55).
- [137] S.-P. Han, “Superlinearly Convergent Variable Metric Algorithms for General Nonlinear Programming Problems,” *Mathematical Programming*, vol. 11, no. 1, pp. 263–282, 1976. (page 55).
- [138] M. J. D. Powell, “Some Global Convergence Properties of a Variable Metric Algorithm for Minimization without Exact Line Searches,” *SIAM-AMS-Proceedings: Nonlinear Programming*, vol. 9, no. 1, pp. 53–72, 1976. (page 55).
- [139] —, “The Convergence of Variable Metric Methods for Nonlinearly Constrained Optimization Calculations,” *Nonlinear Programming 3*, pp. 27–63, 1978. (page 55).
- [140] P. T. Boggs and J. W. Tolle, “Sequential Quadratic Programming,” *Acta Numerica*, vol. 4, no. 1, pp. 1–52, 1995. (page 55).
- [141] P. E. Gill and E. Wong, Eds., *Sequential Quadratic Programming Methods: Technical Report NA-10-03*, University of California, San Diego, La Jolla, 2010. (page 55).
- [142] K. Schittkowski, “The Nonlinear Programming Method of Wilson, Han, and Powell with an Augmented Lagrangian Type Line Search Function Part 1: Convergence Analysis,” *Numerische Mathematik*, vol. 38, no. 1, pp. 83–114, 1981. (page 55).
- [143] —, “The Nonlinear Programming Method of Wilson, Han, and Powell with an Augmented Lagrangian Type Line Search Function Part 2: An Efficient Implementation with Linear Least Squares Subproblems,” *Numerische Mathematik*, vol. 38, no. 1, pp. 115–127, 1981. (page 55).
- [144] —, “On the convergence of a sequential quadratic programming method with an augmented Lagrangian line search function,” *Mathematische Operationsforschung und Statistik. Series Optimization: A Journal of Mathematical Programming and Operations Research*, vol. 14, no. 2, pp. 197–216, 1983. (page 55).
- [145] “MATLAB,” 2013. R2013a. The MathWorks, Inc., Natick, MA, USA. (page 55).
- [146] P. E. Gill, W. Murray, M. A. Saunders, and M. H. Wright, “User’s Guide for NPSOL 5.0: A Fortran Package for Nonlinear Programming,” *Technical Report SOL 86-6*, pp. 1–43, 2001. (page 55).
- [147] P. E. Gill, W. Murray, and M. A. Saunders, “SNOPT: An SQP Algorithm for Large-Scale Constrained Optimization,” *SIAM Review*, vol. 47, no. 1, pp. 99–131, 2005. (page 55).
- [148] —. (2008) User’s Guide for SNOPT Version 7: Software for Large-Scale Nonlinear Programming. [Online]. Available: <http://web.stanford.edu/group/SOL/guides/sndoc7.pdf> [Accessed: 8.10.2014] (page 55).
- [149] K. Schittkowski. (2014) NLPQLP - Nonlinear Programming with Non-Monotone and Distributed Line Search. [Online]. Available: <http://www.ai7.uni-bayreuth.de/nlpqlp.htm> [Accessed: 18.08.2014] (page 55, 55).
- [150] —. (2010) NLPQLP: A Fortran Implementation of a Sequential Quadratic Programming Algorithm with Distributed and Non-Monotone Line Search - User’s Guide, Version 3.1. [Online]. Available: <http://www.ai7.uni-bayreuth.de/NLPQLP.pdf> [Accessed: 8.10.2014]

BIBLIOGRAPHY

- (page 55).
- [151] “LiveLink for MATLAB User’s Guide,” 2014. Version 4.4. COMSOL, Inc., Burlington, MA, USA.
(page 55).
- [152] J. Mengelkamp, “Inverse Calculation Methods in Lorentz Force Evaluation for Laminated Composites,” Ph.D. dissertation, Technische Universitaet Ilmenau, Ilmenau, Germany, 2016.
(pages 66, 70).
- [153] K. Weise, M. Carlstedt, and R. Schmidt, “Defect Depth Study Considering a Long Slit and a Cylindrical Magnet,” *TU Ilmenau Technical Report TET-2015-05*, no. 5, 2015.
(page 67).
- [154] G. Gautschi, *Piezoelectric sensorics: Force, strain, pressure, acceleration and acoustic emission sensors, materials and amplifiers*. Berlin: Springer, 2002.
(page 69).
- [155] R. Schmidt, K. Weise, M. Carlstedt, M. Ziolkowski, H. Brauer, and H. Toepfer, “Optimized Lorentz Force Eddy Current Testing System for Small Metal Injection Molding Specimens,” *20th International Workshop on Electromagnetic Nondestructive Evaluation (ENDE)*, pp. 1–8, 2015.
(page 69).
- [156] O. Moreau, K. Beddek, S. Clenet, and Y. Le Menach, “Stochastic Nondestructive Testing Simulation: Sensitivity Analysis Applied to Material Properties in Clogging of Nuclear Powerplant Steam Generators,” *IEEE Transactions on Magnetism*, vol. 49, no. 5, pp. 1873–1876, 2013.
(page 71).
- [157] K. Beddek, S. Clenet, O. Moreau, V. Costan, Y. Le Menach, and A. Benabou, “Adaptive Method for Non-Intrusive Spectral Projection—Application on a Stochastic Eddy Current NDT Problem,” *IEEE Transactions on Magnetism*, vol. 48, no. 2, pp. 759–762, 2012.
(page 71).
- [158] G. S. Fishman, *Monte Carlo: Concepts, algorithms, and applications*, ser. Springer series in operations research. New York: Springer-Verlag, 1996.
(page 71).
- [159] M. D. McKay, R. J. Beckman, and W. J. Conover, “A Comparison of Three Methods for Selecting Values of Input Variables in the Analysis of Output from a Computer Code,” *Technometrics*, vol. 42, no. 1, pp. 55–61, 2000.
(page 71).
- [160] W. J. Morokoff and R. E. Caflisch, “Quasi-Monte Carlo Integration,” *Journal of Computational Physics*, vol. 122, no. 2, pp. 218–230, 1995.
(page 71).
- [161] L. Plaskota and H. Woźniakowski, *Monte Carlo and Quasi-Monte Carlo Methods 2010*. Berlin, Heidelberg: Springer, 2012, vol. 23.
(page 71).
- [162] D. Xiu, “Fast Numerical Methods for Stochastic Computations: A Review,” *Communications in Computational Physics*, vol. 5, no. 2-4, pp. 242–272, 2009.
(pages 71, 74, 77).
- [163] Le Maitre, O. P. and O. M. Knio, *Spectral Methods for Uncertainty Quantification*. Dordrecht: Springer, 2010.
(pages 71, 75).
- [164] O. M. Knio and Le Maitre, O. P., “Uncertainty propagation in CFD using polynomial chaos decomposition,” *Fluid Dynamics Research*, vol. 38, no. 9, pp. 616–640, 2006.
(page 71).

- [165] D. Xiu and G. E. Karniadakis, "Modeling uncertainty in flow simulations via generalized polynomial chaos," *Journal of Computational Physics*, vol. 187, no. 1, pp. 137–167, 2003.
(page 71).
- [166] S. Hosder, R. Perez, and R. Walters, "A Non-Intrusive Polynomial Chaos Method For Uncertainty Propagation in CFD Simulations," *Proceedings of the 44th AIAA Aerospace Sciences Meeting and Exhibit*, pp. AIAA2006–891(1–19), 2006.
(page 71).
- [167] X. Wan, D. Xiu, and G. E. Karniadakis, "Modeling uncertainty in three-dimensional heat transfer problems," *Proceedings of the International Conference on Heat Transfer*, pp. 1–11, 2004.
(page 71).
- [168] D. Xiu and G. E. Karniadakis, "A new stochastic approach to transient heat conduction modeling with uncertainty," *International Journal of Heat and Mass Transfer*, vol. 46, no. 24, pp. 4681–4693, 2003.
(page 71).
- [169] A. Sandu, C. Sandu, and M. Ahmadian, "Modeling Multibody Systems with Uncertainties. Part I: Theoretical and Computational Aspects," *Multibody System Dynamics*, vol. 15, no. 4, pp. 369–391, 2006.
(page 71).
- [170] C. Sandu, A. Sandu, and M. Ahmadian, "Modeling Multibody Systems with Uncertainties. Part II: Numerical Applications," *Multibody System Dynamics*, vol. 15, no. 3, pp. 241–262, 2006.
(page 71).
- [171] S. Zein, "A Polynomial Chaos Expansion Trust Region Method for Robust Optimization," *Communications in Computational Physics*, 2013.
(page 71).
- [172] K. Weise, L. Di Rienzo, H. Brauer, J. Haueisen, and H. Toepfer, "Uncertainty Analysis in Transcranial Magnetic Stimulation Using Non-intrusive Polynomial Chaos Expansion," *IEEE Transactions on Magnetics*, vol. 51, no. 7, pp. 5 000 408(1–50 004 088), 2015.
(pages 71, 72).
- [173] L. Codecasa, L. Di Rienzo, K. Weise, S. Gross, and J. Haueisen, "Fast MOR-based Approach to Uncertainty Quantification in Transcranial Magnetic Stimulation," *IEEE Transactions on Magnetics*, vol. 52, no. 3, pp. 1–4, 2016 (in press).
(page 71).
- [174] R. G. Ghanem and P. Spanos, *Stochastic finite elements: A spectral approach*. New York: Springer, 1991.
(page 72).
- [175] N. Wiener, "The Homogeneous Chaos," *American Journal of Mathematics*, vol. 60, no. 4, pp. 897–936, 1938.
(page 72).
- [176] D. Xiu and J. S. Hesthaven, "High-Order Collocation Methods for Differential Equations with Random Inputs," *SIAM Journal on Scientific Computing*, vol. 27, no. 3, pp. 1118–1139, 2005.
(page 72).
- [177] I. Babuška, F. Nobile, and R. Tempone, "A Stochastic Collocation Method for Elliptic Partial Differential Equations with Random Input Data," *SIAM Review*, vol. 52, no. 2, pp. 317–355, 2010.
(page 72).
- [178] K. Weise, M. Carlstedt, M. Ziolkowski, and H. Brauer, "Uncertainty Analysis in Lorentz Force Eddy Current Testing," *IEEE Transactions on Magnetics*, vol. 52, no. 3, pp. 1–4, 2016 (in press).
(pages 72, 84, 85, 86, 87, 87).

BIBLIOGRAPHY

- [179] R. Askey and J. W. Wilson, “Some Basic Hypergeometric Orthogonal Polynomials that Generalize Jacobi-Polynomials,” *Memoirs of the American Mathematical Society*, vol. 54, no. 319, pp. 1–55, 1985.
(page 73).
- [180] R. Ghanem and P. D. Spanos, *Stochastic finite elements: A spectral approach*, revised edition ed. New York: Dover Publications, 2003.
(page 74).
- [181] G. H. Golub and J. H. Welsch, “Calculation of Gauss Quadrature Rules,” *Mathematics of Computation*, vol. 23, no. 106, pp. 221–230, 1969.
(page 76).
- [182] I. Sobol, “Global sensitivity indices for nonlinear mathematical models and their Monte Carlo estimates,” *Mathematics and Computers in Simulation*, vol. 55, no. 1-3, pp. 271–280, 2001.
(page 77).
- [183] B. Sudret, “Global sensitivity analysis using polynomial chaos expansions,” *Reliability Engineering & System Safety*, vol. 93, no. 7, pp. 964–979, 2008.
(page 77).
- [184] M. Abramowitz and I. A. Stegun, *Handbook of mathematical functions: With formulas, graphs, and mathematical tables*. New York: Dover Publications, 1970.
(pages 78, 96, 116, 135, 137).
- [185] H. Knoepfel, *Magnetic fields: A comprehensive theoretical treatise for practical use*. New York: Wiley, 2000.
(page 83).
- [186] M. L. Delignette-Muller and C. Dutang, “fitdistrplus: An R Package for Fitting Distributions,” *Journal of Statistical Software*, vol. 64, no. 4, pp. 1–34, 2015.
(page 84).
- [187] A. Singh, “Theory of eddy-current brakes with thick rotating disc,” *Proceedings of the Institution of Electrical Engineers*, vol. 124, no. 4, pp. 373–376, 1977.
(page 89).
- [188] S. Sharif, J. Faiz, and K. Sharif, “Performance analysis of a cylindrical eddy current brake,” *IET Electric Power Applications*, vol. 6, no. 9, pp. 661–668, 2012.
(page 89).
- [189] H.-W. Lee, K.-C. Kim, and J. Lee, “Review of maglev train technologies,” *IEEE Transactions on Magnetics*, vol. 42, no. 7, pp. 1917–1925, 2006.
(page 89).
- [190] J. Miericke and L. Urankar, “Theory of electrodynamic levitation with a continuous sheet track — Part I,” *Applied Physics*, vol. 2, no. 4, pp. 201–211, 1973.
(page 89).
- [191] L. Urankar and J. Miericke, “Theory of electrodynamic levitation with a continuous sheet track — Part II,” *Applied Physics*, vol. 3, no. 1, pp. 67–76, 1974.
(page 89).
- [192] J. E. Xypteras and E. E. Kriezis, “Force on a vertical circular current loop moving above a conducting slab and eddy current distribution,” *Archiv für Elektrotechnik*, vol. 63, no. 6, pp. 309–315, 1981.
(page 89).
- [193] M. Kanamori and Y. Ishihara, “Finite-Element Analysis of an Electromagnetic Damper Taking into Account the Reaction of the Magnetic Field,” *JSME International Journal Series III - Vibration Control Engineering, Engineering for Industry*, vol. 32, no. 1, pp. 36–43, 1989.

- (page 90).
- [194] L. Zuo, X. Chen, and S. Nayfeh, "Design and Analysis of a New Type of Electromagnetic Damper With Increased Energy Density," *Journal of Vibration and Acoustics*, vol. 133, no. 4, pp. 041 006(1–0 410 068), 2011.
(page 90).
- [195] B. Ebrahimi, M. B. Khamesee, and F. Golnaraghi, "Permanent magnet configuration in design of an eddy current damper," *Microsystem Technologies*, vol. 16, no. 1, pp. 19–24, 2010.
(pages 90, 126).
- [196] J. W. Jansen, E. A. Lomonova, and J. M. M. Rovers, "Effects of eddy currents due to a vacuum chamber wall in the airgap of a moving-magnet linear actuator," *Journal of Applied Physics*, vol. 105, no. 7, pp. 07F111–1–3, 2009.
(page 90).
- [197] R. Palomera-Arias, J. J. Connor, and J. A. Ochsendorf, "Feasibility Study of Passive Electromagnetic Damping Systems," *Journal of Structural Engineering*, vol. 134, no. 1, pp. 164–170, 2008.
(page 90).
- [198] Y. Zhang, K. Huang, F. Yu, Y. Gu, and D. Li, "Experimental verification of energy-regenerative feasibility for an automotive electrical suspension system," *Proceedings of the International Conference on Vehicular Electronics and Safety*, pp. 1–5, 2007.
(pages 90, 110).
- [199] J. W. Jansen, B. Gysen, J. J. H. Paulides, and E. A. Lomonova, "Advanced electromagnetic modeling applied to anti-vibration systems for high precision and automotive applications," *International Compumag Society Newsletter*, vol. 1, no. 19, pp. 3–16, 2012.
(page 90).
- [200] L. Collins, "Harvest for the world: Energy harvesting techniques," *Power Engineer*, vol. 20, no. 1, pp. 34–37, 2006.
(page 90).
- [201] L. Zuo and X. Tang, "Large-scale vibration energy harvesting," *Journal of Intelligent Material Systems and Structures*, vol. 24, no. 11, pp. 1405–1430, 2013.
(pages 90, 105).
- [202] L. Zuo, B. Scully, J. Shestani, and Y. Zhou, "Design and characterization of an electromagnetic energy harvester for vehicle suspensions," *Smart Materials and Structures*, vol. 19, no. 4, pp. 045 003(1–0 450 010), 2010.
(pages 90, 126).
- [203] X. Tang, T. Lin, and L. Zuo, "Design and Optimization of a Tubular Linear Electromagnetic Vibration Energy Harvester," *IEEE/ASME Transactions on Mechatronics*, vol. 19, no. 2, pp. 615–622, 2014.
(page 90).
- [204] K. J. W. Pluk, T. A. van Beek, J. W. Jansen, and E. A. Lomonova, "Modeling and Measurements on a Finite Rectangular Conducting Plate in an Eddy Current Damper," *IEEE Transactions on Industrial Electronics*, vol. 61, no. 8, pp. 4061–4072, 2014.
(page 90).
- [205] N. Amati, A. Tonoli, A. Canova, F. Cavalli, and M. Padovani, "Dynamic Behavior of Torsional Eddy-Current Dampers: Sensitivity of the Design Parameters," *IEEE Transactions on Magnetics*, vol. 43, no. 7, pp. 3266–3277, 2007.
(page 90).
- [206] B.-T. Ooi and A. R. Eastham, "Transverse Edge Effects of Sheet Guideways in Magnetic Levitation," *IEEE Transactions on Power Apparatus and Systems*, vol. 94, no. 1, pp. 72–80, 1975.

BIBLIOGRAPHY

- (page 90).
- [207] B.-T. Ooi, “Electromechanical Stiffness and Damping Coefficients in the Repulsive Magnetic Levitation System,” *IEEE Transactions on Power Apparatus and Systems*, vol. 95, no. 3, pp. 936–943, 1976.
(page 90).
- [208] —, “A Dynamic Circuit Theory of the Repulsive Magnetic Levitation System,” *IEEE Transactions on Power Apparatus and Systems*, vol. 96, no. 4, pp. 1094–1100, 1977.
(page 90).
- [209] B. Ooi and O. Jain, “Force Transients at Guideway Butt Joints in Repulsive Magnetic Levitation System,” *IEEE Transactions on Power Apparatus and Systems*, vol. PAS-98, no. 1, pp. 323–330, 1979.
(page 90).
- [210] B.-T. Ooi and Om Jain, “Moments and Force Densities of the Electrodynamic Levitation System,” *IEEE Transactions on Magnetics*, vol. 15, no. 3, pp. 1102–1108, 1979.
(page 90).
- [211] C. Weidemann, I. Sokolov, and A. Thess, “Lorentz Force and Joule Heat Induced in an Electrically Conducting Plate Moving With Time-Dependent Velocity Under the Influence of a Homogeneous Magnetic Field,” *IEEE Transactions on Magnetics*, vol. 50, no. 8, pp. 7027–7029, 2014.
(page 90).
- [212] T. Shiozawa, “Phenomenological and Electron-Theoretical Study of the Electrodynamics of Rotating Systems,” *Proceedings of the IEEE*, vol. 61, no. 12, pp. 1694–1702, 1973.
(page 91).
- [213] J. van Bladel, “Relativistic Theory of Rotating Disks,” *Proceedings of the IEEE*, vol. 61, no. 3, pp. 260–268, 1973.
(page 92).
- [214] T. C. Mo, “Theory of Electrodynamics in Media in Noninertial Frames and Applications,” *Journal of Mathematical Physics*, vol. 11, no. 8, pp. 2589–2610, 1970.
(page 92).
- [215] S. S. Haykin, *Communication systems*, 4th ed. New York: Wiley, 2001.
(page 96).
- [216] G. P. Tolstov and R. A. Silverman, *Fourier series*. New York and London: Dover Publications and Constable, 1976.
(pages 97, 116).
- [217] L. F. Shampine, “Vectorized adaptive quadrature in MATLAB,” *Journal of Computational and Applied Mathematics*, vol. 211, no. 2, pp. 131–140, 2008.
(page 99).
- [218] —, “Weighted quadrature by change of variable,” *Neural, Parallel & Scientific Computations*, vol. 18, no. 2, pp. 195–206, 2010.
(page 99).
- [219] A. Canova and B. Vusini, “Analytical Modeling of Rotating Eddy-Current Couplers,” *IEEE Transactions on Magnetics*, vol. 41, no. 1, pp. 24–35, 2005.
(page 110).
- [220] E. V. Votyakov and A. Thess, “Interaction of a magnetic dipole with a slowly moving electrically conducting plate,” *Journal of Engineering Mathematics*, vol. 77, no. 1, pp. 147–161, 2012.
(page 111).

- [221] A. Viré, B. Knaepen, and A. Thess, “Lorentz force velocimetry based on time-of-flight measurements,” *Physics of Fluids*, vol. 22, no. 12, pp. 125 101(1–1 251 015), 2010.
(page 112).
- [222] F. B. Santara and A. Thess, “Electromagnetic force on a current-carrying coil interacting with a moving electrically conducting cylinder,” *Journal of Engineering Mathematics*, vol. 90, no. 1, pp. 37–49, 2015.
(page 112).
- [223] I. R. Ciric, “Fields, losses and forces due to moving current distributions coaxial with a cylindrical conductor,” *COMPEL - The international journal for computation and mathematics in electrical and electronic engineering*, vol. 20, no. 1, pp. 62–71, 2001.
(pages 112, 116).
- [224] C. S. MacLatchy, “A Quantitative Magnetic Braking Experiment,” *American Journal of Physics*, vol. 61, no. 12, pp. 1096–1101, 1993.
(page 112).
- [225] J. A. Pelesko, M. Cesky, and S. Huertas, “Lenz’s law and dimensional analysis,” *American Journal of Physics*, vol. 73, no. 1, pp. 37–39, 2005.
(page 112).
- [226] Y. Levin, da Silveira, Fernando L., and F. B. Rizzato, “Electromagnetic braking: A simple quantitative model,” *American Journal of Physics*, vol. 74, no. 9, pp. 815–817, 2006.
(page 112).
- [227] G. Ireson and J. Twidle, “Magnetic braking revisited: activities for the undergraduate laboratory,” *European Journal of Physics*, vol. 29, no. 4, pp. 745–751, 2008.
(page 112).
- [228] G. Donoso, C. L. Ladera, and P. Martín, “Magnet fall inside a conductive pipe: motion and the role of the pipe wall thickness,” *European Journal of Physics*, vol. 30, no. 4, pp. 855–869, 2009.
(page 112).
- [229] B. Irvine, M. Kemnetz, A. Gangopadhyaya, and T. Ruubel, “Magnet traveling through a conducting pipe: A variation on the analytical approach,” *American Journal of Physics*, vol. 82, no. 4, pp. 273–279, 2014.
(page 112).
- [230] B. A. Knyazev, I. A. Kotel’nikov, A. A. Tyutin, and V. S. Cherkasskii, “Braking of a magnetic dipole moving with an arbitrary velocity through a conducting pipe,” *Physics-Uspekhii*, vol. 49, no. 9, pp. 937–946, 2006.
(page 112).
- [231] M. H. Partovi and E. J. Morris, “Electrodynamics of a magnet moving through a conducting pipe,” *Canadian Journal of Physics*, vol. 84, no. 4, pp. 253–271, 2006.
(page 112).
- [232] R. Ravaud, G. Lemarquand, V. Lemarquand, and C. Depollier, “Analytical Calculation of the Magnetic Field Created by Permanent-Magnet Rings,” *IEEE Transactions on Magnetics*, vol. 44, no. 8, pp. 1982–1989, 2008.
(page 112).
- [233] S. I. Babic and C. Akyel, “Improvement in the analytical calculation of the magnetic field produced by permanent magnet rings,” *Progress In Electromagnetics Research C*, vol. 5, no. 1, pp. 71–82, 2008.
(page 112).
- [234] H. L. Rakotoarison, J.-P. Yonnet, and B. Delinchant, “Using Coulombian Approach for Modeling Scalar Potential and Magnetic Field of a Permanent Magnet With Radial Polarization,” *IEEE Transactions on Magnetics*, vol. 43, no. 4, pp. 1261–1264, 2007.
(page 112).

BIBLIOGRAPHY

- [235] E. P. Furlani, S. Reznik, and A. Kroll, "A Three-Dimensional Field Solution for Radially Polarized Cylinders," *IEEE Transactions on Magnetics*, vol. 31, no. 1, pp. 844–851, 1995.
(page 112).
- [236] K. Weise, M. Carlstedt, M. Ziolkowski, H. Brauer, and H. Toepfer, "Lorentz Force on Permanent Magnet Rings by Moving Electrical Conductors," *IEEE Transactions on Magnetics*, vol. 51, no. 12, pp. 6202–6211(1–62022112), 2015.
(pages 112, 113, 118, 121, 122, 123, 124, 125).
- [237] P. H. Moon and D. E. Spencer, *Field theory handbook; Including coordinate systems, differential equations and their solutions*, 2nd ed. Berlin and New York: Springer, 1971.
(page 115).
- [238] Pavel Holoborodko, "GaussLegendre," 2014, <http://www.holoborodko.com/pavel/numerical-methods/numerical-integration/>, 03/06/15.
(page 121).
- [239] W. Gander and W. Gautschi, "Adaptive Quadrature - Revisited," *BIT Numerical Mathematics*, vol. 40, no. 1, pp. 84–101, 2000.
(page 121).
- [240] J. R. Dormand and P. J. Prince, "A family of embedded Runge-Kutta formulae," *Journal of Computational and Applied Mathematics*, vol. 6, no. 1, pp. 19–26, 1980.
(page 125).
- [241] J. Chung and G. M. Hulbert, "A Time Integration Algorithm for Structural Dynamics With Improved Numerical Dissipation: The Generalized-alpha Method," *Journal of Applied Mechanics*, vol. 60, no. 2, pp. 371–375, 1993.
(page 125).
- [242] K. Weise, M. Carlstedt, M. Ziolkowski, H. Brauer, and H. Toepfer, "Sensoreinheit, System und Verfahren zur Detektion und Lokalisierung von Anomalien in Prüfobjekten aus elektrisch leitfähigem Material," Germany Patent 10 2015 004 607.1 (pending), 31.03.2015.
(page 127, 127).
- [243] S. N. Rajesh, L. Udpa, and S. S. Udpa, "Estimation of Eddy Current Probability of Detection (PoD) Using Finite Element Method," *Review of Progress in Quantitative Nondestructive Evaluation*, vol. 12, no. 1, pp. 2365–2372, 1993.
(page 131).
- [244] E. Ginzler, "Introduction to the Statistics of NDT," *NDT.net*, vol. 11, no. 5, pp. 1–4, 2006.
(page 131, 131).